UNIVERSITÀ DEGLI STUDI DELL'AQUILA

Department of Civil, Construction-Architectural and
Environmental Engineering

DOCTORAL THESIS

Mathematical and physical models of beams with cellular microstructure

Ph.D Course in Civil, Construction-Architectural and Environmental Engineering

XXXVIII cycle

Candidate

Chiara Pancella

SSD

CEAR-06/A

Course Coordinator

Prof. Federico De Matteis

Thesis Tutor

Prof. Francesco D'Annibale

Co-Tutor

Prof. Manuel Ferretti

Mathematical and physical models of beams with cellular microstructure

Chiara Pancella

Prof. Francesco D'Annibale

Mathematical and physical models of beams with cellular microstructure

Chiara Pancella
Candidate ID number: 289602

Department of Civil, Construction-Architectural and Environmental Engineering-DICEAA
University of L'Aquila

 This thesis has been typeset by LaTeX and phdiceaa class.

Website: http://diceaa.univaq.it/

Abstract

In recent years, metamaterials have been widely studied as they combine the practical demands for structural optimization and material innovation with the desire to explore new frontiers in the mechanics of materials and structures. In fact, thanks to a proper design, they can exhibit characteristics that overcome those of conventional materials, such as low stiffness-to-weight ratio, ductile failure, exotic behaviors, high resilience, and greater impact resistance. For their analysis, homogenization techniques have proven to be particularly effective: despite the transition from a discrete model, with a finite number of degrees of freedom, to a homogenized equivalent continuum, with infinite degrees of freedom, they enable a significant reduction in computational effort thanks to the simplification of the equations that describe their behavior.

This thesis investigates the mechanical behavior of beam-like structures through the development, according to the homogenization approach, and the validation, through comparisons with Finite Element (FE) models, of one-dimensional models embedded in a 2D space. Two types of metamaterials are studied, namely the grain and the grid beam. For both, an equivalent beam model is formulated within the framework of the direct one-dimensional approach, in which the constitutive law is derived through the so-called mixed homogenization procedure. The latter is based on enforcing energy equivalence between a unit cell (the smallest repeatable unit of the periodic model) and a segment of the solid beam (equivalent model) of the same length. The homogenization procedure can be carried out either analytically or numerically, with the numerical approach relying on a FE analysis of the cell.

The grain beam is made of a periodic assembly of grain-pairs interconnected with solid bars. This configuration gives rise to a metamaterial that through a coupled axial-shear mechanical response exhibits chirality, and is indeed here referred to as 'chiral metamaterial'. The equivalent model is formulated under the assumption of rigid cross-sections, both in plane and out of their plane, and the identification of the elastic coefficients is performed, through a cell analysis, analytically and numerically. The analytical procedure also allows a qualitative investigation of the mechanical response, showing that the elastic coefficients depend on specific non-dimensional parameters, thus enabling the design of the chirality itself. The inertial properties are analytically identified under the assumption of masses lumped at the joints.

The grid beam is a framed microstructure made of two orthogonal families of (micro)

beams. Unlike the chiral case, this beam-like structure is identified assuming a rigid in plane and deformable (or rigid) out of plane cross-section. In this framework, the warping phenomenon induced by shear is particularly significant. Nevertheless, it is not adequately described by classical beam theories and, moreover, the models available in the literature for grid beams are able to describe the deformation of the cross-section only on average and for particularly simple case studies. To overcome these limitations, this thesis develops a homogenized beam model that extends classical formulations by introducing additional strain measures capable of capturing both distortional and bi-distortional deformation modes. In this case as well, the elastic coefficients are identified analytically and numerically, while the inertial properties are analytically identified under the assumption of masses lumped at the joints.

The mechanical response of both metamaterials is investigated under static, free dynamic, and buckling conditions where, in this latter, the equivalent model accounts for both the (classical) global and the (non-conventional) local geometric effects. Results obtained from the homogenized models are compared with those derived from FE analyses and, in the grain beam's case, from experimental data, in order to assess the effectiveness and limitations of the proposed equivalent models.

Sommario

Negli ultimi anni i metamateriali sono stati ampiamente studiati poiché combinano le esigenze pratiche di ottimizzazione strutturale e innovazione dei materiali con il desiderio di esplorare nuove frontiere nella meccanica dei materiali e delle strutture. Infatti, grazie a una progettazione adeguata, possono presentare caratteristiche superiori a quelle dei materiali convenzionali, quali un basso rapporto rigidezza-peso, modalità di rottura duttili, comportamenti esotici, elevata resilienza e maggiore resistenza all'impatto. Per la loro analisi, le tecniche di omogeneizzazione si sono dimostrate particolarmente efficaci: nonostante il passaggio da un modello discreto, con un numero finito di gradi di libertà, a un continuo equivalente omogeneizzato, con infiniti gradi di libertà, esse consentono una significativa riduzione dell'onere computazionale grazie alla semplificazione delle equazioni che ne descrivono il comportamento.

Questa tesi analizza il comportamento meccanico di strutture assimilabili a travi attraverso lo sviluppo, secondo la tecnica di omogeneizzazione, e la validazione, mediante confronti con modelli agli elementi finiti, di modelli monodimensionali immersi in uno spazio 2D. Due tipi di metamateriali sono oggetto di studio, ovvero la trave a grani e la trave grid. Per entrambi si formula un modello equivalente di trave nell'ambito dell'approccio diretto monodimensionale, nel quale la legge costitutiva è ricavata tramite la cosiddetta procedura di omogeneizzazione mista. Quest'ultima si basa sull'imposizione dell'equivalenza energetica tra una cella unitaria (cioè, la più piccola unità ripetibile del modello periodico) e un segmento della trave solida (modello equivalente) di pari lunghezza. La procedura di omogeneizzazione può essere eseguita sia analiticamente sia numericamente, con l'approccio numerico basato su un'analisi agli elementi finiti della cella.

La trave a grani è costituita da un assemblaggio periodico di coppie di grani interconnesse mediante barre solide. Tale configurazione dà origine a un metamateriale che, a causa dell'accoppiamento tra deformazioni assiali e di taglio, manifesta chiralità ed è infatti qui denominato come 'metamateriale chirale'. Il modello equivalente è formulato assumendo sezioni rigide, sia nel piano sia fuori dal loro piano, e l'identificazione dei coefficienti elastici è eseguita, attraverso un'analisi della cella, sia analiticamente sia numericamente. La procedura analitica consente inoltre un'indagine qualitativa della risposta meccanica, mostrando che i coefficienti elastici dipendono da specifici parametri adimensionali, rendendo così possibile anche la progettazione mirata della chiralità stessa. Le proprietà

inerziali sono identificate analiticamente assumendo l'ipotesi di masse concentrate ai nodi.

La trave grid è una microstruttura a telaio costituita da due famiglie ortogonali di (micro) travi. A differenza del caso chirale, questa struttura tipo trave è identificata assumendo la sezione trasversale rigida nel piano e deformabile (o rigida) fuori dal piano. In tale contesto, il fenomeno dell'ingobbamento indotto dal taglio risulta particolarmente significativo. Tuttavia, non è descritto in modo soddisfacente dalle teorie classiche delle travi e, inoltre, i modelli disponibili in letteratura per le travi grid riescono a rappresentare la deformazione della sezione soltanto in media e per casi di studio particolarmente semplici. Per superare tali limitazioni, questa tesi sviluppa un modello di trave omogeneizzato che estende le formulazioni classiche introducendo misure di deformazione aggiuntive, capaci di catturare sia i modi distorsionali sia i modi bidistorsionali. Anche in questo caso, i coefficienti elastici sono identificati analiticamente e numericamente, mentre le proprietà inerziali sono identificate analiticamente assumendo l'ipotesi di masse concentrate ai nodi.

La risposta meccanica di entrambi i metamateriali è indagata in condizioni statiche, di dinamica libera e di instabilità, dove, in quest'ultima, il modello equivalente tiene conto degli effetti geometrici sia globali (classici) che locali (non convenzionali). I risultati ottenuti dai modelli omogeneizzati vengono confrontati con quelli derivati da analisi agli elementi finiti e, nel caso della trave a grani, anche con dati sperimentali, al fine di valutarne l'efficacia e le relative limitazioni.

Contents

Chapter 1

Introduction

Metamaterials have proved to be an effective framework for fulfilling specific performance requirements. Indeed, unlike traditional materials, they enable the realization of tailored mechanical responses at the macroscopic level, such as controlled deformability or auxetic behavior, by simply designing the material's microstructure. This capability has opened new frontiers in research, especially in response to demands such as increased stiffness-to-weight ratio, enhanced impact resistance, ductile failure mechanisms, and high resilience.

However, the microstructures' design remains highly dependent on modeling tools that must be able to predict the metamaterial's overall response. In this context, the use of equivalent models, obtained through homogenization, represents a crucial step in reducing computational complexity. As is known, homogenization allows treating heterogeneous materials as if they were homogeneous by replacing their properties with equivalent homogeneous ones that describe the average behavior of the system. Several homogenization approaches have been proposed in the literature, such as heuristic and asymptotic methods, but also the mixed homogenization approach and the Granular Micromechanics Approach, (GMA), each grounded in assumptions that can differ even substantially from one another. Once the homogenized properties are identified, existing analytical models for homogeneous materials can be employed.

Of course, the effectiveness of homogenized models must be assessed. This is typically done through FE analyses, although experimental testing is highly desirable to ensure a more comprehensive validation. These latter are essential to understand if the theoretical assumptions underlying the equivalent models are capable of reproducing the real behavior of the metamaterial. In this context, 3D printing plays a key role, as it enables the fabrication of specimens with complex microstructures. Once the tests have been carried out, advanced measurement techniques such as Digital Image Correlation (DIC) can be applied to obtain high-resolution experimental data, providing valuable insight into the mechanical response of the metamaterial.

Thesis overview

This thesis investigates the mechanical behavior of two metamaterials, the grain and the grid beam, embedded in a 2D space and modeled as equivalent continua through the mixed homogenization approach. These metamaterials exhibit markedly distinct microstructures, whose geometric and topological characteristics give rise to different macroscopic mechanical behaviors.

At first, the grain beam, so called because it is made of a periodic assembly of grain-pairs interconnected with solid bars, is studied under the assumption of in plane and out of plane rigid cross-section. The identification of the elastic coefficients, performed analytically and numerically, requires introducing specific assumptions regarding the geometry of the interconnecting elements between grain pairs and the deformability of these latter. Moreover, a qualitative analysis, based on the analytical identification of the constitutive matrix, has highlighted the dependence of the elastic coefficients on suitably defined non-dimensional parameters, thereby enabling the tailored design of the grain beam microstructure to achieve prescribed macroscopic behaviors. As for the inertial characteristics, they are analytically identified by representing the mass distribution through lumped masses at the joints. The proposed equivalent beam model is then validated by studying the mechanical behavior of the beam under static, dynamic, and buckling conditions, and by comparing the results with those obtained from FE simulations. A further validation in statics is performed through comparison with experimental data, thereby confirming the model's capability to reproduce the experimentally observed behavior.

Then, the grid beam, which is made of a single planar frame composed of two orthogonal families of fibers, is analyzed. Its mechanical behavior is investigated under the assumption of in plane rigid and out of plane deformable (or rigid) cross-section. Within this framework, a generalized beam model is proposed as the equivalent representation, capable of capturing the distortional and bidistortional effects which arise from the out of plane deformability. These latter are not adequately described by classical beam theories. In fact, although de Saint Venant acknowledges their importance, his formulation neglects distributed volumetric loads; similarly, Timoshenko's theory introduces a shear correction factor but still assumes out of plane undeformability of the cross-section. To overcome these limitations, in the present thesis they are accounted for by introducing additional kinematic variables associated with cross-section warping, which in turn give rise to 'new' generalized external forces, namely the static quantities dual to the newly introduced kinematic ones. In this case as well, the constitutive matrix is determined through both analytical and numerical procedures, whereas the inertial properties are evaluated analytically under the assumption of lumped masses located at the joints. The proposed model is validated by comparing its static, dynamic, and buckling responses with the results of FE analyses.

The work is organized as follows. In Chapter 2, some background is supplied. In Chapter 3, the equations of the equivalent beam formulations are set, and the procedure adopted for the identification of elastic and inertial constants is explained. In Chapter 4, the equivalent beam model presented in Chapter 3 is specialized to the grain beam. A qualitative analysis of the mechanical behavior of the microstructure is carried out, and the results obtained from the equivalent beam model are compared with those predicted by the FE model and with findings from preliminary experimental tests. In Chapter 5, the equivalent beam model presented in Chapter 3 is specialized to the grid beam, and comparisons between the proposed model and the FE simulations are discussed. In Chapter 6, some conclusions are drawn. Finally, three appendices close the thesis. Appendix A presents the solution of the boundary value problems obtained through both analytical and numerical methods. Appendix B reports the analytical expressions of the constitutive matrices identified for both metamaterials. Appendix C illustrates an application of the mixed homogenization approach to civil engineering structures, such as buildings and towers, which can be regarded as periodic systems similar to metamaterials.

Chapter 2

State of the art

Several applied disciplines have shown a growing interest in the study of periodic systems with microstructure, such as metamaterials and engineered materials. This phenomenon has been driven both by significant advances in design supported by mathematical modeling and by new opportunities offered by 3D printing for their practical fabrication, see, e.g., [1–10]. Metamaterials are periodic systems whose overall macroscopic mechanical behavior is governed by the geometry and topology of the underlying microstructure, rather than by the intrinsic properties of the material itself. Owing to their microstructured nature, these systems are able to exhibit exceptional characteristics that overcome those of conventional bulk materials (see, e.g. [9–15]), such as, for example, low lightweight-stiffness ratio, non-standard deformation mechanisms, resilience, impact resistance, and exotic behaviors.

Metamaterials are currently investigated and employed in many scientific and engineering disciplines, giving rise to a wide and heterogeneous range of applications. In civil engineering, metamaterials have been investigated as lightweight structural components with a very low lightweight-stiffness ratio, and improved energy dissipation capabilities. Periodic systems based on lattice microstructures have been proposed for vibration mitigation in slender structures, such as towers, bridges, and floors, as well as for the attenuation of dynamic loads induced by wind, traffic, or machinery. Other metamaterials, designed to interact with elastic waves at low frequencies, have opened new perspectives in the mitigation of ground-borne vibrations and, more generally, in seismic protection strategies, where control over wave propagation mechanisms plays a crucial role.

In aerospace and automotive engineering, interest in metamaterials is mainly associated with lightweight structural design, vibration reduction, and multifunctional performance. Lattice and cellular microstructures are currently employed or under investigation as load-bearing components, sandwich panel cores, and energy-absorbing devices, allowing for significant mass reduction while preserving adequate mechanical strength and stiffness. In addition, the frequency-dependent dynamic behavior exhibited by periodic architectures has motivated their use in components designed to suppress undesirable vibrations and noise, which is particularly relevant in aerospace structures and next-generation automo-

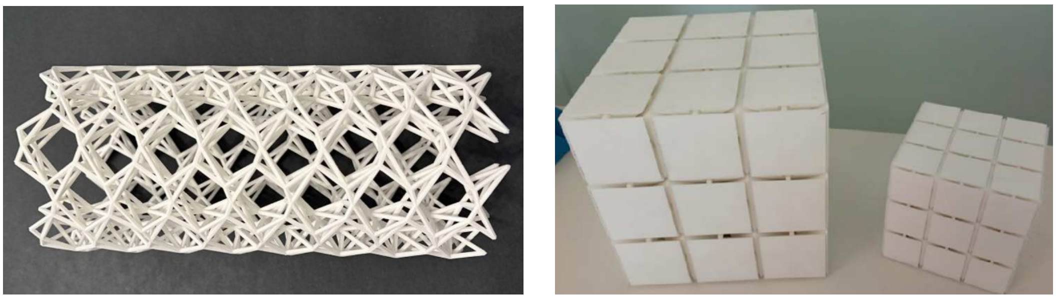

(a) (b)

Figure 2.1. Additive manufactured metamaterials: (a) kagome-tube based lattice with topological polarization (adapted from [16]); (b) three-dimensional elastic metamaterial with low-frequency band gap (adapted from [17]).

tive systems.

A further area of growing relevance concerns the control of wave propagation in elastic and acoustic media. Mechanical and acoustic metamaterials have been developed to manipulate wave transmission, reflection, and localization through the introduction of band gaps and unconventional dispersion properties that are not attainable in traditional materials.

Moreover, recent advances in additive manufacturing technologies have substantially contributed to the development of microstructured materials by enabling the fabrication of complex periodic structures with high accuracy (see Fig. 2.1 for some examples). Fig. 2.1a shows a metamaterial based on the kagome-tube geometry, which in [16] is studied as a topologically polarized mechanical lattices capable of wave manipulation. This structure exhibit directional localization of low-energy deformation and vibration modes, induced by their underlying topological polarization, thereby enabling passive geometry-driven vibration isolation. Fig. 2.1b, instead, depicts a three-dimensional elastic metamaterial which, as demonstrated in [17], exhibits a complete and ultra-wide low-frequency band gap in a sub-wavelength regime. This behavior is enabled by a mode separation mechanism between massive elements and slender elastic ligaments, resulting in an effective mechanical filtering capability. Different additive manufacturing techniques, each exhibiting distinct strengths and limitations in terms of resolution, material selection, and attainable geometric complexity, are currently employed for the realization of architected materials. Among these techniques, Fused Deposition Modeling (FDM) represents one of the most accessible solutions due to its relative simplicity and low cost, and is commonly adopted for the fabrication of polymer-based lattice structures. Stereolithography (SLA) offer significantly higher geometric resolution, making them particularly suitable for the realization of intricate details. Powder-based techniques, such as selective laser sintering or melting, enable the fabrication of metallic metamaterials with enhanced mechanical strength and durability, thereby extending the range of potential structural applications. Ultimately, metamaterials can now be physically realized and experimentally tested. This technological progress has further reinforced the necessity of numerical (or analytical) descriptions capable of capturing the mechanical behavior of periodic structures. Numerical approaches, such as those based on FE analysis, are very important for the detailed design and analysis of periodic structures; nevertheless, there is a growing interest in the literature in getting simple models via homogenization techniques (see, e.g., [18–20] and the recent reviews [21, 22]). In fact, the equivalent models (i) require, in general, a lower computational effort to solve the elastic problem with respect to correspondent finite-element ones, (ii) offer interpretive advantages compared to purely numerical modeling in terms of structural global behavior, and, even more important, (iii) closed-form solutions can be pursued in several problems of engineering interest, such as static, dynamic and buckling analyses of periodic structures.

Different philosophies underlie the homogenization techniques proposed in the literature. Some approaches assume a priori the target model, without explicitly linking microscopic and macroscopic quantities (see, e.g., [23–25]). More rigorous formulations are provided by asymptotic homogenization, where the equivalent continuum is derived from a multiscale analysis (see, e.g., [20, 26, 27]). Between these two extremes, a mixed formulation, namely the mixed homogenization approach, has been developed. This latter combines the heuristic and the asymptotic method since the continuum model is heuristically assumed, but the micro-macro relationships are analytically determined on the ground of energy balances between the smallest repeatable element of the periodic system, i.e. the cell, and a segment of the continuous beam (see, e.g., [28–38]). Moreover, depending on the complexity of the microstructure at hand, the mixed homogenization approach allows to determine the elastic coefficients both analytically and numerically. The above classification is not exhaustive, but it captures the main methodological trends relevant to the present work.

Among the many metamaterials proposed in the literature, the so-called grain and grid beams represent two classes of periodic structures that exhibit markedly different mechanical behaviors. These metamaterials have been extensively investigated through both analytical and numerical approaches. In the following, a brief overview is provided, focusing on the aspects that are most relevant to the present work.

Grain beams

There exist some metamaterial that cannot be superimposed on their mirror image and, therefore, exhibit the property of chirality. These are also known as chiral metamaterials, and the grain beam studied in this work is one of them.

Two-dimensional chiral metamaterials, see, e.g., [39–43], can be used to achieve mechanical anisotropy, as in [39], and an auxetic behavior with a negative Poisson's ratio, as in [40, 41], and also to balance bending loads through tensile loads, as in [42]. For example, in [41], a chiral honeycomb metamaterial, representative of four distinct classes of 2D Euclidean tessellations with hexagonal rotational symmetry, is designed to obtain a new auxetic material. In [42], a tetrachiral unit-cell is studied to demonstrate that the coupling of normal and shear deformations can be used as a primal loadbalancing mechanism. The developed analytical model has been validated through both numerical simulations and experiments. In [43], the chirality in 2D Cosserat-like micromorphic continua is examined, establishing a connection with grain-scale mechanics through the Granular Micromechanics Approach (GMA). The study emphasizes the fact that additional kinematic descriptors are needed in modeling granular materials in order to properly describe grain-relative displacements. Also three-dimensional chiral metamaterials have been extensively studied in the literature, see, e.g., [44–46]. In [44], a gammadion-shaped chiral comprising inclined ligaments was incorporated into the chiral structure to achieve high torsional compliance. In [45], 3D chiral and achiral mechanical metamaterial were designed extending the 2D 'missing-rib' type of chiral cell to 3D with spherical tiling. The chiral design showed the compression-twisting coupling while the achiral design showed an auxetic behavior. In [46], the buckling strength of the chiral lattice columns, constructed by periodically placing the inclined straight beams in a chiral manner, which exhibit compression-twisting coupling effect, was studied. Its deformation was described with a constitutive model based on the Cosserat rod theory and, with the semi-analytical homogenization method proposed, the effects of chirality on the buckling strength and buckling mode were revealed.

As for the first of the two periodic structures of interest in this thesis work, the (chiral) grain beam, it was conceived in [1, 2], as the mechanical (rheological) analog of the peculiar interaction of a granular material that is composed by a set of solid bars connecting two grains. In [2], a non-standard Timoshenko beam model for such a chiral metamaterial, is proposed; accordingly, a numerical procedure, which is grounded on a Finite-Element modeling of the whole periodic structure, is applied for the identification of the constants of the constitutive matrix of the equivalent beam model. The procedure involves solving three distinct types of planar equilibrium problems, referred to as identification tests. The selection of these identification tests, and thus the choice of boundary and load conditions, derives from the necessity to engage a subset of the stiffnesses enabled by the specific microstructure. Simulations were conducted using a 2D Cauchy continuum, with the left and right boundary grains treated as rigid domains. It is worth to notice that the microstructure of [2] is of scientific interest because its behavior reveals common tracts also with mechanical cable models or the analysis of DNA filaments [47–49]. In the literature, numerous microstructures based on chiral geometry exist, each exploring various connections between adjacent cells distinct from the one studied in [2]. As an example, in [50], where the study object is a duoskelion structure, introduced as a discrete spring model, a specific scaling law for micro stiffnesses it's been selected aimed at deriving, via asymptotic homogenization, an internally-constrained Cosserat one-dimensional planar continuum model as the limit of a duoskelion structure. However, duoskelion structures have been studied not only in static but also by analyzing their response to in plane dynamic instability problems, as in [51]. Also structures, obtained through the assembly of duoskelion beams are addressed in the literature, as in [52], in which the microstructure is characterized by the connection of two orthogonal families of parallel equispaced duoskelion beams. Furthermore, other approaches, including experimental ones, have also been developed in [1, 3, 4, 53] to analyze the behavior of the chiral microstructure similar to that of [2]. In [1], the Granular Micromechanics Approach (GMA) was employed to predict the closed-form expressions for elastic constants of a macroscale 2D chiral granular metamaterial. The latter was specifically designed with a grain-pair interaction in order to exhibit shear-normal-rotational coupling. Such coupling prediction was confirmed thanks to tensile experiments conducted on specimens realized through additive manufacturing (3D printing). In [3], Digital Image Correlation (DIC) was carried out on specimens fabricated using 3D printing and tested in an uniaxial testing machine. The designed structures were representative of granular metamaterial composed of rigid grains interacting with each other through grain-pair interaction mechanisms. The repeatability of the measurement was demonstrated and the range of validity of the derived model was assessed by calibration. In this regard, results showed that the calculations matched the measured deformations only at small strain level. In fact, the higher the strain level, the more material and geometrical nonlinearities become significant and thus, due to the effect of boundary layer and nonlinear interactions between grains, some differences from the calculated responses were observed. In [4], a multiscalar DIC methodology was employed, beginning with a macroscale observation of the problem (where the microstructure is overlooked and the construct is treated as a continuum bar), followed by an exploration of the underlying microstructure through microscale DIC analysis. The microscale results revealed that the granular material consists of a collection of nearly rigid grains that store elastic energy through intergranular mechanisms. Moreover, the analyses demonstrated that, under extension, non-standard deformation mechanisms, including grain rotations, occur, and that the transverse displacements of the grains are governed by the behavior of the grain interconnections. Furthermore, it is worth to notice that, in the design and analysis of metamaterials built up with additive manufacturing processes, it is essential to account for the internal structure at the microscale, which, indeed, influences the overall mechanical response at the macroscale. To address this, in [54] a computational scheme applicable to a wide class of substructures is developed to identify metamaterial parameters by utilizing both macroscopic and microscopic scales. This approach is applied to a honeycomb substructure, considering the infill ratio. The parameters identified are related to the mechanical response of the metamaterials, such as elastic behavior and higher-order terms introduced by the substructure.

It is important to underline that the grain beam introduced in [2] has been further investigated in [55], where a one-dimensional Timoshenko-like equivalent beam model, embedded in a 2D space, is developed to describe its linear static behavior. The model is derived within the framework of the mixed homogenization approach, in which, as already mentioned, the continuum model is heuristically adopted, while the micro-macro relationships are analytically determined on the ground of an energy equivalence. In [55] the mixed homogenization approach is formulated both analytically and numerically to assess the robustness of the assumptions underlying the analytical identification. The analytical procedure also highlights the dependence of the elastic coefficients on suitably defined non-dimensional geometric parameters, thus providing effective guidelines for the design of grain beams with tailored macroscopic behavior. The accuracy and the limits of applicability of the homogenized beam model are also assessed through comparisons with FE analyses performed on refined models of grain beams.

Grid beams

As for grid beams, they have been extensively studied in the literature, often through substantially different approaches. For instance, among the recent contributions are [56, 57], which focus on the stability analysis of this type of metamaterials. In [56], a plane metamaterial made up of a periodic square grid of shear deformable beams was braced by crossing cables and investigated by means of analytical and experimental methods. Here, the elastic stability was analyzed through Bloch wave theory. Closed form solutions were derived for the critical modes and the corresponding stability domains, demonstrating that the inclusion of diagonal cables can be effectively exploited to tune and enhance the buckling response of periodic materials. The analytical predictions were successfully validated by means of finite element simulations and experimental tests on 3D printed specimens. In [57], a square grid metamaterial featuring rigid joints of finite size was analyzed to explore the onset of multiscale instabilities. Within a Floquet–Bloch theoretical framework, the authors obtained closed form expressions for the stability domains under generic biaxial macro-stress states, revealing a transition from macroscopic to microscopic critical modes, that is, a pattern transformation phenomenon governed by the size of the rigid joints. Furthermore, a minimum-weight optimization problem was formulated, providing optimal geometrical parameters for lightweight lattice configurations. The predictive accuracy of the model was confirmed through both numerical analyses and experimental investigations on additive manufactured samples.

Beyond these recent studies, grid beams have also been widely investigated in the broader context of structural homogenization. In particular, many earlier works adopt the same strategy employed in the present thesis, namely the aforementioned mixed homogenization approach. This latter has been extensively employed in the study of statics, dynamics, buckling, and aeroelasticity of periodic (planar and three-dimensional) frame structures, such as microstructured grid cylinders [28, 35–37], buildings and towers [29–34, 58–60]. In these papers, shear beam models, also including torsional effect in the three-dimensional (3D) behavior, as well as Timoshenko beam models have been formulated, by identifying the floors and the columns of the periodic frames, with the cross-sections and longitudinal fibers of the continuous beam, respectively, and by introducing some strong hypotheses, separately or in combination, regarding, in particular: in plane (membrane) and out of plane (flexural) undeformability of the cross-sections and inextensibility of the longitudinal fibers. When all these hypotheses are considered, the equivalent model is as a shear–(shear–torsional) beam in a 2-(3)D space; when the extensibility of the longitudinal fibers is taken into account, the equivalent model is a Timoshenko beam. Furthermore, in [35–37, 60], the cross-section's undeformability has been reduced, considering out of plane deformability, specifically the warping of the cross-sections, through the concepts of ‘shear factor’ and ‘flexural factor’. In essence, even when heuristically employing a rigid cross-section beam model, some corrective factors are suitably introduced to better estimate the shear and flexural stiffness of the homogenized beam: this is achieved by incorporating, on an energetic balance (that, again, can be carried out either analytically or numerically, depending on the microstructure complexity), the effect of the neglected warping, akin to the approach taken to incorporate the de Saint-Venant’s theory results into the Timoshenko beam’s theory. Accordingly, this kind of models are able to describe the warping phenomenon only on average.

To properly account for the warping phenomenon, the generalized beam models were developed with the aim of overcoming the limitations of the classical theories. These models introduce a more accurate description of the kinematics and stress distribution in slender structures subjected to complex deformation patterns. A vast body of literature has been devoted to the development of such models for thin walled beams (TWB), for which the Generalized Beam Theory (GBT) is typically adopted. GBT represents a specific and powerful analytical realization within the broader class of generalized beam models. Originally introducted by Schardt [61, 62], widespread by Davies [63, 64] and then extended by Camotim [65, 66], GBT extends Vlasov’s classic TWB theory by encompassing both warping and in plane cross-section deformation. According to GBT, the 3D displacement field is expressed as a linear combination of predefined functions of the transverse coordinates, each modulated by unknown functions of the axial abscissa (i.e. the configuration variables). Accordingly, through a semi-variational formulation, the original 3D problem is reduced to a 1D one, albeit with an increased number of variables.
The generalized beam theory relies on a local description of the displacement field and therefore it has been mainly implemented in numerical form, often coupled with finite element analysis, and has been developed specifically for thin walled beams. An alternative can be found in the literature. In [67–69], the so-called GBT-D, in which 'D' calls for the term 'dynamics', in formulated, where a global representation of the cross-section displacements is derived from an eigenvalue-based dynamic analysis. However, the approach still remains oriented towards numerical treatment of thin walled beams, where warping is mainly investigated in relation to non uniform torsion, as it induces significant complementary stresses in addition to those predicted by the de Saint Venant theory.

However, as said, the Generalized Beam Theory (GBT) can be regarded as part of the broader class of generalized beam models. The foundations of these latter can be traced back to Cosserat-type theories, where each material point of the continuum is endowed not only with a position vector but also with a triad of directors describing the local material rotation, as discussed in [70]. Within this framework, a beam is modeled as a 1D directed medium capable of representing bending, torsion, and shear deformations, as well as warping and micro-rotations, through the introduction of additional balance laws for director moments. Following these principles, in [71] the dynamical theory of hyperelastic rods, derived as a dimensional reduction of the 3D continuum, was derived. In this work, the exact equations of motion for a hyperelastic beam were obtained, and

a hierarchy of approximate theories was constructed by introducing suitable kinematic assumptions. These formulations, later extended and generalized, laid the foundation for modern nonlinear beam theories. Along the same line, in [72, 73] the geometrically exact beam formulation, which ensures invariance under superposed rigid-body motions and allows for the consistent treatment of large rotations, shear, and extension, is proposed. These theories provide a unified framework for both static and dynamic analyses of beams undergoing finite motions, and they have become a cornerstone in the numerical modeling of flexible systems. Within the context of direct 1D modeling, in [74] a beam theory specifically aimed at describing the flexural-torsional behavior and instability of thin-walled members is developed. The model, formulated in terms of strain measures referred to both the centroidal and the shear-center axes, incorporates internal shear constraints and nonlinear hyperelastic constitutive relations. The same framework was subsequently employed to investigate the influence of warping constraints on the critical load and on the corresponding bifurcation modes [75].
Nevertheless, there exist structural classes in which shear-induced warping is expected to play a significant role, such as microstructured beams, for which the phenomenon remains largely unexplored. In this regard, it would be necessary to develop an equivalent generalized beam model capable of accurately capturing these underlying effects.

Chapter 3

Homogenized beam model

3.1 Introduction

This Chapter introduces two different equivalent models that will provide the theoretical framework for the analysis of the metamaterials investigated in the following chapters. The need for two separate formulations arises from the different kinematic assumptions underlying the considered metamaterials. Here, the governing equations of both models in the static, dynamic, and buckling regimes are derived and discussed in detail. The Chapter concludes with the presentation of the identification algorithm used to determine the elastic and inertial parameters of the equivalent beam models studied in the following chapters.

3.2 Model

According to the mixed homogenization approach, in order to describe the mechanical behavior of microstructured beams, a one-dimensional continuum model, internally unconstrained, is heuristically adopted as the target (coarse) model of the microstructured beam (fine) model. Two metamaterials, based on different kinematic hypotheses, are studied: (i) the grain beam, studied under the hypothesis of rigid cross-section (in plane and out of plane); and (ii) the grid beam, studied under the hypothesis of in plane undeformability and out of plane (flexural) deformability (or undeformability) of the cross-section. Therefore, two distinct target models are formulated within the framework of linear kinematics and described as one-dimensional polar continuum embedded in a 2D space.

To investigate the grain beam, a Timoshenko-like beam model (see, e.g., [76–79]) is employed. This choice is made since the Timoshenko-like beam model and the grain beam rely on the same kinematic assumptions. However, when more complex phenomena are of interest, such as the out of plane deformation of the cross-section, the Timoshenko-like model becomes inadequate. Since this behavior occurs in the grid beam studied in this thesis, to capture the local deformability of the cross-section, i.e. the loss of the cross-section's planarity (see [80] for a more general nonlinear formulation in the 3D space), an equivalent model with enriched kinematics, namely the generalized beam model, is introduced. At this stage, the analytical models presented here are not yet specialized to the particular microstructures under investigation, as the focus is exclusively on the derivation of the equivalent beam models. The detailed topology of the metamaterials will be described in the following Chapters. Nevertheless, some general information is provided to establish the framework for the derivation of the equivalent beam models. In general, metamaterials are made of a periodic specifically designed microstructure, whose smallest repeating unit, namely the cell comprised between the cross-sections i and $i+1$, has a characteristic length h. By repeating the cell n times in the $x-$direction (horizontal direction), the metamaterial, namely the microstructured beam, of total length $\ell = n\,h$ is obtained. The equivalent beam model (Fig. 3.1) is assumed to be initially straight, with a flexible axis line and cross-sections orthogonal to the latter in the reference (rectilinear) configuration. The reference coordinate is the material abscissa $x \in [0, \ell]$, spanning the interval of the axis-line $H = A, B$ with A in $x = 0$ and B in $x = \ell$.

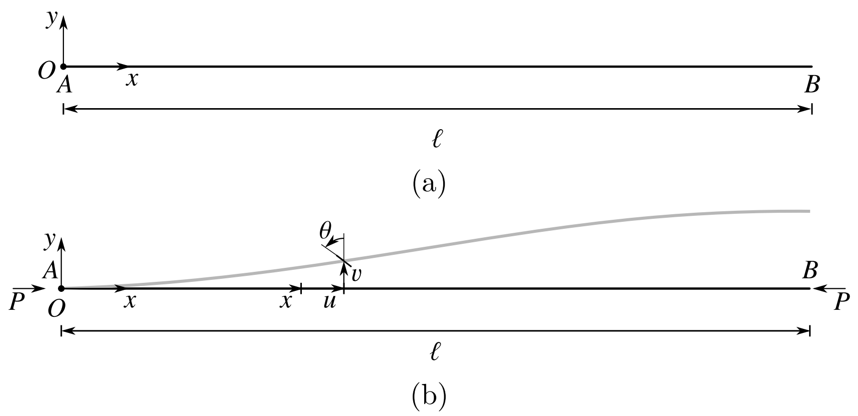

Figure 3.1. Equivalent beam model: (a) reference configuration for static and dynamic analyses; (b) reference and adjacent configuration for buckling analysis.

After introducing the target models, kinematics and equilibrium are set, while leaving the constitutive law unrestricted. The latter can be determined by assuming a linear elastic law for the beam's constitutive behavior and, accordingly, assuming the existence of a suitable strain energy function ϕ. In the static and dynamic analyses, ϕ depends only on the deformation field, $\phi = \phi\,(\boldsymbol{\varepsilon})$ where $\boldsymbol{\varepsilon}$ is the deformation vector. In the buckling analysis, however, it must also account for the work spent by the prestress $\mathring{N}$ on the second-order part of the strain measures [81, 82]. The strain energy takes the form $\phi = \phi\left(\boldsymbol{\varepsilon}, \mathring{N}\right)$ which enables to consider the local geometric effects. In fact, in the buckling analysis both the global and local geometric effects arise. The first is the classical geometric one, and arises from writing the equilibrium in the adjacent configuration, i.e. slightly varied from the rectilinear one. The second, instead, is non-classical and originates from the uniform prestress acting on each fiber in the precritical state.

Once the strain energy function is written, the elastic operator $\mathbf{C}$ is obtained according to the Green's law,

$$\boldsymbol{\sigma} = \frac{\partial \phi}{\partial \boldsymbol{\varepsilon}}, \tag{3.1}$$

where $\boldsymbol{\sigma}$ is the stress vector. It is worth emphasizing that, in the buckling analysis, the elastic operator depends on the prestress $\mathring{N} = -P$, namely it is

$$\mathbf{C} \coloneqq \mathbf{C}\left(\mathring{N}\right) = \mathbf{C}^0 - P\mathbf{C}^*. \tag{3.2}$$

In Eq. (3.2), the superscript zero and asterisk, here and in the following, indicate whether the constitutive matrix has been obtained after linearization by considering the elastic contribution to the energy, $\mathbf{C}^0$, or the geometric one $\mathbf{C}^*$. In any case, the dependence of $\mathbf{C}$ on the prestress implies the existence of specific values of the applied load for which the operator becomes singular, given by the condition $\det\left(\mathbf{C}\left(\mathring{N}\right)\right) = 0$. The smallest of these values represents the cell critical load, P_{cell}, at which a single cell undergoes local buckling. When multiple cells are assembled into a microstrucured beam, however, elastic interactions among them give rise to a global buckling mode. The corresponding critical load, P_c, leads to a bifurcation of the entire structure which precedes the local buckling phenomenon; in fact it is $P_c < P_{cell}$.

In the following, the governing equations describing the kinematic and equilibrium problems of the adopted target models are derived. Once established, these equations allow to pursue the boundary value problem's solutions, namely: the displacement field in static analysis, the modal shapes and angular frequencies in dynamic analysis, the critical mode and load in buckling analysis. Closed form solutions of the boundary value problems can be obtained for the static [83, 84], dynamic [35], and buckling [36] analyses, although this is typically possible only when the microstructure possesses some symmetries and its kinematics remains sufficiently simple. Conversely, when the equations governing the boundary value problem are strongly coupled, analytical solutions are no longer attainable, and numerical approaches must be employed instead. Accordingly, the choice of the solution strategy, analytical or numerical, is made on case by case in this work, depending on the degree of coupling of the equilibrium equations.

3.2.1 Timoshenko-like beam

STRAIN-DISPLACEMENT RELATIONSHIPS

Assuming small displacements and strains, i.e. within the framework of linear theory, the following strain-displacement relationships hold for the Timoshenko beam model [76, 78, 85–88]:

$$\begin{aligned} \varepsilon &= u', \\ \gamma &= v' - \theta, \\ \kappa &= \theta', \end{aligned} \tag{3.3}$$

which link the longitudinal displacement $u(x,t)$, the transverse displacement $v(x,t)$, and the rotation of the cross-section $\theta(x,t)$, to the elongation $\varepsilon(x,t)$, the shear strain $\gamma(x,t)$, and the flexural curvature $\kappa(x,t)$. Here and in what follows, a prime denotes derivation with respect to the (independent) spatial variable, and t is the time. Of course, the time dependence is relevant only in the dynamic problem.
The following geometric boundary conditions are considered for the load and static schemes listed below, where the overbar denote a prescribed quantity:

- For the static analysis, clamped at $H = A$, B with prescribed displacements at B: $u_A = v_A = \theta_A = 0$, $u_B = \bar{u}$, $v_B = \bar{v}$, $\theta_B = \bar{\theta}$;
- For the free-dynamic analysis, clamped at $H = A$, B: $u_H = v_H = \theta_H = 0$;
- For the buckling analysis, clamped at A and constrained by a horizontal slider at B: $u_A = v_A = \theta_A = v_B = \theta_B = 0$.

As for the formulation of the equilibrium problem, depending on whether the static, dynamic, or buckling analysis is considered, it is derived with respect to different configurations, namely the reference (rectilinear) or the adjacent one. Accordingly, a clear distinction between these scenarios is maintained.

Equilibrium

In the static and dynamic analyses, the equilibrium is written in the reference (rectilinear) configuration and the following well-known equations hold [76, 78, 85–88]:

$$\begin{aligned} N' + p_x &= 0, \\ T' + p_y &= 0, \\ M' + T + c_z &= 0, \end{aligned} \tag{3.4}$$

where $N(x,t)$ is the axial force, $T(x,t)$ is the shear force, $M(x,t)$ is the bending moment, $p_x(x,t)$, $p_y(x,t)$, $c_z(x,t)$ are the external forces and couple per unit-length.

Constitutive law

According to the workflow already explained, in order to identify the elastic operator $\mathbf{C}$, the existence of a strain energy function, quadratic in the strain measures, is postulated.

$$\phi(\varepsilon,\gamma,\kappa) = \frac{1}{2}\left[c_{11}\,\varepsilon^2 + c_{22}\,\gamma^2 + c_{33}\,\kappa^2 + 2\left(c_{12}\,\varepsilon\,\gamma\, + c_{13}\,\varepsilon\,\kappa\, + c_{23}\,\gamma\,\kappa\right)\right] \tag{3.5}$$

Eq. (3.5) depends on six elastic constants c_{ij} $(i,j = 1,2,3)$, which must be identified in order to effectively describe the macroscopic behavior of the metamaterial. Then, the Green law (Eq. (3.1)), that can be explicitly written as

$$N = \frac{\partial\phi}{\partial\varepsilon}, \quad T = \frac{\partial\phi}{\partial\gamma}, \quad M = \frac{\partial\phi}{\partial\kappa}, \tag{3.6}$$

is enforced and a fully-coupled constitutive law is obtained. The constitutive law reads as

$$\begin{pmatrix} N \\ T \\ M \end{pmatrix} = \begin{pmatrix} c_{11} & c_{12} & c_{13} \\ & c_{22} & c_{23} \\ \text{SYM} & & c_{33} \end{pmatrix} \begin{pmatrix} \varepsilon \\ \gamma \\ \kappa \end{pmatrix}, \tag{3.7}$$

in which

$$\mathbf{C} := \begin{pmatrix} c_{11} & c_{12} & c_{13} \\ & c_{22} & c_{23} \\ \text{SYM} & & c_{33} \end{pmatrix}, \tag{3.8}$$

is the constitutive matrix.

Elasto-dynamic problem

By using Eqs. (3.3) and (3.7), Eqs. (3.4) can be written in terms of displacements. Moreover, introducing the inertia forces according to the principle of d'Alembert, the following equations of motion are derived:

$$\begin{aligned} -m\ddot{u} + I_y\ddot{\theta} + c_{11}u'' + c_{12}\left(v'' - \theta'\right) + c_{13}\theta'' + p_x &= 0, \\ -m\ddot{v} - I_x\ddot{\theta} + c_{12}u'' + c_{22}\left(v'' - \theta'\right) + c_{23}\theta'' + p_y &= 0, \\ I_y\ddot{u} - I_x\ddot{v} - I_{xy}\ddot{\theta} + c_{13}u'' + c_{23}\left(v'' - \theta'\right) + c_{33}\theta'' + c_{12}u' + c_{22}\left(v' - \theta\right) + c_{23}\theta' + c_z &= 0. \end{aligned} \tag{3.9}$$

In Eq. (3.9), m, I_x, I_y and I_{xy} denote, respectively, the mass, first and second inertia moments per unit-length, while a dot indicates differentiation with respect to the time variable, here and throughout all the work thesis. Since no external loads and no lumped masses are applied at the beam ends, the adopted scheme for both static and dynamic analyses, does not require the imposition of mechanical boundary conditions. Conversely, initial conditions must be specified and, in this regard, it is assumed that the system is initially at rest.

The Eqs. (3.9), together with the boundary conditions, form a system of second-order partial differential equations in the unknown displacement field, which can be recast in matrix form as:

$$\begin{aligned} -\mathbf{M}\ddot{\mathbf{u}} + \mathbf{K}_2\mathbf{u}'' + \mathbf{K}_1\mathbf{u}' + \mathbf{K}_0\mathbf{u} + \mathbf{p} &= \mathbf{0}, \\ \mathbf{u}_A &= \mathbf{0}, \\ \mathbf{u}_B &= \bar{\mathbf{u}}_B, \end{aligned} \tag{3.10}$$

where, here and in what follows, $\mathbf{M}$ is the mass matrix, $\mathbf{K}_i$ $(i = 0, 1, 2)$ are stiffness matrices, and $\mathbf{u}$ and $\mathbf{p}$ are the displacement and load vectors, respectively. The introduced operators are defined as

$$\mathbf{u} := \begin{pmatrix} u \\ v \\ \theta \end{pmatrix}, \qquad \mathbf{p} := \begin{pmatrix} p_x \\ p_y \\ c_z \end{pmatrix}, \qquad \mathbf{M} := \begin{pmatrix} m & 0 & -I_y \\ 0 & m & I_x \\ -I_y & I_x & I_{xy} \end{pmatrix},$$
$$\mathbf{K}_2 := \begin{pmatrix} c_{11} & c_{12} & c_{13} \\ c_{12} & c_{22} & c_{23} \\ c_{13} & c_{23} & c_{33} \end{pmatrix}, \ \mathbf{K}_1 := \begin{pmatrix} 0 & 0 & -c_{12} \\ 0 & 0 & -c_{22} \\ c_{12} & c_{22} & 0 \end{pmatrix}, \ \mathbf{K}_0 := \begin{pmatrix} 0 & 0 & 0 \\ 0 & 0 & 0 \\ 0 & 0 & -c_{22} \end{pmatrix}., \tag{3.11}$$

Moreover, to enforce the aforementioned boundary and load conditions, $\bar{\mathbf{u}}_B = \left(\bar{u}, \bar{v}, \bar{\theta}\right)^T$ and $\bar{\mathbf{u}}_B = \mathbf{0}$ are considered for the static and free dynamic analyses, respectively, while the external load vector is assumed $\mathbf{p} = \mathbf{0}$ for both the analyses.
In this section, the most general framework has been considered, in which the elastic operator Eq. (3.8) is fully coupled, making the problem particularly challenging to solve. However, when the model described by Eqs. (3.10) is applied to the grain beam examined in this thesis, the static problem significantly simplifies and, although the governing equations remain coupled, a closed-form analytical solution can still be derived.
The dynamic eigenvalue problem, instead, is addressed by setting $\mathbf{p} = \mathbf{0}$ and $\mathbf{u} = \hat{\mathbf{u}}\,(x)\, e^{\lambda t}$, where λ and $\hat{\mathbf{u}}\,(x)$ denote the eigenvalues and eigenvectors of the system, respectively, in Eqs. (3.10). This leads to a (spatial) boundary value problem in which, due to the conservative nature of the system, the eigenvalues are purely imaginary, namely $\lambda_j = \pm i\omega_j$, with ω_j being the angular frequency of the $j-$th mode. When the equation of motion are not too coupled, the closed-form solution is theoretically attainable, although it still requires the numerical solution of the dispersion relation between the eigenvalue λ and the wave-number μ.
In the case of the grain beam, however, the dynamic equations exhibit a much stronger coupling than in the static analysis, making an analytical solution difficult to pursue. For this reason, the free-dynamic problem is solved numerically by means of the Finite Difference Method.
A detailed account of both the static closed-form solution, for the boundary condition with $\bar{\mathbf{u}}_B = (\bar{u}, \bar{v}, 0)^T$ studied in this work, and the numerical algorithm adopted for the dynamic analysis is provided in Appendix A.

Buckling problem

The equilibrium is enforced in the adjacent (slightly varied from the rectilinear one) configuration through the Virtual Work Principle (VWP), and the virtual work spent by the prestress, $\mathring{N} = -P$, on the second-order part of the unit extension, $\varepsilon^{(2)}$, is accounted [81, 82]. No incremental loads are applied hence, expanding in series the unit extension ε [76–78, 85–87]

$$\varepsilon := \varepsilon^{(1)} \quad + \varepsilon^{(2)} + \ldots = u' - \frac{1}{2}\theta^2 + v'\theta + \ldots, \tag{3.12}$$

the VWP reads

$$\int_0^\ell \left(N\,\delta u' + T\,\delta\left(v' - \theta\right) + M\,\delta\theta'\right) \mathrm{d}x - \int_0^\ell P\delta\left(v'\theta - \frac{1}{2}\theta^2\right) \mathrm{d}x = 0, \tag{3.13}$$

$\forall\left(\delta u, \delta v, \delta\theta\right)$, which, neglecting precritical strains, yields the following equilibrium equations

$$\begin{aligned} N' &= 0, \\ T' - P\theta' &= 0, \\ M' + T + P\left(v' - \theta\right) &= 0, \end{aligned} \tag{3.14}$$

Eqs. (3.14), where $N\left(x\right)$ and $T\left(x\right)$ denote the (incremental) axial and shear internal forces, respectively, while $M\left(x\right)$ represents the (incremental) bending moment, allows the equivalent beam model to take into account for the global geometric effect. From Eq. (3.13), the mechanical boundary conditions can be derived for the following static scheme

- Clamped at A and constrained by a horizontal slider at B: $N_B = 0$.

As mentioned, a linear hyper-elastic law is assumed, linking incremental stresses $\boldsymbol{\sigma} = \left(N, T, M\right)^T$ to incremental strains $\boldsymbol{\varepsilon} = \left(\varepsilon, \gamma, \kappa\right)^T$, in which the elastic operator $\mathbf{C}$ depends not only on the deformation measures but also on the prestress, see Eq. (3.2). It is derived by assuming the existence of a suitable strain energy function, $\phi = \phi\left(\varepsilon, \gamma, \kappa, \mathring{N}\right)$, and by applying the Green's law (Eq. (3.6)). Accordingly, the hyper-elastic law is defined as follows

$$\begin{pmatrix} N \\ T \\ M \end{pmatrix} = \begin{pmatrix} c_{11} & c_{12} & c_{13} \\ & c_{22} & c_{23} \\ \text{SYM} & & c_{33} \end{pmatrix} \begin{pmatrix} \varepsilon \\ \gamma \\ \kappa \end{pmatrix} - P \begin{pmatrix} c_{11}^* & c_{12}^* & c_{13}^* \\ & c_{22}^* & c_{23}^* \\ \text{SYM} & & c_{33}^* \end{pmatrix} \begin{pmatrix} \varepsilon \\ \gamma \\ \kappa \end{pmatrix}, \tag{3.15}$$

which, thanks to the dependence of the constitutive law on the applied load P, enables the equivalent beam model to take into account for the local geometric effects. In particular, as previously discussed, the load value that destabilizes the unit cell, thus inducing a local buckling phenomenon, is determined from the condition $\det\left(\mathbf{C}\left(\mathring{N}\right)\right) = 0$. The smallest value satisfying this condition defines the critical load of the cell, P_{cell}.
Eqs. (3.14) can be written in terms of displacements by combining the kinematic relations (Eq. (3.3)) together with the constitutive equations (Eq. (3.15)). Recasting the system in matrix form yields

$$\begin{aligned} \mathbf{K}_2\mathbf{u}'' + \mathbf{K}_1\mathbf{u}' + \mathbf{K}_0\mathbf{u} &= \mathbf{0}, \\ \mathbf{u}_A &= \mathbf{0}, \\ \mathbf{B}_1\mathbf{u}_B' + \mathbf{B}_0\mathbf{u}_B &= \mathbf{0}. \end{aligned} \tag{3.16}$$

where, here and in the following, $\mathbf{B}_i$ $(i = 0, 1)$ denote the boundary operators. Eq. (3.16a) is a system of partial differential equations sided by geometric and mechanical boundary conditions (Eq. (3.16b,c)) at the ends $H = A\,B$. The stiffness matrices in Eq. (3.16) are given by

$$
\begin{aligned}
\mathbf{K}_2 &:= \begin{pmatrix} c_{11} & c_{12} & c_{13} \\ & c_{22} & c_{23} \\ \text{SYM} & & c_{33} \end{pmatrix} - P \begin{pmatrix} c_{11}^* & c_{12}^* & c_{13}^* \\ & c_{22}^* & c_{23}^* \\ \text{SYM} & & c_{33}^* \end{pmatrix}, \\
\mathbf{K}_1 &:= \begin{pmatrix} 0 & 0 & -c_{12} + P c_{12}^* \\ & 0 & -c_{22} + P\left(c_{22}^* - 1\right) \\ \text{SKW} & & 0 \end{pmatrix}, \\
\mathbf{K}_0 &:= \begin{pmatrix} 0 & 0 & 0 \\ & 0 & 0 \\ \text{SYM} & & -c_{22} + P\left(c_{22}^* - 1\right) \end{pmatrix},
\end{aligned}
\tag{3.17}
$$

while the boundary operators are defined as follows

$$
\begin{aligned}
\mathbf{B}_1 &:= \begin{pmatrix} c_{11} - P c_{11}^* & c_{12} - P c_{12}^* & c_{13} - P c_{13}^* \\ 0 & 0 & 0 \\ 0 & 0 & 0 \end{pmatrix}, \\
\mathbf{B}_0 &:= \begin{pmatrix} 0 & 0 & -c_{12} + P c_{12}^* \\ 0 & 1 & 0 \\ 0 & 0 & 1 \end{pmatrix}.
\end{aligned}
\tag{3.18}
$$

The smallest load $P = P_c$ for which the boundary value problem Eq. (3.16) admits nontrivial solutions triggers incipient instability of the beam; P_c is therefore referred to as the global critical load. To evaluate this latter, Eq. (3.16a) must be solved. This task can be easily accomplished in closed form [36] by: (i) finding the general solution of Eq. (3.16a) by solving its characteristic equation and determining the associated eigenvectors; (ii) enforcing the boundary conditions Eq. (3.16b,c), which provide a (homogeneous) system of algebraic equations in the arbitrary constants; (iii) imposing that this system admits nontrivial solutions, which leads to a transcendent equation in P, whose smallest root is P_c.

However, the workflow already outlined above is not always applicable. In this Section the most general framework of the buckling problem, in which the elastic operator is fully coupled, is addressed. When applied to the grain beam investigated in this thesis, only a few off-diagonal terms of the constitutive matrix vanish. As a consequence, several couplings persist, preventing the derivation of a closed-form analytical solution and thus making a numerical approach necessary. The resulting eigenvalue problem is solved by means of the Finite Difference Method, whose detailed implementation is provided in Appendix A.

3.2.2 Generalized beam

Similarly to the Timoshenko-like beam model, the generalized beam model is developed within the framework of linear theory. In this formulation, when a geometric transformation occurs, the model is able to describe not only rigid-body motion, i.e. the translations in the (x, y) −plane and rotation around the z−axis, represented by the well-known displacement fields $u(x,t)$, $v(x,t)$ and $\theta(x,t)$, but also local deformation, expressed by the product $a(x,t)\,\psi(y)$, with $[a] = [L^0]$ and $[\psi] = [L]$. Here, $a(x,t)$ is a scalar displacement representing the amplitude of the warping function $\psi(y)$, which accounts for the distortion of the cross-section, i.e. describes its planarity defect while it is assumed to keep its in plane shape.

Limiting the analysis to a single warping mode, the beam is characterized by four scalar configuration variables. Together with their first derivatives with respect to the longitudinal coordinate, these variables yield a total of eight degrees of freedom. Among them, three correspond to rigid-body motions, two planar translations and one rotation, thus the beam can undergo five independent deformation modes, i.e. the well-known unit extension $\varepsilon(x,t)$, shear strain $\gamma(x,t)$ and curvature $\kappa(x,t)$, together with two quantities that describe local deformation. These latter are the distortional strain and the distortion gradient, $\alpha(x,t)$ and $\beta(x,t)$, respectively. The time dependence is relevant only in the dynamic analysis.

Strain-displacement relationships

The strain-displacement relationships are

$$\begin{aligned}
\varepsilon &= u', \\
\gamma &= v' - \theta, \\
\kappa &= \theta', \\
\alpha &= a, \\
\beta &= a'.
\end{aligned} \tag{3.19}$$

Since the kinematic is expressed by five equations and four scalar displacements, the locally deformable beam is internally overconstrained and, therefore, the compatibility condition

$$\alpha' - \beta = 0, \tag{3.20}$$

has to be enforced. The following geometric boundary conditions are considered for the load and static schemes listed below:

- For the static analysis, clamped at A and free at B with a force P_y applied at B: $u_A = v_A = \theta_A = a_A = 0$;

- For the static analysis, clamped at $H = A$, B with a prescribed displacement $\bar{v}$ at B: $u_H = v_A = \theta_H = a_H = 0$, $v_B = \bar{v}$;

- For the free dynamic analysis, clamped at A and free at B: $u_A = v_A = \theta_A = a_A = 0$;

- For the buckling analysis, clamped at A and constrained by a horizontal roller at B: $u_A = v_A = \theta_A = a_A = v_B = 0$.

As already done for the Timoshenko-like beam model, a clear distinction between the formulation of the equilibrium problem for the static, dynamic and buckling analysis is preferred.

Equilibrium

Due to the richer kinematics of the generalized beam model, compared with the locally undeformable Timoshenko-like beam (Section 3.2.1), additional stresses, beyond the classical axial force $N(x,t)$, shear force $T(x,t)$ and bending moment $M(x,t)$, arise. These additional quantities, denoted as the distortional $D(x,t)$ and the bi-distortional $B(x,t)$ forces, are introduced as the dual quantities of the distortional strain $\alpha(x,t)$ and its gradient $\beta(x,t)$, respectively. The equilibrium equations are derived via the VWP, requiring the equality between the internal $\mathcal{W}_i$ and the external $\mathcal{W}_e$ virtual work for any virtual strain-displacement field satisfying the kinematics (Eq. (3.19)). Specifically, these are expressed as:

$$\begin{aligned}
\mathcal{W}_i &:= \int_0^\ell (N\delta\varepsilon + T\delta\gamma + M\delta\kappa + D\delta\alpha + B\delta\beta)\,\mathrm{d}x, \\
\mathcal{W}_e &:= \int_0^\ell (p_x\delta u + p_y\delta v + c_z\delta\theta + q\delta a)\,\mathrm{d}x + P_x\delta u_H + P_y\delta v_H + C_z\delta\theta_H + Q\delta u_H,
\end{aligned} \tag{3.21}$$

where $p_x(x,t)$, $p_y(x,t)$, $c_z(x,t)$ are the already defined external forces and couples per unit-length acting in the domain, while P_x, P_y, and C_z are the lumped forces and couples acting at the ends. The terms $q(x,t)$ and Q, instead, are the distortional forces acting within the domain and at the boundary, respectively. By substituting Eq. (3.19) into Eq. (3.21) and integrating by parts, the following equilibrium equations

$$\begin{aligned}
N' + p_x &= 0, \\
T' + p_y &= 0, \\
M' + T + c_z &= 0, \\
B' - D + q &= 0,
\end{aligned} \tag{3.22}$$

and mechanical conditions

$$nN = P_x, \quad nT = P_y, \quad nM = C_z, \quad nB = Q, \quad \text{with } n = \mp 1 \text{ in } x = 0, \ell, \tag{3.23}$$

are derived.

Constitutive law

In order to identify the elastic operator $\mathbf{C}$, the existence of a strain energy function, quadratic in the strain measures, is postulated as

$$\begin{aligned}\phi\left(\varepsilon,\gamma,\kappa,\alpha,\beta\right) =& \frac{1}{2}\left[c_{11}\varepsilon^2 + c_{22}\gamma^2 + c_{33}\kappa^2 + c_{44}\alpha^2 + c_{55}\beta^2 + 2\left(c_{12}\varepsilon\,\gamma + c_{13}\varepsilon\,\kappa + c_{14}\varepsilon\,\alpha\right.\right.\\ &\left.\left. +\ c_{15}\varepsilon\,\beta + c_{23}\gamma\,\kappa + c_{24}\gamma\,\alpha + c_{25}\gamma\,\beta + c_{34}\kappa\,\alpha + c_{35}\kappa\,\beta + c_{45}\alpha\,\beta\right)\right].\end{aligned} \tag{3.24}$$

which depends on the fifteen elastic constants c_{ij} $(i,j=1,2,\ldots,5)$, to be identified in order to reproduce the macroscopic behavior of the metamaterial. By enforcing the Green's law (Eq. (3.1)), which in explicit form is written as

$$N = \frac{\partial\phi}{\partial\varepsilon},\quad T = \frac{\partial\phi}{\partial\gamma},\quad M = \frac{\partial\phi}{\partial\kappa},\quad D = \frac{\partial\phi}{\partial\alpha},\quad B = \frac{\partial\phi}{\partial\beta}, \tag{3.25}$$

a fully-coupled constitutive law is obtained

$$\begin{pmatrix} N \\ T \\ M \\ D \\ B \end{pmatrix} = \begin{pmatrix} c_{11} & c_{12} & c_{13} & c_{14} & c_{15} \\ & c_{22} & c_{23} & c_{24} & c_{25} \\ & & c_{33} & c_{34} & c_{35} \\ & & & c_{44} & c_{45} \\ \text{SYM} & & & & c_{55} \end{pmatrix} \begin{pmatrix} \varepsilon \\ \gamma \\ \kappa \\ \alpha \\ \beta \end{pmatrix}, \tag{3.26}$$

in which

$$\mathbf{C} := \begin{pmatrix} c_{11} & c_{12} & c_{13} & c_{14} & c_{15} \\ & c_{22} & c_{23} & c_{24} & c_{25} \\ & & c_{33} & c_{34} & c_{35} \\ & & & c_{44} & c_{45} \\ \text{SYM} & & & & c_{55} \end{pmatrix}, \tag{3.27}$$

is the constitutive matrix.

Elasto-dynamic problem

Introducing the inertia forces according to the principle of d'Alembert, the following equations of motion are derived:

$$\begin{aligned} -m\ddot{u} + I_y\ddot{\theta} - I_\psi\ddot{a} + N' + p_x &= 0, \\ -m\ddot{v} - I_x\ddot{\theta} + T' + p_y &= 0, \\ I_y\ddot{u} - I_x\ddot{v} - I_{xy}\ddot{\theta} + I_{\psi y}\ddot{a} + M' + T + c_z &= 0, \\ -I_\psi\ddot{u} + I_{\psi y}\ddot{\theta} - I_{\psi\psi}\ddot{a} + B' - D + q &= 0, \end{aligned} \tag{3.28}$$

where m, I_x, I_y and I_{xy} are the already defined mass, first and second inertia moments per unit-length, while I_ψ, $I_{\psi y}$ and $I_{\psi\psi}$ represent analogous inertia quantities associated with the warping function. No lumped masses are applied at the ends of the beam and it is assumed that the system is initially at rest. The following mechanical boundary conditions are considered for the load and static schemes listed below:

- For the static analysis, clamped at A and free at B with a force P_y applied at B: $N_B = M_B = B_B = 0$, $T_B = P_y$;

- For the free dynamic analysis, clamped at A and free at B: $N_B = T_B = M_B = B_B = 0$.

Eqs. (3.28) can be rewritten in terms of displacements by means of Eqs. (3.19) and (3.26). The resulting system consists of second-order partial differential equations in the unknown displacement field, sided by the geometric and mechanical boundary conditions. Both the equations of motion and the boundary conditions can be cast in matrix form. The equations of motion read

$$-\mathbf{M}\ddot{\mathbf{u}} + \mathbf{K}_2\mathbf{u}'' + \mathbf{K}_1\mathbf{u}' + \mathbf{K}_0\mathbf{u} + \mathbf{p} = \mathbf{0}, \tag{3.29}$$

where $\mathbf{u} = (u, v, \theta, a)^T$ and $\mathbf{p} = (p_x, p_y, c_z, q)^T$ are the displacement and load vectors. The mass matrix $\mathbf{M}$, together with the stiffness matrices $\mathbf{K}_i$ $(i = 0, 1, 2)$, take the form

$$\begin{aligned}
\mathbf{M} &:= \begin{pmatrix} m & 0 & -I_y & I_\psi \\ & m & I_x & 0 \\ & & I_{xy} & -I_{\psi y} \\ \text{SYM} & & & I_{\psi\psi} \end{pmatrix}, \quad
\mathbf{K}_2 := \begin{pmatrix} c_{11} & c_{12} & c_{13} & c_{15} \\ & c_{22} & c_{23} & c_{25} \\ & & c_{33} & c_{35} \\ \text{SYM} & & & c_{55} \end{pmatrix}, \\
\mathbf{K}_1 &:= \begin{pmatrix} 0 & 0 & -c_{12} & c_{14} \\ & 0 & -c_{22} & c_{24} \\ & & 0 & c_{25} + c_{34} \\ \text{SKM} & & & 0 \end{pmatrix}, \quad
\mathbf{K}_0 := \begin{pmatrix} 0 & 0 & 0 & 0 \\ & 0 & 0 & 0 \\ & & -c_{22} & c_{24} \\ \text{SYM} & & & -c_{44} \end{pmatrix}.
\end{aligned} \tag{3.30}$$

The boundary conditions, instead, read as

- clamped at A and free at B

$$\begin{aligned} \mathbf{u}_A &= \mathbf{0}, \\ \mathbf{B}_1\mathbf{u}'_B + \mathbf{B}_0\mathbf{u}_B &= \mathbf{P}, \end{aligned} \tag{3.31}$$

where the load vector is $\mathbf{P} = (0, P_y, 0, 0)^T$ and $\mathbf{P} = \mathbf{0}$ for the static and free dynamic analyses, respectively, while the boundary operators, $\mathbf{B}_i$ $(i = 0, 1)$ are defined as

$$\mathbf{B}_1 := \mathbf{K}_2, \quad \mathbf{B}_0 := \begin{pmatrix} 0 & 0 & -c_{12} & c_{14} \\ 0 & 0 & -c_{22} & c_{24} \\ 0 & 0 & -c_{23} & c_{34} \\ 0 & 0 & -c_{25} & c_{45} \end{pmatrix}, \tag{3.32}$$

- clamped at $H = A$, B with a prescribed displacement $\bar{v}$ at B

$$\begin{aligned} \mathbf{u}_A &= \mathbf{0}, \\ \mathbf{u}_B &= \bar{\mathbf{u}}_B, \end{aligned} \tag{3.33}$$

  where the prescribed displacement vector is $\bar{\mathbf{u}}_B = (0, \bar{v}, 0, 0)^T$.

In both the static and dynamic analyses the external load vector is assumed $\mathbf{p} = \mathbf{0}$. The model described by Eq. (3.29), together with the boundary conditions (Eqs. (3.31) and (3.33)), represents the most general framework, in which the elastic operator is fully coupled. Once the topology of the microstructure is specified, some terms may be null. Nevertheless, it is important to emphasize that the degree of coupling in the constitutive matrix does not depend only on the microstructure's topology, but also by the choice of the target model. Indeed, for example, if the microstructure is doubly symmetric and the metamaterial behavior is described by a model with a reduced set of kinematic variables, such as the Timoshenko beam model, the constitutive matrix is diagonal [37, 82]. Conversely, when a more refined kinematic description is adopted, as in the generalized beam model, the constitutive matrix may exhibits coupling terms. In particular, when the model described by Eqs. (3.28) is applied to the grid beam, only a few terms vanish, and the resulting governing equations remain strongly coupled, thus requiring a numerical solution. Both the static and dynamic problems are solved by means of the Finite Difference Method, detailed in Appendix A.

Buckling problem

As already seen in the Timoshenko-like equivalent beam model, the equilibrium equations are derived through the VWP, taking into account the work spent by the prestress $\mathring{N}$on the second-order part of the unit extension $\varepsilon^{(2)}$ (Eq. (3.12)). No incremental loads are applied hence, neglecting precritical strains, the VWP reads

$$\int_0^\ell \left(N\,\delta u' + T\,\delta\left(v' - \theta\right) + M\,\delta\theta' + D\,\delta a + B\,\delta a'\right) \mathrm{d}x - \int_0^\ell P\delta\left(v'\theta - \frac{1}{2}\theta^2\right) \mathrm{d}x = 0, \tag{3.34}$$

$\forall\left(\delta u, \delta v, \delta\theta, \delta a\right)$, which leads to the equilibrium equations

$$\begin{aligned} N' &= 0, \\ T' - P\theta' &= 0, \\ M' + T + P\left(v' - \theta\right) &= 0, \\ B' - D &= 0, \end{aligned} \tag{3.35}$$

where all the stresses involved, $N\left(x\right)$, $T\left(x\right)$, $M\left(x\right)$, $D\left(x\right)$ and $B\left(x\right)$, are the incremental ones. From Eq. (3.34), the mechanical boundary conditions can be derived for the following static scheme

- Clamped at A and constrained by a horizontal roller at B: $N_B = M_B = B_B = 0$.

As already seen, a linear hyper-elastic law is assumed linking incremental stresses $\boldsymbol{\sigma} = (N, T, M, D, B)^T$ to incremental strains $\boldsymbol{\varepsilon} = (\varepsilon, \gamma, \kappa, \alpha, \beta)^T$, in which the elastic operator $\mathbf{C}$ depends not only on the deformation measures but also on the prestress, see Eq. (3.2). $\mathbf{C}$ is derived by assuming the existence of a suitable strain energy function, $\phi = \phi\left(\varepsilon, \gamma, \kappa, \alpha, \beta, \mathring{N}\right)$, and by applying the Green's law (Eq. (3.25)). The hyper-elastic law is defined as follows

$$\begin{pmatrix} N \\ T \\ M \\ D \\ B \end{pmatrix} = \begin{pmatrix} c_{11} & c_{12} & c_{13} & c_{14} & c_{15} \\ & c_{22} & c_{23} & c_{24} & c_{25} \\ & & c_{33} & c_{34} & c_{35} \\ & & & c_{44} & c_{45} \\ \text{SYM} & & & & c_{55} \end{pmatrix} \begin{pmatrix} \varepsilon \\ \gamma \\ \kappa \\ \alpha \\ \beta \end{pmatrix} - P \begin{pmatrix} c^*_{11} & c^*_{12} & c^*_{13} & c^*_{14} & c^*_{15} \\ & c^*_{22} & c^*_{23} & c^*_{24} & c^*_{25} \\ & & c^*_{33} & c^*_{34} & c^*_{35} \\ & & & c^*_{44} & c^*_{45} \\ \text{SYM} & & & & c^*_{55} \end{pmatrix} \begin{pmatrix} \varepsilon \\ \gamma \\ \kappa \\ \alpha \\ \beta \end{pmatrix}. \tag{3.36}$$

The generalized beam model is derived within the same framework adopted for the grain beam. Therefore, the following statements also hold in this case: (i) the chosen equivalent model is capable of capturing both global and local geometric effects, through the equilibrium equations and the constitutive law, respectively; (ii) the load value that destabilizes the unit cell and induces local buckling is the smallest among those obtained from the condition $\det\left(\mathbf{C}\left(\mathring{N}\right)\right) = 0$.

By combining the kinematics (Eq. (3.19)) and the constitutive law (Eq. (3.36)), the Eqs. (3.35) can be expressed in terms of displacements. The problem can be recasted in matrix form as

$$\begin{aligned} \mathbf{K}_2\mathbf{u}'' + \mathbf{K}_1\mathbf{u}' + \mathbf{K}_0\mathbf{u} &= \mathbf{0}, \\ \mathbf{u}_A &= \mathbf{0}, \\ \mathbf{B}_1\mathbf{u}'_B + \mathbf{B}_0\mathbf{u}_B &= \mathbf{0}, \end{aligned} \tag{3.37}$$

where the stiffness matrices are given by

$$\begin{aligned} \mathbf{K}_2 &:= \begin{pmatrix} c_{11} & c_{12} & c_{13} & c_{15} \\ & c_{22} & c_{23} & c_{25} \\ & & c_{33} & c_{35} \\ \text{SYM} & & & c_{55} \end{pmatrix} - P \begin{pmatrix} c^*_{11} & c^*_{12} & c^*_{13} & c^*_{15} \\ & c^*_{22} & c^*_{23} & c^*_{25} \\ & & c^*_{33} & c^*_{35} \\ \text{SYM} & & & c^*_{55} \end{pmatrix}, \\ \mathbf{K}_1 &:= \begin{pmatrix} 0 & 0 & -c_{12} + Pc^*_{12} & c_{14} - Pc^*_{14} \\ & 0 & -c_{22} + P\left(c^*_{22} - 1\right) & c_{24} - Pc^*_{24} \\ & & 0 & c_{25} + c_{34} - P\left(c^*_{25} + c^*_{34}\right) \\ \text{SKW} & & & 0 \end{pmatrix}, \\ \mathbf{K}_0 &:= \begin{pmatrix} 0 & 0 & 0 & 0 \\ & 0 & 0 & 0 \\ & & -c_{22} + P\left(c^*_{22} - 1\right) & c_{24} - Pc^*_{24} \\ \text{SYM} & & & -c_{44} + Pc^*_{44} \end{pmatrix}, \end{aligned} \tag{3.38}$$

while the boundary operators for the boundary condition at hand are defined as follows

$$
\begin{aligned}
\mathbf{B}_1 &:= \begin{pmatrix} c_{11} - Pc^*_{11} & c_{12} - Pc^*_{12} & c_{13} - Pc^*_{13} & c_{15} - Pc^*_{15} \\ 0 & 0 & 0 & 0 \\ c_{13} - Pc^*_{13} & c_{23} - Pc^*_{23} & c_{33} - Pc^*_{33} & c_{35} - Pc^*_{35} \\ c_{15} - Pc^*_{15} & c_{25} - Pc^*_{25} & c_{35} - Pc^*_{35} & c_{55} - Pc^*_{55} \end{pmatrix}, \\
\mathbf{B}_0 &:= \begin{pmatrix} 0 & 0 & -c_{12} + Pc^*_{12} & c_{14} - Pc^*_{14} \\ 0 & 1 & 0 & 0 \\ 0 & 0 & -c_{23} + Pc^*_{23} & c_{34} - Pc^*_{34} \\ 0 & 0 & -c_{25} + Pc^*_{25} & c_{45} - Pc^*_{45} \end{pmatrix}.
\end{aligned}
\tag{3.39}
$$

Eq. (3.37a) is a second-order partial differential equation, complemented by the boundary conditions Eq. (3.37b,c). As discussed for the Timoshenko-like beam model, the smallest load $P = P_c$ for which the boundary value problem Eq. (3.37) admits nontrivial solutions is referred to as the global critical load, since it triggers incipient instability of the beam. The model is derived in the most general framework, where the elastic operator is fully coupled. When this formulation is specialized to the grid beam, some of the off-diagonal terms vanish, although the degree of coupling remains significant enough to make a closed form solution difficult to pursue. A numerical solution is therefore adopted, based on the Finite Difference Method, whose detailed implementation is provided in Appendix A.

3.3 Elastic and inertial constants identification algorithm

The identification of the constitutive matrix is carried out following the homogenization procedure outlined in [28, 37]. This approach enforces an appropriate energy equivalence between the (fine) 3D model and the (coarse) 1D one, as detailed below. The identification developed in this section seeks to extend the mixed homogenization approach to two cases: (i) the grain beam, studied under the assumption of rigid (both in and out of plane) cross-section; and (ii) the grid beam, studied under the assumption of rigid in plane and deformable out of plane cross-section, where the loss of planarity is accounted for through a warping function suitably derived.

It should be noted that the identification algorithm is presented with reference to the generalized beam model, i.e. the equivalent model described in Section 3.2.2 and characterized by the richest kinematics among those introduced in this work, as it provides the most general framework. Starting from this comprehensive formulation, the algorithm for simplified models such as the Timoshenko-like beam theory can be straightforwardly obtained by neglecting all contributions related to the warping phenomenon, which corresponds to prescribing $a\,(x) = 0$, and by reducing the operators' dimension.

The first stage of the identification algorithm calls for establishing a discrete map that connects the displacements of the fine model with those of the coarse one. Since the metamaterial under consideration is non-homogeneous, the identification is carried out at selected sampled abscissas, namely $x_i := i\,h$ $(i = 0, 1, ..., n)$, where h represents the period of the microstructure. At each x_i, the fine model possesses a cross-section $\mathcal{D}_i$ occupying a domain of the $(x, y)-$plane, while two successive cross-sections $\mathcal{D}_i$, $\mathcal{D}_{i+1}$ bound the cell. Fig. 3.2 depicts a generic metamaterial's cell, for which the specific topology has not yet been prescribed, where ℓ_y denotes the height of the $i-$th cross-section.

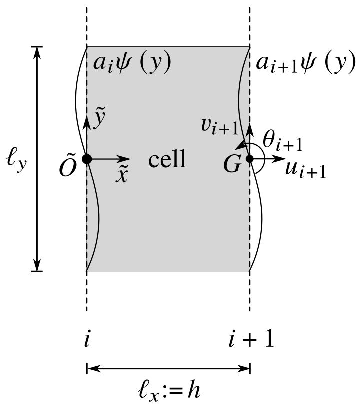

Figure 3.2. Generic periodic microstructure of a metamaterial.

To define a discrete map, a kinematic constraint is introduced: each sampled cross-section $\mathcal{D}_i$ is assumed to remain plane, whereas displacements within the cells are left unconstrained. The rigid displacement of $\mathcal{D}_i$, with $i = 0, 1, \ldots, n$, can thus be written as:

$$\begin{aligned} \tilde{u}\,(x_i, y) &= u\,(x_i) - \theta\,(x_i)\,y_i + a\,(x_i)\,\psi\,(y)\,, \\ \tilde{v}\,(x_i, y) &= v\,(x_i) + \theta\,(x_i)\,x_i, \end{aligned} \tag{3.40}$$

where, here and throughout this work, the tilde denotes a quantity related to the fine model. It is important to emphasize that the rotation $\theta\,(x)$ of the (flexurally) rigid cross-section of the equivalent beam model should be understood as the averaged rotation of the (flexurally deformable, i.e. warpable) sampled cross-section of the (fine) 3D model.

However, some clarifications are required regarding the warping function. The out of plane deformability implicitly corresponds to a displacement of the cross-section along the $x-$direction, namely $u\,(x)$. According to the de Saint-Venant's theory, the warping displacement can be expressed as the sum of a rigid component u_r and a purely deformative one u_d, $u = u_r + u_d$, which are orthogonal; this implies:

$$\int_{-\ell_y/2}^{\ell_y/2} u_r u_d \mathrm{d}y = 0. \tag{3.41}$$

Since the general rigid displacement can be written as $u_r = \hat{u} - \hat{\theta}y$, and the orthogonality condition (Eq. (3.41)) must hold $\forall\left(\hat{u}, \hat{\theta}\right)$, it follows that

$$\int_{-\ell_y/2}^{\ell_y/2} u_d \mathrm{d}y = 0, \quad \int_{-\ell_y/2}^{\ell_y/2} u_d y\, \mathrm{d}y = 0. \tag{3.42}$$

Here, the purely deformative component u_d is the unknown warping function ψ, which is a zero-mean function with a null static moment. By substituting $u_d = u - u_r$ into Eq. (3.42), the expressions for the rigid components' parameters can be easily obtained as

$$\hat{u} = \frac{1}{\ell_y} \int_{-\ell_y/2}^{\ell_y/2} u\,(y)\,\mathrm{d}y, \quad \hat{\theta} = -\frac{12}{\ell_y^3} \int_{-\ell_y/2}^{\ell_y/2} u\,(y)\,y\mathrm{d}y, \tag{3.43}$$

where $\hat{u}$ denotes the mean longitudinal translation of the cross-section and $\hat{\theta}$ its mean rotation about the $z-$axis. Consequently, once the total displacement u and its rigid component u_r are known, the purely deformative one is straightforwardly determined as $u_d\,(y) = u\,(y) - u_r\,(y) := \psi\,(y)$.

The second stage of the identification algorithm involves the so-called 'cell analysis', which requires enforcing the equivalence of elastic energies stored by the cell (fine model) and a beam segment of equal length (coarse model), when both models undergo identical displacements at their ends. In particular, the averaged energy density of the cell, namely $\tilde{\phi} := \tilde{U}/h$, where $\tilde{U}$ is the elastic energy, is determined as a function of the configuration variables of the equivalent beam, according to Eq. (3.40), as:

$$\tilde{\phi} = \frac{1}{h}\tilde{U}\left(u\,(x_i)\,, v\,(x_i)\,, \theta\,(x_i)\,, a\,(x_i)\,, u\,(x_{i+1})\,, v\,(x_{i+1})\,, \theta\,(x_{i+1})\,, a\,(x_{i+1})\right). \tag{3.44}$$

Finally, the last step of the procedure entails the comparison between the energy densities ϕ and $\tilde{\phi}$, defined in Eqs. (3.24) and (3.44), respectively. This comparison is carried out by expressing the displacements in terms of strains. Accordingly, the strain-displacement relationships Eq. (3.19) are integrated in the $(x_i,\, x_{i+1})-$interval for a prescribed test strain field. The simplest one is considered, assuming constant values with respect to ε, γ, κ and β, while α varies linearly with x in order to satisfy the compatibility condition (Eq. (3.20)). Therefore, it is:

$$\begin{aligned}
&\varepsilon\,(x) = \varepsilon_0 \\
&\gamma\,(x) = \gamma_0 \\
&\kappa\,(x) = \kappa_0 \qquad\qquad \forall x \in (x_i, x_{i+1}) \\
&\alpha\,(x) = \alpha_0 + \beta_0\,(x - x_i) \\
&\beta\,(x) = \beta_0
\end{aligned} \tag{3.45}$$

where the subscript 0 denotes a constant value. The corresponding end displacements (with rigid-body motions removed) are:

$$\begin{aligned}
u\,(x_i) &= 0, & u\,(x_{i+1}) &= \varepsilon_0\,h, \\
v\,(x_i) &= 0, & v\,(x_{i+1}) &= \gamma_0\,h + \frac{1}{2}\kappa_0\,h^2, \\
\theta\,(x_i) &= 0, & \theta\,(x_{i+1}) &= \kappa_0\,h, \\
a\,(x_i) &= a_0, & a\,(x_{i+1}) &= a_0 + \beta_0\,h.
\end{aligned} \tag{3.46}$$

Substituting Eq. (3.46) into Eq. (3.44) and enforcing the equality:

$$\phi = \tilde{\phi}, \qquad \forall\,(\varepsilon, \gamma, \kappa, \alpha, \beta)\,, \tag{3.47}$$

the elastic constants $\mathbf{C} := (c_{ij})$ are found. It is worth noting that the cell's boundary displacements defined in Eq. (3.46) can be interpreted as the superposition of five independent deformation modes:

- an extensional mode (E), in which the rigid cross-section $\mathcal{D}_{i+1}$ translates, without deformation, along $x-$direction;
- a shear mode (S), in which the rigid cross-section $\mathcal{D}_{i+1}$ translates, without deformation, along $y-$direction;
- a flexural mode (F), in which the rigid cross-section $\mathcal{D}_{i+1}$ rotates and translates, around the $z-$axis and along the $y-$direction, respectively, without deformation;
- a uniform distortional mode (UD), in which both the cross-sections, $\mathcal{D}_i$ and $\mathcal{D}_{i+1}$, deform without translation or rotation, following the same displacement field;
- a non uniform distortional mode (NUD), in which only the cross-section $\mathcal{D}_{i+1}$ deforms without translation or rotation;

which are depicted in Fig. 3.3 for a generic microstructure.

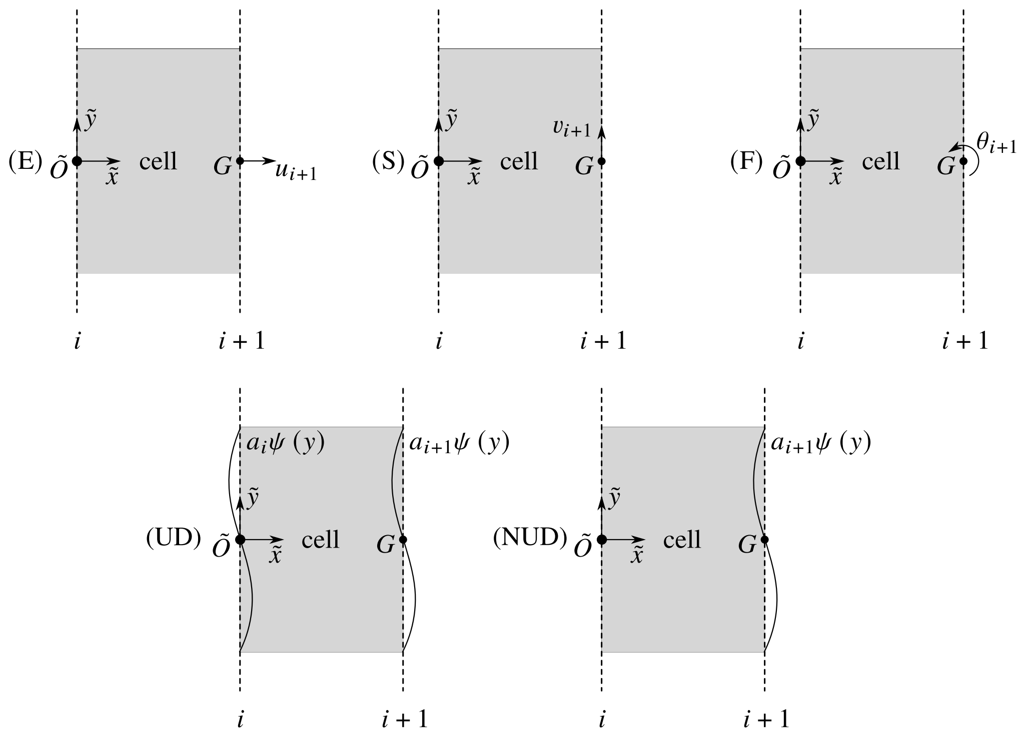

Figure 3.3. Deformation modes assigned to the generic periodic microstructure of a metamaterial: (E) extensional; (S) shear; (F) flexural; (UD) uniform distortional; (NUD) non uniform distortional.

In Fig. 3.3, since the warping function depends on the microstructure under investigation, the displacement fields depicted for the UD and NUD modes, namely $a_i\psi\left(y\right)$ and $a_{i+1}\psi\left(y\right)$, are intended for illustrative purposes only.

It is important to underline that in the aforementioned list, the extensional, shear, and flexural modes are applied under the assumption that the cross-section $\mathcal{D}_{i+1}$ translates and rotates as a rigid body, without undergoing deformation. Regarding the extensional and flexural modes, even if they were applied to a 3D cell model with a cross-section rigid in plane but deformable out of plane, no deformation would occur, as warping phenomena can only be induced by shear in a 2D framework. However, even the shear mode is applied under the assumption that the cross-section translates as a rigid body, without undergoing deformation. This approach is feasible because the chosen equivalent model features an enriched kinematic description, in which warping effects are explicitly represented through dedicated kinematic quantities, thereby allowing for a clear distinction between the purely deformative effects (induced by shear) and those arising from rigid-body translation. This modeling choice provides an effective means of incorporating warping effects within the enhanced kinematic description.

Since there are five strains, corresponding to the five independent deformation modes of the cell, and fifteen unknown elastic constants, all possible combinations of the independent modes must be systematically selected and applied to the cell. Therefore, coupled deformation modes, identified through the superposition of effects, are also applied to the cell, namely: extensional and shear (ES), extensional and flexural (EF), extensional and uniform distortional (EUD), extensional and non uniform distortional (ENUD), shear and flexural (SF), shear and uniform distortional (SUD), shear and non uniform distortional (SNUD), flexural and uniform distortional (FUD), flexural and non uniform distortional (FNUD), uniform and non uniform distortional (UNUD). For coupled modes, the energy contributions of the pure modes have to be subtracted from the total energy of the coupled one.

The procedure for the analytical evaluation of $\tilde{\phi}$ for the microstructures under consideration, as well as the algorithm adopted for the numerical algorithm adopted for the identification of the elastic coefficient, will be presented in detail in the following chapters.

It is worth highlighting that deriving an analytical closed-form expression for the elastic energy of the cell represents a challenging task, feasible only for sufficiently simple microstructure's topology. For more complex configurations, this step becomes difficult to pursue; nevertheless, a numerical identification procedure [35] is always viable. Within the framework of the mixed homogenization approach, the elastic properties of the equivalent beam model are numerically identified by enforcing an energy equivalence between a representative periodic cell of the frame and a segment of the homogenized beam occupying the same volume, when both models undergo identical displacement. The cell, regardless of the microstructure's topology, is bounded by two transverse cross-sections, each endowed with half of the stiffness, and is constrained at the periodic joints by external hinges. The equivalent beam segment, on the other hand, is clamped at the ground. The same deformation modes adopted in the analytical identification procedure are applied to both models, and the corresponding elastic energies are computed. For the equivalent beam, the elastic energy is evaluated as $U = \phi\, h$, with ϕ being the elastic potential energy density of the slice of the equivalent beam model. For the periodic cell, the elastic energy is determined according to Clapeyron's theorem, based on the reactions induced at the constrained joints, which, given the numerical character of the algorithm, are evaluated with a FE analysis of the cell. By enforcing the equality of the elastic energies over a suitable set of independent deformations, all the elastic constants of the constitutive matrix of the homogenized beam can be systematically and efficiently identified in a numerical framework.

Once the elastic constants are identified, the inertial properties required for the free dynamic analysis are determined following the same homogenization strategy. In fact, the procedure relies on enforcing the energy equivalence between the kinetic energy of the cell (fine model) and a beam segment of equal length (coarse model) subjected to a uniform velocity field. The masses are assumed to be lumped at the discontinuity joints, with translational inertia accounted for all the elements that make up the cell and rotational inertia included only when it cannot be considered negligible with respect to the translational counterpart.
Similarly to the evaluation of $\tilde{\phi}$, the explicit form of the kinetic energy $\tilde{\mathcal{T}}$ depends on the microstructure at hand; therefore, it is presented in detail in the following Chapters.

Chapter 4

Grain beam

4.1 Introduction

In this Chapter, attention is focused on the mechanical behavior of the grain beam. This metamaterial has been widely studied in the literature since its distinctive topology confers the property of chirality, namely the property by which the coupling of deformation modes is achieved.
The elastic coefficients governing the response of the equivalent beam are identified using both analytical and numerical procedures, and their comparison provides a measure of the extent of the approximation due to the hypotheses introducted in the analytical approach. The inertial coefficients, on the other hand, are determined analytically. To gain deeper insight into the chiral behavior, a qualitative analysis of the chiral beam's mechanical response, based on the analytical identification of the elastic coefficients, is presented. This study, previously introduced by the author in [55], also provides the case studies for the following analyses.
Finally, the effectiveness and limitations of applicability of the equivalent beam model are assessed through numerical simulations carried out on selected case studies in static, dynamic, and buckling conditions. Subsequently, a preliminary experimental validation of the equivalent beam model under static loading is carried out by means of a uniaxial tensile test performed on a 3D printed sample, with the acquired data post-processed using an advanced measurement technique, namely the Digital Image Correlation (DIC).

4.2 Topology of the microstructure

The topology of the grain beam is described. The cell in Fig. 4.1 is referred to a (local) cartesian coordinate system $\tilde{O}\tilde{x}\tilde{y}$, originating at the centroid of the left grain $\tilde{O}$. The cell, which as has already been said has a length h, is composed of two semicircular half grains, of radius R, which are connected by two families of (micro) bodies, also referred to as 'fibers' throughout the Chapter, whose axis-lines are dashed in the figure, namely: (i) those parallel to the (local) $\tilde{x}-$axis of the cell, i.e. the horizontal fibers, and (ii) that parallel to the (local) $\tilde{y}-$axis of the cell, i.e. the vertical one. The width of the horizontal and vertical bodies is taken equal to t_ν ($\nu = x, y$) where the subscript refers to the $\nu-$axis orientation ($x-$ or $y-$ parallel); furthermore, the thickness of the cell, i.e. its dimension along the $z-$axis, not depicted in Fig. 4.1, is set to t_z for all the fibers, and assumed to be negligible with respect to cell length and height. As a consequence, a predominantly plane stress behavior occurs when in plane loads are applied to the cell. Finally, the length ℓ_c denotes the distance between the vertical diameter of the grain and the intersection between the grain's circumference and the intrados or extrados of horizontal fibers. Accordingly, the length of the horizontal fibers, namely ℓ_x, results to be $\ell_x = h/2 - \ell_c$, while that of the vertical fiber is denoted as ℓ_y, both referred to their axis-lines.

It's important to remark that the cell lacks symmetry axes, thus resulting in some strains coupling at the macro-scale, the type of which depends on the microstructure's design. In particular, as discussed in [1, 2], if the horizontal fibers have the same cross-sections, even if it is different from that of the vertical one, only shear–axial strains coupling occurs at the macro-scale, independently on the lengths ℓ_x and ℓ_y; on the other hand, if the horizontal fibers have different cross-sections (or lengths), independently on the length and cross-section of the vertical one, also the other couplings arise at the macro-level, such as axial–flexural and shear–flexural strains coupling. In what follows, the general cases $\ell_x \neq \ell_y$ and $t_x \neq t_y$ will be considered in the identification of the homogenized (equivalent) beam model, while numerical analyses will be carried out assuming $t_x = t_y =: t$. Therefore, only the coupling between shear and axial strains will be observed.

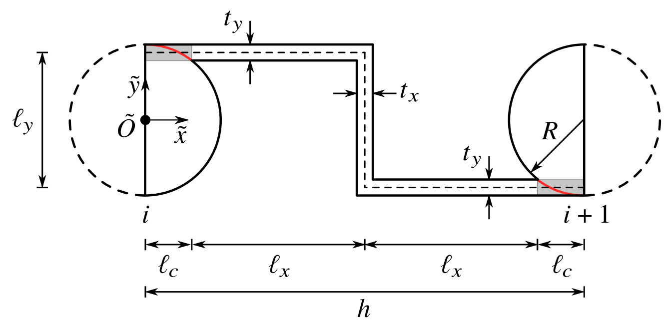

Figure 4.1. Periodic microstructure of the grain beam.

Furthermore, the grain beam is build up, as shown in Fig. 4.2, where the (local and global) horizontal axes are taken coincident, namely $\tilde{x} \equiv x$, the origin O of the global coordinate system is assumed to be located on the $i = 0$ grain and, accordingly the local axis $\tilde{y}$ is parallel to $y-$axis, for each cell.

As previously detailed in Section 3.2.1, in order to describe the statics, dynamics and buckling behavior of the (fine) grain beam, the Timoshenko-like equivalent beam model is heuristically adopted as the target (and coarse) model, according to the mixed homogenization approach.

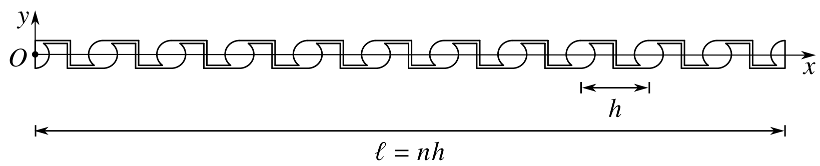

Figure 4.2. Study object: the grain beam.

4.3 Identification of the elastic and inertial coefficients

4.3.1 Analytical identification of the elastic constants

The identification algorithm explained in Section 3.3 is now specialized for the grain beam. The procedure for the analytical evaluation of $\tilde{\phi}$ is detailed as follows (see, also, [55]) but, first of all, some modeling assumptions concerning the microstructure in Fig. 4.1 are introduced. It is considered as an assembly of rigid-body semi-grains connected to each other through sufficiently slender bodies, namely the fibers, which, in turn, are assumed to behave as Timoshenko (micro) beams, of length ℓ_x and ℓ_y, and rectangular cross-sections of sides t_z and t_ν ($\nu = x, y$), whose assembly results in a planar frame. Another modeling assumption concerns the choice of the length ℓ_c, since it quantifies the extension of the region in which a transition between a rigid-body behavior, i.e. that of the semi-grains (whose boundaries are denoted in red in the figure), and a deformable one, i.e. that of the fibers, occurs. These regions, assumed to behave as rigid-bodies, are shaded in gray in Fig. 4.1, from which it is also apparent that the definition of the length ℓ_c is not unique, i.e. it can be chosen in a range which varies (approximately) from zero, corresponding to the case of very thin horizontal beams compared to the grain radius and, as denoted in figure, up to the distance between the vertical diameter and the intrados or extrados of the horizontal beams. It has to be highlighted that the choice made here appears to be the most appropriate for describing the effective (i.e., deformable) length of the horizontal fibers, particularly when they are sufficiently slender and assumed to behave as Timoshenko beams connected to rigid grains. Each fiber constituting the frame is characterized by axial, shear, and bending stiffnesses, namely EA_ν, GA_ν^*, and EI_ν. Here, E and G are the elastic and tangential modulus, respectively, $A_\nu = t_\nu \times t_z$ the fiber's cross-section area, $A_\nu^* = 5/6\,(t_\nu \times t_z)$ the shear area, and $I_\nu = 1/12\,(t_\nu^3 t_z)$ the inertia moment with respect to its cross-section principal axis, which is parallel to $z-$axis, respectively ($\nu = x, y$). With these assumptions, the fine model of the grain microstructure is schematized as reported in Fig. 4.3, where the axis-line of three Timoshenko beams is sketched. The beams are rigidly linked at their ends to the centroids of the grains by means of ideal rigid bars (denoted with a thicker line in the figure). These bars, placed at the cross-sections $\mathcal{D}_i$ and $\mathcal{D}_{i+1}$ which identify the grain and thus define the boundaries of the cell, are in turn constrained at the periodicity interfaces of the cell through external hinges.

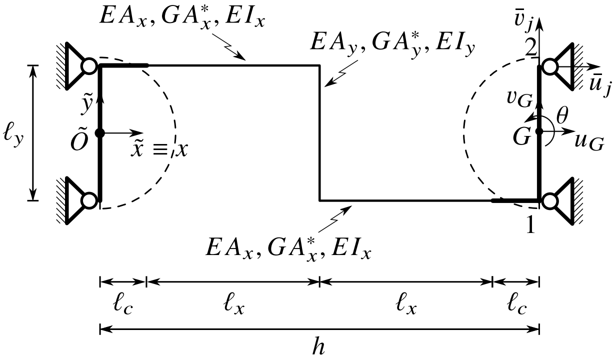

Figure 4.3. Periodic microstructure of the grain beam modeled as an assembly of Timoshenko beams, rigidly connected to the grain-pairs.

Once the cell is modeled, its elastic energy is evaluated by assigning the deformation modes described in Section 3.3, i.e. by applying proper boundary displacements at the (periodicity) hinges (denoted with 1 and 2 in Fig. 4.3), and by pursuing a static analysis of the planar frame. In particular, the (left) cross-section $\mathcal{D}_i$ is kept fixed and a suitable rigid motion is assigned to the (right) cross-section $\mathcal{D}_{i+1}$, according to Eq. (3.46).

It is worth recalling that the identification algorithm presented in Section 3.3 is formulated with reference to the equivalent beam model characterized by the richest kinematic, namely the generalized beam model. However, the grain beam is represented through a Timoshenko-like model, which assumes the cross-section to remain rigid, both in plane and out of plane, and therefore does not account for local deformation phenomena. Accordingly, following the procedure outlined in Section 3.3, all contributions associated with deformation effects are neglected by setting the amplitude of the deformation function $a\,(x)$ equal to zero, and by reducing the operators' dimension.

Therefore, Eq. (3.46) can be interpreted as the superposition of three pure deformation modes, the extensional (E), shear (S), and flexural (F) one, applied under the assumption that the cross-section $\mathcal{D}_{i+1}$ translates and rotates as a rigid body, without undergoing deformation. In the Timoshenko-like beam model, there are three strains corresponding to the three independent deformation modes of the cell, and six unknown elastic constants, all possible combinations of the independent modes must be systematically selected and applied to the cell. In this way, coupled deformation modes, identified through the superposition of effects, are also applied to the cell, namely: extensional and shear (ES), extensional and flexural (EF), and shear and flexural (SF). Of course, when a coupled mode is applied, the energy of the involved deformation modes needs to be subtracted from the energy of the coupled ones.

This procedure can be pursued starting from Eq. (3.46), which also defines the displacements of the centroid G of the cross-section $\mathcal{D}_{i+1}$, reads: $u_G = u\,(x_{i+1})$, $v_G = v\,(x_{i+1})$ and $\theta = \theta\,(x_{i+1})$. Then, for each deformation mode to be assigned in the algorithm, i.e. for a known set of centroid displacements, Eq. (3.40) supplies the (rigid) displacements $\tilde{u}\,(x_{i+1}, \mp\ell_y/2) =: \bar{u}_j$, $\tilde{v}\,(x_{i+1}, \mp\ell_y/2) =: \bar{v}_j$ of the $j-$th hinges $(j = 1, 2)$, namely (remember that $\tilde{O}$ is different from G), namely:

$$\bar{u}_j = u_G \pm \theta \frac{\ell_y}{2}, \quad \bar{v}_j = v_G + \theta\left(\tilde{x}_{i+1} - h\right) = v_G, \quad \text{with} \quad j = 1, 2. \tag{4.1}$$

However, from a computational point of view, it is more convenient to: (i) assign unitary displacements at the hinges, (ii) express the centroid displacements by using Eq. (4.1), and (iii) evaluate the associated strains through Eq. (3.46). By summarizing, the algorithm to apply is detailed in what as follows.

1. Extensional mode (E) is assigned, in which $\mathcal{D}_{i+1}$ translates axially. Therefore, $\bar{u}_j = 1$ $(j = 1, 2)$ is set and, since $u_G = 1$, $v_G = 0$, $\theta = 0$, then $\varepsilon_0 = 1/h$, $\gamma_0 = 0$, $\kappa_0 = 0$; c_{11} is computed.

2. Shear mode (S) is assigned, in which $\mathcal{D}_{i+1}$ translates transversely. Therefore, $\bar{v}_j = 1$ $(j = 1, 2)$ is set and, since $u_G = 0$, $v_G = 1$, $\theta = 0$, then $\varepsilon_0 = 0$, $\gamma_0 = 1/h$, $\kappa_0 = 0$; c_{22} is computed.

3. Flexural mode (F) is assigned, in which $\mathcal{D}_{i+1}$ rotates around the z-axis and translates transversely. Therefore, $\bar{u}_j = -\tilde{y}_j$ together with $\bar{v}_j = h/2 + \tilde{x}_j$ $(j = 1, 2)$ are set; since $u_G = 0$, $v_G = h/2$, $\theta = 1$, then $\varepsilon_0 = 0$, $\gamma_0 = 0$, $\kappa_0 = 1/h$; c_{33} is computed.

4. Extensional and shear mode (ES), i.e. the superposition of the pure modes (E), (S), is assigned, for which $\varepsilon_0 = 1/h$, $\gamma_0 = 1/h$, $\kappa_0 = 0$; since c_{11}, c_{22} are known, c_{12} is computed.

5. Extensional and flexural mode (EF), i.e. the superposition of the pure modes (E), (F), is assigned, for which $\varepsilon_0 = 1/h$, $\gamma_0 = 0$, $\kappa_0 = 1/h$; since c_{11}, c_{33} are known, c_{13} is computed.

6. Shear and flexural mode (SF), i.e. the superposition of the pure modes (S), (F), is assigned, for which $\varepsilon_0 = 0$, $\gamma_0 = 1/h$, $\kappa_0 = 1/h$; since c_{22}, c_{33} are known, c_{23} is computed.

Remarkably, for each of the (pure and coupled) assigned deformation mode, an analytical (exact) solution of the elasto-static problem for such a planar frame, subject to given displacements at the right hinges, as shown in Fig. 4.4, is determined; accordingly, displacement, strain and stress fields of the $k-$th Timoshenko (micro) beam, with $k = 1, 2, 3$ are found. In particular, for each of the six problems shown Fig. 4.4, the elastic energy of the cell $\tilde{U^0}$ is evaluated as the sum of the elastic energy of the k-th beam $\tilde{U^0_k}$, namely:

$$\tilde{U^0}\left(\varepsilon, \gamma, \kappa\right) = \sum_{k=1}^{3} \tilde{U^0_k}, \quad \text{with} \quad k = 1, 2, 3, \tag{4.2}$$

where

$$\tilde{U}_k^0(\varepsilon,\gamma,\kappa) = \frac{1}{2}\int_0^{\ell_x} \left(EA_x\varepsilon_k^2 + GA_x^*\gamma_k^2 + EI_x\kappa_k^2\right)\mathrm{d}x, \quad \text{with} \quad k = 1,2$$
$$\tilde{U}_3^0(\varepsilon,\gamma,\kappa) = \frac{1}{2}\int_0^{\ell_y} \left(EA_y\varepsilon_3^2 + GA_y^*\gamma_3^2 + EI_y\kappa_3^2\right)\mathrm{d}x, \tag{4.3}$$

in which $\tilde{U}_1^0$ and $\tilde{U}_2^0$ are the elastic energies of the horizontal fibers and $\tilde{U}_3^0$ is that of the vertical one. Finally, since $\tilde{\phi}^0 = \tilde{U}^0/h$, the Green's law Eq. (3.6) supplies for the elastic matrix that, in the static and dynamic problem, is $\mathbf{C}^0 \coloneqq \mathbf{C}$.

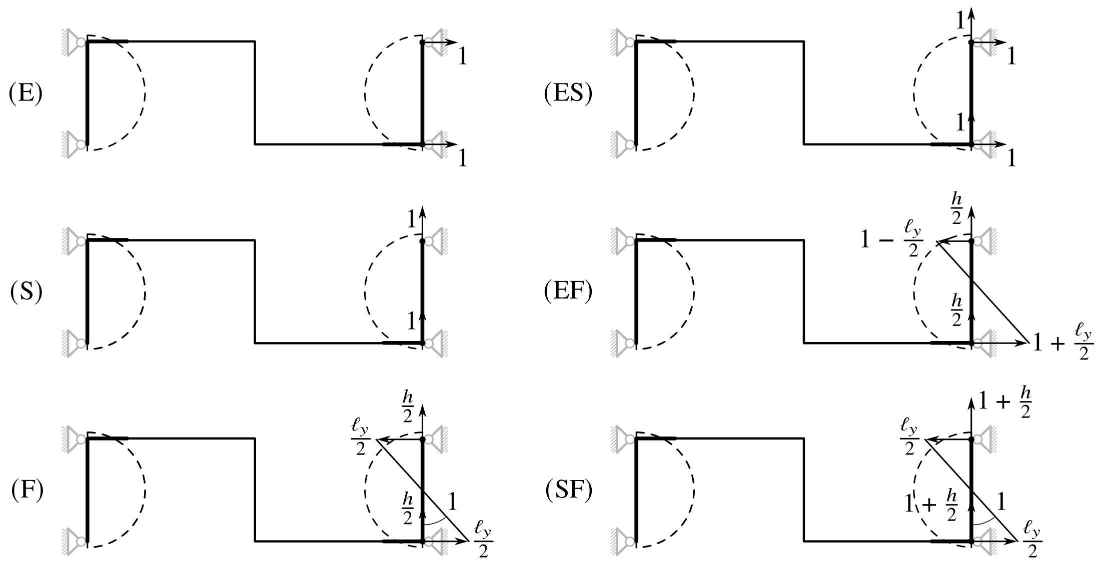

Figure 4.4. Deformation modes assigned to the periodic microstructure modeled as an assembly of Timoshenko (micro) beams: (E) extensional; (S) shear; (F) flexural; (ES) extensional and shear; (EF) extensional and flexural; (SF) shear and flexural.

As already mentioned, a shear-axial displacement coupling at the macro-scale is observed in the case at hand, so that Eq. (3.8) turns out to be defined as:

$$\mathbf{C} = \begin{pmatrix} c_{11} & c_{12} & 0 \\ & c_{22} & 0 \\ \text{SYM} & & c_{33} \end{pmatrix}, \tag{4.4}$$

where the chiral behavior is represented by the off-diagonal term $c_{12} \neq 0$. The analytical expression of the elastic coefficients is reported in Appendix B for both the cases $t_x \neq t_y$ and $t_x = t_y$.

The analytical identification of the elastic coefficients is often the most challenging step in the identification process. In fact, it is achievable in the present case due to the simple fiber arrangement, i.e. when modeled as beams, and the assumption of rigid boundary cross-sections, which neglect micro-warping and account for the contribution of the (rigid) half-grains. However, in cases where the interconnecting elements cannot be modeled as beams or the grains cannot be treated as rigid bodies, a numerical identification procedure, such as one based on FE analysis, becomes mandatory, as will be discussed shortly.

However, in the buckling analysis the elastic operator $\mathbf{C}$ depends on both the strains and the prestress (see Section 3.2), according to Eq. (3.2). This dependence originates from the uniform prestress state acting on each fiber of the cell in the precritical configuration. Accordingly, when writing the energy for deriving the constitutive matrix $\mathbf{C}$, both the elastic term $\tilde{U}_k^0$ (Eq. (4.3)), namely the work spent by the stresses in the first-order strains $\varepsilon^{(1)}$, and the geometric term $\tilde{U}_k^*$, namely the work spent by the prestress $\mathring{N}$ in the second-order strains $\varepsilon^{(2)}$, must be considered. To determine the prestress acting in each fiber, the cell is constrained at the periodicity joints by external hinges at the cross-section $\mathcal{D}_i$, and by external horizontal rollers at the cross-section $\mathcal{D}_{i+1}$, thus allowing the horizontal translation of the latter. By deriving the analytical (exact) solution of the elasto-static problem for such a planar frame, subject to the prestressing force $\mathring{N} = -P$ at the cross-section $\mathcal{D}_{i+1}$ (see Fig. 4.5), the stress fields of the $k-$th Timoshenko beam are obtained, and the corresponding prestress in each fiber can be determined.

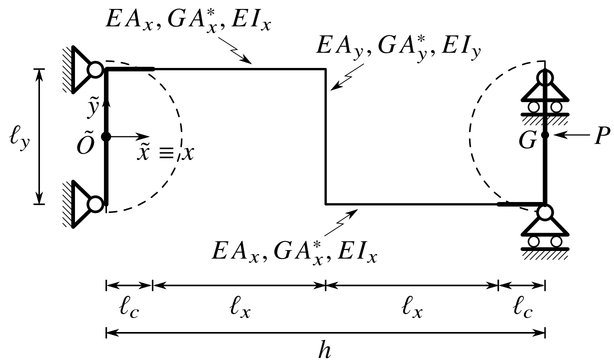

Figure 4.5. Periodic microstructure of the grain beam modeled as an assembly of Timoshenko beams, rigidly connected to the grain-pairs and subject to the prestress force $\mathring{N} = -P$.

The horizontal and vertical fibers are subjected to uniform prestress, namely $\mathring{N}_k = -P$ for $k = 1, 2$ and $\mathring{N}_3 = -\zeta P$. The analytical expression of the coefficient ζ is provided in Appendix B, for both the cases $t_x \neq t_y$ and $t_x = t_y$. Accordingly, the geometric contribution to the elastic energy reads

$$
\begin{aligned}
\tilde{U}_k^*\left(\varepsilon, \gamma, \kappa, \mathring{N}\right) &= \int_0^{\ell_x} \left(\mathring{N}_k \varepsilon_k^{(2)}\right) \mathrm{d}x, \quad \text{with} \quad k = 1, 2 \\
\tilde{U}_3^*\left(\varepsilon, \gamma, \kappa, \mathring{N}\right) &= \int_0^{\ell_y} \left(\mathring{N}_3 \varepsilon_3^{(2)}\right) \mathrm{d}x.
\end{aligned}
\tag{4.5}
$$

where $\tilde{U}_1^*$ and $\tilde{U}_2^*$ are the geometric energies of the horizontal fibers, and $\tilde{U}_3^*$ that of the vertical one. By applying the Green's law also the fully coupled matrix

$$
\mathbf{C}^* = \begin{pmatrix} c_{11}^* & c_{12}^* & c_{13}^* \\ & c_{22}^* & c_{23}^* \\ \text{SYM} & & c_{33}^* \end{pmatrix}, \tag{4.6}
$$

is obtained, whose analytical expression is reported in Appendix B for both the cases

$t_x \neq t_y$ and $t_x = t_y$.

4.3.2 Numerical identification of the elastic constants

Following the same steps described for the analytical identification, a numerical identification of the elastic matrix is also pursued. The procedure is outlined in [35], when a framed microstructure is taken into account and here extended to a grain beam for which the cell is modeled as a 2D Cauchy continuum. Therefore, grains are deformable but, as in the analytical identification, cross-sections $\mathcal{D}_i$ and $\mathcal{D}_{i+1}$ are assumed as rigid-bodies. Moreover, to better understand the effect of the presence of the grains in the model, the numerical identification is developed under two different cases (see Fig. 4.6), namely with and without grains, named respectively NC (Numerical Cauchy, Fig. 4.6a) and NC-ng (Numerical Cauchy - no grains, Fig. 4.6b). Accordingly, in the former model, the grains contribute to the elastic energy of the cell with their deformability, while in the latter no contribution is given since they behave as rigid bodies. Furthermore, in the former case the cross-sections $\mathcal{D}_i$ and $\mathcal{D}_{i+1}$ are hinged at the periodicity joints while in the latter one the cell is considered as clamped in the correspondence of the boundary between the grains and the horizontal fibers.

For each deformation mode, the displacements u_G, v_G and θ of the centroid of the cross-section $\mathcal{D}_{i+1}$ are the same considered in the analytical identification procedure. Also those to be applied at the hinged joints are the same in the NC case (Fig. 4.6a); while, for the NC-ng case (Fig. 4.6b), they are evaluated at the clamped boundary through Eq. (4.1).

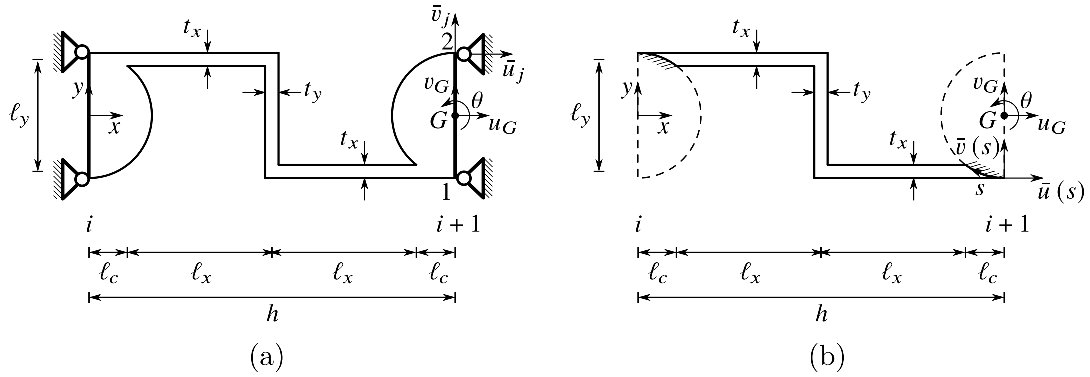

Figure 4.6. Periodic microstructure of the grain beam modeled as an assembly of plate/membrane (2D Cauchy continuum): (a) with grains; (b) without grains.

The algorithm for the evaluation of the constitutive matrix, in the numerical identification procedure, consists of two steps:

1. in the first step a FE analysis of the cell is performed and its elastic energy evaluated, for each assigned deformation mode, through the application of the Clapeyron's theorem, namely: (i) $\tilde{U} = \frac{1}{2}\sum_{j=1}^{2}(r_{xj}\bar{u}_j + r_{yj}\bar{v}_j)$, for the NC case in Fig. 4.6a, where r_{xj} and r_{yj} are the horizontal and vertical components of the hinges' reactions,

respectively; (ii) $\tilde{U} = \frac{1}{2}\int_0^{\ell_s}\left[r_x(s)\,\bar{u}(s) + r_y(s)\,\bar{v}(s)\right]\mathrm{d}s$ for the NC-ng case in Fig. 4.6b, where $r_x(s)$ and $r_y(s)$ are the (distributed) horizontal and vertical components of the clamp reactions in the $[0, \ell_s]$ clamped region, spanned by the s abscissa, expending work on the horizontal and vertical components of the displacement $\bar{u}(s)$ and $\bar{v}(s)$, respectively;

2. then, by requiring Eq. (3.47) holds for any ε, γ, κ in which $\tilde{\phi}^0 = \tilde{U}^0/h$, the unknown six elastic constants are computed.

Finally, it is worth to notice that the first step of the algorithm calls for assigning proper boundary displacements at the cell, in the same way described in Section 3.3, which is graphically recalled in Fig. 4.7 for the case of cell modeled as a Cauchy 2D-elements assembly.

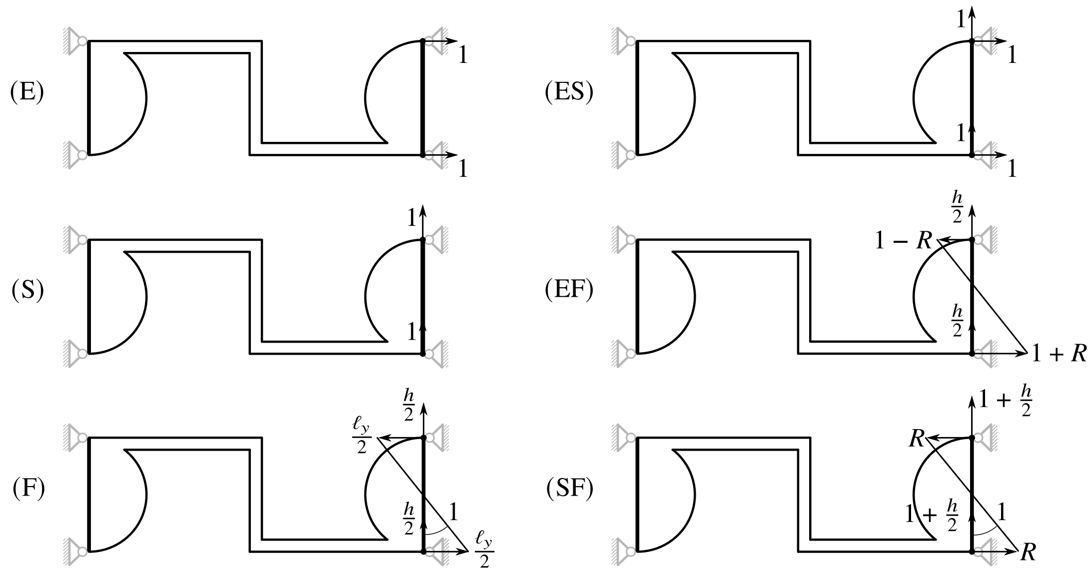

Figure 4.7. Deformation modes assigned to the periodic microstructure modeled as a plate assembly (Cauchy 2D): (E) extensional; (S) shear; (F) flexural; (ES) extensional and shear; (EF) extensional and flexural; (SF) shear and flexural.

4.3.3 Identification of the inertial properties

The analytical identification of the inertial properties is performed. To this end, the cell depicted in Fig. 4.1 is considered again under the same modeling assumptions adopted for the analytical identification of the elastic coefficients. Moreover, the masses are assumed to be lumped at the $j-$th discontinuity joint of the cell (Fig. 4.8).

Nevertheless, to more accurately reproduce the actual mass distribution of the grain beam, additional modeling assumptions are required. When the microstructure is modeled as in Fig. 4.3, rigid bodies with cross-section area $A_\nu = t_\nu \times t_z$ and lengths ℓ_y and ℓ_c are used to represent the semi-grains and the transition region between rigid-body and deformable behavior. However, in the cell's fine model (Fig. 4.1), the semi-grains and the transition

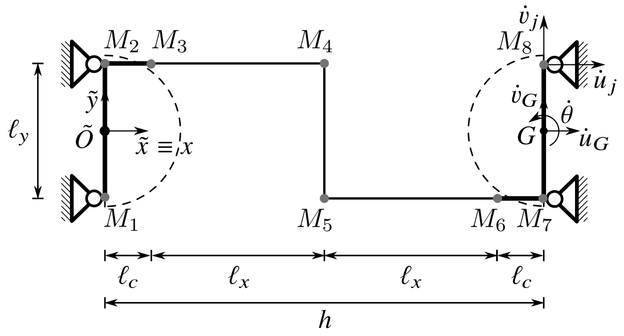

Figure 4.8. Periodic microstructure of the grain beam with lumped masses at the periodicity joints.

regions occupy in the $(x,\ y)$-plane the semicircular area $\pi R^2/2$ and the triangular area A_t, respectively. The latter corresponds to the region shown in Fig. 4.1, bounded by the red grain arc and the intrados (or extrados) of the horizontal fibers. Of course, these regions contribute to the overall mass of the cell in a manner that differs significantly from the contribution provided by the rigid bodies used to model them in the analytical approximation. To ensure consistency between the fine and the coarse models, equivalent mass densities are assigned to the rigid bodies in order to account for the actual mass distribution. Moreover, the translational inertia is considered for all the elements that make up the cell, whereas rotational inertia is regarded non-negligible (compared to the translational one) only for the semi-grains. Accordingly, the kinetic energy $\tilde{\mathcal{T}}$ of a cell subjected to a constant velocity field reads:

$$\tilde{\mathcal{T}} = \frac{1}{2}\left[\sum_{j=1}^{8} M_j \left(\dot{\tilde{u}}_j^2 + \dot{\tilde{v}}_j^2\right) + \frac{M_g}{2} R^2 \dot{\theta}^2\right], \tag{4.7}$$

where M_j are the lumped masses at the $j-$th joint with coordinates $(\tilde{x}_j, \tilde{y}_j)$, $M_g/2$ (with $M_g = \rho\pi R^2 t_z$) is the semi-grains' mass, $\dot{\tilde{u}}_j$, $\dot{\tilde{v}}_j$ are the translational velocities, and $\dot{\theta}$ is the rotational one.

By applying the displacement map (Eq. (4.1)) and equating $\tilde{\mathcal{T}}$ to the kinetic energy $\mathcal{T}$ of a beam segment of the same length h, the following inertial properties of the equivalent beam model are determined (Eq. (3.11c)).

$$m = \frac{1}{h}\sum_{j=1}^{8} M_j, \quad I_x = \frac{1}{h}\sum_{j=1}^{8} M_j \tilde{x}_j, \quad I_y = \frac{1}{h}\sum_{j=1}^{8} M_j \tilde{y}_j, \quad I_{xy} = \frac{1}{h}\left[\sum_{j=1}^{8} M_j \left(\tilde{x}_j^2 + \tilde{y}_j^2\right) + \frac{M_g}{2} R^2\right]. \tag{4.8}$$

4.4 Qualitative analysis of the mechanical behavior

The analytical identification of the constitutive matrix supplies closed-form expressions which relates micro and macro quantities, see Eqs. (B.1) and (B.4) in Section 4.3.1.

Such identification gives the possibility to design the microstructure behavior, aiming at obtaining a targeted macroscopic behavior of the grain beam.

To accomplish this task, in this section a qualitative analysis of the mechanical behavior of the grain beam is carried out by conducting a parametric analysis of the identified constitutive coefficients while varying the geometric characteristics of the microstructure. The analysis is carried out by considering the horizontal and vertical fibers of the same cross-section, i.e. $t_z \times t$, with $t = t_x = t_y$, and, therefore, $A_\nu = A$, $A^*_\nu = A^*$, $I_\nu = I$, the radius of gyration of the cross-section is defined as $\rho = \sqrt{I/A}$, as well as the non-dimensional beam's stiffness ratio $\mu_\nu = 12EI/GA^*\ell_\nu^2$ with respect to ν-axis ($\nu = x, y$). Given the geometry of the cell shown in Fig. 4.1, the following relations hold:

$$h = 2\left(\ell_c + \ell_x\right), \quad \ell_c = \sqrt{t\left(2R - t\right)}, \quad \ell_y = 2R - t. \tag{4.9}$$

Then, it is useful to introduce two non-dimensional parameters, namely $\hat{\alpha} := h/2R$ and $\hat{\beta} := \ell_x/\ell_y$, which represent, respectively the aspect ratio of the cell, i.e. the ratio between its length and height, and the ratio between the lengths of horizontal and vertical beams. By making use of Eqs. (4.9), it is:

$$\hat{\beta} = \frac{\hat{\alpha} - \sqrt{\hat{\eta}\left(2 - \hat{\eta}\right)}}{2 - \hat{\eta}}, \tag{4.10}$$

where $\hat{\eta} := t/R$, is the non-dimensional thickness-radius ratio. Equation (4.10) shows that, for a given cell's aspect ratio $\hat{\alpha}$ (and radius R), $\hat{\beta}$ (nonlinearly) depends on the $\hat{\eta}$ and, as it will be clear soon, it can be seen as an (indirect) measure of the fibers' slenderness. In particular, within the range $0 < \hat{\eta} < 1$, for which $R > t$, from Eqs. (4.9) and (4.10), it can be observed that: (i) when $\hat{\eta} \to 0$, i.e. the fibers have a vanishing thickness ($t \to 0$), then $\hat{\beta} \to \hat{\alpha}/2$, $\ell_y \to 2R$, $\ell_c \to 0$, $h \to 2\ell_x$; (ii) when $\hat{\eta} \to 1$, i.e. the fibers have a thickness comparable to the grain's radius ($t \to R$), then $\hat{\beta} \to \hat{\alpha} - 1$, $\ell_y \to R$, $\ell_c \to R$, $h \to 2\left(R + \ell_x\right)$. Moreover, in the (limit) case $\hat{\eta} \to 2$, occurring when the fibers have a thickness comparable to the double of the grain's radius ($t \to 2R$), then $\hat{\beta} \to \infty$, thus entailing that the horizontal fibers are superimposed and the vertical fiber no longer exist, namely $\ell_y \to 0$, together with $\ell_c \to 0$ and $h \to 2\ell_x$.

In order to better highlight the meaning of the parameter $\hat{\beta}$, Eq. (4.10) is expanded in series for small $\hat{\eta}$ (retaining $\hat{\alpha}$ of order one in the expansion), thus obtaining:

$$\hat{\beta} \simeq \frac{\hat{\alpha}}{2} - \frac{\sqrt{\hat{\eta}}}{\sqrt{2}} + \frac{\hat{\alpha}\hat{\eta}}{4} + \mathcal{O}\left(\hat{\eta}^{3/2}\right). \tag{4.11}$$

Equation (4.11) shows that $\hat{\beta}$ differs form $\hat{\alpha}/2$ due to a small (not vanishing) $\hat{\eta}$ and it can increase or decrease with $\hat{\eta}$ depending on the magnitude of the second and third term on the right side of Eq. (4.11). Indeed, from Eq. (4.11) it can be estimated that: when $\hat{\eta} > \hat{\eta}_{lim} := 8/\hat{\alpha}^2$, then $\hat{\beta}$ increases with $\hat{\eta}$, i.e. the greater is $\hat{\beta}$ the thicker are the fibers; on the contrary, when $\hat{\eta} < 8/\hat{\alpha}^2$, then $\hat{\beta}$ decreases with $\hat{\eta}$, i.e. the greater is $\hat{\beta}$ the slender are the fibers. Furthermore, an exact analysis of the dependency of $\hat{\eta}$ from the parameters $\hat{\alpha}$ and $\hat{\beta}$ can be simply pursued. In particular, by squaring and manipulating Eq. (4.10), an algebraic second-order equation for $\hat{\eta}$ is obtained, namely:

$$\left(1+\hat{\beta}^2\right)\hat{\eta}^2+\left(2\hat{\alpha}\hat{\beta}-4\hat{\beta}^2-2\right)\hat{\eta}+\left(\hat{\alpha}-2\hat{\beta}\right)^2=0, \tag{4.12}$$

from which the two following roots $\hat{\eta}_{\pm}\left(\hat{\alpha},\hat{\beta}\right)$ can be found

$$\begin{aligned}
\hat{\eta}_{+}\left(\hat{\alpha},\hat{\beta}\right) &= \frac{1-\hat{\alpha}\hat{\beta}+2\hat{\beta}^2+\sqrt{1+2\hat{\alpha}\hat{\beta}-\hat{\alpha}^2}}{1+\hat{\beta}^2} \quad \text{if } \hat{\alpha}>1 \quad \text{and} \begin{cases} \hat{\alpha}>2\hat{\beta} \text{ and } \hat{\alpha}^2<1+2\hat{\beta}\hat{\alpha} \\ \text{or} \\ \hat{\alpha}<2\hat{\beta} \end{cases} \\
&\qquad \text{or} \\
&\qquad \text{if } \hat{\alpha}<1 \quad \text{and} \quad \hat{\alpha}\neq 2\hat{\beta} \\
\hat{\eta}_{-}\left(\hat{\alpha},\hat{\beta}\right) &= \frac{1-\hat{\alpha}\hat{\beta}+2\hat{\beta}^2-\sqrt{1+2\hat{\alpha}\hat{\beta}-\hat{\alpha}^2}}{1+\hat{\beta}^2} \quad \text{if } \hat{\alpha}>2\hat{\beta} \quad \text{and} \begin{cases} \hat{\alpha}<1 \\ \text{or} \\ \hat{\alpha}>1 \text{ and } 1+2\hat{\beta}\hat{\alpha}>\hat{\alpha}^2 \end{cases}
\end{aligned} \tag{4.13}$$

where the existence conditions $\hat{\alpha}>0$, $\hat{\beta}>0$ and $0<\hat{\eta}<2$ are enforced to ensure the positivity of the geometric parameters and the geometric consistency of the cell. Moreover, it is apparent from Eq. (4.13), that the two roots $\hat{\eta}_{\pm}\left(\hat{\alpha},\hat{\beta}\right)$ exist if the radicand $1+2\hat{\alpha}\hat{\beta}-\hat{\alpha}^2>0$.

Figure 4.9 shows the diagrams of the roots $\hat{\eta}_{\pm}\left(\hat{\alpha},\hat{\beta}\right)$ as the non-dimensional parameters $\hat{\alpha}$ and $\hat{\beta}$ vary. In Fig.4.9a the 3D plot of the surface $\hat{\eta}_{\pm}=\hat{\eta}_{\pm}\left(\hat{\alpha},\hat{\beta}\right)$ is depicted; it is shown that, to the multivalued function $\hat{\eta}_{\pm}\left(\hat{\alpha},\hat{\beta}\right)$, correspond two branches of the surface, which, in turn, are related to the first and second solution of Eq. (4.12), namely the upper ($\hat{\eta}_{+}$) and the lower branch ($\hat{\eta}_{-}$), respectively. In Fig. 4.9b,c two $\hat{\alpha}$-isolines of the surface $\hat{\eta}_{\pm}\left(\hat{\beta};\hat{\alpha}\right)$ are shown, namely for $\hat{\alpha}=1.50$ and $\hat{\alpha}=5$, respectively, to assess whether the behavior is qualitatively consistent depending on the aspect ratio. In both cases it is found that as $\hat{\beta}$ increases: (i) $\hat{\eta}_{+}=\hat{\eta}_{+}\left(\hat{\beta};\hat{\alpha}\right)$ increases leading, for a given radius of the grain, to the design of thicker cells, i.e. cells in which, due to the increasing of the fibers' thickness, the joints between the fibers becomes increasingly thick until $\hat{\eta}_{+}\left(\hat{\beta};\hat{\alpha}\right)\to 2$ is reached at $\hat{\beta}_{max}\to\infty$, as discussed above; (ii) $\hat{\eta}_{-}\left(\hat{\beta};\hat{\alpha}\right)$ decreases until it is equal to zero at $\hat{\beta}_{max}:=\hat{\alpha}/2$ leading, for a given radius of the grain, to the design of slender cells, i.e. cells composed by an assembly of fibers with thinner sections; (iii) the two branches share the same minimum value $\hat{\beta}_{min}:=\frac{\hat{\alpha}^2-1}{2\hat{\alpha}}$, for which $\hat{\eta}\equiv\hat{\eta}_{lim}=\frac{2}{1+\hat{\alpha}^2}$ (highlighted with a black dot in the figure), obtained by setting the radicand in Eq. (4.13), i.e. the discriminant of Eq. (4.12), equal to zero, namely: $1+2\hat{\alpha}\hat{\beta}-\hat{\alpha}^2=0$, and solving for $\hat{\beta}$. Moreover, the trend of $\hat{\eta}_{\pm}\left(\hat{\beta};\hat{\alpha}\right)$ is qualitatively unchanged in the two cases considered, even if when

$\hat{\alpha} = 5$, the greater aspect ratio allows greater heights of the beam and, therefore, the upper branch is more extended respect to the one obtained for $\hat{\alpha} = 1.50$.

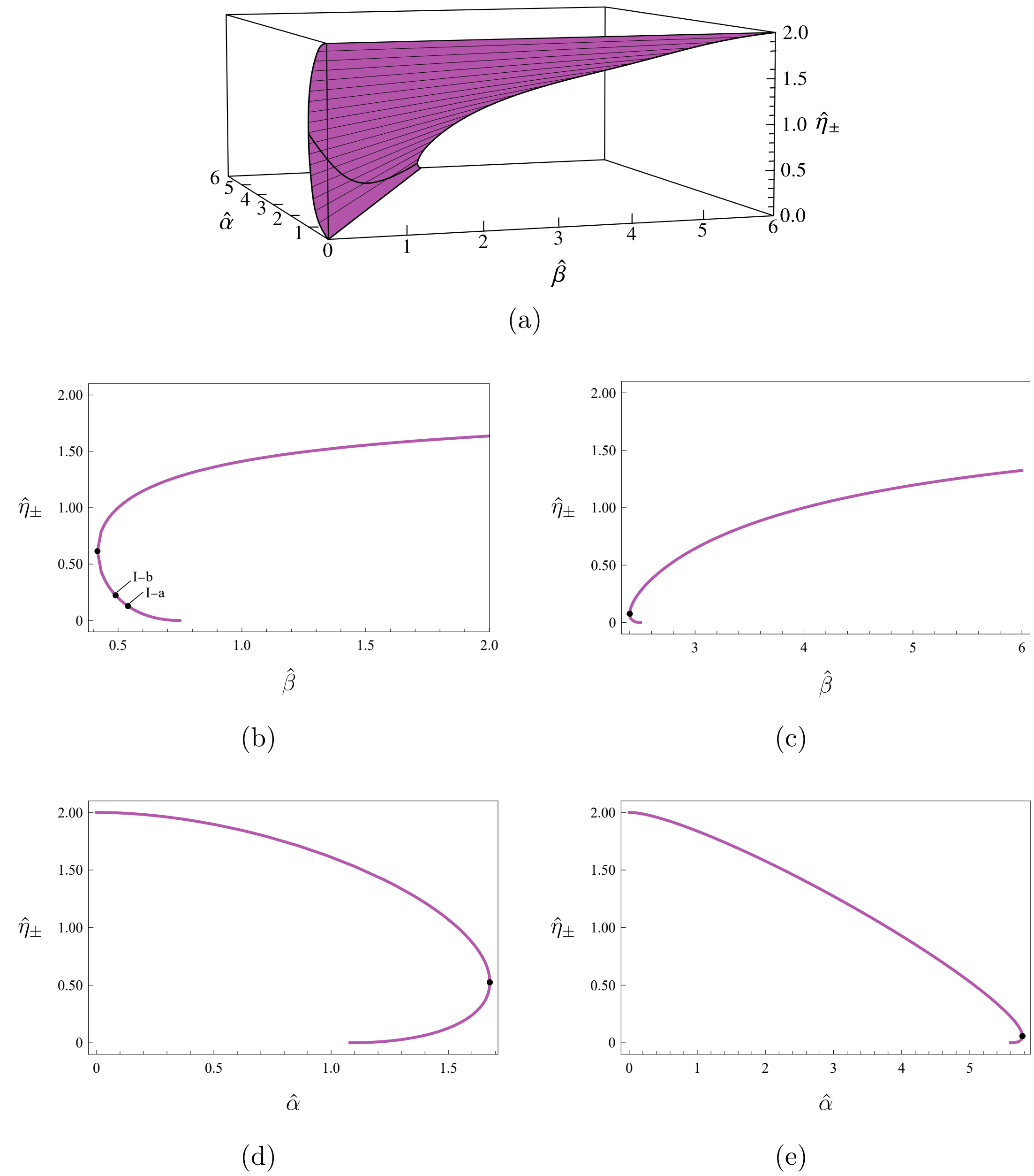

Figure 4.9. Plot of the roots $\hat{\eta}_\pm\left(\hat{\alpha}, \hat{\beta}\right)$ of Eq. (4.12): (a) 3D plot $\hat{\eta}_\pm = \hat{\eta}_\pm\left(\hat{\alpha}, \hat{\beta}\right)$; (b) and (c) $\hat{\alpha}$-isolines for $\hat{\alpha} = 1.50$ and $\hat{\alpha} = 5$, respectively; (d), (e) $\hat{\beta}$-isolines for $\hat{\beta} = 0.54$ and $\hat{\beta} = 2.80$, respectively.

Analogous considerations can be made when observing the isolines $\hat{\eta}_\pm\left(\hat{\alpha}; \hat{\beta}\right)$ for fixed values of $\hat{\beta}$. In Fig. 4.9d, e two $\hat{\beta}$-isolines of the surface are shown, namely for $\hat{\beta} = 0.54$ and $\hat{\beta} = 2.80$, respectively. In both cases it is found that as $\hat{\alpha}$ decreases: (i) $\hat{\eta}_+\left(\hat{\alpha}; \hat{\beta}\right)$ increases until $\hat{\eta}_+\left(\hat{\alpha}; \hat{\beta}\right) \to 2$ is reached at $\hat{\alpha}_{min} := 0$; (ii) $\hat{\eta}_-\left(\hat{\alpha}; \hat{\beta}\right)$ decreases until zero is attained at $\hat{\alpha}_{min} = 2\hat{\beta}$; (iii) the two branches share the same maximum value $\hat{\alpha}_{max} := \hat{\beta} + \sqrt{1 + \hat{\beta}^2}$, for which $\hat{\eta} \equiv \hat{\eta}_{lim} = 1 - \frac{\hat{\beta}}{\sqrt{1+\hat{\beta}^2}}$, highlighted with a black dot in the figure, obtained again by setting the radicand in Eq. (4.13), i.e. the discriminant of Eq. (4.12), equal to zero and solving for $\hat{\alpha}$. Again, the trend of $\hat{\eta}_{\pm}\left(\hat{\alpha};\hat{\beta}\right)$ is qualitatively unchanged in the two considered cases, even if the greater is $\hat{\beta}$, the greater is the extension of the upper branch.

It is important to remark that, the above discussion about the two roots $\hat{\eta}_{\pm}\left(\hat{\alpha},\hat{\beta}\right)$, which allows to highlight the dependency of the thickness over radius coefficient $\hat{\eta}$ upon the parameters $\hat{\alpha}$ and $\hat{\beta}$, is very useful to design the cell. Indeed, it serves as a guide for designing the interconnecting fibers between the two semi-grains of the cell, thereby enabling the a priori determination of whether the cell is slender or thicker.

In order to analyze the dependence of the constitutive matrix upon parameters $\hat{\alpha}$ and $\hat{\beta}$, these are firstly introduced in Eq. (B.1) of Subsection 4.3.1, by keeping the simplifications made at the beginning of this section. In this way, for a given grain's radius R and thickness of the fibers t_z, the constitutive matrix Eq. (4.4) is obtained as function of the parameters, namely $\mathbf{C}_{\pm} = \mathbf{C}_{\pm}\left(\hat{\alpha},\hat{\beta}\right)$, as:

$$\mathbf{C}_{\pm}\left(\hat{\alpha},\hat{\beta}\right) = \begin{pmatrix} \frac{10\hat{\alpha}p_{\pm}^2\left(24\hat{\beta}p_{\pm}^2+5p_{\pm}^2+40\hat{\beta}^3q_{\pm}^2\right)}{\left(1+\hat{\beta}^2\right)^3 p_{\pm}s_{\pm}} & -\frac{300\hat{\alpha}\hat{\beta}^2p_{\pm}^2q_{\pm}}{\left(1+\hat{\beta}^2\right)^3 s_{\pm}} & 0 \\ & \frac{10\hat{\alpha}p_{\pm}^2\left(20\left(1+6\hat{\beta}\right)\left(1\mp r_{\pm}\right)+\left(17+40\hat{\beta}\right)r_{\pm}^2\right)}{\left(1+\hat{\beta}^2\right)s_{\pm}q_{\pm}} & 0 \\ \text{SYM} & & R^2\frac{\hat{\alpha}p_{\pm}^2}{6\left(1+2\hat{\beta}\right)\left(1+\hat{\beta}^2\right)\left(\mp q_{\pm}\right)} \end{pmatrix} \tag{4.14}$$

where $p_{\pm}\left(\hat{\alpha},\hat{\beta}\right)$, $q_{\pm}\left(\hat{\alpha},\hat{\beta}\right)$, $r_{\pm}\left(\hat{\alpha},\hat{\beta}\right)$ and $s_{\pm}\left(\hat{\alpha},\hat{\beta}\right)$, are convenient definitions to compact the writing of the constitutive matrix, provided below (Eq.(4.15)), and in which the subscripts ($\pm$) refers to the first (Eq. (4.13a)) and second solution (Eq. (4.13b)) of Eq. (4.12), which have been used to express the thickness t in terms of $\hat{\alpha}$ and $\hat{\beta}$, respectively.

$$\begin{aligned} p_{\pm}\left(\hat{\alpha},\hat{\beta}\right) &:= \pm\left(1+2\hat{\beta}^2-\hat{\beta}\hat{\alpha}\right)+\sqrt{2\hat{\alpha}\hat{\beta}-\hat{\alpha}^2+1}, \\ q_{\pm}\left(\hat{\alpha},\hat{\beta}\right) &:= \pm\left(-1-\hat{\alpha}\hat{\beta}\right)+\sqrt{2\hat{\alpha}\hat{\beta}-\hat{\alpha}^2+1}, \\ r_{\pm}\left(\hat{\alpha},\hat{\beta}\right) &:= \frac{p_{\pm}}{1+\hat{\beta}^2}, \\ s_{\pm}\left(\hat{\alpha},\hat{\beta}\right) &:= \mp 1600\hat{\beta}^3\left(3\hat{\beta}+2\right)+3200\hat{\beta}^3 r_{\pm}\left(3\hat{\beta}+2\right)\mp 20r_{\pm}^2\left(440\hat{\beta}^4+336\hat{\beta}^3+144\hat{\beta}^2+54\hat{\beta}+5\right) \\ &\quad + 20r_{\pm}^3\left(200\hat{\beta}^4+176\hat{\beta}^3+144\hat{\beta}^2+54\hat{\beta}+5\right)\mp r_{\pm}^4\left(700\hat{\beta}^4+680\hat{\beta}^3+960\hat{\beta}^2+608\hat{\beta}+85\right). \end{aligned} \tag{4.15}$$

Accordingly, it is apparent that also the constitutive matrix $\mathbf{C}$ is splits into two matrices, $\mathbf{C}_{+}\left(\hat{\alpha},\hat{\beta}\right)$ and $\mathbf{C}_{-}\left(\hat{\alpha},\hat{\beta}\right)$, depending on each roots of Eq. (4.12), respectively.

In Fig. 4.10 the 3D plot of the elastic coefficients, $c_{ij} = c_{ij}\left(\hat{\alpha},\hat{\beta}\right)$ is shown: in it, for the sake of representational convenience, the coefficient $\hat{c}_{33} := \frac{c_{33}}{R^2}$ has been defined, that coincides with the bending coefficient c_{33} for a unitary grain's radius.

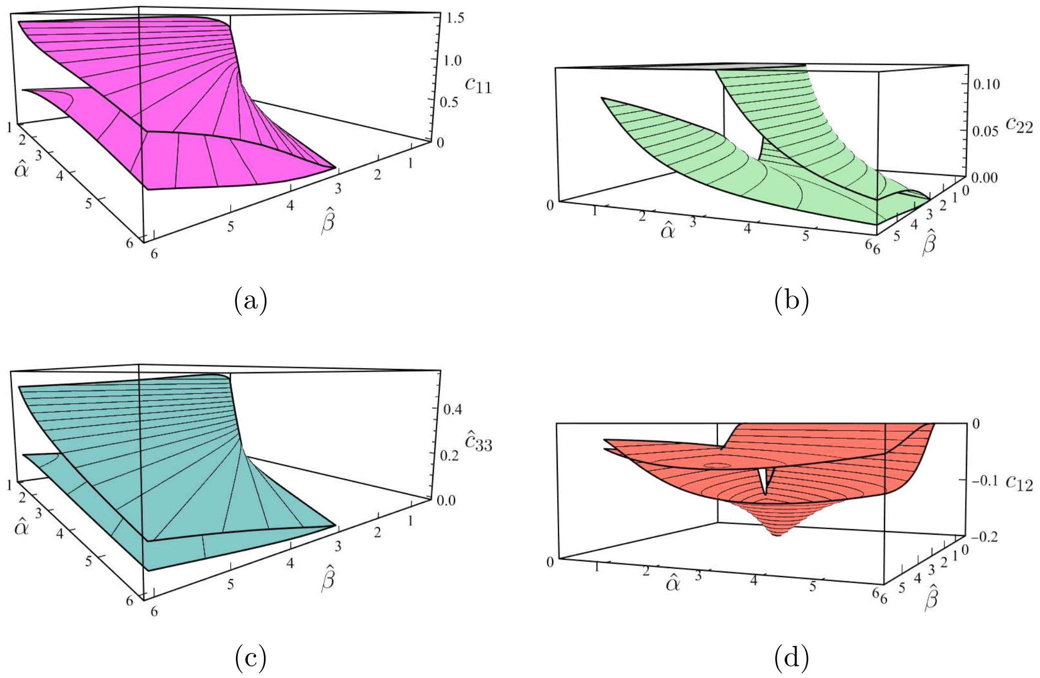

Figure 4.10. Plot of the elastic coefficients $c_{ij} = c_{ij}\left(\hat{\alpha}, \hat{\beta}\right)$: (a) $c_{11} = c_{11}\left(\hat{\alpha}, \hat{\beta}\right)$; (b) $c_{22} = c_{22}\left(\hat{\alpha}, \hat{\beta}\right)$; (c) $\hat{c}_{33} = \hat{c}_{33}\left(\hat{\alpha}, \hat{\beta}\right)$; (d) $c_{12} = c_{12}\left(\hat{\alpha}, \hat{\beta}\right)$.

In particular, as it is expected from the previous analysis, two-branches surfaces are found for each c_{ij}, corresponding to the the variation of the coefficients of the matrices $\mathbf{C}_+$ and $\mathbf{C}_-$ in Eq. (4.14) as functions of the parameters $\hat{\alpha}$ and $\hat{\beta}$, respectively. The plots in Fig. 4.10 are shown in the following order: $c_{11} = c_{11}\left(\hat{\alpha}, \hat{\beta}\right)$ in Fig. 4.10a, $c_{22} = c_{22}\left(\hat{\alpha}, \hat{\beta}\right)$ in Fig. 4.10b, $\hat{c}_{33} = \hat{c}_{33}\left(\hat{\alpha}, \hat{\beta}\right)$ in Fig. 4.10c and $c_{12} = c_{12}\left(\hat{\alpha}, \hat{\beta}\right)$ in Fig. 4.10d. Furthermore, in Fig. 4.11 the $\hat{\alpha}$- and $\hat{\beta}$-isolines of the 3D surfaces, which highlight the trend of the two-branches elastic coefficients for the same fixed values of $\hat{\alpha}$ and $\hat{\beta}$ selected above, i.e. $\hat{\alpha} = 1.50, 5$ (subfigures 4.11a,b) and $\hat{\beta} = 0.54, 2.80$ (subfigures 4.11c,d), are reported. The transition between one branch to the other (denoted with a dot in the subfigures) occurs at $\hat{\beta} = \hat{\beta}_{min}$ for the $\hat{\alpha}$-isolines in Fig. 4.11a,b and for $\hat{\alpha} = \hat{\alpha}_{max}$ for the $\hat{\beta}$-isolines in Fig. 4.11c,d.

In particular, with reference to the isoline for the smaller aspect ratio, namely $\hat{\alpha} = 1.50$, depicted in Fig. 4.11a, and in the zoomed region, close to $\hat{\beta}_{min}$, at the top right box in the figure, as $\hat{\beta}$ increases from $\hat{\beta}_{min}$, the coefficients of $\mathbf{C}_+$ modifies as follows: (i) the axial stiffness c_{11}, although it is not evident within the considered $\hat{\beta}$-interval, manifests a non-trivial behavior since it increases up to a maximum (at $\hat{\beta} = 5.25$) and then, decreases very slowly; (ii) also the shear stiffness c_{22} manifests a non-trivial behavior since it increases up to a maximum (at $\hat{\beta} = 0.65$) and then, decreases rapidly; (iii) the bending stiffnesses $\hat{c}_{33}$ monotonically increase with $\hat{\beta}$; (iv) $\hat{c}_{33} < c_{22}$ in the considered $\hat{\beta}$-interval, but for greater $\hat{\beta}$-values, particularly at $\hat{\beta} = 8.10$, the trend reverses, namely $\hat{c}_{33} > c_{22}$; (iv) the axial-shear coupling stiffness c_{12} exhibits an opposite behavior with respect to the other elastic coefficients (note that upper and lower solutions are inverted for this coefficient), decreasing up to a minimum (at $\hat{\beta} = 0.54$) and then increasing; (v) all the coefficients c_{ij} of the matrix $\mathbf{C}_+$ tend to a limit value reached at $\hat{\beta} \to \infty$, namely $c_{11}^{\infty} = 1$, $c_{22}^{\infty} = 0.22$, $\hat{c}_{33}^{\infty} = 0.33$ and $c_{12}^{\infty} = 0$, in which, in particular, the coupling term tends to zero since, for sufficiently large $\hat{\beta}$ values, the vertical beam no longer exists. Moreover, the constitutive coefficients of $\mathbf{C}_-$, for the same $\hat{\alpha}$-isoline, shows the following trend as $\hat{\beta}$ increases from $\hat{\beta}_{min}$: (i) the coefficients c_{ii} $(i = 1, 2, 3)$ decrease, whereas the coupling term c_{12} increases exhibiting, similarly to the constitutive coefficients of $\mathbf{C}_+$, an opposite behavior to that of the c_{ii} coefficients; (ii) consistently with the behavior of $\hat{\eta}_-\left(\hat{\alpha}; \hat{\beta}\right)$ in Fig. 4.9, all the coefficients c_{ij} of the matrix $\mathbf{C}_-$ tend to zero at $\hat{\beta} = \hat{\beta}_{max}$.

Then, by focusing on the isoline associated with the larger aspect ratio, i.e. $\hat{\alpha} = 5$, shown in Fig. 4.11b and in the zoomed region, close to $\hat{\beta}_{min}$, at the top right box in the figure, it can observed that, as $\hat{\beta}$ increases from $\hat{\beta}_{min}$, a qualitatively similar behavior is observed with respect to the former isoline, albeit with some differences. More specifically: (i) the coefficients c_{11}, $\hat{c}_{33}$ and c_{12} of $\mathbf{C}_+$ manifest a qualitatively similar behavior already recognized for the former isoline while c_{22} does not, since it monotonically increase with $\hat{\beta}$. In particular, the axial stiffness increases up to $\hat{\beta} = 29.71$ and then decreases, while the axial-shear coupling stiffness decreases up to $\hat{\beta} = 4.77$ and then increases; (ii) a slower growth with $\hat{\beta}$ is recognized for all the c_{ij}, toward c_{ij}^{∞} (i.e. toward their values attained at $\hat{\beta} \to \infty$, which, in this case, are $c_{11}^{\infty} = 1$, $c_{22}^{\infty} = 0.036$, $\hat{c}_{33}^{\infty} = 0.33$ and $c_{12}^{\infty} = 0$); (iii) the elastic coefficients evaluated with the matrix $\mathbf{C}_-$ tend more rapidly to zero at $\hat{\beta} = \hat{\beta}_{max}$. When reference is made to the isoline for the smaller fibers' lengths ratio, namely $\hat{\beta} = 0.54$, depicted in Fig. 4.11c, and in the zoomed region, close to $\hat{\alpha}_{max}$, at the top right box in the figure, as $\hat{\alpha}$ decreases from $\hat{\alpha}_{max}$, the coefficients of $\mathbf{C}_+$ behaves as follows: (i) c_{ii} $(i = 1, 2, 3)$ monotonically increase and, in particular, it is $c_{22} > c_{11}$, when $\hat{\alpha} > 0.91$, while, for smaller values, the trend reverses, namely $c_{22} < c_{11}$; (ii) $\hat{c}_{33} < c_{22}$ in the whole $\hat{\alpha}$-region; (iii) c_{12}, as for the $\hat{\alpha}$-isoline, exhibits an opposite behavior respect to the elastic coefficients c_{ii} in fact, it manifests a non-trivial behavior decreasing up to a minimum (at $\hat{\alpha} = 1.59$) and then increasing; (iv) for $\hat{\alpha} \to 0$, all the c_{ii} $(i = 1, 2, 3)$ coefficients of the matrix $\mathbf{C}_+$ tend to infinity, namely $c_{11}^{0} \to \infty$, $c_{22}^{0} \to \infty$, $\hat{c}_{33}^{0} \to \infty$, while the coupling term tends to zero, $c_{12}^{0} \to 0$, since, as mentioned for the previous cases, for small $\hat{\alpha}$ values the vertical beam, and accordingly the particular geometry that entails the coupling, no longer exists. Moreover, the constitutive coefficients of $\mathbf{C}_-$, for the same $\hat{\beta}$-isoline, shows the following trend, as $\hat{\alpha}$ decreases from $\hat{\alpha}_{max}$: (i) the coefficients c_{ij} exhibit an analogous behavior to that of the constitutive coefficients of $\mathbf{C}_-$ for the $\hat{\alpha}$-isoline, i.e. the coefficients c_{ii} $(i = 1, 2, 3)$ decrease, while c_{12} increases; (ii) consistently with the behavior of $\hat{\eta}_-\left(\hat{\alpha}; \hat{\beta}\right)$ in Fig. 4.9, all the coefficients c_{ij} of the matrix $\mathbf{C}_-$ tend to zero at $\hat{\alpha} = \hat{\alpha}_{min}$.

Finally, by focusing on the isoline associated with the fibers' lengths ratio, i.e. $\hat{\beta} = 2.80$, shown in Fig. 4.11d and in the zoomed region, close to $\hat{\alpha}_{max}$, at the top right box in the figure, it can observed that, as $\hat{\alpha}$ decreases from $\hat{\alpha}_{max}$, a qualitatively similar behavior is observed with respect to the former isoline, notwithstanding some differences arise. In

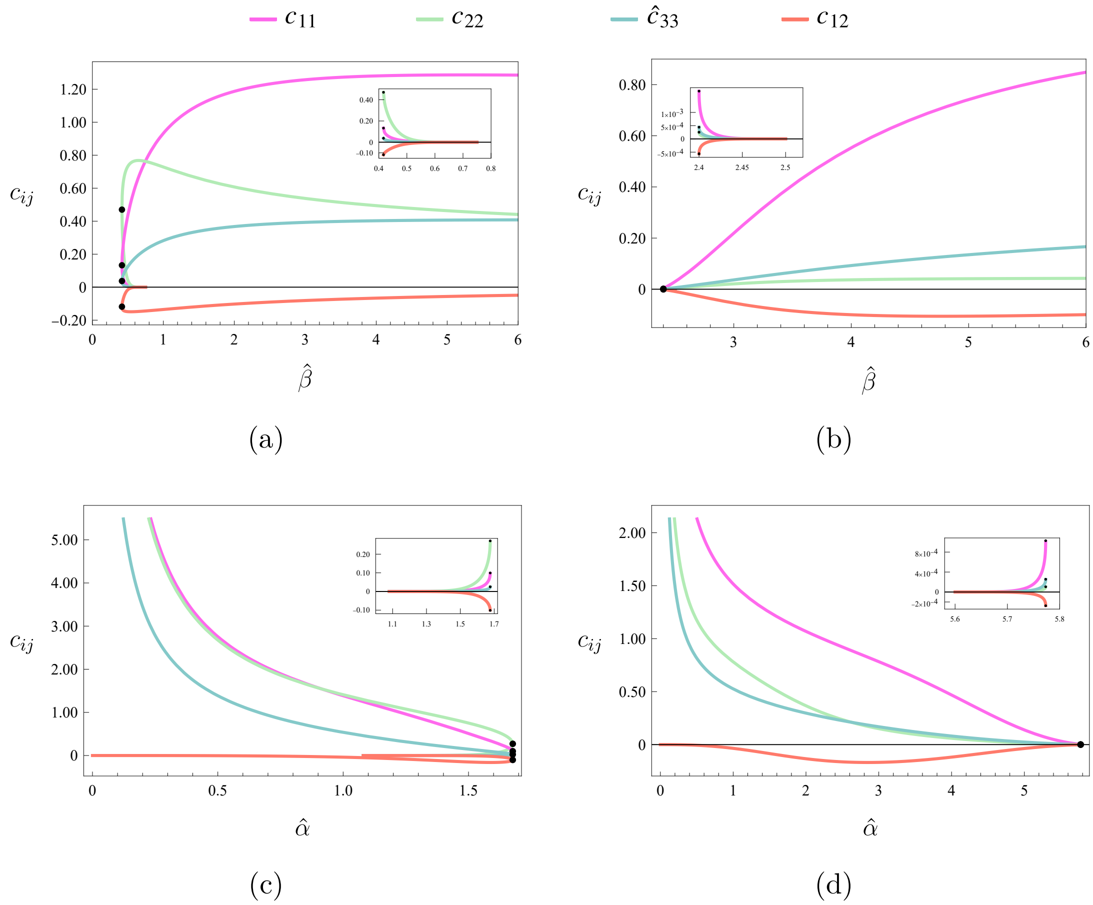

Figure 4.11. Isolines of the surfaces $c_{ij} = c_{ij}\left(\hat{\alpha}, \hat{\beta}\right)$ shown in Fig. 4.10: (a), (b) $\hat{\alpha}$-isolines for $\hat{\alpha} = 1.50$ and $\hat{\alpha} = 5$, respectively; (c), (d) $\hat{\beta}$-isolines for $\hat{\beta} = 0.54$ and $\hat{\beta} = 2.80$, respectively.

particular: (i) the coefficients c_{ij} of $\mathbf{C}_+$ manifest a qualitatively similar behavior already recognized for the former isoline, with the axial-shear coupling stiffness that decreases up to $\hat{\alpha} = 2.84$ and then increases, but $c_{22} < c_{11}$ in the whole $\hat{\alpha}$-region and, moreover, it is $c_{22} < \hat{c}_{33}$ when $\hat{\alpha} > 2.62$ while, for smaller values, the trend reverses, namely $c_{22} > \hat{c}_{33}$; (ii) a slower growth with $\hat{\alpha}$ decreasing is recognized for all the c_{ij}, toward c_{ij}^0 (i.e. toward their values attained at 0, which are $c_{11}^0 \to \infty$, $c_{22}^0 \to \infty$, $\hat{c}_{33}^0 \to \infty$ and $c_{12}^0 \to 0$); (iii) the elastic coefficients evaluated with the matrix $\mathbf{C}_-$ tends more rapidly to zero at $\hat{\alpha} = \hat{\alpha}_{min}$.

In conclusion of this section, it is worth emphasizing that, through the analytical identification of the constitutive matrix and the subsequent parametric analysis conducted here, it becomes possible to design the cell to achieve a targeted set of elastic constants and their associated ratios. In this context, both the macroscopic behavior of the homogenized equivalent beam and its chiral characteristics can be purposefully engineered.

4.5 Numerical results

Numerical results are referred to some grain beams, taken as case studies, made of Acrilonitrile Butadiene Stirene (ABS), a thermoplastic polymer characterized by an elastic modulus $E = 2180\text{N/mm}^2$, Poisson coefficient $\nu = 0$ and mass density $\rho = 1040\text{kg/m}^3$. The layout of the bodies that make up the cell is shown in Fig. 4.1.
Depending on the type of analysis, static, dynamic or buckling, as well as on the experimental validation of the analytical model, different case studies are selected. The selection criteria and the reasons behind the definition of multiple case studies will be discussed in the following sections. For the moment, it is sufficient to recall that the geometric dimensions of the case studies are defined thanks to the qualitative analysis of mechanical behavior illustrated in Section 4.4, i.e. by choosing dimensions R, t_z and parameters $\hat{\alpha}$, $\hat{\beta}$. Then, since $\hat{\eta}_\pm\left(\hat{\alpha}, \hat{\beta}\right)$, the thickness of the fibers t is automatically determined which, thanks to Eqs (4.9), allows to evaluate all the other geometric dimensions of the cell, namely ℓ_x, ℓ_y, ℓ_c and h.
Moreover, two FE models are built up to validate the homogenized beam model solution, namely: (i) the first one, here referred to as "Fine Model (Cauchy)", in which the grain beam is modeled as an assembly of bi-dimensional Cauchy continuum elements, i.e. plate elements; (ii) the second one, here referred to as "Fine Model (Beams)", in which the grain beam is schematized as an assembly of Timoshenko beams and rigid bodies. In particular, the vertical elements in the Fine Model (Beams) located at $x_i = i\,h$ with $i = 0, 1, \ldots, n$ representing the (rigid) grains and the horizontal elements representing the transition region of length ℓ_c (remember Fig. 4.3), are accounted for in the model as rigid bodies. Moreover, as for the identification of the equivalent beam model's inertial properties (Section 4.3.3), appropriate equivalent mass densities are assigned to the rigid bodies in order to account for the actual mass distribution of these regions and, therefore, to ensure consistency between the Fine Model (Beams) and the Fine Model (Cauchy).
The following analyses aim to assess the capability of the analytically identified equivalent beam model to accurately reproduce the static, dynamic, and buckling responses of the grain beam.

4.5.1 Static and dynamic analyses

First of all, it is necessary to define the case studies. In Fig. 4.9 the plots of $\hat{\eta}_\pm\left(\hat{\beta}; \hat{\alpha}\right)$ for the aspect ratios $\hat{\alpha} = 1.50, 5$ are reported. For these values, the lower branches exist within the ranges $0.416 < \hat{\beta} < 0.75$ and $2.40 < \hat{\beta} < 2.50$, respectively. Conversely, the upper branches share the same minimum value of the lower ones ($\hat{\beta} = 0.416$ and $\hat{\beta} = 2.40$) and then increase monotonically, approaching the asymptotic limit $\hat{\eta}_+\left(\hat{\beta}; \hat{\alpha}\right) \to 2$ as $\hat{\beta} \to \infty$.
For the present investigation, the case study for both the static and dynamic analyses refers to the $\hat{\alpha}$-isoline $\hat{\alpha} = 1.50$, hereafter referred to as case study I, even if additional case studies corresponding to $\hat{\alpha} = 5$ have been analyzed in the framework of the static analysis in [55]. The values of $\hat{\eta}_\pm$ are selected along the lower branch and are marked with

a dot in Fig. 4.9b. In particular, two values of $\hat{\beta}$ are chosen in such a way the fibers can be considered, respectively, as: (i) thin fibers, and the relevant case study is denoted with label "-a" and here referred to as "thin cell"; (ii) thick fibers and the relevant case study is denoted with label "-b" and here referred to as "thick cell". Accordingly, in the former case the fibers connecting the grains are sufficiently slender elements, whose behavior can be described by Timoshenko beam theory, while, in the latter case, they are more similar to plates. The chosen values of $\hat{\beta}$ are $\hat{\beta} = 0.54$ and $\hat{\beta} = 0.49$, denoted as case study I-a and I-b in Fig. 4.9b.

As mentioned, once $\hat{\alpha}$ and $\hat{\beta}$ are set, all the geometric dimensions of the cell are defined thanks to $\hat{\eta}_{\pm}\left(\hat{\alpha}, \hat{\beta}\right)$ and using Eqs. (4.9). These are reported in Tab. 4.1 and giving rise to the two cells sketched in Fig. 4.12, where $R = 5$ mm and $t_z = 4$ mm have been chosen.

		Case study	
		I-a	**I-b**
ℓ_x	[mm]	5.06	4.35
ℓ_y	[mm]	9.36	8.89
ℓ_c	[mm]	2.44	3.15
t	[mm]	0.64	1.11
h	[mm]	15	15
ℓ	[mm]	330	330

Table 4.1. Cell's geometric dimensions for case study I-a and I-b.

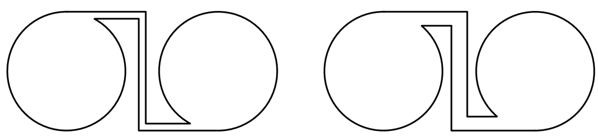

Figure 4.12. Case study I-a and I-b.

Both the static response and free dynamics of a clamped beam at the ends $H = A$, B, whose microstructure is made by $n = 22$ cells, are considered for the numerical analyses. No static loads are applied to the beam, i.e. $p_x = p_y = c_z = 0$, while boundary displacements at the end B are assigned, namely: $\bar{u}_B = -1\,\text{mm}$, $\bar{v}_B = 1\,\text{mm}$, $\bar{\theta}_B = 0\,\text{mm}$. As for the equivalent beam model, the analytical (exact) solution of the static problem under such boundary conditions, as well as the numerical solution of the eigenvalue problem obtained using the Finite Difference Method by discretizing the domain into $L = 1200$ elements, are reported in Appendix A.

As mentioned, two FE models are built up to validate the homogenized beam model solution, namely the Fine Model (Cauchy) and Fine Model (Beams). In the former, the geometry of the grain beam is discretized using a triangular mesh with a quadratic displacement field; in the latter, the geometry is discretized using a fine mesh with a cubic displacement field and a quadratic rotation field. Moreover, as an order of magnitude of degrees of freedom for case study I-a, it is approximately 233000 and 870 for Fine Model (Cauchy) and Fine Model (Beams), respectively.

Discussion about the elastic coefficients and definition of the inertial coefficients

The elastic coefficients for the case studies at hand are obtained through both the analytical (see 4.3.1) and numerical (see 4.3.2) identification procedure of the mixed homogenization approach. They are reported in Tab. 4.2, where NC, NC-ng and AB stand for the constants evaluated with the numerical procedure with grains (Numerical Cauchy), numerical procedure without grains (Numerical Cauchy - no grains) and the analytical procedure (Analytical Beams), respectively. The percentage differences of the elastic constants evaluated with different identification procedures, namely ϵ_1, ϵ_2 and ϵ_3, are reported in the last three columns of each subtable of Tab. 4.2. In particular, naming c_{ij}, c_{ij}^{ng} and c_{ij}^{a} the constitutive coefficients determined with NC, NC-ng and AB, respectively, it is $\epsilon_1 := 100\left(c_{ij} - c_{ij}^{ng}\right)/c_{ij}$, $\epsilon_2 := 100\left(c_{ij}^{ng} - c_{ij}^{a}\right)/c_{ij}^{ng}$ and $\epsilon_3 := 100\left(c_{ij} - c_{ij}^{a}\right)/c_{ij}$.

At first, results obtained from NC and NC-ng cells' homogenization are discussed, related to the percentage difference ϵ_1. It is found that for both the case studies, the constitutive coefficients of NC-ng are always greater than the one evaluated with NC. This is a quite expected result, as it is due to the different modeling of the grain which is deformable in one case (NC) and considered rigid in the other (NC-ng). Therefore, regarding the influence of the grain on the constitutive matrix, it is concluded that, when grain deformability is introduced in the cell schematization, it induces a softening effect on the elastic coefficients.

Afterward, results obtained from the numerical and analytical homogenization procedures are analyzed. First, constitutive coefficients relevant to NC-ng and AB models, related to percentage difference ϵ_2, are considered. In both the cases the grain is considered as a rigid body, and, as it is expected, the percentage differences are quite low for the thinner cell (case I-a), with the greater difference being around 6%, while there is a slight increase for the thicker one (case I-b) up about to 11%. These percentage differences are conjectured to be due to two geometric reasons: (i) the modeling choice of the length ℓ_c which, determines the transition region between rigid and deformable behavior at grain-fiber intersection, and (ii) the intersection (joint) between horizontal and vertical fibers which, for the thicker cells, possesses a finite dimension, i.e., nonzero dimension, as opposed to the beam model approximation. More precisely, the slender the beams, the thinner the intersections, the more the joint can be assimilated to the (dimensionless) intersection between beams. It can be concluded that, for thinner cells, the first geometric reason is prevalent in the percentage difference ϵ_2, while, in the thicker ones, both the geometric reasons contribute in the difference ϵ_2.

Finally, results obtained from NC and AB cells' homogenization are discussed, related to the percentage difference ϵ_3. This is the greater difference recognized for the different identification procedures, occurring for all the case studies considered. The higher difference are due to the presence of a deformable grain in the NC model, as well as to the two above-mentioned geometric reasons. However, analytical identification remains sufficiently close to the NC one in the cases of thin cells, while, the percentage differences are greater for the thicker ones. In what follows, the effect of these more pronounced differences will be discussed on the static response of the beam.

		Case study I-a					
		NC	**NC-ng**	**AB**	ϵ_1	ϵ_2	ϵ_3
c_{11}	[N]	23.15	23.58	22.33	-1.84	5.30	3.56
c_{22}	[N]	63.76	69.80	74.46	-9.47	-6.67	-16.77
c_{33}	[N $\times$ mm^2]	142.59	145.06	145.68	-1.73	-0.42	-2.16
c_{12}	[N]	-29.51	-31.08	-30.61	-5.34	1.54	-3.72

		Case study I-b					
		NC	**NC-ng**	**AB**	ϵ_1	ϵ_2	ϵ_3
c_{11}	[N]	146.41	152.62	135.07	-4.24	11.50	7.74
c_{22}	[N]	405.60	490.62	542.71	-20.96	-10.62	-33.80
c_{33}	[N $\times$ mm^2]	819.09	848.85	855.15	-3.63	-0.74	-4.40
c_{12}	[N]	-185.61	-207.59	-195.80	-11.84	5.68	-5.48

Table 4.2. Elastic coefficients of the equivalent beam model for case studies I-a, I-b and different identification procedures.

To investigate the dynamic response as well, the inertial properties of the equivalent beam model are evaluated. This requires computing the area of the triangular region illustrated in Fig. 4.1, which is bounded by the red grain arc and the intrados (or extrados) of the horizontal fibers. The resulting areas are $A_t = 0.51$ mm^2 and $A_t = 1.11$ mm^2 for case study I-a and I-b, respectively. The inertial properties are analytically derived and reported in Tab. 4.3, where, for both cases, it is $I_y = 0$.

		Case study	
		I-a	**I-b**
m	[kg/mm]	2.55×10^{-5}	2.78×10^{-5}
I_x	[kg]	1.91×10^{-4}	2.09×10^{-4}
I_{xy}	[kg $\times$ mm]	3.53×10^{-3}	3.66×10^{-3}

Table 4.3. Mass coefficients of the equivalent beam model for case study I-a and I-b.

Displacement field

The static analysis of the grain beam, which leads to a comparison between the FE model (Beams), the FE model (Cauchy) and the Equivalent beam model, is now discussed. For the latter model, the elastic constants evaluated with the analytical procedure (AB constants) are considered. The comparison is made in terms of longitudinal displacement $u(x)$, transverse displacement $v(x)$, and rotation $\theta(x)$. In the following plots, the displacement and abscissa unit is millimeters (mm), while the rotation unit is milliradians (mrad).

For case studies I-a and I-b, a very good agreement between the Equivalent beam model (AB constants) and FE model (Beams) is shown in Fig. 4.13. There is a slight deviation between the FE model (Beams) and FE model (Cauchy), which is more evident for case study I-b. This is due to the modeling of the horizontal fibers as beams that, as discussed above, for the case study I-b, is a strong approximation. The percentage difference, in terms of displacements, between the Equivalent beam model and the discrete FE Model (Cauchy), at the abscissa in which minimum and maximum vertical displacement $v(x)$ is achieved, i.e. at $x = h, 21h$ respectively, is -22% and less than -1% for case study I-a, -49% and less than -1% for case study I-b. The percentage error for the rotation $\theta(x)$ evaluated at the mid-span $x = 11h$ is about -4% and -8% for case study I-a and I-b, respectively. The very good agreement between the Equivalent beam model and FE models is also shown in Fig. 4.14 where the deformed shape of the grain beam in the case study I-a, is reported. It is important to remark that, the percentage difference determined for $v(h)$ appears to be quite high, even if it is practically not noticeable in Fig. 4.13; this is due to the fact that the difference arises in the presence of very small vertical displacements (of the order of -0.01mm) rendering the effect negligible. Therefore, a good agreement between the FE model (Cauchy) and the Equivalent beam model is confirmed.

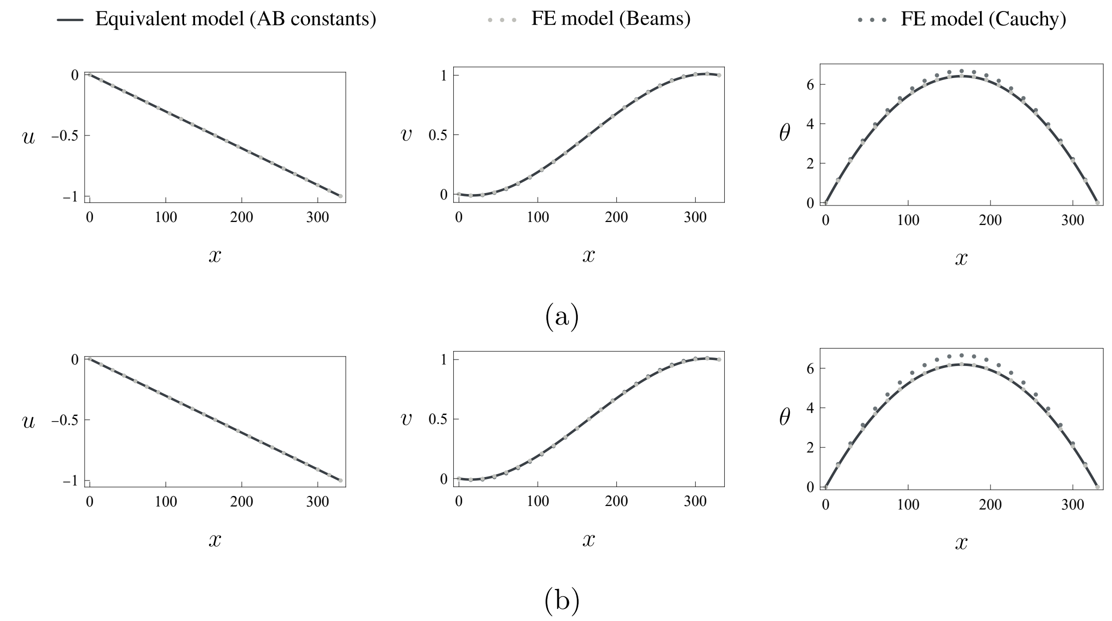

Figure 4.13. Static response of the Equivalent beam model (AB constants) vs. the discrete FE models (Beams) and (Cauchy) in terms of longitudinal and transverse displacements and rotation of the cross-section for: (a) case study I-a; (b) case study I-b.

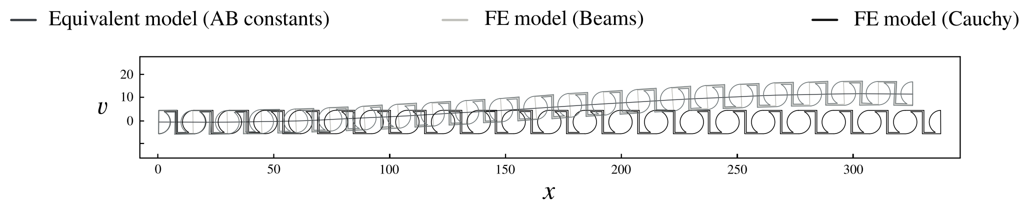

Figure 4.14. Comparison between the deformed shapes of the Equivalent beam model (AB constants) and the FE models (Beams) and (Cauchy) for the case study I-a.

However, it should be remarked that, the high percentage difference, even if is due to numerical approximation of the percentage differences, is also related to the modeling choices of the cell, and, in particular, to the choice of the transition length ℓ_c (see, Sect. 4.3.1). Indeed, it is evident that reducing ℓ_c in the AB model would result in a larger ℓ_x, thereby producing more slender horizontal fibers. This, in turn, brings the analytical elastic coefficients closer to those of the NC model. More specifically, if one defines ℓ_c as the distance between the vertical diameter of the grain and the intersection of the horizontal fiber's axis line with the grain's circumference, it reduces the percentage difference in displacements between the Equivalent Beam model (using AB constants) and the FE model (Cauchy). However, such a choice would result in the AB model becoming further detached from the NC-ng model, as due to an overestimation of the length of the horizontal beams. Indeed, the choice of ℓ_c was carefully made to ensure that the AB model remained as consistent as possible with the fine model under the same assumptions, thereby aligning it with the NC-ng model, based on the relevant rigid body assumption for the grains.

It is worth to notice that, the difference between the Equivalent beam model (AB constants) and the FE model (Cauchy), also arises from the choice to use the elastic constants identified with the analytical procedure. In particular, if a more precise solution is desired, the elastic constants evaluated by the NC procedure need to be used (see Fig. 4.15). In this way, the order of magnitude of the error, in terms of displacements, between Equivalent beam model (with NC constitutive coefficients) and the FE model (Cauchy) at $x = h, 21h$ for the vertical displacement $v\left(x\right)$ reveals to be -2% and less than -1% for case study I-a, and -1.5% and less than -1% for case study I-b. The percentage error for the rotation $\theta\left(x\right)$ evaluated at $x = 11h$ is less than -1% for both the case studies.

Finally, to emphasize the chirality, a Timoshenko beam with the diagonal constitutive matrix, is studied. The constitutive matrix is evaluated by considering an equivalent cross-section, such as to obtain the same constitutive matrix used for the grain beam, but without the off-diagonal term.
A clamped beam at $H = A, B$, with displacement $\bar{u} = 1\,\text{mm}$, $\bar{v} = 0\,\text{mm}$ and $\bar{\theta} = 0$ imposed at end B and no static loads applied, is considered. The exact solution for the static problem is discussed in Appendix A for the grain beam, i.e. with $c_{12}\neq 0$; in this case, it will be enough to impose $c_{12} = 0$. The numerical solution is obtained from the FE model (Beams), in which the grain beam is modeled as an assembly of Timoshenko beams. In the Fine Model (Beams) the geometry is again discretized using a fine mesh with

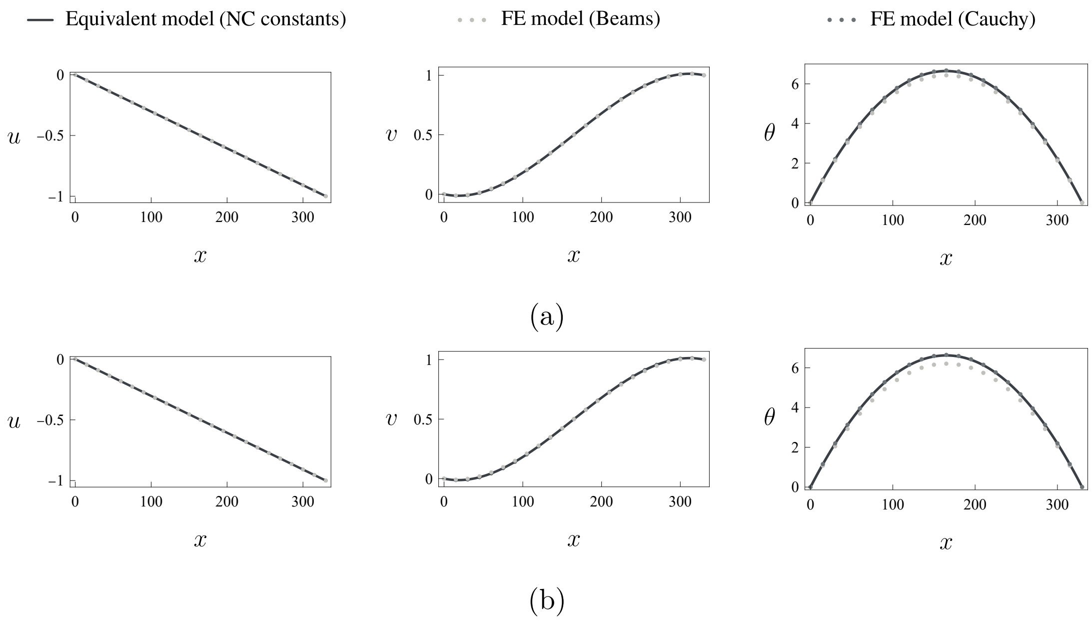

Figure 4.15. Static response of the Equivalent beam model (NC constants) vs. the discrete FE models (Beams) and (Cauchy) in terms of longitudinal and transverse displacements and rotation of the cross-section for: (a) case study I-a; (b) case study I-b.

a cubic displacement field and a quadratic rotation field. From the comparison between the analytical and numerical solution, the property of chirality is highlighted in fact, when applying a pure extensional mode, the Timoshenko beam model only extends while the grain beam shows the coupling between extensional and shear deformation modes (see Fig. 4.16).

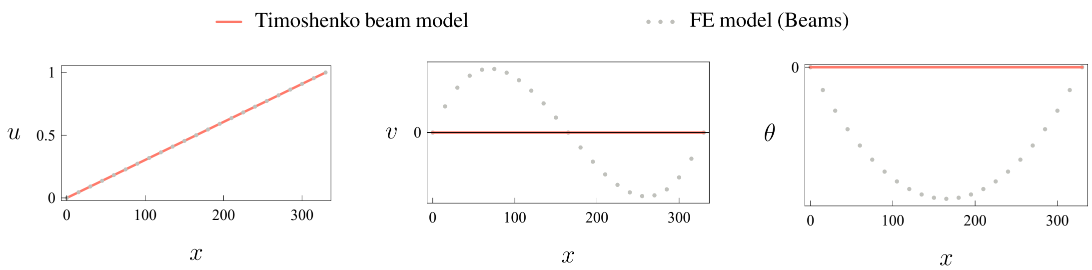

Figure 4.16. Static response of the Timoshenko beam model vs. the discrete FE model (Beams) in terms of longitudinal and transverse displacements and rotation of the cross-section for the case study I-a.

Frequencies and modal shapes

As in the static case, in the dynamic analysis of the grain beam comparisons are made between the Equivalent beam model, the FE model (Cauchy) and the FE model (Beams). For the Equivalent beam model, the elastic and inertial coefficients are those obtained through the analytical homogenization procedure. The comparison is carried out in terms of the first four natural frequencies and the corresponding modal shapes. The frequency values are reported in Tab. 4.4, where ω_{EQ}, ω^c_{FE} and ω^b_{FE} denote the frequencies evaluated with the Equivalent beam model, the FE model (Cauchy) and FE model (Beams), respectively. The percentage differences between the frequencies obtained from the three models, defined as $\epsilon_1 = 100 \left(\omega_{EQ} - \omega^c_{FE}\right) / \omega_{EQ}$, $\epsilon_2 = 100 \left(\omega_{EQ} - \omega^b_{FE}\right) / \omega_{EQ}$ and $\epsilon_3 = 100 \left(\omega^c_{FE} - \omega^b_{FE}\right) / \omega^c_{FE}$, are reported in the last three columns.

First, focusing on the percentage difference ϵ_1, the results in terms of angular frequencies

Case study	**Mode**	ω_{EQ} [rad]	ω^c_{FE} [rad]	ω^b_{FE} [rad]	ϵ_1 [%]	ϵ_2 [%]	ϵ_3 [%]
I-a	1	15.46	15.47	15.55	−0.06	−0.58	−0.52
	2	41.72	42.72	42.96	−2.40	−2.97	−0.56
	3	79.19	83.78	84.38	−5.80	−6.55	−0.72
	4	125.73	138.58	139.82	−10.22	−11.21	−0.89
I-b	1	35.72	35.53	36.08	0.53	−1.01	−1.55
	2	96.48	98.05	99.65	−1.63	−3.29	−1.63
	3	183.48	192.24	195.69	−4.77	−6.65	−1.79
	4	291.83	317.82	324.17	−8.91	−11.08	−2.00

Table 4.4. Angular frequencies of the first four modes for case study I-a and I-b. ω_{EQ}, ω^c_{FE} and ω^b_{FE} refer to Equivalent beam Model (AB constants), FE Model (Cauchy) and FE Model (Beams), respectively.

obtained from the Equivalent beam model and the FE (Cauchy) model are discussed. For both case studies, the Equivalent beam model provides an accurate approximation of the frequencies predicted by the FE (Cauchy) model, especially for the first mode, where the percentage difference is up about 0.50%. The same observation holds when analyzing ϵ_2, which compares the results obtained from the Equivalent beam model with those of the FE model (Beams). Moreover, it is observed that, for both comparisons, the percentage differences of the higher modes increase; this is due to scale effects. The proposed Equivalent beam model relies on the fundamental assumption that the overall size of the metamaterial and, in the case of static analysis, the magnitude of the applied loads, are significantly larger than the size of the cell. However, as the mode number increases, the modal wavelength becomes comparable to the microscale. Consequently, the deformation of the microstructure becomes relevant, leading to a partial violation of the underlying assumption. Nevertheless, the discrepancies remain limited, reaching about 11% for the highest mode.

Afterward, ϵ_3 highlights the difference between the two FE models. As expected, the percentage differences remain small for both case studies, approximately 0.5% and 1.5% for the thinner and thicker case, respectively.

The greater percentage difference observed for the thicker cell is not related to the mass distribution, but rather to stiffness representation. Specifically, in this case, the fibers connecting the grains behave more like plates than beams. As previously highlighted, modeling these fibers as beam elements introduces is a great approximation. Nonetheless, the differences remain small, confirming that even the thicker cell can still be effectively treated as an assembly of beams.

Finally, an excellent agreement between the models is also observed in terms of modal shapes, which, due to the chiral geometry, exhibit a coupled flexural-extensional behavior. Since the flexural component remains predominant up to the fourth mode, it is only the only one plotted in Fig. 4.17, in which the abscissa unit is expressed in millimeters (mm).

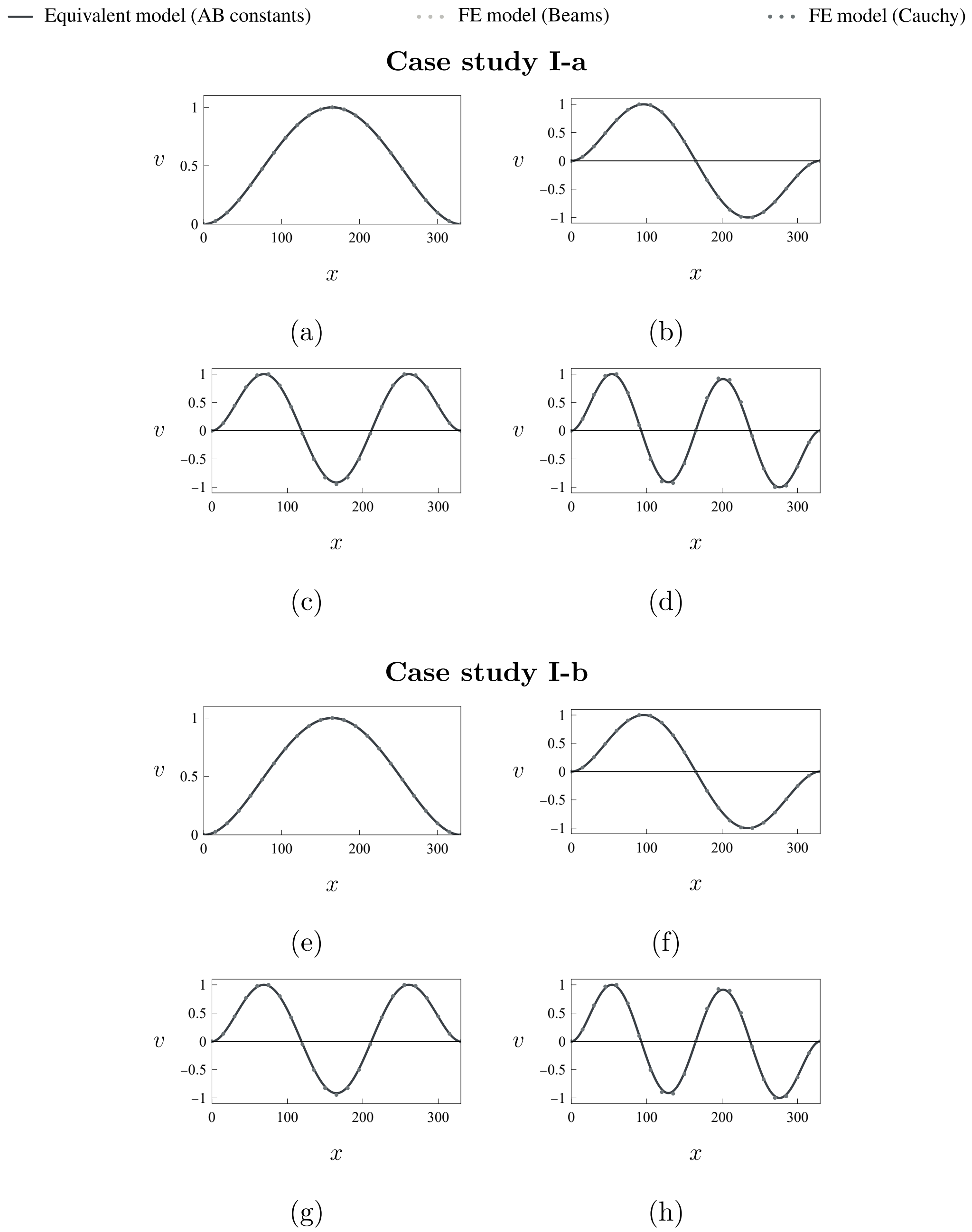

Figure 4.17. Modal shapes of the Equivalent beam Model (AB constants) Vs. the discrete FE Model (Beams) Vs. the discrete FE Model (Cauchy). (a-d) Flexural component of modes 1-4, for case study I-a. (e-h) Flexural component of modes 1-4, for case study I-b.

4.5.2 Buckling analysis

An additional case study is selected for the buckling investigation, motivated by the need to enhance the stability of the metamaterial, thereby ensuring a sufficiently high critical load suitable for interpretation and potential experimental validation. The selected microstructure corresponds to $\hat{\alpha} = 2$ and $\hat{\beta} = 0.76$, and is hereafter referred to as case study II. Once $\hat{\alpha}$ and $\hat{\beta}$ are set, t is found thanks to $\hat{\eta}_{\pm}\left(\hat{\alpha}, \hat{\beta}\right)$, while all the geometric dimensions of the cell, namely ℓ_x, ℓ_y, ℓ_c and h, are determined through Eqs. (4.9). Tab. 4.5 reports the computed geometric parameters, where $R = 10$ mm and $t_z = 6$ mm have been chosen. The resulting cell geometry is illustrated in Fig. 4.18. Similarly to the configurations previously denoted with the suffix "-b", the fibers connecting the grains exhibit a mechanical behavior more closely resembling that of plates rather than beams.

		Case study II
ℓ_x	[mm]	13.10
ℓ_y	[mm]	17.24
ℓ_c	[mm]	6.90
t	[mm]	2.76
h	[mm]	40
ℓ	[mm]	600

Table 4.5. Cell's geometric dimensions for case study II.

II

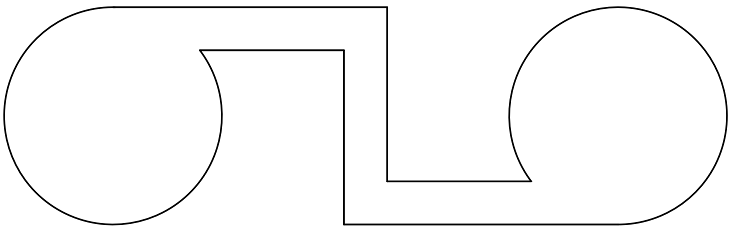

Figure 4.18. Case study II.

The buckling behavior of a grain beam clamped at A and constrained by a horizontal slider at B, realized by the repetition along the $x-$direction of $n = 15$ cells, is studied. For the equivalent beam model, the solution is computed using the Finite Difference Method, discretizing the domain into $L = 400$ elements. The corresponding formulation is detailed in Appendix A. As for the static and dynamic analyses, the results of the homogenized beam model are validated through the Fine Model (Cauchy) and Fine Model (Beams). In the former, the geometry of the grain beam is discretized using a triangular mesh with a quadratic displacement field. In the latter, the geometry is discretized using an extremely fine mesh with a cubic displacement field and a quadratic rotation field. The number of degrees of freedom amounts to approximately 212000 for the Fine Model (Cauchy) and 600 for the Fine Model (Beams). The elasto-geometric characteristics of the equivalent beam model, evaluated according to the analytical identification procedure, together with the cell's critical load, are listed in Tab. 4.6.

		Case study II
c_{11}	[N]	910.98
c_{12}	[N]	-869.54
c_{22}	[N]	1420.21
c_{33}	$[\mathrm{N} \times \mathrm{mm}^2]$	21066.40
c_{11}^*	$[-]$	5.02×10^{-1}
c_{12}^*	$[-]$	1.87×10^{-2}
c_{13}^*	[mm]	3.44
c_{22}^*	$[-]$	1.64
c_{23}^*	[mm]	19.71
c_{33}^*	$[\mathrm{mm}^2]$	427.66
ζ	$[-]$	0.16
P_{cell}	[N]	44.27

Table 4.6. Elastic coefficients of the equivalent beam model for case study II.

Critical mode

The buckling behavior of the grain beam is here examined through a comparison between the Equivalent beam model, where he elastic constants obtained through the analytical procedure (AB constants) are considered, the FE model (Cauchy) and the FE model (Beams). The comparison is carried out with respect to both the critical load and the associated critical mode. In the following table, the critical loads P_{cr}, P_{cr}^c and P_{cr}^b refer to the Equivalent beam model, the FE model (Cauchy), and the FE model (Beams), respectively. The percentage differences between the models are also reported, and defined as $\epsilon_1 = 100\,(P_{cr} - P_{cr}^c)\,/P_{cr}$, $\epsilon_2 = 100\left(P_{cr} - P_{cr}^b\right)/P_{cr}$ and $\epsilon_3 = 100\left(P_{cr}^c - P_{cr}^b\right)/P_{cr}^c$.

Case study	P_{cr} [N]	P_{cr}^c [N]	P_{cr}^b [N]	ϵ_1 [%]	ϵ_2 [%]	ϵ_3 [%]
II	2.28	2.23	2.30	2.19	-0.88	-3.14

Table 4.7. Critical load for case study II of the Equivalent beam Model Vs. the discrete FE Model (Beams) Vs. the discrete FE Model (Cauchy).

As a first step, attention is focused on the percentage difference ϵ_1, which compares the critical loads computed from the Equivalent beam model and the FE model (Cauchy). The results indicate that the equivalent model provides a good approximation of the critical load predicted by the finite element model. The observed discrepancy arises from the assumption adopted in the equivalent formulation, where the fibers connecting the grains are treated as beams. However, these elements are not slender enough and behave more like plates than beams. Nevertheless, it is worth noting that this percentage discrepancy could be reduced by adopting a finer discretization in the finite difference solution of the

equivalent beam model. For instance, for $L = 800$, the critical load would be $P_{cr} = 2.22$ N with $\epsilon_1 = -0.45$ %. However, such a choice would significantly increase the computational effort, which is precisely what the homogenized beam model is intended to mitigate.
Then ϵ_2, which compares the results obtained from the Equivalent beam model and the FE model (Beams), confirms the accuracy of the analytical model, as the predicted critical load exhibits an excellent agreement with the numerical one.
Finally, ϵ_3, which quantifies the difference between the two FE models, is analyzed. In this case, the percentage difference remains reasonably small, though slightly larger than in the previous comparisons. This behavior can once again be attributed to the adopted geometry, as already noted in the case of ϵ_1.
The critical mode associated with the critical load reported in Tab. 4.7 is shown in Fig. 4.19, where the abscissa unit is expressed in millimeters (mm). The critical mode is normalized so that its maximum displacement is attained at $v = 1$.

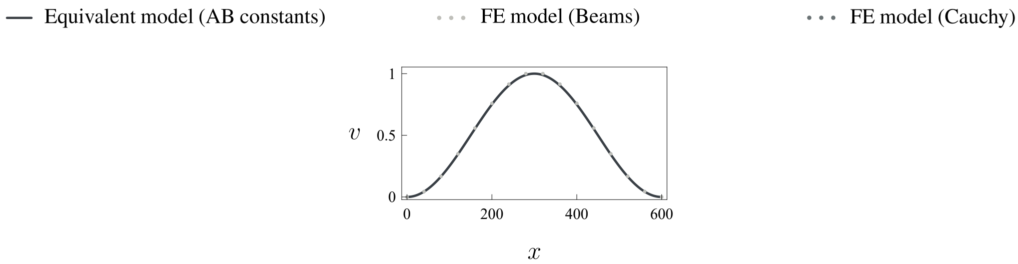

Figure 4.19. Critical mode for case study II of the Equivalent beam model (AB constants) vs. the discrete FE models (Beams) and (Cauchy).

4.6 Preliminary experimental results

The analytical model was validated not only with the FE models, but also through experimental testing[1]. To investigate their mechanical behavior, a preliminary study, only one specimen was 3D printed and tested under a uniaxial tensile test. The mechanical response under loading was assessed through the Digital Image Correlation (DIC) technique, enabling an accurate definition of the displacement fields throughout the test. This technique, unlike traditional ones based on strain gauges or displacement transducers, capable of capturing only localized information, enables the acquisition of distributed data over an extended surface, thus offering a more comprehensive and detailed description of the deformation behavior.

The fundamental principle of DIC consists in comparing a reference image, corresponding to the preload specimen's configuration, with one (or more) images captured during the test, therefore corresponding to the deformed specimen. The comparison is carried out in terms of gray level intensity variations between the reference image and the images

[1]The author wishes to thank Ph.D. Alessandro Ciallella, for the significant scientific contribution to the experimental laboratory activities and their scientific framing.

of the deformed configurations. Two DIC approaches can be distinguished: (i) the local approach, where the reference image is discretized into multiple Zones of Interest (ZOI), each analyzed independently; and (ii) the global approach, which assumes a continuous displacement field over the entire Region of Interest (ROI) and enforces kinematic compatibility throughout the domain. Moreover, both the local and global formulations can be implemented using either an incremental or a direct correlation strategy. The first correlates each image with its immediate predecessor in the acquisition sequence. This procedure is highly robust in the presence of large displacements and significant deformations; however, its main drawback is the gradual accumulation of errors over time, which may necessitate specific correction techniques when long image sequences are processed. The second correlates each image of the deformed specimen with the reference one, thereby providing the total displacement field with respect to the undeformed state. This method avoids the accumulation of numerical errors and is particularly effective when displacements and strains remain small.

In the present work, a global DIC formulation is employed, as it enhances both the numerical stability of the analysis and the physical consistency of the computed displacement fields. Moreover, a direct strategy is adopted because, in order to remain within linear kinematic and elastic conditions, and thus enable a consistent comparison with the developed equivalent model, the applied displacements are small.

As in the buckling analysis, a new case study was defined. Its selection was guided by two main constraints: (i) the limitations imposed by the 3D printing process, since the overall specimen length was restricted by the dimensions of the printer chamber; and (ii) practical limitations inherent to the testing setup, since if the fibers composing the cell were too slender and the overall beam length too long, the specimen would exhibit excessive flexibility and would deflect under its own weight when clamped in the testing machine grips. To prevent such issues, and following the parametric study discussed in Section 4.4, a new microstructure was selected but first some clarifications about the specimen realization are necessary.

The specimen was fabricated using a 3D printer based on the stereolithography technique (SLA) at the Laboratory of Innovative Building Materials (Laboratorio di Materiali Innovativi per l'Edilizia - LMIE) of the Department of Civil, Construction-Architectural, and Environmental Engineering at the University of L'Aquila. SLA is a high-precision additive manufacturing technology that creates components layer by layer by selectively curing a liquid photopolymer resin with an ultraviolet (UV) laser. This process is particularly suitable for producing small-scale prototypes, as it provides excellent dimensional accuracy and smooth surface finishing.

Despite the generally high accuracy of SLA printing, small discrepancies between the designed and the printed geometries may still arise, especially when dealing with slender or particular features. For this reason, the following workflow was adopted. First, a microstructure with $\hat{\alpha} = 1.5$ was designed, while the value of $\hat{\beta}$ was selected so that the fibers connecting the two grains would be sufficiently thick to behave more as shell-like elements rather than beam-like ones. Then, t and the other geometric dimensions of the cell are found thanks to $\hat{\eta}_{\pm}\left(\hat{\alpha},\hat{\beta}\right)$ and Eqs. (4.9), respectively. Moreover, $R = 5$ mm and $t_z = 4$ mm were adopted, and the metamaterial was chosen to be made of $n = 10$ cells. Second, the specimen was printed and some measurements were performed, such as: the metamaterial's overall length, together with the fibers' height t and the thickness t_z, where the latter two were measured using a caliber. It was found, for instance, that the printed specimen exhibited an average fibers' height of $t = 2.27$ mm, whereas for the designed geometry it was $t = 2.25$ mm. These measurements confirmed that the printed geometry was essentially identical to the designed one, thereby validating the high manufacturing accuracy achieved with SLA. Although the difference was on the order of only a few hundredths of a millimeter, the unit cell was redesigned by changing the parameter $\hat{\beta}$, so that the geometry of both the finite element models and the equivalent beam model would, on average, match the geometry of the printed specimen. The corresponding geometric parameters are reported in Tab. 4.8, for which $\hat{\beta} \simeq 0.43$.

		Case study III
ℓ_x	[mm]	3.31
ℓ_y	[mm]	7.73
ℓ_c	[mm]	4.19
t	[mm]	2.27
h	[mm]	15
ℓ	[mm]	150

Table 4.8. Cell's geometric dimensions for case study III.

The tested specimen, shown in Fig. 4.20, was printed using White Resin, characterized by an elastic modulus $E = 2800\text{N/mm}^2$. Moreover, since DIC analysis relies on gray level intensity variations, the specimen surface was prepared by applying a random speckle pattern prior to testing. This pattern was designed to ensure sufficient contrast, thereby enabling accurate image tracking throughout the test. The specimen was then subjected to a uniaxial tensile test using the universal testing machine Zwick Z100 SN 'AllroundLine' equipped with a 5 kN load cell, which meets the requirements of Accuracy Class 0.5 as specified in the ISO 7500 standard.

Prior to this test, a tensile failure experiment was performed to identify the range of end displacements over which the specimen response remained essentially elastic. This preliminary characterization allowed us to define the displacements for which a meaningful comparison with the equivalent model, formulated under the assumptions of small displacements (i.e. within the framework of linear theory), could be carried out. Based on these results, a total extension of 2 mm was selected as a representative value within the experimentally identified elastic range, and the grain beam was stretched at a rate of 0.0025 mm/s up.

As for the hardware parameters of the optical setup, they are all listed in Tab. 4.9 and, moreover, to facilitate data extraction from images, a black background was adopted. For the purpose of image acquisition, LED panel was used to provide uniform illumination of the specimens.

Camera	Sony rx10 IV
Definition	3648×3648 pixels
Gray Levels amplitude	8 bits
Lens	ZEISS Vario-Sonnar T
Image scale	$\approx 49\,\mu$m/px (B&W image)
Stand-off distance	$\approx$ 100 cm
Image acquisition rate	1/10
Patterning technique	Sprayed white and black dots

Table 4.9. DIC hardware parameters.

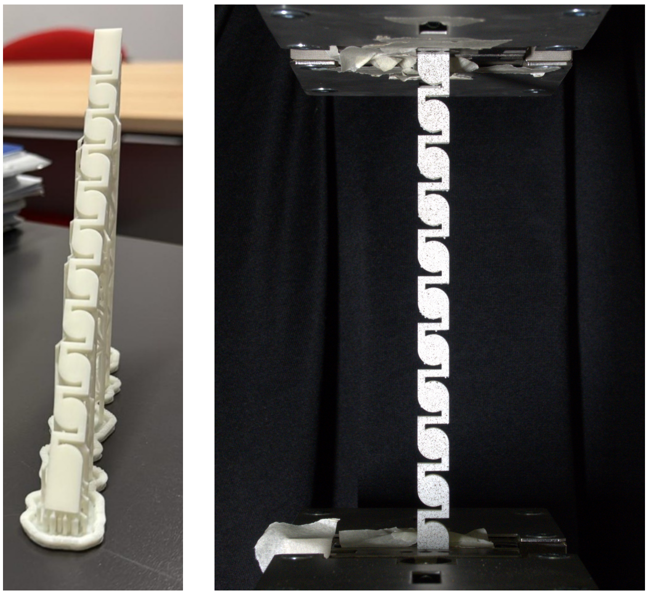

(a) (b)

Figure 4.20. (a) 3D printed specimen with SLA technology. (b) 3D printed specimen positioned in the testing machine and when clamped in the testing machine grips.

Once the mechanical test was completed, the DIC analysis was performed. Thanks to the specimen's speckled pattern, displacement data were available over the entire surface of each grain.

However, performing DIC requires a preliminary step, i.e. the definition of a mesh suitable for tracking the grain beam's displacement field. This mesh must be consistent with the actual printed specimen which, despite the high precision of SLA technology, may inevitably exhibit geometric imperfections, slight thickness variations, and minor deviations from the ideal shape. To this end, a nominal mesh is first generated from the grain beam's FE model, which is therefore perfectly straight and free of imperfections. Subsequently, a backtracking procedure is employed, in which the DIC algorithm is used to reconstruct the displacement field that maps the virtual twin (i.e., the nominal mesh) onto the specimen's image in its undeformed reference configuration, namely the reference image acquired before starting the loading step in the test. Thus, a 'modified' mesh, hereafter referred to as the experimental mesh, is obtained and is used in DIC for tracking the grain beam's displacement field during testing.

Furthermore, another crucial step requires the assessment of the DIC performance, i.e. it is necessary to verify if the displacement fields obtained from the analysis correspond to real deformations of the specimen, rather than artifacts introduced by acquisition noise. Therefore, a quantification of the measurement uncertainties is required. The procedure adopted here consists of acquiring several images before the beginning of the test, namely when the specimen is completely motionless, and performing between pairs of these 'at-rest' images the DIC procedure. For consistency with the experimental procedure, this latter has been carried out using the direct method. Since the specimen is motionless, any nonzero displacement field obtained originates from acquisition noise (camera sensor noise, lighting fluctuations). Therefore, DIC is applied to each image pair and the root mean square (RMS) displacement is computed for each one of them, enabling the final uncertainty estimate by averaging all the RMS. The resulting noise level is $1 \cdot 10^{-3}$ mm and represents the sensitivity threshold of the measurement system, providing an objective assessment of the DIC method's ability to distinguish true displacements from acquisition noise and ensuring the reliability of the experimental results.

It is specified that the captured images during testing were converted to gray scale to optimize DIC processing. As the correlation algorithm operates solely on light-intensity variations, gray scale conversion reduces data volume while improving pixel-tracking accuracy. In this format, each pixel, at abscissa x, is assigned a gray level intensity $I_0(x)$ ranging from 0 (black) to 255 (white), representing the local brightness of the speckle pattern. These variations constitute the basis for tracking the specimen's displacement field. The acquired images were processed through the DIC algorithm Correli 3.0 [4, 89], which determines the displacement field that best matches the observed gray level variations between the reference and deformed configurations. This is achieved by minimizing a least-squares cost function, namely the gray level residual $\eta_c^2(\{\mathbf{b}\})$, that quantifies the intensity differences across corresponding regions, thereby ensuring an accurate and consistent reconstruction of the deformation pattern. The least-squares cost function for each pixel within the ROI is reported below

$$\eta_c^2(\{\mathbf{b}\}) = \sum_{\mathbf{x}\in\mathrm{ROI}} \left[I_0(\mathbf{x}) - I_t(\mathbf{x} + \mathbf{u}(\mathbf{x}))\right]^2, \tag{4.16}$$

where $I_0(\mathbf{x})$ and $I_t(\mathbf{x} + \mathbf{u}(\mathbf{x}))$ denote the gray level of the image in the reference and deformed configurations, respectively. Both quantities vary with the pixel position $\mathbf{x}$, while $\mathbf{u}(\mathbf{x})$ represents the displacement field between the two configurations which can be expressed as

$$\mathbf{u}(\mathbf{x}) = \sum_i \mathbf{b}_i \mathbf{N}_i(\mathbf{x}), \tag{4.17}$$

in which $\mathbf{b}_i$ is the vector of unknown amplitudes to be determined so as to minimize the gray level residual, while $\mathbf{N}_i(\mathbf{x})$ are the trial displacement functions which are assumed to be linear. Actually, to handle regions with low material contrast and to minimize the noise effect, a mechanical regularization term is added to constrain the solution space by enforcing mechanical equilibrium conditions. This penalty improves robustness and stability in estimating the displacement field. It penalizes mechanically inconsistent incremental displacements, with the regularization strength controlled by the regularization weight w_{eq}. Using the stiffness matrix associated with the finite element discretization of the ROI, the mechanical regularization integrates physical constraints directly into the correlation algorithm. The mechanical penalty term reads

$$\eta_{eq}^2(\{\mathbf{b}\}) = \{\mathbf{b}\}^T [\mathbf{K}]^T \quad [\mathbf{K}]\{\mathbf{b}\}. \tag{4.18}$$

In other words, in our case the procedure does not simply minimize Eq. (4.16), that is, the DIC residuals themselves. Instead, the formulation is regularized by introducing an additional term that quantifies the equilibrium gap. Ultimately, the quantity being minimized is therefore the combination of these two contributions, namely

$$\eta^2(\{\mathbf{b}\}) = \eta_c^2(\{\mathbf{b}\}) + w_{eq}\eta_{eq}^2(\{\mathbf{b}\}) \quad . \tag{4.19}$$

In Eq. (4.19), the regularization weight w_{eq} is determined in order to obtain an optimal trade-off between the two cost functions

$$\{\mathbf{b}\}_{\text{meas}} = \text{argmin}_{\{\mathbf{b}\}}\left(\eta_c^2(\{\mathbf{b}\}) + w_{eq}\eta_{eq}^2(\{\mathbf{b}\})\right) \tag{4.20}$$

using the L-curve criterion [90]. In the following, results obtained from the experimental test are discussed.

Displacement field

Fig. 4.21 shows two images acquired at different instants of the experimental test. Fig. 4.21a corresponds to the undeformed configuration, prior to the onset of loading. The underlying image is therefore the reference one, and the mesh visible on the specimen is the backtracked one. Fig. 4.21b, instead, is taken during the test, in fact the specimen is deformed. The mesh follows the specimen's motion, and the nodal displacements computed through the DIC analysis are displayed as red arrows.

In Tab. 4.10 the displacement fields obtained from the DIC measurements at selected instants during the test are reported. These measurements, although the experimental setup imposes a purely longitudinal displacement $u(\ell)$ imposed by the experimental setup, revealed the presence of a small transverse displacement $v(\ell)$.

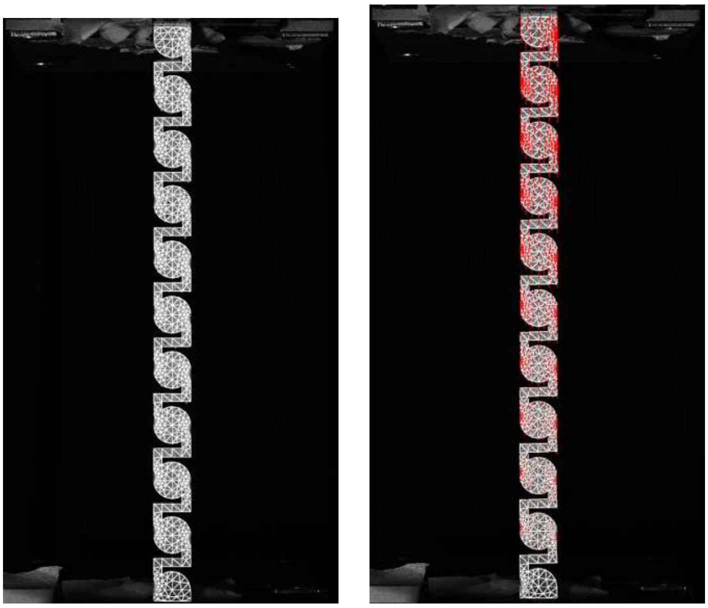

(a) (b)

Figure 4.21. (a) Backtracked mesh superimposed on the (undeformed) reference image. (b) Mesh following the specimen's motion during test, where the red arrows are the performed displacements.

Image	$u(\ell)$ [mm]	$v(\ell)$ [mm]
1	0.19	-1.25×10^{-3}
2	0.34	2.83×10^{-3}
3	0.51	2.04×10^{-3}
4	1.01	2.77×10^{-3}

Table 4.10. Displacements evaluated from the DIC analysis on the tested specimen.

For Image 1, the transverse displacement detected by the DIC is negligible and can be attributed to measurement noise. Conversely, for the subsequent images, the measured transverse components appear more consistent and are likely influenced by external factors, such as slight motions of the loading frame or minor artefacts introduced by the DIC itself. These artefacts may arise from variations in illumination or reflections occurring as the specimen progressively moves during the test.

However, for the sake of consistency in comparing the experimentally measured displacement fields with those predicted by the equivalent beam model and the FE model, both displacement components are applied to the equivalent beam and FE models. This choice ensures that all models are subjected to the same kinematic boundary conditions actually recorded by the DIC, thereby allowing a rigorous and unbiased assessment of the predictive capabilities of the different modeling approaches.

In the following, a comparison in terms of longitudinal displacement $u(x)$ and transverse displacement $v(x)$, between the experimental results, the Equivalent Beam model, and the FE model, is reported. The static response of the equivalent model is evaluated using the elastic constants obtained through the numerical procedure (NC constants), which provide more reliable predictions since, in the geometry adopted in case study III, the fibers connecting the grains are thick and therefore behave more like plates than beams. Moreover, two distinct FE models are developed: the first based on the nominal (straight) mesh, and the second one on the backtracked experimental mesh. These are referred to as FE model (Cauchy-NM) and FE model (Cauchy-EM), respectively. Comparisons are shown for the same set of images whose displacements evaluated with the DIC are reported in Tab. 4.10. Fig. 4.22, in which the displacement and abscissa unit is millimeters (mm),

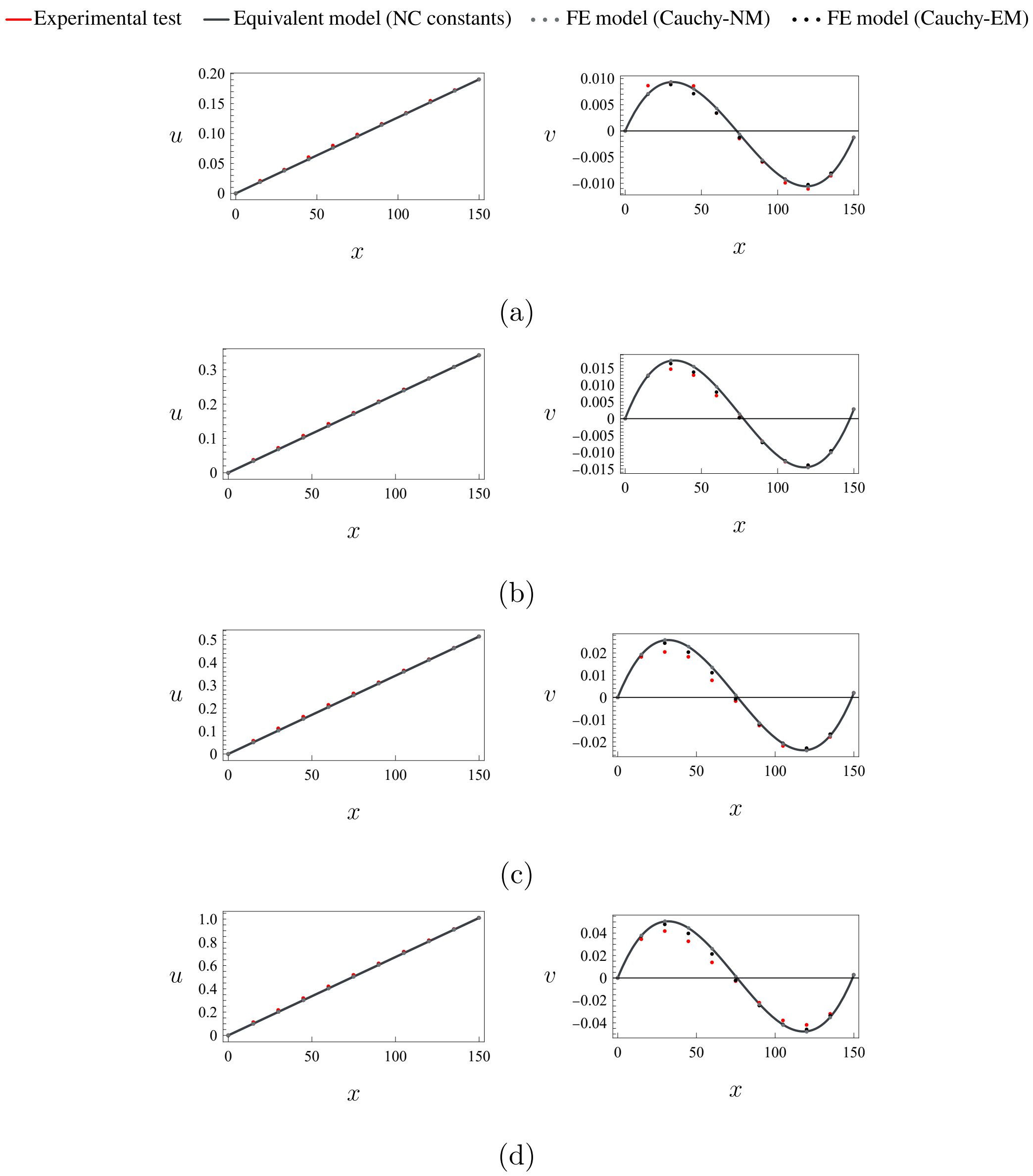

Figure 4.22. Static response of the 3D printed specimen vs. Equivalent beam model (NC constants) vs. the discrete FE models (Cauchy-NM) and (Cauchy-EM). (a-d) comparison in terms of longitudinal and transverse displacements for case study III at the selected loading instants named Image 1-4 in Tab. 4.10.

shows that the FE model (Cauchy-EM) reproduces the experimental displacement field with excellent accuracy, as expected, since its geometry, derived from the back-tracked experimental mesh, directly reflects the actual specimen. The comparison between the experimental data and the FE model (Cauchy-NM), built instead from the nominal (straight) mesh, also reveals a high level of agreement. This confirms what was previously observed: the specimen was manufactured with high fidelity, without significant printing defects, and was correctly positioned within the grips of the testing machine. An improper alignment during clamping would have resulted in an initial pre-deformed configuration, inevitably leading to discrepancies between the experimental response and the predictions of the nominal-mesh model. As for the Equivalent Beam model, it also reproduces the experimental behavior with high accuracy, in line with the previous comparisons, further confirming both the correct alignment of the specimen during testing and the reliability of the numerical identification procedure used to determine the constitutive matrix governing the grain beam.

Moreover, when an experimental approach is adopted, assessing the overall stiffness of the tested specimen is essential. Accordingly, the comparison is extended to the force-displacement response. Fig. 4.23 depicts the reaction force and the imposed displacement s applied by the crosshead to the beam at $x = \ell$ at a given instant of the test. This result confirm, again, a very good agreement between the Equivalent Beam model, the FE models, and the experimental measurements. Although these tests are still preliminary, the level of consistency achieved so far is already highly satisfactory. In the following figure, the displacement s is expressed in millimeters (mm), while the force F is expressed in newton (N).

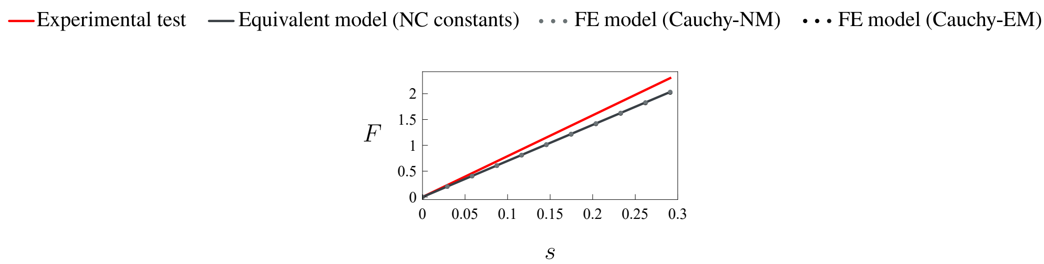

Figure 4.23. Force-displacement diagram of the 3D printed specimen vs. Equivalent beam model (NC constants) vs. the discrete FE models (Cauchy-NM) and (Cauchy-EM) .

Chapter 5

Grid beam

5.1 Introduction

In this Chapter, attention is focused on the mechanical behavior of the grid beam, examined under the assumption of a cross-section that is rigid in plane, and deformable (or rigid) out of plane. The aim is to develop an equivalent generalized beam model capable of accurately reproducing the deformation mechanisms of the metamaterial's cross-section by introducing suitable distortional and bi-distortional strain measures.

The elastic coefficients governing the response of the equivalent beam are identified using both analytical and numerical procedures, the inertial coefficients, on the other hand, are determined analytically. Furthermore, the internal and external forces of the equivalent model are derived to ensure full consistency with those of the fine model. Finally, the predictive capabilities of the proposed equivalent beam model are assessed through numerical simulations, in which the grid beam is analyzed under static, dynamic, and buckling conditions.

5.2 Topology of the microstructure

The topology of the grid beam is described in this section. The microstructure, depicted in Fig. 5.1, is made of a single planar frame composed of two orthogonal families of (micro) beams, hereinafter referred to as 'fibers', arranged in a periodic rectangular pattern with cell size h. Analogously to the grain beam, the cell is referred to a (local) cartesian coordinate system $\tilde{O}\tilde{x}\tilde{y}$, whose origin $\tilde{O}$ coincides with the centroid of the left cross-section. The families of fibers are: (i) those parallel to the (local) $\tilde{x}-$axis of the cell, i.e. the horizontal fibers, which are n_y, and (ii) those parallel to the (local) $\tilde{y}-$axis of the cell, i.e. the vertical one, which are n_x. The same notation adopted for the previous microstructure is employed here. Accordingly, the heights of the horizontal and vertical beams are denoted by t_ν, where the subscript $\nu = x, y$ indicates the fiber orientation along the respective axes. Moreover, all micro-beams share the same out of plane thickness t_z, measured along the $z-$axis (not represented in the figure). The horizontal and vertical fibers have lengths ℓ_x and ℓ_y, respectively, with $\ell_x := h$. In what follows, the identification of the homogenized (equivalent) beam model is carried out for the general case $\ell_x \neq \ell_y$ with $t_x \neq t_y$, whereas numerical analyses are performed assuming $\ell_x = \ell_y =: h$ and $t_x = t_y =: t$.

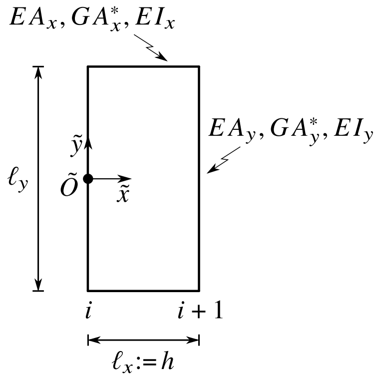

Figure 5.1. Periodic microstructure of the grid beam.

By the periodic repetition of the microstructure in the $x-$direction, the grid beam is built up, as shown in Fig. 5.2. The local and global horizontal axes are taken coincident, namely $\tilde{x} \equiv x$. The global coordinate system origin O is located at the cross-section $i = 0$; accordingly, the local vertical axis $\tilde{y}$ is parallel to $y-$axis, for each cell. To describe the static, dynamic and buckling behavior of the grid beam, the equivalent beam model introduced in Section 3.2.2, namely the generalize beam model, is heuristically adopted as the target (and coarse) model within the framework of the mixed homogenization approach.

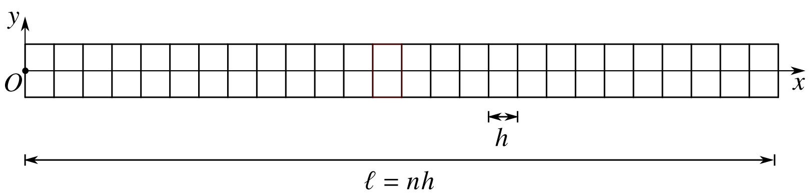

Figure 5.2. Study object: the grid beam.

5.3 Model identification

5.3.1 Analytical identification of the elastic constants

The identification algorithm explained in Section 3.3 is now specialized for the grid beam but, before presenting the analytical procedure adopted to evaluate $\tilde{\phi}$, some clarifications regarding the modeling assumptions of the microstructure are required. A cell bounded by two adjacent cross-sections $\mathcal{D}_i$ and $\mathcal{D}_{i+1}$ is considered, to which half of the stiffness is assigned to the fibers located on the boundaries. Moreover, while the nodal points of these boundary fibers are constrained to remain in the same plane, the fibers themselves

are allowed to warp around it, undergoing a deformation mode referred to in [37] as micro-warping.
All the fibers are modeled as Timoshenko (micro) beams, hence exhibit axial, shear, and bending stiffnesses denoted by EA_ν, GA^*_ν, and EI_ν, respectively. As defined in Section 4.3.1, E and G are the elastic and tangential modulus, while A_ν, A^*_ν, and I_ν, are the fiber's cross-section area, the shear area, and the inertia moment, respectively, with respect to its cross-section principal axis ($\nu = x, y$). Moreover, the limit case of a microstructure composed of Euler-Bernoulli (micro) beams can be easily derived from the Timoshenko formulation, by introducing the dimensionless stiffness ratio $\mu_\nu := 12EI_\nu/GA^*_\nu\ell^2_\nu$ and enforcing the condition $\mu_\nu \to 0$.

The equivalent model adopted to describe the mechanical behavior of the grid beam is the Generalized Beam Model (GBM), since the idea is to develop a formulation capable of capturing the out of plane deformability of the cross-section, thereby overcoming the limitations observed in the models available in the literature.
As discussed in Chapter 2, several studies [35–37, 60] have investigated grid beams under the assumption of an in plane rigid and out of plane deformable cross-section, within the framework of the mixed homogenization approach; however, none of these works selects a target model endowed with a kinematic description capable of faithfully representing the deformation of the cross-section. In those studies, the target model is a beam with a rigid cross-section, and the out of plane deformability is accounted for through a shear factor, which acts as a corrective parameter for the shear stiffness, enabling the target model to reproduce (on average) the non-rigid behavior of the cross-section. This type of model may be referred to as Timoshenko Beam Model-Modified (TBM-M) when, for example, the Timoshenko beam model is adopted as the equivalent rigid cross-section model and its shear stiffness is 'modified' through the shear factor.
Although the GBM provides a more advanced and comprehensive framework compared to shear factor based models, it is still meaningful in the validation phase, where the predictions of the proposed model are compared with finite element results, to include such a reference model in the analysis. For this reason, in the following there is not only the algorithm adopted to analytically determine the elastic constants of the GBM, but also the procedure used for the TBM-M. Regarding the kinematic relations and equilibrium equations of the latter, they have already been presented in Section 3.2.1.

5.3.1.1 Timoshenko Beam Model 'Modified' (TBM-M)

As already mentioned, the identification of the elastic coefficients for the Timoshenko Beam Model 'Modified' (TBM-M) is based on the mixed homogenization approach described in Section 3.3. This formulation relies on an equivalent model endowed with an enriched kinematic description, in which warping effects are explicitly represented through additional kinematic variables. Therefore, when the target model features a reduced kinematics, as in the case of the Timoshenko beam model, some clarifications are required.

First, all contributions explicitly accounting for warping are neglected by enforcing

$a(x) = 0$ in Eq. (3.40), and by reducing the operators' dimension. As a consequence, the boundary displacements of the representative cell (Eq. (3.46)) are expressed as the superposition of three independent deformation modes, namely extensional (E), shear (S), and flexural (F), rather than the five modes required by the generalized beam model. However, in Section 3.3, the E, S, and F modes are applied under the assumption that the cross-section $\mathcal{D}_{i+1}$ undergoes a rigid translation without deforming. As already explained, this is possible only thanks to the GBM's enriched kinematic description. When the kinematic is limited as in the TBM-M, the E, S, and F modes have to be imposed by allowing the cross-section to undergo both translation and deformation. However, before evaluating the elastic potential energies associated with each deformation modes, the following hypothesis are introduced: (i) in the shear mode, in which the cross-section $\mathcal{D}_{i+1}$ translates along $y-$direction of $v(x_{i+1}) = \gamma_0 h$ (Eq. (3.46)), all nodes rotate by an unknown angle φ (see Fig. 5.3); (ii) in the flexural mode, the effects of micro-warping are neglected, since the strain energy associated with the extension of the fibers oriented along the $y-$direction is negligible.

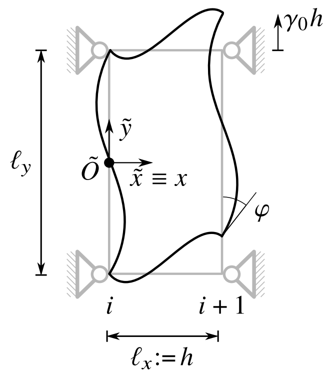

Figure 5.3. Representation of the kinematic hypothesis introduced for the shear (S) mode of the TBM-M.

In [35–37, 60], several case studies are examined. However, since in the present work the TBM-M is employed exclusively as a comparison for the case study analyzed in Section 5.4, only the analytical expression of the elastic coefficients for that specific configuration are reported below. In particular, the analysis is focused on a grid beam made of a single squared cell ($n_y = 2$) of side h, in which all fibers, both in the $x-$ and $y-$directions, are characterized by the same cross-section, namely $EA_\nu := EA$, $GA^*_\nu := GA^*$.

$$
\begin{aligned}
c_{11} &= 2EA, & c^*_{22} &= \chi^* \frac{6 + 10\mu}{5\,(1+\mu)^2}, \\
c_{22} &= \chi \frac{24EI}{h^2\,(1+\mu)}, & c^*_{23} &= \frac{h}{2}, \\
c_{33} &= 2EI + EA \sum_{k=1}^{2} y_k^2, & c^*_{33} &= \frac{h^2}{3}.
\end{aligned}
\tag{5.1}
$$

In Eq. (5.1), all other terms of the 3×3 constitutive matrix $\mathbf{C}$ are omitted since they are zero, while

$$\begin{aligned} \chi &= \frac{n_y - 1}{2n_y - 1}, \\ \chi^* &= \frac{\left[5\mu\left(3\mu+8\right)+21\right]n_y^2 - 2\left[5\mu\left(\mu+4\right)+11\right]n_y + 6 + 10\mu}{2\left(5\mu+3\right)\left(1-2n_y\right)^2}, \end{aligned} \tag{5.2}$$

are the shear factors accounting for the flexibility of the $y-$fibers in the elastic $\mathbf{C}^0$ and in the geometric $\mathbf{C}^*$ part of the constitutive matrix (see Eq. (3.2)), respectively. Since $n_y = 2$, it is $\chi = 0.33$ and $\chi^* = \frac{[5\mu(3\mu+8)+21]4-[5\mu(\mu+4)+11]4+6+10\mu}{18(5\mu+3)}$.

5.3.1.2 Generalized Beam Model (GBM)

The analytical procedure adopted to define the elastic constants of the Generalized Beam Model is outlined below. As discussed in Section 3.3, the elastic energy is computed by imposing appropriate deformation modes, i.e. by prescribing boundary displacements, according to Eq. (3.46), at the (periodicity) hinges and performing a static analysis of the planar frame.

It is worth to remind that the boundary displacements described by Eq. (3.46) can be interpreted as the superposition of five independent deformation modes. Three of these are the classical rigid (in plane and out of plane) cross-section modes, i.e. the extensional (E), shear (S), and flexural (F) mode, whose cross-sections are highlighted with a thicker line in the following figures to emphasize their rigid behavior. The remaining two, i.e. the uniform distortional (UD) and non-uniform distortional (NUD) modes, describe pure distortional deformations of the cross-sections, without any rigid-body translation or rotation. Since there are five independent deformation modes (pure modes) and fifteen unknown elastic constants, all possible combinations of the pure modes are systematically selected and applied to the cell. Therefore, the independent and coupled deformation modes are applied; for the latter, the procedure relies on the superposition of effects, where the energy of the pure deformation modes must, of course, be subtracted from that of the coupled ones.

The procedure can be pursued starting from Eq. (3.46), which defines the displacements $u_G = u\left(x_{i+1}\right)$, $v_G = v\left(x_{i+1}\right)$ and $\theta = \theta\left(x_{i+1}\right)$ of the centroid G of the cross-section, as well as the amplitudes $a = a\left(x_{i+1}\right)$ and $a = a\left(x_i\right)$ of the warping function of the cross-sections.

At first, the E, S and F modes are considered. For each of these rigid cross-section deformation mode prescribed in the algorithm (i.e., for a known set of centroid displacements), Eq. (3.46) provides the (rigid) displacements $\tilde{u}\left(x_{i+1}, \mp\ell_y/2\right) =: \bar{u}_j$, $\tilde{v}\left(x_{i+1}, \mp\ell_y/2\right) =: \bar{v}_j$ of the $j-$th hinges (denoted with 1 and 2 in Fig. 5.4). Therefore, the complete kinematic mapping is the same as the one of the grain beam and is reported in Eq. (4.1).

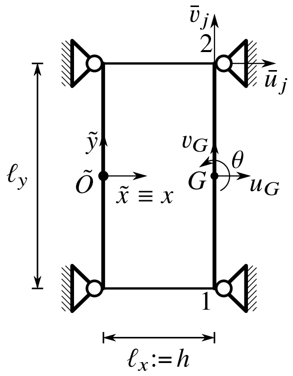

Figure 5.4. Periodic microstructure of the grid beam with applied displacement for the evaluation of the rigid cross-section modes.

For the uniform (UD) and non-uniform distortional (NUD) modes, instead, the procedure is slightly more elaborated. In the case of the UD mode, a unit distortion must be prescribed at the centroids G of both cross-sections $\mathcal{D}_i$ and $\mathcal{D}_{i+1}$, whereas for the NUD mode the unit distortion is imposed only at $\mathcal{D}_{i+1}$. To this end, suitable displacements are applied at the periodicity $j-$th hinges ($j = 1, 2$), namely $u\left(\pm\frac{\ell_y}{2}\right) = \mp 1$ mm, in order to deform the cross-section. As explained in Section 3.3, when a cross-section is deformable, the resulting displacement field $u\,(y)$ can be decomposed into a rigid component $u_r\,(y) = \hat{u} - \hat{\theta} y$, where the parameters $\hat{u}$ and $\hat{\theta}$ are determined by e Eqs. (3.43), and into a purely deformative component $u_d\,(y)$. As mentioned, this latter is the warping function $\psi\,(y)$ needed for defining the cell's pure distortional modes. Subtracting the rigid contribution from the total displacement field $u\,(y)$, which for the case of a one framed grid beam composed of Timoshenko (micro) beams is

$$u\,(y) = \frac{1}{1+\mu_y}\left[4\frac{y^3}{\ell_y^3} - (3+2\mu_y)\,\frac{y}{\ell_y}\right], \tag{5.3}$$

leads to the following expression for the warping function:

$$u_d\,(y) \coloneqq \psi\,(y) = \frac{1}{1+\mu_y}\left(4\frac{y^3}{\ell_y^3} - \frac{3}{5}\frac{y}{\ell_y}\right). \tag{5.4}$$

Its interesting to note that, up to a constant, the warping function Eq. (5.4) coincides with the exact de Saint-Venant solution for the problem of non-uniform bending of a thin rectangular cross-section. Moreover, the limit case of a microstructure made of Euler-Bernoulli (micro) beams is easily achieved by enforcing the condition $\mu_y \to 0$.

The displacement field $u\,(y)$ and its rigid and deformative components are depicted in Fig. 5.5.

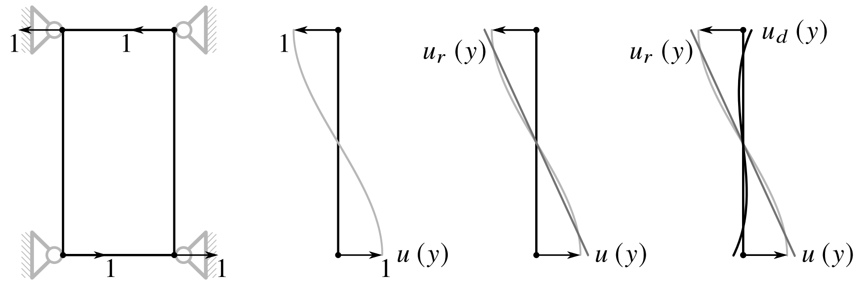

Figure 5.5. Displacement field $u(y)$ of the cross-section $\mathcal{D}_i$ after applying the imposed displacements required to evaluate the warping function, together with its rigid and purely deformative components. Continuous light gray line: total displacement field $u(y)$. Continuous dark gray line: rigid component to the displacement field $u_r(y)$. Continuous black line: purely deformative component to the displacement field $u_d(y)$.

It is convenient to follow the same strategy adopted in Section 4.3.1, namely: (i) assign unit displacements at the hinges; (ii) compute the corresponding centroid displacements via the kinematic map; and (iii) evaluate the associated strains using Eq. (3.46).
The algorithm adopted for the identification of the elastic coefficients is summarized below. Since the E, S, and F pure modes are the rigid (both in plane and out of plane) cross-section deformation modes, their evaluation, together with that of the associated coupled modes ES, EF, and SF, follows exactly the same procedure described for the grain beam. Accordingly, reference is made to Section 4.3.1 for a detailed description. In what follows, only the additional steps required for the identification of the elastic coefficients of the GBM are reported.

1. Uniform distortional mode (UD) is assigned, in which both $\mathcal{D}_i$ and $\mathcal{D}_{i+1}$ undergo deformation according to the warping shape $\psi(y)$, without translation or rotation. Since $u_G = 0$, $v_G = 0$ and $\theta = 0$, then $\varepsilon_0 = 0$, $\gamma_0 = 0$ and $\kappa_0 = 0$. The fourth scalar displacement component is set as $a = 1$ at both cross-sections, multiplying the warping function. Consequently, $\alpha_0 = 1$ at $\mathcal{D}_i$ and $\alpha_0 + \beta_0 h = 1$ at $\mathcal{D}_{i+1}$ (Eq. (3.46)). However, since the assigned deformation mode is a uniform distortional one, the same distortion is applied to both cross-sections, and therefore the distortion gradient $\beta_0 = 0$ by definition. Finally; c_{44} is computed.

2. Non uniform distortional mode (NUD) is assigned, in which only $\mathcal{D}_{i+1}$ undergo deformation according to the warping shape $\psi(y)$, without translation or rotation, while $\mathcal{D}_i$ is kept fixed. Since $u_G = 0$, $v_G = 0$ and $\theta = 0$, then $\varepsilon_0 = 0$, $\gamma_0 = 0$ and $\kappa_0 = 0$. The fourth scalar displacement component is set as $a = 1$, multiplying the warping function. Consequently, since the assigned deformation mode is the non uniform distortional one, it is $\alpha_0 = 0$ and $\beta_0 = 1/h$. Finally; c_{55} is computed.

3. Extensional and uniform distortional (EUD), i.e. the superposition of the pure modes (E), (UD), is assigned, for which $\varepsilon_0 = 1/h$, $\gamma_0 = 0$, $\kappa_0 = 0$, $\alpha_0 = 1$, $\beta_0 = 0$; since c_{11}, c_{44} are known, c_{14} is computed.

4. Extensional and non uniform distortional (ENUD), i.e. the superposition of the pure modes (E), (NUD), is assigned, for which $\varepsilon_0 = 1/h$, $\gamma_0 = 0$, $\kappa_0 = 0$, $\alpha_0 = 0$, $\beta_0 = 1/h$; since c_{11}, c_{55} are known, c_{15} is computed.

5. Shear and uniform distortional (SUD), i.e. the superposition of the pure modes (S), (UD), is assigned, for which $\varepsilon_0 = 0$, $\gamma_0 = 1/h$, $\kappa_0 = 0$, $\alpha_0 = 1$, $\beta_0 = 0$; since c_{22}, c_{44} are known, c_{24} is computed.

6. Shear and non uniform distortional (SNUD), i.e. the superposition of the pure modes (S), (NUD), is assigned, for which $\varepsilon_0 = 0$, $\gamma_0 = 1/h$, $\kappa_0 = 0$, $\alpha_0 = 0$, $\beta_0 = 1/h$; since c_{22}, c_{55} are known, c_{25} is computed.

7. Flexural and uniform distortional (FUD), i.e. the superposition of the pure modes (F), (UD), is assigned, for which $\varepsilon_0 = 0$, $\gamma_0 = 0$, $\kappa_0 = 1/h$, $\alpha_0 = 1$, $\beta_0 = 0$; since c_{33}, c_{44} are known, c_{34} is computed.

8. Flexural and non uniform distortional (FNUD), i.e. the superposition of the pure modes (F), (NUD), is assigned, for which $\varepsilon_0 = 0$, $\gamma_0 = 0$, $\kappa_0 = 1/h$, $\alpha_0 = 0$, $\beta_0 = 1/h$; since c_{33}, c_{55} are known, c_{35} is computed.

9. Uniform and non uniform distortional (UNUD), i.e. the superposition of the pure modes (U), (NUD), is assigned, for which $\varepsilon_0 = 0$, $\gamma_0 = 0$, $\kappa_0 = 0$, $\alpha_0 = 1$, $\beta_0 = 1/h$; since c_{44}, c_{55} are known, c_{45} is computed.

Fig. 5.6 and 5.7 show the deformation modes prescribed to the periodic microstructure and the corresponding deformed shapes, respectively.

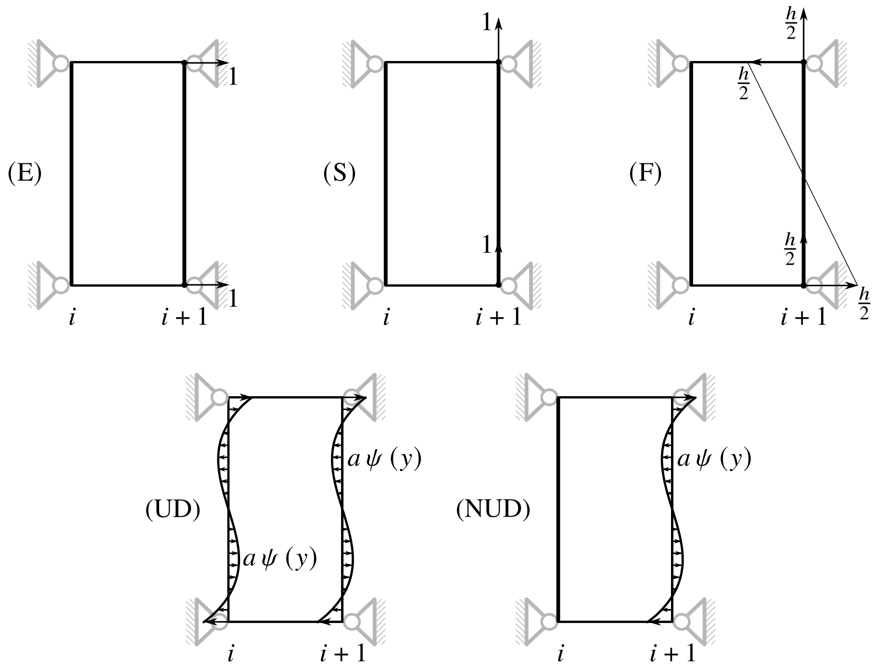

Figure 5.6. Deformation modes assigned to the periodic microstructure: (E) extensional; (S) shear; (F) flexural; (UD) uniform distortional; (NUD) non uniform distortional.

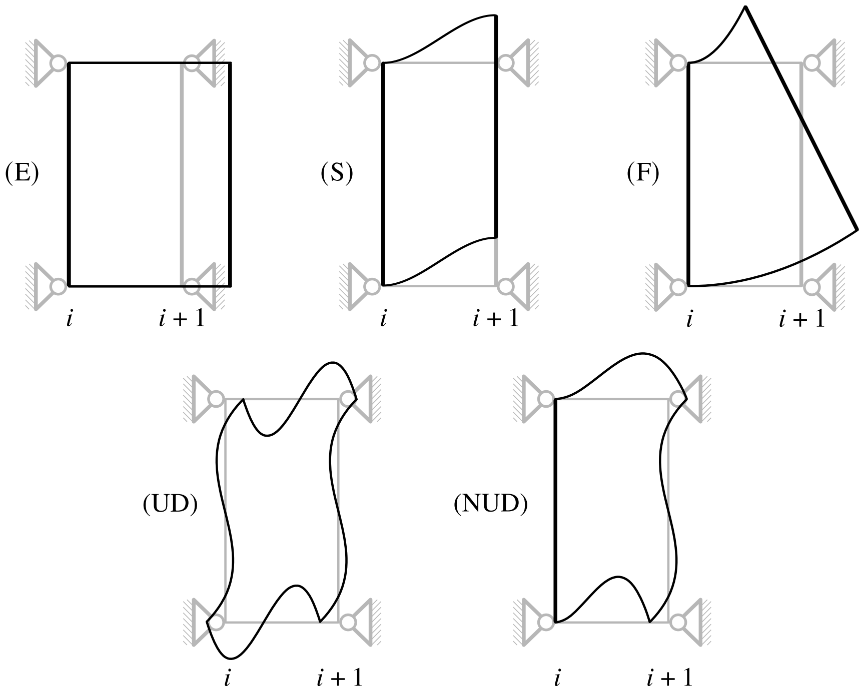

Figure 5.7. Deformed shapes of the modes assigned to the periodic microstructure: (E) extensional; (S) shear; (F) flexural; (UD) uniform distortional; (NUD) non uniform distortional.

For each assigned deformation mode, the analytical solution of the static problem for the planar frame subjected to prescribed displacements is obtained. In particular, for the pure extensional, shear, and flexural modes, only the $x-$beams ($k = 1, 2$) contribute to the elastic energy of the cell. Conversely, in the pure uniform distortional mode, both the $x-$ and $y-$beams ($k = 1, \ldots, 4$) contribute to the elastic energy, whereas in the non uniform distortional mode the elastic energy is provided by beams $k = 1, 2, 4$, i.e. the two $x-$beams and the $y-$beam at the cross-section $\mathcal{D}_{i+1}$. Accordingly, for each of the fifteen problems, the elastic energy of the cell $\tilde{U^0}$ is computed as the sum of the elastic energies of the $k-$th beam $\tilde{U^0_k}$, namely:

$$\tilde{U^0}\left(\varepsilon, \gamma, \kappa, \alpha, \beta\right) = \sum_{k=1}^{4} \tilde{U^0_k}, \quad \text{with} \quad k = 1, \ldots 4. \tag{5.5}$$

A clarification is required regarding the evaluation of the elastic energy associated with the $y-$beams when the uniform and non uniform distortional modes are considered. In these deformation modes, the $y-$beams deform due to the imposed displacement field $a\,\psi\left(y\right)$, which is longitudinal with respect to the microstructure's global reference system but transverse in the beam's local coordinate system. Since the $y-$beams are modeled as Timoshenko beams, their elastic energy accounts, among other contributions, for the work spent by the shear force in the shear strain. The latter is given by the well-known relation $\gamma\left(y\right) = v'\left(y\right) - \theta\left(y\right)$, where $v\left(y\right) = a\,\psi\left(y\right)$ is the prescribed displacement field, while $\theta\left(y\right)$ is the corresponding rotation field. This latter is unknown since $v\left(y\right)$ is not the solution from the boundary value problem with prescribed displacements at the beam's end. In fact, it is obtained from the total displacement field $u\,(y)$ once its rigid component $u_r\,(y)$ has been removed. Therefore, the rotation field compatible with the applied transverse displacement has to be determined. Since the equilibrium equations must be satisfied, $\theta\,(y)$ can be determined by requiring that, together with the $v\,(y)$, it fulfills the equilibrium, namely

$$\begin{aligned} GA_y^*\left(v'' - \theta'\right) &= 0, \\ EI_y\theta'' + GA_y^*\left(v' - \theta\right) &= 0. \end{aligned} \tag{5.6}$$

From Eq. (5.6a) it follows that $\theta = v' + c$, where c is a constant determined through Eq. (5.6b). Since it is $c = \frac{EI_y}{GA_y^*}v'''$, the rotation field is obtained and takes the form

$$\theta\,(y) = a\frac{60y^2 - \ell_y^2\left(3 - 10\mu_y\right)}{5\ell_y^3\left(1 + \mu_y\right)}. \tag{5.7}$$

In contrast, for a microstructure composed of Euler-Bernoulli (micro) beams, the problem becomes significantly simpler since, due to the hypothesis of shear undeformability, the rotation field is already known. In fact, it is $\theta\,(y) = v'\,(y) = a\,\psi'\,(y)$.

Finally, since $\tilde{\phi}^0 = \tilde{U}^0/h$, the Green's law Eq. (3.25) supplies for the elastic matrix $\mathbf{C}^0$ that in the static and dynamic problem is $\mathbf{C}^0 \coloneqq \mathbf{C}$. Eq. (3.27) thus takes the form

$$\mathbf{C} = \begin{pmatrix} c_{11} & 0 & c_{13} & 0 & c_{15} \\ & c_{22} & 0 & c_{24} & c_{25} \\ & & c_{33} & 0 & c_{35} \\ & & & c_{44} & c_{45} \\ \text{SYM} & & & & c_{55} \end{pmatrix}. \tag{5.8}$$

The analytical expressions of the elastic coefficients are provided in Appendix B for the general case of a one framed rectangular microstructure, i.e. with $\ell_x \neq \ell_y$, made of Timoshenko (micro) beams.

As highlighted in Section 4.3.1 for the grain beam, obtaining the analytical expression of $\mathbf{C}^0$ is among the most challenging stages of the identification procedure. In the present case, it is possible only thanks to the simple geometric arrangement of the fibers. A fully numerical identification strategy could in principle be employed and will be introduced later; however, such an approach would still require the warping function to be imposed within the finite element model. Consequently, the analytical determination of the warping function remains an essential preliminary step.

As for the buckling analysis, the elastic operator $\mathbf{C}$ depends on both the strains and the prestress, according to Eq. (3.2). Unlike the grain beam, is straightforward to determine that, in the precritical configuration, each $x-$fiber of the cell is uniformly prestressed by $\mathring{N}_k = -P/n_y$ (with $n_y = 2$ in the case at hand), whereas the $y-$fibers are not prestressed.

The geometric contribution to the elastic energy takes the form:

$$\tilde{U}_k^* \left(\varepsilon, \gamma, \kappa, \alpha, \beta, \mathring{N}\right) = \int_0^h \left(\mathring{N}_k \varepsilon_k^{(2)}\right) \mathrm{d}x, \quad \text{with} \quad k = 1, 2. \tag{5.9}$$

Then, thanks to the Green's law also the matrix $\mathbf{C}^*$can be found

$$\mathbf{C}^* = \begin{pmatrix} 0 & 0 & 0 & 0 & 0 \\ & c_{22}^* & c_{23}^* & c_{24}^* & c_{25}^* \\ & & c_{33}^* & 0 & c_{35}^* \\ & & & c_{44}^* & c_{45}^* \\ \text{SYM} & & & & c_{55}^* \end{pmatrix}, \tag{5.10}$$

whose analytical expression is reported in Appendix B for the general case of a one framed rectangular microstructure, i.e. with $\ell_x \neq \ell_y$, made of Timoshenko (micro) beams.

5.3.2 Numerical identification of the elastic constants

As already discussed in Section 4.3.2, the elastic constants can be identified not only analytically but also numerically. This latter, in the framework of the mixed homogenization approach applied to a grid beam, has already been outlined in [35]. In that work, however, it is formulated for a framed microstructure whose target model is the Timoshenko beam, and is therefore based on a significantly simpler kinematic description than the one adopted in the present Chapter.

The numerical identification is performed on the same cell adopted in the analytical procedure (see Fig. 5.1); therefore, the beams are modeled as (micro) Timoshenko beams and, moreover, those belonging to the cross-sections $\mathcal{D}_i$ and $\mathcal{D}_{i+1}$ contribute to the total elastic energy with half of their stiffness. For each deformation mode, the same displacement fields as those of the analytical identification procedure are imposed.
Accordingly, for the extensional (E), shear (S), and flexural (F) modes, the prescribed displacements are applied at the centroid of $\mathcal{D}_{i+1}$, assuming the cross-sections to be rigid in plane and out of plane. In these cases, cross-sections $\mathcal{D}_i$ and $\mathcal{D}_{i+1}$ are hinged at the periodicity joints. For the uniform (UD) and non uniform (NUD) distortional modes, instead, the displacement and the rotation fields, given respectively by Eq. (5.4) and Eq. (5.7), are applied to both $\mathcal{D}_i$ and $\mathcal{D}_{i+1}$ in the uniform case, and only to $\mathcal{D}_{i+1}$ for the non uniform case. To impose these fields, each cross-section is discretized into N segments, resulting in $N+1$ joints on which the corresponding displacement and rotation components are prescribed. Therefore, in order to correctly account for the reaction forces and moments associated with the imposed kinematics, the entire cross-sections are considered clamped. Of course, if the microstructure is composed of Euler-Bernoulli beams, the displacement field to apply is obtained by enforcing $\mu_y \to 0$ in Eq. (5.4).

The algorithm for evaluating the constitutive matrix in the numerical identification procedure consists of two main steps. First, a FE analysis of the cell is carried out for each deformation mode, and the corresponding elastic energy is computed by applying

Clapeyron's theorem. For the extensional, shear, and flexural modes, the energy is computed as

$$\tilde{U}_{E,S,F} = \frac{1}{2}\sum_{j=1}^{2}\left(r_{xj}\bar{u}_j + r_{yj}\bar{v}_j\right), \tag{5.11}$$

where $j = 1, 2$ identify the periodicity joints (see Fig. 5.4) at which the prescribed displacements are applied, and r_{xj}, r_{yj} denote the reaction forces corresponding to the imposed horizontal and vertical displacements, respectively. For the uniform and non uniform distortional modes, both displacement and rotation fields are applied. In this case, the Clapeyron's theorem takes the form

$$\tilde{U}_{UD,NUD} = \frac{1}{2}\sum_{i}\sum_{j=1}^{N+1}\left(r_{xj,i}\bar{u}_{j,i} + r_{yj,i}\bar{v}_{j,i} + \mu_{zj,i}\bar{\theta}_{j,i}\right), \tag{5.12}$$

where $j = 1, \ldots, N+1$ are the joints belonging to the $i-$th cross-section, and $r_{xj,i}$, $r_{yj,i}$ and $\mu_{zj,i}$ represent the reaction forces and reaction moment corresponding to the imposed displacement and rotation at the $j-$th joint of the $i-$th cross-section. Unlike the extensional, shear, and flexural modes, here the explicit reference to the $i-$th cross-section is required: in the uniform distortional mode, the energy must be evaluated on both cross-sections, $\mathcal{D}_i$ and $\mathcal{D}_{i+1}$, whereas in the non-uniform mode it is evaluated only on the right-hand cross-section $\mathcal{D}_{i+1}$. Finally, by requiring Eq. (3.47) to hold for any combination of ε, γ, κ, α and β, with $\tilde{\phi}^0 = \tilde{U}^0/h$, the unknown fifteen elastic constants are computed.

5.3.3 Identification of the external and internal forces

To identify the external forces of the equivalent model, reference is made to the external virtual work performed by the forces acting on the grid beam. The latter are assumed to be subjected to point forces, $\tilde{P}_{x,j}$ and $\tilde{P}_{y,j}$, and couples, $\tilde{C}_j$, applied at each $j-$th joint (with $j = 1, 2$ for the case study examined in this thesis) of the $i-$th cross-section $\mathcal{D}_i$ ($i = 0, 1, \ldots, n_x$). These loads spent virtual work on the corresponding virtual displacements, so that the external virtual work for the fine and homogenized model reads:

$$\tilde{\mathcal{W}}_e = \sum_{j=1}^{2}\left(\tilde{P}_{x,j}\delta\tilde{u} + \tilde{P}_{y,j}\delta\tilde{v} + \tilde{C}_{z,j}\delta\tilde{\theta}\right), \quad \mathcal{W}_e = P_x\delta u + P_y\delta v + C_z\delta\theta + Q\delta a. \tag{5.13}$$

By substituting the kinematic map (Eq. (3.40)) in Eq. (5.13a), and requiring the equivalence between the two models' external virtual work, $\tilde{\mathcal{W}}_e = \mathcal{W}_e$, the following expressions for the equivalent model's generalized external forces of are obtained:

$$P_x = \sum_{j=1}^{2}\tilde{P}_{x,j}, \quad P_y = \sum_{j=1}^{2}\tilde{P}_{y,j}, \quad C_z = \sum_{j=1}^{2}\left(\tilde{C}_{z,j} - \tilde{P}_{x,j}\tilde{y}_j\right), \quad Q = \sum_{j=1}^{2}\tilde{P}_{x,j}\psi\left(\tilde{y}_j\right). \tag{5.14}$$

Here, P_x, P_y, C_z and Q are the concentrated loads where, as seen in Section 3.2.2, the latter is a concentrated distortional force, which spends virtual work on the cross-section's warping. The corresponding distributed loads of the homogenized model can be easily determined by spreading the concentrated loads, applied to the $i-$th cross-section over the cell length h, namely over the length of influence:

$$p_x = \frac{P_x}{h}, \quad p_y = \frac{P_y}{h}, \quad c_z = \frac{C_z}{h}, \quad q = \frac{Q}{h}. \tag{5.15}$$

in which p_x, p_y and c_z are the classical distributed loads, whereas q is a distributed distortional load.

The identification of the equivalent beam model's internal forces is more challenging. The procedure is carried out at the level of the representative cell, the same used for the evaluation of the elastic constants (see Fig. (5.1)), rather than at that of the entire beam. By enforcing the equivalence between the internal virtual work of the homogenized model, $\mathcal{W}_i$, and that of the fine model, $\tilde{\mathcal{W}}_i$, the internal forces of the latter can be derived. The internal virtual work of the generalized beam model is given by

$$\mathcal{W}_i := \int_0^h (N\delta\varepsilon + T\delta\gamma + M\delta\kappa + D\delta\alpha + B\delta\beta)\,\mathrm{d}x. \tag{5.16}$$

However, evaluating the fine model's internal virtual work is less straightforward, as the distribution of internal forces along both $x-$ and $y-$fibers is not directly known. To overcome this limitation, the relationship between the internal virtual work and the elastic strain energy stored in the cell can be exploited. In fact, for each pure deformation mode, the strain energy $\tilde{U^0}$ was already evaluated (see Eq. (5.5)), and the corresponding internal virtual work follows as

$$\tilde{\mathcal{W}}_i := 2\tilde{U^0}. \tag{5.17}$$

Since $\tilde{\mathcal{W}}_i$ is known for each imposed deformation mode, the generalized internal forces of the equivalent model can be obtained by enforcing the equivalence condition $\tilde{\mathcal{W}}_i = \mathcal{W}_i$.

This leads to the following analytical expressions:

$$
\begin{aligned}
N\left(x_i\right) &= \left(\sum_{j=1}^{2} \tilde{N}_j\right)_i , \\
T\left(x_i\right) &= \left(\sum_{j=1}^{2} \tilde{T}_j\right)_i , \\
M\left(x_i\right) &= \left[\sum_{j=1}^{2} \left(\tilde{M}_j - \tilde{N}_j s_j\right)\right]_i , \\
D\left(x_i\right) &= \left\{\sum_{j=1}^{2} \tilde{T}_j \left[\psi'\left(s_j\right) + \frac{\ell_y^2 \mu_y}{12}\psi'''\left(s_j\right)\right]\right. \\
&\quad \left. + \frac{1}{h}\int_{-\ell_y/2}^{\ell_y/2} \left\{-\tilde{T}_s\left(s\right)\frac{\ell_y^2\mu_y}{12}\psi'''\left(s\right) + \tilde{M}_s\left(s\right)\left[\psi''\left(s\right) + \frac{\ell_y^2\mu_y}{12}\psi''''\left(s\right)\right]\right\} \mathrm{d}s \right\}_i , \\
B\left(x_i\right) &= \left\{\sum_{j=1}^{2} \left\{\tilde{N}_j \psi\left(s_j\right) - \tilde{M}_j \left[\psi'\left(s_j\right) + \frac{\ell_y^2\mu_y}{12}\psi'''\left(s_j\right)\right]\right\}\right. \\
&\quad \left. + \int_{-\ell_y/2}^{\ell_y/2} \left\{-\tilde{T}_s\left(s\right)\frac{\ell_y^2\mu_y}{12}\psi'''\left(s\right) + \tilde{M}_s\left(s\right)\left[\psi''\left(s\right) + \frac{\ell_y^2\mu_y}{12}\psi''''\left(s\right)\right]\right\} \mathrm{d}s \right\}_i ,
\end{aligned}
\tag{5.18}
$$

with $i = 0, 1, \ldots, n_x$ and where, for the sake of clarity, a local coordinate $s \in [-\ell_y/2, \ell_y/2]$ is introduced to parametrize the height of the $i-$th cross-section, and is defined as illustrated in Fig. 5.8. Moreover, $\tilde{N}_j$, $\tilde{T}_j$ and $\tilde{M}_j$ denote the axial force, shear force, and bending moment evaluated at the $j-$th joint of the $i-$th cross-section; while the functions $\tilde{T}_s\left(s\right)$ and $\tilde{M}_s\left(s\right)$ describe the variation of the internal shear force and bending moment along the height of the cross-section and must here be interpreted with respect to the local coordinate system (of each fiber), rather than the global coordinate system (of the microstructure).

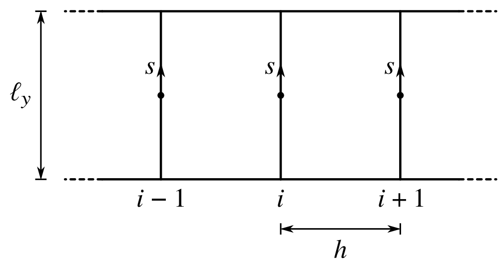

Figure 5.8. Definition of the local coordinate s along the height of the $i-$th cross-section.

5.3.4 Identification of the inertial properties

To identify the inertial properties a representative cell, distinct from that previously employed for the evaluation of the elastic constants, is considered. This cell includes the $y-$fiber belonging to a generic cross-section $\mathcal{D}_i$, together with one half of the $x-$fiber located immediately below and above the cross-section $\mathcal{D}_i$. The fibers' mass is assumed to be lumped at the joints, whose rotational inertia is considered negligible compared to the translational one. As a consequence, only translational inertia effects are retained. The kinetic energy $\tilde{\mathcal{T}}$ of the cell, subjected to a uniform velocity field, is written as

$$\tilde{\mathcal{T}} = \frac{1}{2}\sum_{j=1}^{2} M_j \left(\dot{\tilde{u}}_j^2 + \dot{\tilde{v}}_j^2\right), \tag{5.19}$$

where, analogously to the grain beam formulation, M_j denotes the lumped mass at the $j-$th joint of the cross-section $\mathcal{D}_i$, located at $(\tilde{x}_j, \tilde{y}_j)$, while $\dot{\tilde{u}}_j$ and $\dot{\tilde{v}}_j$ are the corresponding translational velocities. By substituting the displacement map given by Eq. (3.40) into Eq. (5.19), and enforcing the energy equivalence $\tilde{\mathcal{T}} = \mathcal{T}$, where $\mathcal{T}$ is the kinetic energy of a beam segment of length equal to that of the cell, h, the inertial properties of the equivalent beam model (see Eq. 3.30) are obtained.

$$\begin{aligned}
m =&\frac{1}{h}\sum_{j=1}^{2} M_j, & I_x =&\frac{1}{h}\sum_{j=1}^{2} M_j \tilde{x}_j, & I_y =&\frac{1}{h}\sum_{j=1}^{2} M_j \tilde{y}_j,\\
I_\psi =&\frac{1}{h}\sum_{j=1}^{2} M_j \psi\left(\tilde{y}_j\right), & I_{xy} =&\frac{1}{h}\sum_{j=1}^{2} M_j \left(\tilde{x}_j^2 + \tilde{y}_j^2\right), & I_{\psi y} =&\frac{1}{h}\sum_{j=1}^{2} M_j \tilde{y}_j\, \psi\left(\tilde{y}_j\right),\\
I_{\psi\psi} =& \frac{1}{h}\sum_{j=1}^{2} M_j \psi^2\left(\tilde{y}_j\right).
\end{aligned} \tag{5.20}$$

5.4 Numerical results

Numerical results are referred to a grid beam, taken as case study, made of a thermoplastic polymer, namely Acrilonitrile Butadiene Stirene (ABS). The material is characterized by an elastic modulus $E = 2180\mathrm{N/mm}^2$, Poisson coefficient $\nu = 0$ and mass density $\rho = 1040\mathrm{kg/m}^3$. A square shaped dell layout is considered, so that the longitudinal and transverse beams have equal lengths $\ell_y = \ell_x := h$, and all the fibers have square cross-section of side 1.5 mm. Accordingly, when modeled as an assembly of Timoshenko (micro) beams, each fiber exhibits axial, shear and flexural stiffness, denoted as $EA_\nu := EA$, $GA_\nu^* := GA^*$ and $EI_\nu := EI$, respectively. In particular, it is $EA = 4905\,\mathrm{N}$, $GA^* = 2043.75\,\mathrm{N}$ and $EI = 919.69\,\mathrm{Nmm}^2$, where A, A^* and I denote the cross-section area, the shear area, and the second moment of inertia. Of course, in the Euler-Bernoulli formulation, being a non-deformable shear beam model, the shear stiffness is infinite.

The considered boundary conditions are: (i) clamped at A and free at B, case study I, for the static and dynamic analyses; (ii) clamped at $H = A$, B, case study II, for the static analysis; and (iii) clamped at A and constrained by a horizontal roller at B, case study III, for the buckling analysis. The grid beam's microstructure is composed by (micro) Euler-Bernoulli beams for all boundary conditions, except for case study I, which, in statics, is also examined using (micro) Timoshenko beams. The grid beam is composed of $n_x = 40$ cells, with a characteristic size of $h = 10$ mm.

The GBM is validated with an FE model, where the grid beam is modeled as a 2D frame, to assess its ability to accurately reproduce the static, dynamic, and buckling behavior of the metamaterial. In order to evaluate the improvements achieved over existing formulations based on the same homogenization procedure, its predictions are compared with those of the TBM-M.

Moreover, the elastic coefficients of the equivalent beam model are determined through both the analytical and numerical identification procedures of the mixed homogenization approach (see Section 5.3.1 and 5.3.2). However, both procedures yield identical values for all elastic constants. The inertial parameters are, in turn, derived analytically within the same homogenization framework.

5.4.1 Static and dynamic analyses

In this section, the static and free-dynamic responses of the grid beam are analyzed. The static behavior is investigated for case studies I and II, whereas the dynamic analysis is carried out only for case study I.
For the static analysis, no distributed loads are applied to the beam, i.e. $p_x = p_y = c_z = 0$, and the boundary conditions are defined as follows: (i) in case study I, a force directed along the $y-$axis, $P_y = -0.004$ N, is applied ate the free end; (ii) in case study II, a prescribed displacement is imposed at end B, namely $\bar{v} = 1\,\text{mm}$.

Tab. 5.1 and 5.2 report the nonzero elastic coefficients of the GBM and TBM-M elastic operators, respectively, for a microstructure composed of (micro) Euler–Bernoulli or Timoshenko beams. As for the inertial properties, in Tab. 5.3 all the nonzero coefficients of the GBM's mass matrix **M** are reported in which, by retaining only the principal 3×3 submatrix, also the TBM-M's mass matrix are defined.

		Euler-Bernoulli	**Timoshenko**
c_{11}	[N]	9810	9810
c_{22}	[N]	220.73	209.42
c_{24}	[N]	52.97	49.83
c_{25}	[N × mm]	264.87	249.15
c_{33}	[N × mm^2]	247089	247089
c_{35}	[N × mm^2]	−10251.50	−9745.08
c_{44}	[N]	17.13	16.05
c_{45}	[N × mm]	85.64	80.23
c_{55}	[N × mm^2]	1036.92	963.22

Table 5.1. Elastic coefficients of the GBM for a microstructure composed of Euler-Bernoulli and Timoshenko (micro) beams.

From these tables, it becomes apparent that the boundary value problem associated with the TBM-M is diagonal in both the static and dynamic problems, whereas the GBM is characterized by a significant degree of coupling in both cases. Therefore, as discussed in Section 3.2.2, the solution for the static and dynamic analyses of the TBM-M can be

		Euler-Bernoulli	Timoshenko
c_{11}	[N]	9810	9810
c_{22}	[N]	73.57	69.80
c_{33}	$[\mathrm{N} \times \mathrm{mm}^2]$	247089	247089
χ	$[-]$	0.33	0.33

Table 5.2. Elastic coefficients of the TBM-M for a microstructure composed of Euler-Bernoulli and Timoshenko (micro) beams.

obtained in closed form. Conversely, due to the strong coupling among the equations of motion, the analytical solution of the GBM is derived using the Finite Difference Method for which, as an order of magnitude, for case study I the domain is discretized into $L = 1600$ and $L = 480$ elements for the static and dynamic analysis, respectively. Both the detailed formulations are reported in Section 3.2.2 and Appendix A, respectively

To validate the homogenized beam model solution, an FE model, where the geometry is discretized using an extremely fine mesh with a cubic displacement field and a quadratic rotation field, is built. As a reference, the static analysis of case study I involves approximately 36000 degrees of freedom. Furthermore, as previously noted, exact Euler-Bernoulli finite elements are used to model the fibers of the grid beam for all boundary conditions, except in the static analysis of case study I, where exact Timoshenko finite elements are also considered.

m	[kg/mm]	7.02×10^{-9}
I_{xy}	$[\mathrm{kg} \times \mathrm{mm}]$	1.75×10^{-7}
$I_{\psi y}$	[kg]	7.02×10^{-9}
$I_{\psi\psi}$	$[\mathrm{kg} \times \mathrm{mm}]$	2.81×10^{-10}

Table 5.3. Inertial properties of both the equivalent beam model.

Displacement field

The static analysis leads to a comparison between the Equivalent beam model (GBM) and the FE model in terms of: (i) transverse displacement $v(x)$ and rotation $\theta(x)$; (ii) the purely deformative component of the longitudinal displacement evaluated along the beam axis $u_d(x)$; (iii) longitudinal displacement of the grid cross-sections at selected abscissas $x = \bar{x}$; (iv) internal forces, namely the shear force $T(x)$, bending moment $M(x)$, distortional $D(x)$ and bi-distortional $B(x)$ forces. A comparison is also carried out with the Timoshenko Beam Model-Modified (TBM-M), for all quantities that can be captured with its reduced kinematics. In the following figures, the displacements and abscissas are expressed in millimeters (mm), rotations in milliradians (mrad), while the internal forces are expressed in newton (N) and millimeters (mm).

For case study I, excellent agreement is observed among the GBM, TBM-M, and FE solutions for both the microstructure made of Euler-Bernoulli beams (Fig. 5.9a) and

Timoshenko beams (Fig. 5.9b). Such agreement with the TBM-M is fully consistent with its capability to accurately describe the global behavior of the grid beam.

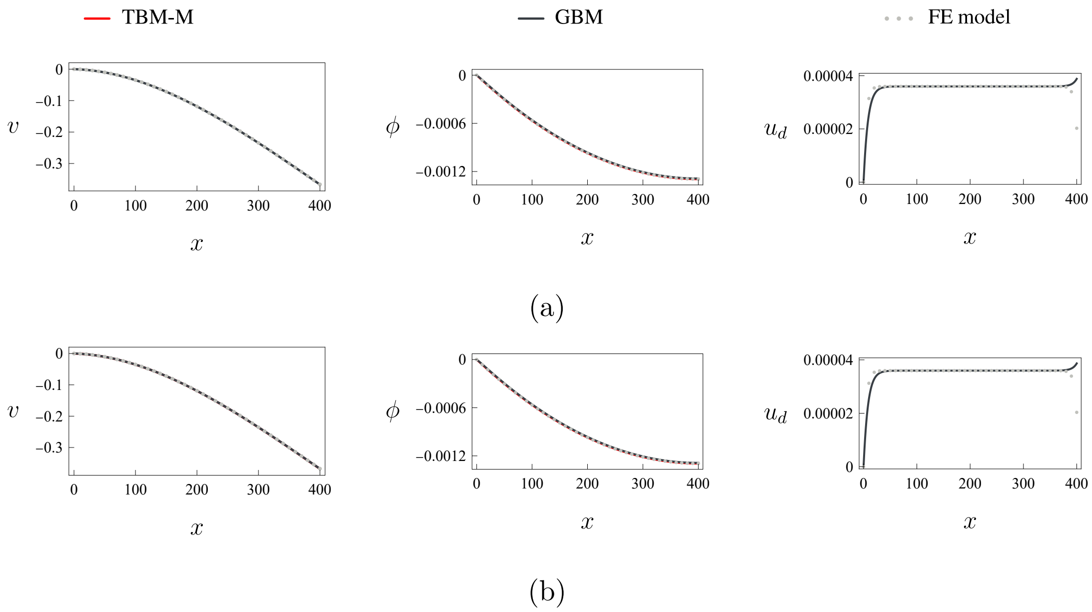

Figure 5.9. Static response of the Equivalent beam models (GBM and TBM-M) vs. the discrete FE model, in terms of transverse displacement, cross-section rotation, and purely deformative component $u_d\,(x)$, for case study I with microstructure composed of: (a) Euler-Bernoulli beams; (b) Timoshenko beams.

Fig. 5.9 shows also the purely deformative component evaluated along the beam axis, $u_d\,(x)$. In this case, the comparison can be made only between the GBM and the FE model. The equivalent beam fits very well the numerical results, except near the free end, where it exhibits a slightly smaller warping amplitude. This discrepancy arises from the modeling assumptions adopted in the FE model. In the solutions shown in Fig. 5.9 the vertical load P_y was applied in the FE model at $(\tilde{x}, \tilde{y}) = (\ell, 0)$. However, enforcing the same load in a statically equivalent manner leads to a different response in the FE model. Fig. 5.10 illustrates two loading configurations that are statically equivalent to the aforementioned case, together with the corresponding results obtained in terms of $u_d\,(x)$. In particular, in Fig. 5.10a half an additional cell is modeled; the vertical force is applied as shown therefore, an additional horizontal force $P_x = P_y/2$ is required to ensure static equivalence with the original loading scheme. Conversely, in the configuration depicted in Fig. 5.10b one additional cell is modeled; the vertical force is applied as shown, and the required additional horizontal force is $P_x = P_y$.

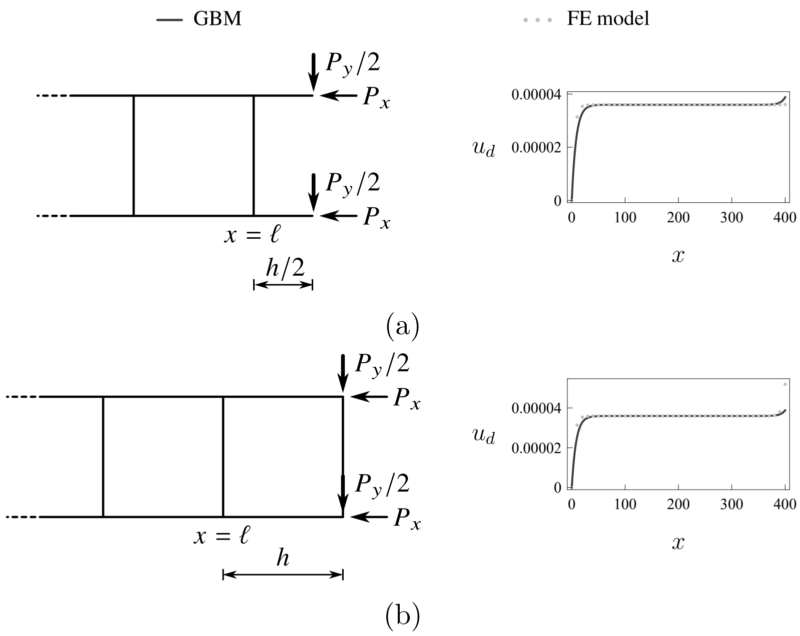

Figure 5.10. Purely deformative component $u_d\,(x)$ evaluated by applying the load through statically equivalent schemes to the case where P_y is applied at $(\tilde{x}, \tilde{y}) = (\ell, 0)$.

These results highlight the significant sensitivity of the FE model to the adopted loading scheme. Nevertheless, this does not compromise the validity of the proposed equivalent beam model, since the observed discrepancies are restricted to the beam ends, precisely where, according to the de Saint Venant's theory, boundary layer effects are expected to occur over a distance approximately equal to the cross-section height, namely h in this case. Beyond this distance, the beam's state of stresses and strains is no longer influenced by the specific distribution of the forces applied to the ends, but only by the characteristics of the stress acting on the bases.

Comparisons can be made also in terms of longitudinal displacement of the grid cross-sections at selected abscissas $x = \bar{x}$. Figures 5.11 and 5.12 show the total displacement $u\,(y)$ at $x = h, \ell/2$, together with its rigid component $u_r\,(y)$ and its purely deformative counterpart $u_d\,(y)$, for a microstructure composed of Euler-Bernoulli and Timoshenko beams, respectively. These figures show that the TBM-M model, which is compared with the GBM and FE model only in terms of $u\,(y)$, as expected, reproduces only on average the total deformation of the cross-section, and this is particularly evident especially at $x = h$ (see Fig. 5.11a and 5.12a). Conversely, the GBM provides an accurate representation of both the rigid and purely deformative components, and therefore of the total deformation. In Fig. 5.11b and 5.12b, it seems that the TBM-M model provides a reasonable approximation of the total deformation at $x = \ell/2$, despite its intrinsic inability to reproduce the purely deformative component. This occurs because, moving away from the free end, the cross-section becomes less free to warp; consequently, its deformative component is not predominant, unlike at $x = \ell$.

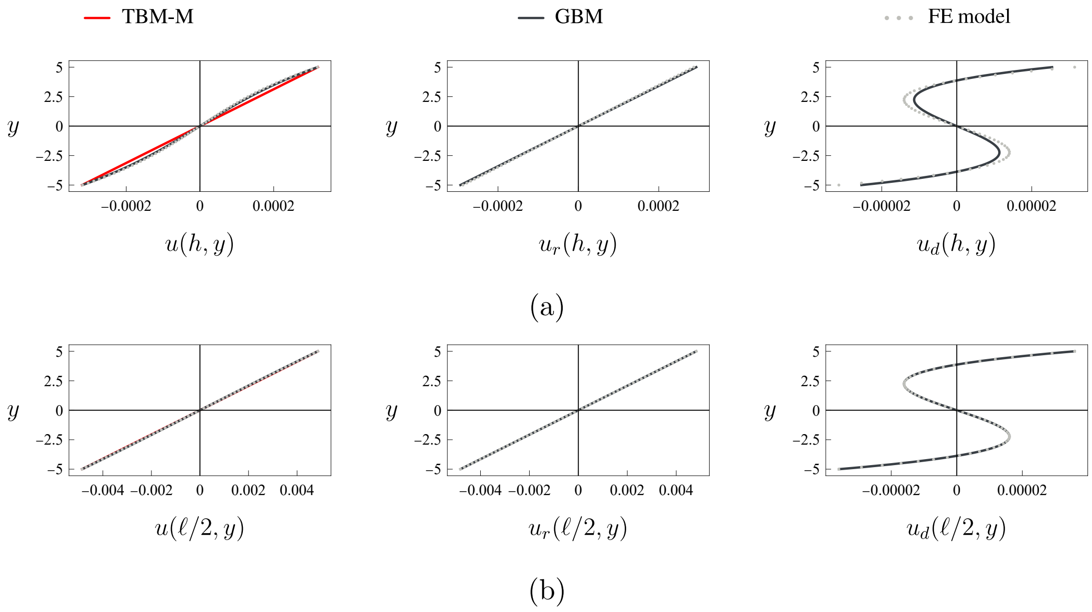

Figure 5.11. Static response of the Equivalent beam models (GBM and TBM-M) vs. the discrete FE model, in terms total displacement $u(y)$ of the cross-section, its rigid component $u_r(y)$ and purely deformative component $u_d(y)$, for case study I with microstructure composed of Euler-Bernoulli beams, at $x = h, \ell/2$ (a,b).

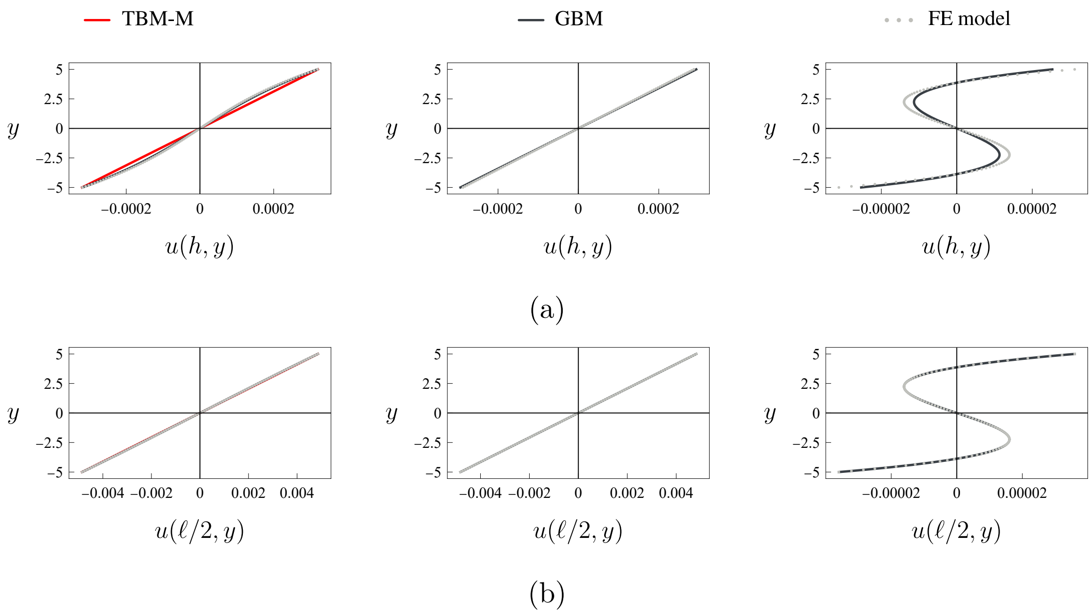

Figure 5.12. Static response of the Equivalent beam models (GBM and TBM-M) vs. the discrete FE model, in terms total displacement $u(y)$ of the cross-section, its rigid component $u_r(y)$ and purely deformative component $u_d(y)$, for case study I with microstructure composed of Timoshenko beams, at $x = h, \ell/2$ (a,b).

Similar considerations can be drawn for case study II (see Fig. 5.13 and 5.14), where the microstructure is composed of Euler-Bernoulli beams. Here, since the beam is clamped at both ends, it cannot warp at abscissas $x = 0, \ell$; therefore, no boundary layer effects arise in the evaluation of the purely deformative component $u_d(x)$.

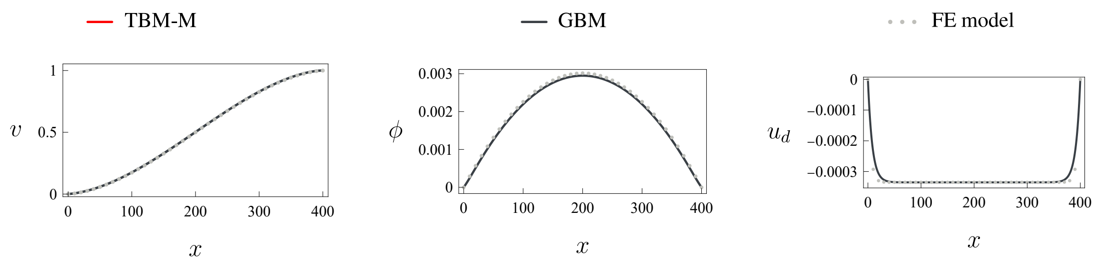

Figure 5.13. Static response of the Equivalent beam models (GBM and TBM-M) vs. the discrete FE model, in terms of transverse displacement, cross-section rotation, and purely deformative component $u_d(x)$, for case study II with microstructure composed of Euler-Bernoulli beams.

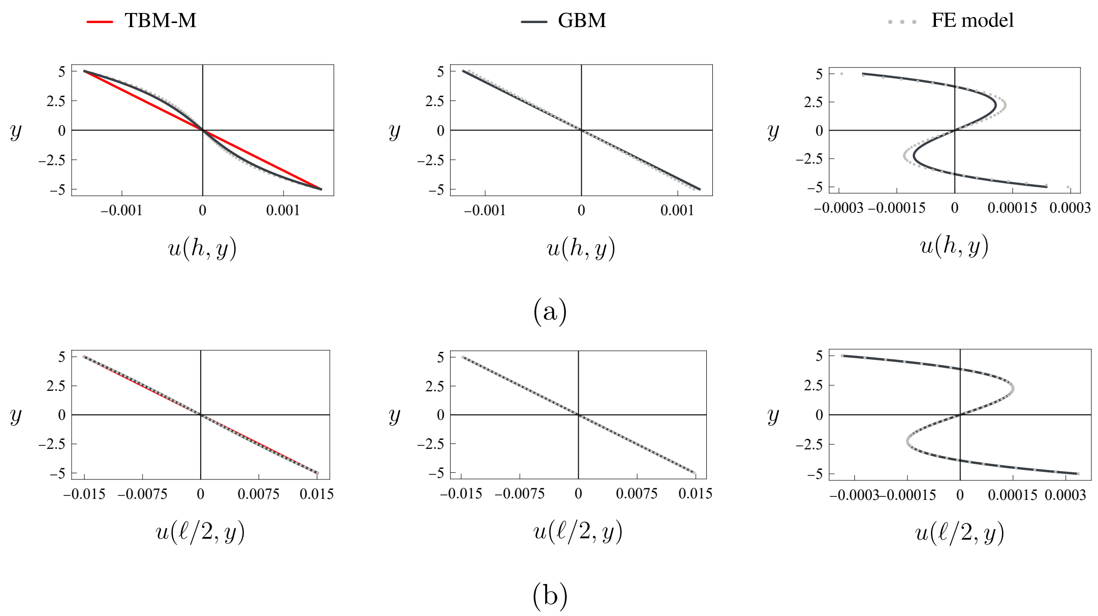

Figure 5.14. Static response of the Equivalent beam models (GBM and TBM-M) vs. the discrete FE model, in terms total displacement $u(y)$ of the cross-section, its rigid component $u_r(y)$ and purely deformative component $u_d(y)$, for case study II with microstructure composed of Euler-Bernoulli beams, at $x = h, \ell/2$ (a,b).

In Fig. 5.15 and Fig. 5.16, are reported the comparison in terms of the internal forces for case study I with microstructure composed of Euler-Bernoulli and Timoshenko beams, respectively. The GBM and the FE model show an excellent agreement for both the shear force $T(x)$ and the bending moment $M(x)$. More interesting, however, is the comparison of the distortional and bi-distortional force. For the distortional force, the equivalent beam reproduces very well the numerical results, except near the free end. This discrepancy originates from the same phenomenon observed for $u_d(x)$, namely from the modeling assumptions adopted in the FE model, where, in this case, the vertical load P_y is applied at $(\tilde{x}, \tilde{y}) = (\ell, 0)$. In fact, when the load is applied using the statically equivalent configurations shown in Fig. 5.10, the distortional response changes and follows the same trend already observed for $u_d(x)$ for the different loading conditions. This confirms that the inconsistency is primarily related to the FE modeling assumptions rather than to a limitation of the equivalent model.

As for the bi-distortional force, both figures show that the 3D and 1D results are shifted by an (almost) constant amount. This behavior stems from the limited number of cells used for the grid beam at hand ($n_x = 40$) which is not greater enough to fully capture the bi-distortional effects. When a greater number of cells is considered, for instance $n_x = 100$, the discrepancy between the two models becomes significantly smaller (see Fig. 5.17). This confirms the well-known principle that the accuracy of homogenization improves as the number of cells in the fine model increases. This means that the GBM for the grid beam made of $n_x = 40$ cells is already able to well capture the fine model behavior in terms of global displacements and cross-section's deformation, whereas the accurate prediction of the bi-distortional force requires a greater number of cells.

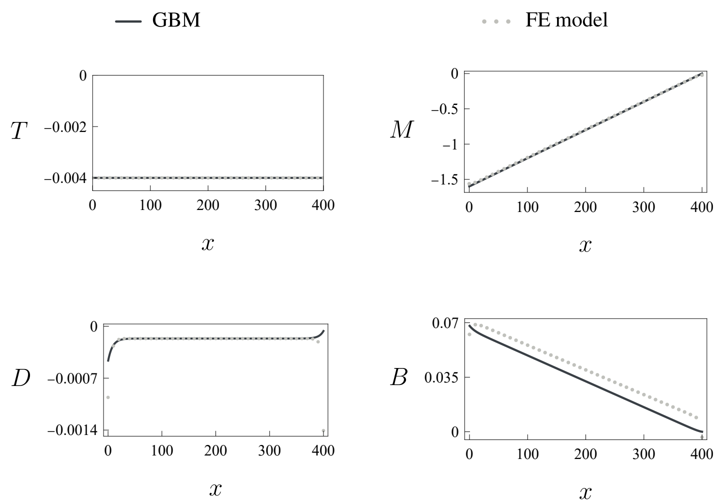

Figure 5.15. Static response of the Equivalent beam model (GBM) vs. the discrete FE model, in terms of internal forces, for case study I with microstructure composed of Euler-Bernoulli beams and $n_x = 40$.

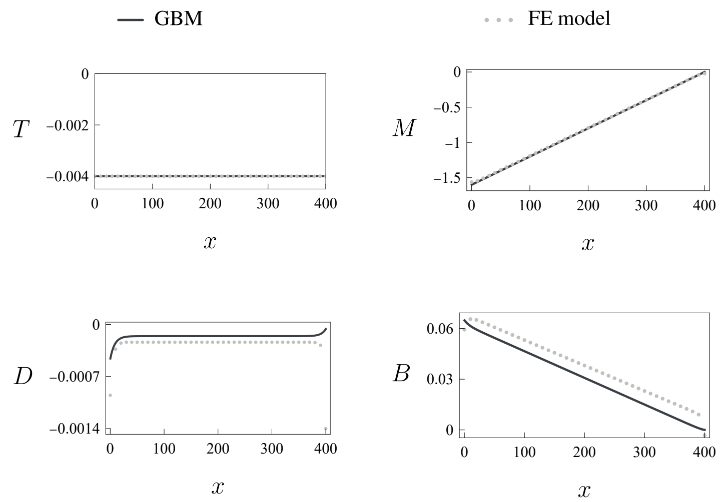

Figure 5.16. Static response of the Equivalent beam models (GBM) vs. the discrete FE model, in terms of internal forces, for case study I with microstructure composed of Timoshenko beams and $n_x = 40$.

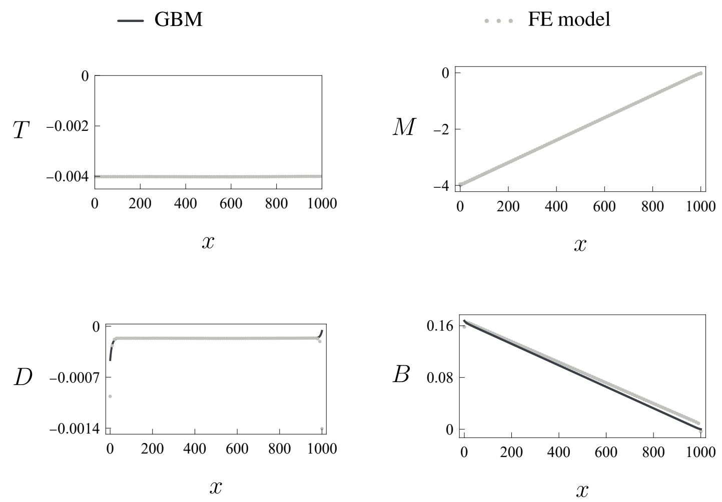

Figure 5.17. Static response of the Equivalent beam model (GBM) vs. the discrete FE model, in terms of internal forces, for case study I with microstructure composed of Euler-Bernoulli beams and $n_x = 100$.

Frequencies and modal shapes

The dynamic behavior of the grid beam is investigated by comparing the results obtained from Equivalent beam model (GBM) and the FE model in terms of: (i) natural frequencies and the corresponding modal shapes; (ii) purely deformative component of the longitudinal displacement evaluated along the beam axis $u_d(x)$; (iii) longitudinal displacement of the grid cross-sections at selected abscissas $x = \bar{x}$. Of course, as for the static analysis, a comparison is carried out also with the TBM-M but only in terms of natural frequencies

and modal shapes, since $u_d(x)$ cannot be captured with its reduced kinematics.
As already mentioned, the dynamic analysis is limited to case study I with microstructure composed of Euler-Bernoulli beams, since the model had already been validated for the Timoshenko microstructure and additional results would have been redundant.
In Tab. 5.4, ω_{TBM-M}, ω_{GBM} and ω_{FE} denote the frequencies obtained with the equivalent beam models TBM-M and GBM, respectively, and the FE one. The last two columns show the percentage differences, defined as $\epsilon_1 = 100\,(\omega_{TBM-M} - \omega_{FE})\,/\omega_{TBM-M}$, $\epsilon_2 = 100\,(\omega_{GBM} - \omega_{FE})\,/\omega_{GBM}$.

Case study	**Mode**	ω_{TBM-M} [rad]	ω_{GBM} [rad]	ω_{FE} [rad]	ϵ_1 [%]	ϵ_2 [%]
I	1	124.39	124.49	123.55	0.68	0.76
	2	629.14	632.11	631.04	-0.30	0.17
	3	1428.73	1440.67	1443.92	-1.06	-0.23
	4	2285.09	2312.81	2323.18	-1.67	-0.45
	5	3156.90	3208.65	3227.42	-2.23	-0.58
	6	4018.94	4104.96	4135.09	-2.89	-0.73

Table 5.4. Angular frequencies of the first six modes for case study I with microstructure composed of Euler-Bernoulli beams. ω_{TBM-M}, ω_{GBM} and ω_{FE} refer to the equivalent beam models TBM-M and GBM, and the FE Model, respectively.

The comparison of the natural frequencies highlights distinct behaviors for the two equivalent beam models. Considering ϵ_1, which measures the discrepancy between the TBM-M and the fine FE model, it is evident that the TBM-M well captures the frequencies for the lower modes. However, the percentage difference increases for the higher modes, a trend already observed for the equivalent model of the grain beam (Section 4.5.1). This behavior arises from scale effects: higher modes correspond to shorter wavelengths, comparable to the scale of the microstructure, so that the microstructure's deformation becomes increasingly significant. Since the TBM-M model accounts for this deformation only on average, greater percentage differences naturally occur for the higher modes.
In contrast, ϵ_2, which compares the GBM frequencies with the FE ones, remains consistently small across all modes. This result reflects the GBM's enhanced capability to reproduce the actual behavior of the cross-section, ensuring accurate prediction even for higher-order modal shapes. For instance, for the sixth mode $\epsilon_1 = -2.89$ whereas $\epsilon_2 = -0.73$; notably, the GBM's percentage difference is essentially the same as in the first mode, whereas the TBM-M's percentage difference is approximately four times larger. These results clearly demonstrate the improved predictive accuracy of the GBM, especially for shorter wavelength modes.
Figures 5.18, 5.19, and 5.20, where the abscissa unit is expressed in millimeters (mm), show the comparison between the equivalent beam models and the FE model for the first three modal shapes, normalized so that $v(\ell) = 1$. As expected, the modal shapes are well captured by both equivalent beam models.

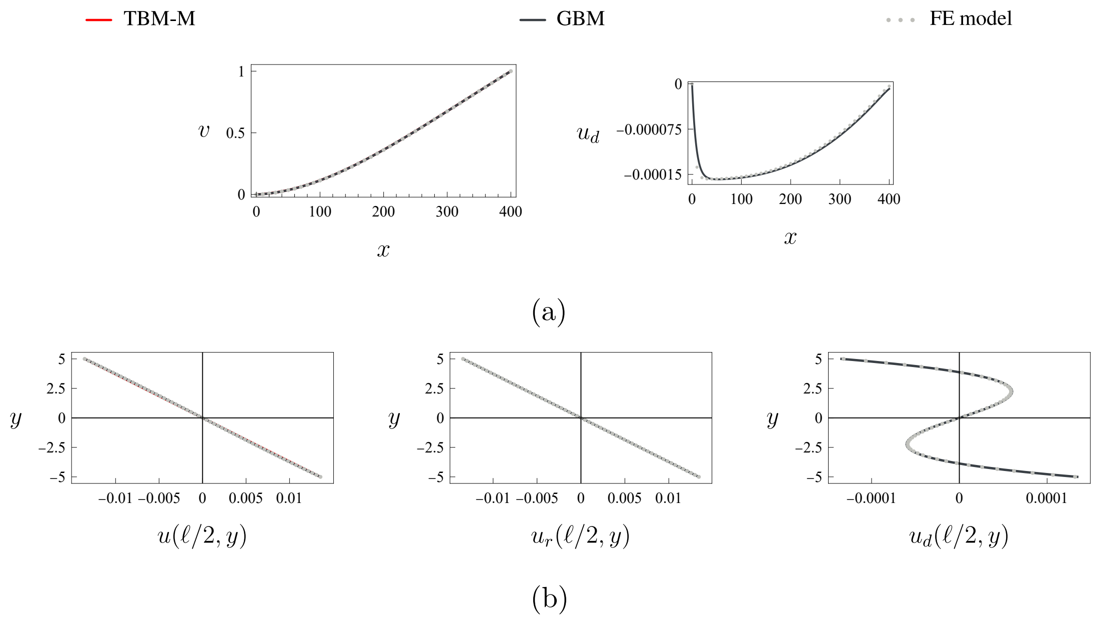

Figure 5.18. Dynamic response of the Equivalent beam models (GBM and TBM-M) vs. the discrete FE model for case study I with microstructure composed of Euler-Bernoulli beams. (a) first modal shape and purely deformative component $u_d\,(x)$. (b) total displacement $u\,(y)$ of the cross-section, its rigid component $u_r\,(y)$ and purely deformative component $u_d\,(y)$ at $x = \ell/2$.

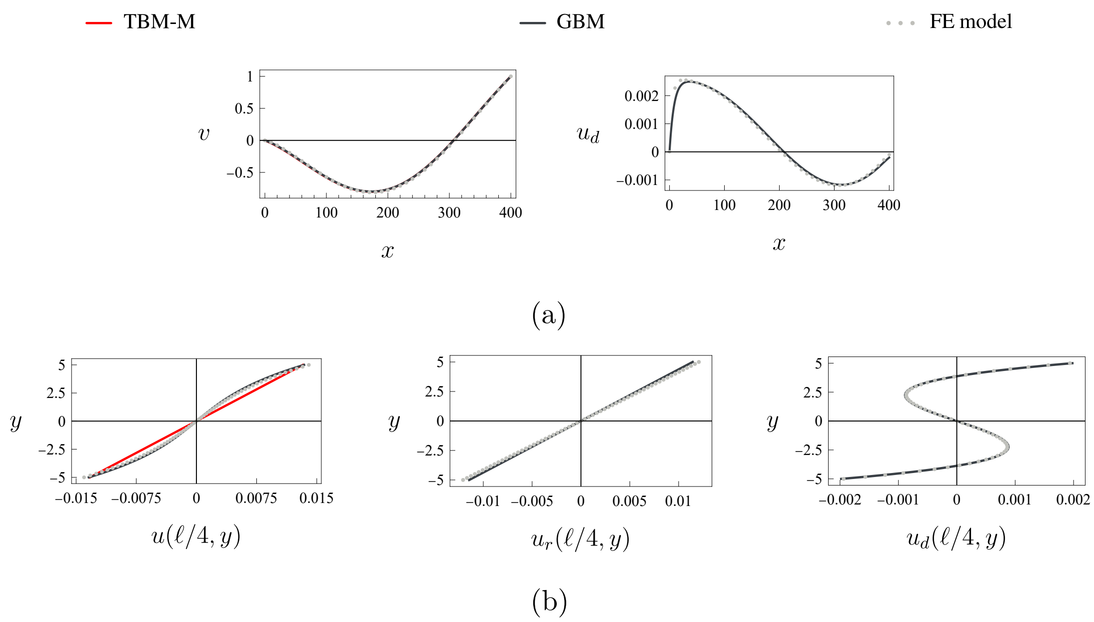

Figure 5.19. Dynamic response of the Equivalent beam models (GBM and TBM-M) vs. the discrete FE model for case study I with microstructure composed of Euler-Bernoulli beams. (a) second modal shape and purely deformative component $u_d\,(x)$. (b) total displacement $u\,(y)$ of the cross-section, its rigid component $u_r\,(y)$ and purely deformative component $u_d\,(y)$ at $x = \ell/4$.

Comparisons are also performed in terms of the longitudinal displacement of the cross-sections at selected abscissas $x = \bar{x}$. In particular, it is carried out at $x = \ell/2$ for odd

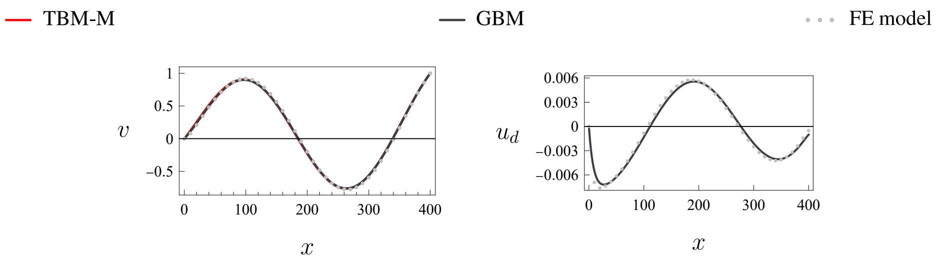

(a)

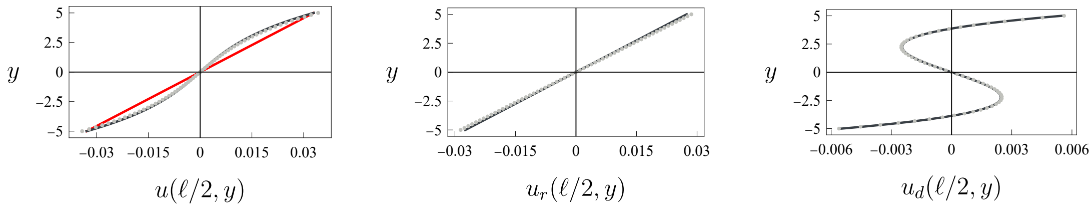

(b)

Figure 5.20. Dynamic response of the Equivalent beam models (GBM and TBM-M) vs. the discrete FE model for case study I with microstructure composed of Euler-Bernoulli beams. (a) third modal shape and purely deformative component $u_d\,(x)$. (b) total displacement $u\,(y)$ of the cross-section, its rigid component $u_r\,(y)$ and purely deformative component $u_d\,(y)$ at $x = \ell/2$.

vibration modes and at $x = \ell/4$ for even one. As expected, the GBM provides an accurate representation of both the rigid and purely deformative components, and therefore of the total displacement as well. For the TBM-M, the comparison can only be made in terms of the total displacement $u\,(y)$, which the model reproduces correctly, once again, on average. An exception occurs for the first vibration mode, where the equivalent model matches the numerical one quite closely rather than merely on average. This behavior arises because the first mode does not strongly activate the cross-section's deformation, making the TBM-M approximation sufficiently accurate for this specific case. Moreover, the comparison of the purely deformative component $u_d\,(x)$ between the GBM and FE model is also reported. Even in the dynamic analysis, the equivalent model is able to faithfully reproduce the numerical trend.

5.4.2 Buckling analysis

The buckling behavior is examined for case study III, namely a beam clamped at A and constrained by a horizontal roller at B, whose microstructure is made of Euler-Bernoulli beams.

In the framework of the equivalent beam model, the elastic operator governing the buckling behavior is expressed as $\mathbf{C} = \mathbf{C}^0 - P\mathbf{C}^*$. The coefficients defining $\mathbf{C}^0$ are already listed in Tab. 5.1 and Tab. 5.2 for the GBM and the TBM-M, respectively, while the coefficients associated with $\mathbf{C}^*$, together with the cell's critical load, are reported in Tab. 5.5 for the two models.

Similarly to what was observed in the static and dynamic problems, these tables clearly show that the degree of coupling among the equilibrium equations allows to obtain a closed-form solution for the TBM-M, previously discussed in Section 3.2.1, but not for the GBM. Consequently, for the latter, the solution is once again derived using the Finite Difference Method, whose formulation is detailed in Appendix A. As an order of magnitude for the finite-difference solution, the domain is discretized into $L = 120$ elements. Moreover, to validate the GBM, an FE model with approximately 3500 degrees of freedom is developed, in which the geometry is discretized using elements with a cubic displacement field and a quadratic rotation field.

		GBM	**TBM-M**
c_{22}^*	$[-]$	1.20	1.02
c_{23}^*	[mm]	5	5
c_{24}^*	$[-]$	4.80×10^{-2}	$-$
c_{25}^*	[mm]	0.24	$-$
c_{33}^*	$[\mathrm{mm}^2]$	33.33	33.33
c_{35}^*	$[\mathrm{mm}^2]$	-2	$-$
c_{44}^*	$[-]$	1.15×10^{-2}	$-$
c_{45}^*	[mm]	5.76×10^{-2}	$-$
c_{55}^*	$[\mathrm{mm}^2]$	0.768	$-$
χ^*	$[-]$	$-$	0.85
P_{cell}	[N]	55.03	71.49

Table 5.5. Elastic coefficients of the GBM and the TBM-M for a microstructure composed of Euler-Bernoulli (micro) beams.

Critical mode

The buckling analysis is investigated by comparing the results obtained from the Equivalent beam model (GBM) and the FE model in terms of: (i) the critical load and mode; (ii) the purely deformative component of the longitudinal displacement evaluated along the beam axis $u_d(x)$; (iii) the longitudinal displacement of the grid cross-sections at selected abscissas $x = \bar{x}$. The comparison is also extended to the TBM-M but only in terms of critical load and mode.

In Tab. 5.6, P_{cr}^{TBM-M}, P_{cr}^{GBM} and P_{cr}^{FE} denote the critical loads obtained with the equivalent beam models TBM-M and GBM, respectively, and the FE model. The percentage differences between these models are also provided and are defined as $\epsilon_1 = 100\left(P_{cr}^{TBM-M} - P_{cr}^{FE}\right)/P_{cr}^{TBM-M}$, $\epsilon_2 = 100\left(P_{cr}^{GBM} - P_{cr}^{FE}\right)/P_{cr}^{GBM}$.

Case study	P_{cr}^{TBM-M} [N]	P_{cr}^{GBM} [N]	P_{cr}^{FE} [N]	ϵ_1 [%]	ϵ_2 [%]
III	21.19	21.20	21.47	-1.32	-1.27

Table 5.6. Critical loads for case study III of the Equivalent beam models (GBM and TBM-M) vs. the discrete FE model.

From Tab. 5.6, it can be observed that the critical loads predicted by the two equivalent beam models are very close to each other. The percentage differences ϵ_1 and ϵ_2, which quantify the differences between the TBM-M and GBM results from the FE solution, are almost identical, confirming the good capability of both models to predict the critical load. The corresponding critical mode is shown in Fig. 5.21, where both the equivalent beam model's fit the solution obtained from the FE model. Here, the abscissa is expressed in millimeters (mm) and the mode has been normalized in order to obtain $v = 1$ at the point of maximum displacement.

At first sight, these results might suggest that the GBM does not provide a substantial improvement over the TBM-M, but this would be a misleading conclusion. The TBM-M is indeed known to provide a reasonable approximation of the global buckling behavior of the metamaterial. Nevertheless, by examining the longitudinal displacement of the grid cross-section at abscissa $x = \ell/2$ reported in Fig. 5.21b, it becomes evident, as already seen for the static and dynamic analyses, that the TBM-M only captures the average deformation of the cross-section, whereas the GBM also reproduces the purely deformative component, thereby providing a more consistent description of the actual deformation.

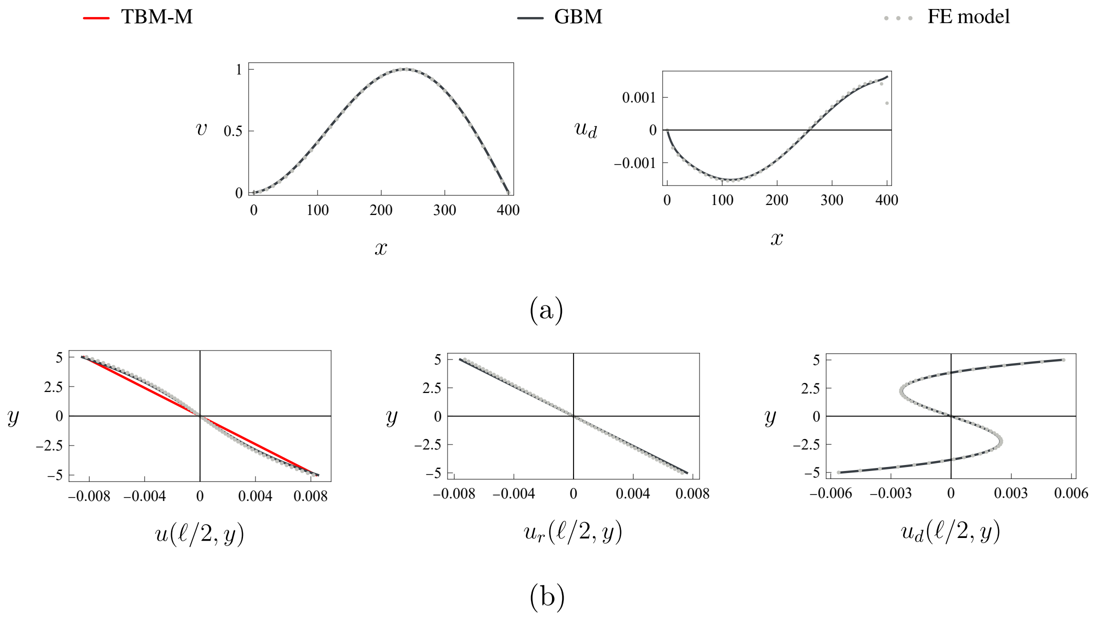

Figure 5.21. Buckling response of the Equivalent beam models (GBM and TBM-M) vs. the discrete FE model for case study III with microstructure composed of Euler-Bernoulli beams. (a) critical mode and purely deformative component $u_d\,(x)$. (b) total displacement $u\,(y)$ of the cross-section, its rigid component $u_r\,(y)$ and purely deformative component $u_d\,(y)$ at $x = \ell/2$.

Fig. 5.21a also reports the purely deformative component $u_d\,(x)$. Here, the comparison can be performed only between the GBM and the FE model. As observed in the static analysis, the equivalent beam provides an excellent agreement with the numerical results, except near the free end, where the FE solution exhibits a slightly smaller warping amplitude. This minor discrepancy arises from the modeling choice, according to which the instability load was chosen to be applied at $(\tilde{x}, \tilde{y}) = (\ell, 0)$, and in any case it occurs exactly where a boundary layer effect is expected. Therefore, it does not compromise the validity of the analytical solution.

Chapter 6

Conclusions and perspectives

In this thesis, a general framework for the analysis of beam-like structures was proposed. Two metamaterials embedded in a 2D space, the grain and grid beam, were investigated with the aim of developing equivalent models capable of capturing their mechanical behavior through a mixed homogenization technique. The latter is based on the energy equivalence between the cell of the periodic grain beam and a segment of the equivalent beam, under the same point-wise displacement fields.
The proposed models are developed to mitigate the computational effort typically required by finite element analyses while still capturing the key deformation mechanisms governed by the microstructure, whenever present. In the following, the grain beam and the grid beam are examined separately.

Grain beam

A Timoshenko-like equivalent beam model has been formulated to analyze the static, dynamic, and buckling behavior of grain beams, and then validated, in static, with a preliminary experimental test.
The elastic constants have been determined under the assumption of a rigid cross-section (in plane and out of plane) using with both analytical and numerical identification procedures, and the influence of the deformability of the grain on the constitutive matrix has been highlighted. A qualitative analysis, grounded on the analytical identification procedure, has revealed the dependence of the elastic coefficients upon properly defined non dimensional parameters, such as the cell aspect ratio and the slenderness of horizontal and vertical fibers. This is believed to be an important result in terms of designing the microstructure of grain beams in order to achieve a targeted macroscopic response. Moreover, the inertial properties have been evaluated through an analytical approach.
The chirality of the grain metamaterial has also been highlighted by comparing the analytical and numerical static responses of a grain beam with those of a classical Timoshenko beam. The effectiveness and the limits of applicability of the Timoshenko-like equivalent beam model have been discussed through numerical analyses, carried out on some grain beams, taken as case studies.

The following conclusions are drawn.

1. A good agreement between the elastic coefficients obtained through both the analytical and numerical identification procedures is detected, particularly in the cases of thin cells.

2. A good agreement is also detected by comparing the solutions obtained from the static, dynamic, and buckling analyses of the Equivalent beam model (AB) with those obtained with the FE models (Beams) and (Cauchy). Therefore, the equivalent beam model is effective in describing the mechanical behavior of grain beams.

3. Numerical identification (NC) of the constitutive matrix of the Equivalent beam model provides an excellent agreement in terms of static response in both cases of thin and thick cells.

4. Although the test is entirely preliminary and would require repetition on a larger number of specimens, an excellent agreement is observed among the experimental result, Equivalent beam model (NC), and the he FE models (Cahuchy-NM) and (Cauchy-EM). This consistency confirms the accuracy of the equivalent model in reproducing the physical response of the metamaterial.

The main perspective of this work on grain beam concerns accounting for geometric and constitutive nonlinearities, which are absent in the developed model (based on linear kinematics and linear elasticity), and would require further investigation. Future research will also address the design and analysis of structures obtained by assembling chiral objects, so that particular macroscopic behaviors can be achieved. From an experimental point of view, a systematic experimental campaign conducted on a larger number of specimens is envisaged to further validate the equivalent beam model by assessing its robustness and predictive capabilities across different geometric configurations.

Grid beam

The mechanical behavior of a grid beam, in terms of static, dynamic, and buckling response, has been investigated under the assumption of an in plane rigid but out of plane deformable cross-section, thereby enabling the of warping phenomenon. Since this effect is typically neglected in classical formulations such as the Euler-Bernoulli and Timoshenko theories, a generalized beam model has been formulated as an equivalent representation in which additional kinematic variables are introduced specifically to account for the out of plane deformability.

The constitutive law of the generalized beam model has been determined through both analytical and numerical procedures within the mixed homogenization framework. The model has also been completed by identifying the generalized internal and external forces of the equivalent beam model, ensuring full consistency with the fine (microstructured) model, and by analytically determining the inertial coefficients. The equivalent model has been validated by comparing its predictions with those obtained from FE simulations. Particular attention has been devoted to assessing the improvements offered by the equivalent beam model developed in this thesis, denoted as the Generalized Beam Model (GBM), with respect to a model already available in the literature, which likewise relies on the mixed homogenization technique, denoted as the Timoshenko Beam Model-Modified (TBM-M).

The following conclusions are drawn.

1. A complete agreement between the elastic coefficients obtained through both analytical and numerical identification procedures is detected.
2. The generalized equivalent beam model is effective in describing the static, dynamic, and buckling behavior of grid beams, successfully capturing both the global response and the local deformative mechanisms induced by cross-section warping.
3. An excellent agreement is detected when comparing the results obtained from the generalized beam model with those obtained from the FE simulations, for all the investigated boundary conditions and loading scenarios.
4. A significantly improved description of the cross-section deformability is detected when comparing the GBM with the TBM-M. While the latter captures only the average deformation of the cross-section, the former also accounts for the purely deformative components, providing a more consistent representation of the mechanical behavior.

The main perspective of this work on grid beams concerns the extension of the proposed model to configurations characterized by a higher number of frames. Further developments will focus on the experimental validation of the theoretical predictions through systematic experimental campaigns supported by Digital Image Correlation (DIC) technique, enabling a detailed analysis of deformation mechanisms. Moreover, further improvements of the generalized beam model are envisaged through the inclusion of additional warping modes, since only a single warping mode has been considered in the present formulation.

Overall, the work carried out demonstrates that:

- equivalent models derived through mixed homogenization provide an effective framework for representing metamaterials;
- a substantial reduction in computational cost can be achieved without compromising predictive accuracy;
- the introduction of suitable additional kinematic variables is required whenever the microstructure is studied assuming a out of plane deformable cross-section;
- the proposed approach provides a solid basis for future extensions to alternative microstructures.

Chapter A

Solution of the boundary value problem

Analytical solution

When Eq. (3.10) is specialized for the grain beam, i.e. a beam whose constitutive equation is Eq. (4.4), in extended form, it reads:

$$\begin{aligned} c_{11}u'' + c_{12}\left(v'' - \theta'\right) + p_x &= 0, \\ c_{12}u'' + c_{22}\left(v'' - \theta'\right) + p_y &= 0, \\ c_{33}\theta'' + c_{12}u' + c_{22}\left(v' - \theta\right) + c_z &= 0. \end{aligned} \tag{A.1}$$

The solution of this latter is the sum of the general solution of the homogeneous counterpart of Eq. (A.1) and the particular solution of the non-homogeneous Eq. (A.1). The general solution depends on arbitrary constants C_i $(i = 1, ..., 6)$, determined once the boundary conditions are enforced, namely Eqs. (3.10b) and (3.10c). The particular solution is easily evaluated once the loads are specified. In particular, for the case at hand it is $\mathbf{p} = \mathbf{0}$ and $\bar{\mathbf{u}}_B = (\bar{u}, \bar{v}, 0)^T$, so that the solution of the static problem (A.1) is found to be:

$$\begin{aligned} u\left(x\right) &= \bar{u}\frac{x}{\ell}, \\ v\left(x\right) &= \frac{x\left[-c_{12}\,\bar{u}\left(\ell - 2x\right)\left(\ell - x\right) + c_{22}\,\bar{v}\,x\left(3\ell - 2x\right) + 12c_{33}\,\bar{v}\right]}{\ell\left(c_{22}\,\ell^2 + 12c_{33}\right)}, \\ \theta\left(x\right) &= \frac{6x\left(\ell - x\right)\left(c_{12}\,\bar{u} + c_{22}\,\bar{v}\right)}{\ell\left(c_{22}\,\ell^2 + 12c_{33}\right)}. \end{aligned} \tag{A.2}$$

Numerical solution

The solutions of the static, free dynamic, and buckling problems are briefly outlined here according to the Finite Differences Method. The domain $x \in [0, \ell]$ is divided in L elements and $L+1$ nodes of coordinates $x_i = i\,\Delta$ with $i = 0, 1, \ldots, L$ and $\Delta = \ell/L$. However, when required to impose boundary conditions at the beam ends $H = A$, B, dummy nodes are added at $x_{-1} = -\Delta$ and $x_{L+1} = (L+1)\,\Delta$, respectively. Using central finite differences, the derivatives of the displacement field are approximated as:

$$\mathbf{u}_i = \mathbf{u}\left(x_i\right), \quad \mathbf{u}_i' = \frac{\mathbf{u}_{i+1} - \mathbf{u}_{i-1}}{2\Delta}, \quad \mathbf{u}_i'' = \frac{\mathbf{u}_{i+1} - 2\mathbf{u}_i + \mathbf{u}_{i-1}}{\Delta^2}. \tag{A.3}$$

Thanks to Eq. (A.3), the boundary value problem, which is usually a system of partial differential equations, is transformed into an algebraic system, which is notably easier to solve. The finite difference method has been adopted to solve the static problem for the grid beam, and the dynamic and buckling problem for both the grain beam and the grid beam. In the following, the algebraic formulations are specialized according to the problem under consideration.

Static analysis

The static response of the grid beam is obtained by letting $\mathbf{M} = \mathbf{0}$ and $\mathbf{p} = \mathbf{0}$ in Eq. (3.29). In the following, the reduced algebraic system of the boundary value problem (Eqs. (3.29), (3.31) and (3.33)), for two boundary conditions, are reported:

- clamped at A and free at B with a force P_y applied at B;

$$\begin{aligned} \mathbf{u}_0 &= \mathbf{0}, \\ \left(\frac{\mathbf{K}_2}{\Delta^2} - \frac{\mathbf{K}_1}{2\Delta}\right)\mathbf{u}_{i-1} + \left(\mathbf{K}_0 - \frac{2\mathbf{K}_2}{\Delta^2}\right)\mathbf{u}_i + \left(\frac{\mathbf{K}_2}{\Delta^2} + \frac{\mathbf{K}_1}{2\Delta}\right)\mathbf{u}_{i+1} &= \mathbf{0}, \quad i = 1, \dots, L \\ -\frac{\mathbf{B}_1}{2\Delta}\mathbf{u}_{L-1} + \mathbf{B}_0\mathbf{u}_L + \frac{\mathbf{B}_1}{2\Delta}\mathbf{u}_{L+1} &= \mathbf{P}. \end{aligned} \tag{A.4}$$

- clamped at $H = A$, B with a prescribed displacement at B;

$$\begin{aligned} \mathbf{u}_0 &= \mathbf{0}, \\ \left(\frac{\mathbf{K}_2}{\Delta^2} - \frac{\mathbf{K}_1}{2\Delta}\right)\mathbf{u}_{i-1} + \left(\mathbf{K}_0 - \frac{2\mathbf{K}_2}{\Delta^2}\right)\mathbf{u}_i + \left(\frac{\mathbf{K}_2}{\Delta^2} + \frac{\mathbf{K}_1}{2\Delta}\right)\mathbf{u}_{i+1} &= \mathbf{0}, \qquad i = 1, \dots, L-1 \\ \mathbf{u}_L &= \bar{\mathbf{u}}_B, \end{aligned} \tag{A.5}$$

Eqs. (A.4) and (A.5) can be recast in compact form

$$\boldsymbol{K}\boldsymbol{u} = \boldsymbol{s}, \tag{A.6}$$

where, here and in the following, $\boldsymbol{u}$ is the vector of unknown displacements, $\boldsymbol{s}$ collects the prescribed displacements, and $\boldsymbol{K}$ is the (discrete) stiffness matrix of dimensions $4\,(L+2) \times 4\,(L+2)$ and $4\,(L+1) \times 4\,(L+1)$, for the first and the second boundary condition at hand, respectively. Eq. (A.6) thus provide the discrete counterpart of the boundary value problem. The resulting linear systems are solved by direct inversion of the associated algebraic relations.

Free dynamic analysis

The free dynamic eigenvalue problem is carried out by letting $\mathbf{p} = \mathbf{0}$ and $\mathbf{u} = \hat{\mathbf{u}}\,(x)\,e^{\lambda t}$ in Eqs. (3.10) and Eqs. (3.29), for the grain and grid beam, respectively. Here, λ and $\hat{\mathbf{u}}\,(x)$ are the eigenvalues and eigenvectors of the system, respectively. This substitution leads to a (spatial) boundary value problem whose closed-form solution is theoretically attainable, but requires the numerical solution of the dispersion relation between the eigenvalue λ and the wave-number μ.

For this reason, a numerical approach based on the Finite Difference Method is adopted to analyze the free-dynamic response of both the grain and the grid beam. Two boundary conditions are analyzed:

- clamped at $H = A$, B, for the grain beam for which the (spatial) boundary value problem is written as

$$\begin{aligned} -\lambda^2 \mathbf{M}\hat{\mathbf{u}} + \mathbf{K}_2\hat{\mathbf{u}}'' + \mathbf{K}_1\hat{\mathbf{u}}' + \mathbf{K}_0\hat{\mathbf{u}} &= \mathbf{0}, \\ \hat{\mathbf{u}}_H &= \mathbf{0}. \end{aligned} \tag{A.7}$$

  which, thanks to the discretization (Eq. (A.3)), is reduced to the following algebraic system.

$$\begin{aligned} \hat{\mathbf{u}}_0 &= \mathbf{0}, \\ \left(\frac{\mathbf{K}_2}{\Delta^2} - \frac{\mathbf{K}_1}{2\Delta}\right)\hat{\mathbf{u}}_{i-1} + \left(\mathbf{K}_0 - \frac{2\mathbf{K}_2}{\Delta^2}\right)\hat{\mathbf{u}}_i + \left(\frac{\mathbf{K}_2}{\Delta^2} + \frac{\mathbf{K}_1}{2\Delta}\right)\hat{\mathbf{u}}_{i+1} - \lambda^2\mathbf{M}\hat{\mathbf{u}}_i &= \mathbf{0}, \quad i = 1, \ldots, L-1 \\ \hat{\mathbf{u}}_L &= \mathbf{0}. \end{aligned} \tag{A.8}$$

- clamped at A and free at B, for the grid beam for which the (spatial) boundary value problem reads

$$\begin{aligned} -\lambda^2 \mathbf{M}\hat{\mathbf{u}} + \mathbf{K}_2\hat{\mathbf{u}}'' + \mathbf{K}_1\hat{\mathbf{u}}' + \mathbf{K}_0\hat{\mathbf{u}} &= \mathbf{0}, \\ \hat{\mathbf{u}}_A &= \mathbf{0} \\ \mathbf{B}_1\hat{\mathbf{u}}_B' + \mathbf{B}_0\hat{\mathbf{u}}_B &= \mathbf{0}, \end{aligned} \tag{A.9}$$

  which, after the discretization, becomes the following

$$\begin{aligned} \hat{\mathbf{u}}_0 &= \mathbf{0}, \\ \left(\frac{\mathbf{K}_2}{\Delta^2} - \frac{\mathbf{K}_1}{2\Delta}\right)\hat{\mathbf{u}}_{i-1} + \left(\mathbf{K}_0 - \frac{2\mathbf{K}_2}{\Delta^2}\right)\hat{\mathbf{u}}_i + \left(\frac{\mathbf{K}_2}{\Delta^2} + \frac{\mathbf{K}_1}{2\Delta}\right)\hat{\mathbf{u}}_{i+1} - \lambda^2\mathbf{M}\hat{\mathbf{u}}_i &= \mathbf{0}, \quad i = 1, \ldots, L \\ -\frac{\mathbf{B}_1}{2\Delta}\hat{\mathbf{u}}_{L-1} + \mathbf{B}_0\hat{\mathbf{u}}_L + \frac{\mathbf{B}_1}{2\Delta}\hat{\mathbf{u}}_{L+1} &= \mathbf{0}. \end{aligned} \tag{A.10}$$

Eqs. (A.8) and (A.10) can be recast in the compact form

$$\left(\boldsymbol{K} - \lambda^2\boldsymbol{M}\right)\boldsymbol{u} = \mathbf{0} \quad , \tag{A.11}$$

where $\boldsymbol{M}$ is the (discrete) mass matrix which, together with the stiffness matrix $\boldsymbol{K}$, has dimensions $3\,(L+1) \times 3\,(L+1)$ and $4\,(L+2) \times 4\,(L+2)$, for the two cases at hand, respectively. Eq. (A.11) provides the discrete counterpart of the continuous eigenvalue problem and can be solved by using standard numerical algorithms.

Buckling analysis

The solution to the buckling analysis it is carried out for two boundary conditions:

- clamped at A and constrained by a horizontal slider at B, for the grain beam;
- clamped at A and constrained by a horizontal roller at B, for the grid beam.

In both cases, the boundary value problem (see Eqs. (3.16) and (3.37), respectively) reduces to the algebraic system:

$$\begin{aligned} \mathbf{u}_0 &= \mathbf{0}, \\ \left(\frac{\mathbf{K}_2}{\Delta^2} - \frac{\mathbf{K}_1}{2\Delta}\right)\mathbf{u}_{i-1} + \left(\mathbf{K}_0 - \frac{2\mathbf{K}_2}{\Delta^2}\right)\mathbf{u}_i + \left(\frac{\mathbf{K}_2}{\Delta^2} + \frac{\mathbf{K}_1}{2\Delta}\right)\mathbf{u}_{i+1} &= \mathbf{0}, \quad i = 1, \ldots, L \\ -\frac{\mathbf{B}_1}{2\Delta}\mathbf{u}_{L-1} + \mathbf{B}_0\mathbf{u}_L + \frac{\mathbf{B}_1}{2\Delta}\mathbf{u}_{L+1} &= \mathbf{0}, \end{aligned} \tag{A.12}$$

which in compact form reads as follows

$$\left(\boldsymbol{K}_e - \mu \boldsymbol{K}_g\right)\boldsymbol{u} = \mathbf{0}, \tag{A.13}$$

where $\boldsymbol{K}_e$ and $\boldsymbol{K}_g$ are the (discrete) elastic and the geometric stiffness matrices of dimensions $3\,(L+2) \times 3\,(L+2)$ for the grain beam and $4\,(L+2) \times 4\,(L+2)$ for the grid beam, respectively. The eigenvalue problem (Eq. (A.13)) admits m real roots. Among these, the smallest positive value, μ_c, is the critical load at which global instability occurs. The associated eigenvector, u_c, is the critical mode.

Chapter B

Analytical expression of the constitutive matrices

Grain beam

The analytical expression of the grain beam coefficients of the constitutive matrix $\mathbf{C}$ (Eq. (3.2)) for the case $t_x \neq t_y$ is first reported. For the elastic counterpart $\mathbf{C}^0$, the coefficients are:

$$
\begin{aligned}
c_{11} &= \frac{12EA_xEI_xEI_yh\left[\left(4+\mu_x\right)EA_y\ell_x^3+6EI_x\ell_y\right]}{d},\\
c_{12} &= -\frac{36EA_xEA_yEI_xEI_yh\ell_x^2\ell_y}{d}.\\
c_{22} &= \frac{6EA_yEI_xh\left[\left(1+\mu_y\right)EA_xEI_x\ell_y^3+6EA_xEI_y\ell_x\ell_y^2+24EI_xEI_y\ell_x\right]}{d},\\
c_{33} &= \frac{EI_xEI_yh}{EI_x\ell_y+2EI_y\ell_x},
\end{aligned}
\tag{B.1}
$$

where $\mu_\nu := 12EI_\nu/GA_\nu^*\ell_\nu^2$ $(\nu = x, y)$ is the non-dimensional stiffness ratio and

$$
\begin{aligned}
d := {} & EA_y\ell_x^3\left\{EI_x\left(4+\mu_x\right)\left[\left(1+\mu_y\right)EA_x\ell_y^3+24EI_y\ell_x\right]+6\left(1+\mu_x\right)EA_xEI_y\ell_x\ell_y^2\right\}\\
& +6EI_x\ell_y\left[\left(1+\mu_y\right)EA_xEI_x\ell_y^3+6EA_xEI_y\ell_x\ell_y^2+24EI_xEI_y\ell_x\right].
\end{aligned}
\tag{B.2}
$$

The coefficients of the geometric part $\mathbf{C}^*$, instead, are given by:

$$
\begin{aligned}
c^*_{11} = & -\frac{2EA_x^2 h\ell_y^2}{5d^2}\Big\{-36EI_x^2\ell_y^2\Big[\zeta\, EI_x^2\ell_y^3\,(3+5\mu_y)+30\zeta\, EI_xEI_y\ell_x\ell_y^2\,(1+\mu_y)\\
& +30EI_y^2\ell_x^2\,(2\ell_x+3\zeta\ell_y)\Big]-12EA_yEI_x\ell_x^3\ell_y\Big[15\zeta\, EI_xEI_y\ell_x\ell_y^2\,(5+2\mu_x)\,(1+\mu_y)\\
& +\zeta\, EI_x^2\ell_y^3\,(4+\mu_x)\,(3+5\mu_y)+15EI_y^2\ell_x^2\,(1+\mu_x)\,(\ell_x+6\zeta\ell_y)\Big]\\
& +EA_y^2\ell_x^6\Big\{-30\zeta\, EI_xEI_y\ell_x\ell_y^2\,(1+\mu_x)\,(4+\mu_x)\,(1+\mu_y)-\zeta EI_x^2\ell_y^3\,(4+\mu_x)^2\,(3+5\mu_y)\\
& +6EI_y^2\ell_x^2\Big\{\ell_x\,[-4-5\mu_x\,(1-\mu_x)]-15\ell_y\zeta\,(1+\mu_x)^2\Big\}\Big\}\Big\}\,,\\
c^*_{12} = & \frac{3EA_xEA_yh\ell_x^2\ell_y}{5d^2}\Big\{EA_yEI_y\ell_x^5\Big\{-6EA_xEI_y\ell_x\ell_y^2\Big(1-5\mu_x^2\Big)+EI_x\,[4+5\mu_x\,(1+\mu_x)]\\
& \Big[24EI_y\ell_x+EA_x\ell_y^3\,(1+\mu_y)\Big]\Big\}+EA_yEI_x\ell_x^3\ell_y\zeta\Big[720EI_y^2\ell_x^2\,(1+\mu_x)\\
& +120EI_xEI_y\ell_x\ell_y\,(4+\mu_x)\,(1+\mu_y)+EA_xEI_x\ell_y^4\,(4+\mu_x)\Big(5\mu_y^2-1\Big)\Big]\\
& +6EI_x\ell_y\Big\{5EI_y\ell_x^2\Big\{6EA_xEI_y\ell_x\ell_y^2\,(1+\mu_x)+EI_x\,(5+\mu_x)\Big[24EI_y\ell_x+EA_x\ell_y^3\,(1+\mu_y)\Big]\Big\}\\
& +EI_x\ell_y\zeta\Big[720EI_y^2\ell_x^2+120EI_xEI_y\ell_x\ell_y\,(1+\mu_y)+EA_xEI_x\ell_y^4\Big(5\mu_y^2-1\Big)\Big]\Big\}\Big\}\,,\\
c^*_{13} = & \frac{EA_xh\ell_y^2}{2d}\Big\{36EI_xEI_y\ell_x^2+6\zeta\, EI_x\ell_y\,[6EI_y\ell_x+EI_x\ell_y\,(1+\mu_y)]\\
& +\zeta\, EA_y\ell_x^3\,[6EI_y\ell_x\,(1+\mu_x)+EI_x\ell_y\,(4+\mu_x)\,(1+\mu_y)]\Big\}\,,\\
c^*_{22} = & \frac{EA_y^2h\ell_x^4}{5d^2}\Big\{36EA_x^2EI_y^2\ell_x^3\ell_y^4\,(3+5\mu_x)+6EA_xEI_xEI_y\ell_x^2\ell_y^2\,(21+25\mu_x)\\
& \Big[24EI_y\ell_x+EA_x\ell_y^3\,(1+\mu_y)\Big]+EI_x^2\Big\{4\ell_x\,(12+5\mu_x)\Big[24EI_y\ell_x+EA_x\ell_y^3\,(1+\mu_y)\Big]^2\\
& +9\ell_y\zeta\Big[2880EI_y^2\ell_x^2+EA_x^2\ell_y^6\Big(1-5\mu_y^2\Big)\Big]\Big\}\Big\}\,,\\
c^*_{23} = & \frac{EA_yh\ell_x^3}{2d}\Big\{6EA_xEI_y\ell_x\ell_y^2\,(1+\mu_x)+EI_x\,(4+\mu_x)\Big[EA_x\ell_y^3\,(1+\mu_y)+24EI_y\ell_x\Big]\\
& +72\zeta\, EI_xEI_y\ell_y\}\,,\\
c^*_{33} = & \frac{h\Big[(3\ell_x+\zeta\ell_y)\Big(3EI_xEI_y\ell_x\ell_y+EI_x^2\ell_y^2\Big)+EI_y^2\ell_x^2\,(8\ell_x+3\zeta\ell_y)\Big]}{3\,(2EI_y\ell_x+EI_x\ell_y)^2},
\end{aligned}
\tag{B.3}
$$

where $\zeta := \dfrac{3EA_yEI_y\ell_x^2\ell_y}{6EI_xEI_y\ell_y+EA_y\ell_x^2\,[6EI_x\ell_y+EI_y\ell_x\,(16+\mu_x)]}$.

However, when $t_x = t_y$ as in the case at hand, it is $A_x = A_y =: A$, $A_x^* = A_y^* =: A^*$, $I_x = I_y =: I$, and, therefore, $\mu_\nu = 12EI/GA^*\ell_\nu^2$ $(\nu = x, y)$. As a consequence, the constitutive coefficients of $\mathbf{C}^0$ become:

$$
\begin{aligned}
c_{11} &= \frac{12EA\,EIh\left[(4+\mu_x)\,EA\ell_x^3 + 6EI\ell_y\right]}{d},\\
c_{12} &= -\frac{36EA^2EIh\ell_x^2\ell_y}{d},\\
c_{22} &= \frac{6EA\,EIh\left[EA\ell_y^2\left(6\ell_x + \mu_y\ell_y + \ell_y\right) + 24EI\ell_x\right]}{d},\\
c_{33} &= \frac{EIh}{2\ell_x + \ell_y},
\end{aligned}
\tag{B.4}
$$

with

$$
\begin{aligned}
d :=\ & 144EI^2\ell_x\ell_y + EA^2\ell_x^3\ell_y^2\left[6\ell_x\left(1+\mu_x\right) + \left(4+\mu_x\right)\left(1+\mu_y\right)\ell_y\right]\\
& + 6EA\,EI\left[4\ell_x^4\left(4+\mu_x\right) + 6\ell_x\ell_y^3 + \left(1+\mu_y\right)\ell_y^4\right].
\end{aligned}
\tag{B.5}
$$

The geometric coefficients of $\mathbf{C}^*$ reduce to

$$
\begin{aligned}
c_{11}^* =\ & -\frac{2EA^2EI^2h\ell_y^2}{5d^2}\left\{-36EI^2\ell_y^2\left\{60\ell_x^3 + \ell_y\zeta\left[90\ell_x^2 + 30\ell_x\ell_y\left(1+\mu_y\right) + \ell_y^2\left(3+5\mu_y\right)\right]\right\}\right.\\
& + 12EA\,EI\ell_x^3\ell_y\left\{-15\ell_x^3\left(1+\mu_x\right) - \ell_y\zeta\left[90\ell_x^2\left(1+\mu_x\right) + 15\ell_x\ell_y\left(5+2\mu_x\right)\left(1+\mu_y\right)\right.\right.\\
& \left.\left.+\ell_y^2\left(4+\mu_x\right)\left(3+5\mu_y\right)\right]\right\} + EA^2\ell_x^6\left\{6\ell_x^3\left[-4-5\mu_x\left(1-\mu_x\right)\right] - \ell_y\zeta\left[90\ell_x^2\left(1+\mu_x\right)^2\right.\right.\\
& \left.\left.\left.+30\ell_x\ell_y\left(1+\mu_x\right)\left(4+\mu_x\right)\left(1+\mu_y\right) + \ell_y^2\left(4+\mu_x\right)^2\left(3+5\mu_y\right)\right]\right\}\right\},\\
c_{12}^* =\ & \frac{3EA^2h\ell_x^2\ell_y}{5d^2}\left\{720EI^2\ell_x\ell_y\left[\ell_x^2\left(5+\mu_x\right) + \ell_y\zeta\left(6\ell_x + \ell_y + \ell_y\mu_y\right)\right]\right.\\
& + EA^2\ell_x^3\ell_y^2\left\{-6\ell_x^3\left(1-5\mu_x^2\right) + \ell_x^2\ell_y\left[4+5\mu_x\left(1+\mu_x\right)\right]\left(1+\mu_y\right) - \ell_y^3\zeta\left(4+\mu_x\right)\left(1-5\mu_y^2\right)\right\}\\
& + 6EAEI\left\{\ell_x^2\left\{4\ell_x^4\left[4+5\mu_x\left(1+\mu_x\right)\right] + 30\ell_x\ell_y^3\left(1+\mu_x\right) + 5\ell_y^4\left(5+\mu_x\right)\left(1+\mu_y\right)\right\}\right.\\
& \left.\left.+\ell_y\zeta\left[120\ell_x^5\left(1+\mu_x\right) + 20\ell_x^4\ell_y\left(4+\mu_x\right)\left(1+\mu_y\right) - \ell_y^5\left(1-5\mu_y^2\right)\right]\right\}\right\},\\
c_{13}^* =\ & \frac{EAh\ell_y^2}{2d}\left\{EA\ell_x^3\zeta\left[6\ell_x\left(1+\mu_x\right) + \ell_y\left(4+\mu_x\right)\left(1+\mu_y\right)\right]\right.\\
& \left.+6EI\left[6\ell_x^2 + \ell_y\zeta\left(6\ell_x + \ell_y + \ell_y\mu_y\right)\right]\right\},\\
c_{22}^* =\ & \frac{EA^2h\ell_x^4}{5d^2}\left\{48EA\,EI\ell_x^2\ell_y^2\left[\ell_x\left(63+75\mu_x\right) + 4\ell_y\left(12+5\mu_x\right)\left(1+\mu_y\right)\right]\right.\\
& + 576EI^2\ell_x^2\left[4\ell_x\left(12+5\mu_x\right) + 45\ell_y\zeta\right] + EA^2\ell_y^4\left[36\ell_x^3\left(3+5\mu_x\right)\right.\\
& \left.\left.+6\ell_x^2\ell_y\left(21+25\mu_x\right)\left(1+\mu_y\right) + 4\ell_x\ell_y^2\left(12+5\mu_x\right)\left(1+\mu_y\right)^2 + 9\ell_y^3\zeta\left(1-5\mu_y^2\right)\right]\right\},\\
c_{23}^* =\ & \frac{EAh\ell_x^3}{2d}\left\{EA\ell_y^2\left[6\ell_x\left(1+\mu_x\right) + \ell_y\left(4+\mu_x\right)\left(1+\mu_y\right)\right]\right.\\
& \left.+24EI\left[\ell_x\left(4+\mu_x\right) + 3\ell_y\zeta\right]\right\},\\
c_{33}^* =\ & \frac{h\left[8\ell_x^3 + \ell_y^3\zeta + 3\ell_x\ell_y^2\left(1+\zeta\right) + 3\ell_x^2\ell_y\left(3+\zeta\right)\right]}{3\left(2\ell_x + \ell_y\right)^2},
\end{aligned}
\tag{B.6}
$$

where $\zeta := \dfrac{3EA\ell_x^2\ell_y}{6EI\ell_y + EA\ell_x^2\left[6\ell_y + \ell_x\left(16+\mu_x\right)\right]}$.

Grid beam

The analytical expression of the grid beam coefficients of the constitutive matrix in the case of microstructure made of a single rectangular frame, i.e. with $\ell_x \neq \ell_y$ and $\ell_x := h$, made of Timoshenko (micro) beams is reported. For the elastic counterpart $\mathbf{C}^0$, the coefficients are:

$$
\begin{aligned}
c_{11} &= \sum_{k=1}^{2} EA_{x,k}, \\
c_{13} &= -\sum_{k=1}^{2} EA_{x,k} y_k, \\
c_{15} &= \sum_{k=1}^{2} EA_{x,k} \psi\left(y_k\right), \\
c_{22} &= \sum_{k=1}^{2} \frac{12EA_{x,k}}{h^2\left(1+\mu_{x,k}\right)}, \\
c_{24} &= \sum_{k=1}^{2} \frac{12EI_{x,k}}{h^2\left(1+\mu_{x,k}\right)}\left[\psi'\left(y_k\right) + \frac{\ell_y^2\mu_y}{12}\psi'''\left(y_k\right)\right], \\
c_{25} &= \sum_{k=1}^{2} \frac{6EI_{x,k}}{h\left(1+\mu_{x,k}\right)}\left[\psi'\left(y_k\right) + \frac{\ell_y^2\mu_y}{12}\psi'''\left(y_k\right)\right], \\
c_{33} &= \sum_{k=1}^{2}\left(EI_{x,k} + EA_{x,k}y_k^2\right), \\
c_{35} &= -\sum_{k=1}^{2} EA_{x,k} y_k \psi\left(y_k\right) - \sum_{k=1}^{2} EI_{x,k}\left[\psi'\left(y_k\right) + \frac{\ell_y^2\mu_y}{12}\psi'''\left(y_k\right)\right], \\
c_{44} &= \frac{EI_y}{h}\left\{\frac{\ell_y^2\mu_y}{12}\int_{-\ell_y/2}^{\ell_y/2}\left[\psi'''\left(y\right)\right]^2 \mathrm{d}y + \int_{-\ell_y/2}^{\ell_y/2}\left[\psi''\left(y\right) + \frac{\ell_y^2\mu_y}{12}\psi''''\left(y\right)\right]^2 \mathrm{d}y\right\} \\
&\quad + \sum_{k=1}^{2} \frac{12EI_{x,k}}{h^2\left(1+\mu_{x,k}\right)}\left[\psi'\left(y_k\right) + \frac{\ell_y^2\mu_y}{12}\psi'''\left(y_k\right)\right]^2, \\
c_{45} &= \frac{EI_y}{2}\left\{\int_{-\ell_y/2}^{\ell_y/2}\left[\psi''\left(y\right) + \frac{\ell_y^2\mu_y}{12}\psi''''\left(y\right)\right]^2 \mathrm{d}y + \frac{\ell_y^2\mu_y}{12}\int_{-\ell_y/2}^{\ell_y/2}\left[\psi'''\left(y\right)\right]^2 \mathrm{d}y\right\} \\
&\quad + \sum_{k=1}^{2} \frac{6EI_{x,k}}{h\left(1+\mu_{x,k}\right)}\left[\psi'\left(y_k\right) + \frac{\ell_y^2\mu_y}{12}\psi'''\left(y_k\right)\right]^2, \\
c_{55} &= \frac{EI_y h}{2}\left\{\int_{-\ell_y/2}^{\ell_y/2}\left[\psi''\left(y\right) + \frac{\ell_y^2\mu_y}{12}\psi''''\left(y\right)\right]^2 \mathrm{d}y + \frac{\ell_y^2\mu_y}{12}\int_{-\ell_y/2}^{\ell_y/2}\left[\psi'''\left(y\right)\right]^2 \mathrm{d}y\right\} \\
&\quad + \sum_{k=1}^{2} EA_{x,k}\left[\psi\left(y_k\right)\right]^2 + \sum_{k=1}^{2} EI_{x,k}\frac{4+\mu_{x,k}}{1+\mu_{x,k}}\left[\psi'\left(y_k\right) + \frac{\ell_y^2\mu_y}{12}\psi'''\left(y_k\right)\right]^2,
\end{aligned}
\tag{B.7}
$$

while coefficients of the geometric part $\mathbf{C}^*$ are given by

$$\begin{aligned}
c^*_{22} &= \sum_{k=1}^{2} \frac{3+5\mu_{x,k}}{5\left(1+\mu_{x,k}\right)^2},\\
c^*_{23} &= \frac{h}{2},\\
c^*_{24} &= \sum_{k=1}^{2} \frac{1-5\mu_{x,k}^2}{10\left(1+\mu_{x,k}\right)^2}\left[\psi'\left(y_k\right)+\frac{\ell_y^2\mu_y}{12}\psi'''\left(y_k\right)\right],\\
c^*_{25} &= \sum_{k=1}^{2} \frac{h\left(1-5\mu_{x,k}^2\right)}{20\left(1+\mu_{x,k}\right)^2}\left[\psi'\left(y_k\right)+\frac{\ell_y^2\mu_y}{12}\psi'''\left(y_k\right)\right],\\
c^*_{33} &= \frac{h^2}{3},\\
c^*_{35} &= -\sum_{k=1}^{2} \frac{h^2}{24}\left[\psi'\left(y_k\right)+\frac{\ell_y^2\mu_y}{12}\psi'''\left(y_k\right)\right],\\
c^*_{44} &= \sum_{k=1}^{2} \frac{1-5\mu_{x,k}^2}{10\left(1+\mu_{x,k}\right)^2}\left[\psi'\left(y_k\right)+\frac{\ell_y^2\mu_y}{12}\psi'''\left(y_k\right)\right]^2,\\
c^*_{45} &= \sum_{k=1}^{2} \frac{h\left(1-5\mu_{x,k}^2\right)}{20\left(1+\mu_{x,k}\right)^2}\left[\psi'\left(y_k\right)+\frac{\ell_y^2\mu_y}{12}\psi'''\left(y_k\right)\right]^2,\\
c^*_{55} &= \sum_{k=1}^{2} \frac{h^2\left[4+5\mu_{x,k}\left(1-\mu_{x,k}\right)\right]}{60\left(1+\mu_{x,k}\right)^2}\left[\psi'\left(y_k\right)+\frac{\ell_y^2\mu_y}{12}\psi'''\left(y_k\right)\right]^2.
\end{aligned} \tag{B.8}$$

Chapter C

An application to civil engineering: the case of tall buildings

In this Appendix, an application of the mixed homogenization approach, extensively examined in the previous Chapters for the analysis of metamaterials, is presented in the context of civil engineering structures embedded in a 3D space. The aim is to demonstrate how the theoretical framework developed for periodic microstructured systems can be extended to structural assemblies characterized by a spatial arrangement of beams and columns, thereby enabling the construction of equivalent beam models capable of capturing their global mechanical behavior. The procedure is illustrated through selected case studies, whose elastic properties of the equivalent model are analytically identified. Then, the equivalent beam models are validated with FE models in static and dynamic in order to highlight both the strengths and inherent limitations of the homogenized formulation when applied to periodic spatial frames, thus providing further insight into its potential range of applicability.

C.1 Model

A spatial multi-story frame composed of n_x in plane rigid but out of plane deformable floors, connected by n_c flexible columns, is considered. Two adjacent floors, each having half of the stiffness, connected by columns form a pattern, usually called cell, of height h (Fig. C.1) that repeated n_x times in $x-$direction determine the height of the building ℓ. The cell is bounded by two cross-sections, $\mathcal{D}_i$ and $\mathcal{D}_{i+1}$, located at the abscissas x_i, x_{i+1}. Two families of fibers are detected: (i) those parallel to the beam $x-$axis, referred to as longitudinal fibers, which are n_y in the $y-$direction and $n_z$in the $z-$direction; (ii) those lying in the $n+1$ planes orthogonal to the axis-line, referred to as transverse fibers, parallel to the $(y,z)-$plane. The origin of the coordinate system is at the lower end A. The structural elements are modeled as Timoshenko beams and are therefore characterized by the axial stiffness EA_ξ, the shear stiffness GA^*_ξ, the bending stiffness $EI_{\xi\nu}$ and the torsional stiffness GJ_ξ. Here, the subscript ξ distinguishes the type of structural element, columns ($\xi = c$) or beams ($\xi = b$) , while the subscript ν identifies the principal axis of the cross-section with respect to which the mechanical quantity is evaluated ($\nu = y, z$). In this notation, E and G are the elastic and tangential modulus, respectively, A_ξ the cross-section area, A_ξ^* the shear area and $I_{\xi\nu}$ the inertia moment about the $\nu-$axis, and J_ξ the torsional inertia.

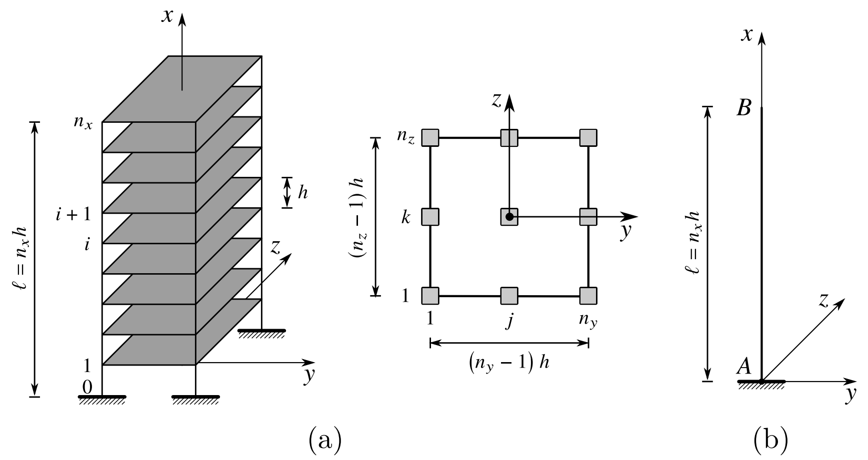

Figure C.1. Study object: (a) multi-story building and general cross-section; (b) equivalent beam model.

The building is modeled as a linear Timoshenko beam embedded in a 3D space. The beam is a 1D internally unconstrained continuum, made of a deformable axis and initially orthogonal rigid cross-section. A cantilever beam, clamped at the end A and free at the end B, is considered whose material abscissa $x \in [0, \ell]$ spans the interval (A, B) of total length $\ell := n_x\, h$. The strain-displacement relationships are:

$$\varepsilon = u', \quad \gamma_y = v' - \theta_z, \quad \gamma_z = w' + \theta_y, \quad \kappa_x = \theta_x', \quad \kappa_y = \theta_y', \quad \kappa_z = \theta_z', \tag{C.1}$$

where $\varepsilon\,(x,t)$ is the elongation, $\gamma_y\,(x,t)$ and $\gamma_z\,(x,t)$ the shear strains, $\kappa_x\,(x,t)$ the torsional curvature, $\kappa_y\,(x,t)$ and $\kappa_z\,(x,t)$ the flexural curvature, $u\,(x,t)$ is the longitudinal displacement, $v\,(x,t)$ and $w\,(x,t)$ the transverse displacement in $y-$direction and $z-$direction, respectively, $\theta_\nu\,(x,t)$ is the rotation of the cross-section with respect to $\nu-$axis ($\nu = x, y, z$), t is the time, and a prime denotes differentiation with respect to the abscissa x. The balance equations are

$$\begin{aligned}
-m\ddot{u} - I_y\ddot{\theta}_y + I_z\ddot{\theta}_z + N' + p_x &= 0,\\
-m\ddot{v} - I_y\ddot{\theta}_x + T_y' + p_y &= 0,\\
-m\ddot{w} - I_z\ddot{\theta}_x + T_z' + p_z &= 0,\\
I_y\ddot{v} - I_z\ddot{w} - I_{xx}\ddot{\theta}_x + M_x' + c_x &= 0,\\
-I_y\ddot{u} - I_{yy}\ddot{\theta}_y + I_{yz}\ddot{\theta}_z + M_y' - T_z + c_y &= 0,\\
I_z\ddot{u} + I_{yz}\ddot{\theta}_y - I_{zz}\ddot{\theta}_z + M_z' + T_y + c_z &= 0,
\end{aligned} \tag{C.2}$$

where $N(x,t)$, $T_y(x,t)$ and $T_z(x,t)$ are the axial and shear internal forces, respectively, $M_x(x,t)$ is the torsional moment, $M_y(x,t)$ and $M_z(x,t)$ are the bending moments, while $p_\nu(x,t)$, $c_\nu(x,t)$ are the external forces and couple per unit-length ($\nu = x, y, z$). m, I_ν and $I_{\nu\nu}$ are the mass, first and second inertia moments per unit-length, evaluated with respect to the centroid ($\nu = x, y, z$), and a dot denotes time-differentiation. The problem has no lumped masses and is complemented with the following geometric and mechanical boundary conditions.

$$\begin{aligned} u_A = v_A = w_A = \theta_{xA} = \theta_{yA} = \theta_{zA} = 0, \\ N_B = T_{yB} = T_{zB} = M_{xB} = M_{yB} = M_{zB} = 0. \end{aligned} \tag{C.3}$$

By postulating a complete quadratic polynomial expression for the elastic potential energy density
$\phi = \phi(\varepsilon, \gamma_y, \gamma_z, \kappa_x, \kappa_y, \kappa_z)$, a linear hyperelastic law is introduced.

$$\begin{aligned} \phi =& \frac{1}{2}\left[c_{11}\,\varepsilon^2 + c_{22}\,\gamma_y^2 + c_{33}\,\gamma_z^2 + c_{44}\,\kappa_x^2 + c_{55}\,\kappa_y^2 + c_{66}\,\kappa_z^2\right. \\ &+ 2\left(c_{12}\,\varepsilon\gamma_y + c_{13}\,\varepsilon\gamma_z + c_{14}\,\varepsilon\kappa_x + c_{15}\,\varepsilon\kappa_y + c_{16}\,\varepsilon\kappa_z + c_{23}\,\gamma_y\gamma_z + c_{24}\,\gamma_y\kappa_x + c_{25}\,\gamma_y\kappa_y\right. \\ &\left.\left.+\ c_{26}\,\gamma_y\kappa_z + c_{34}\,\gamma_z\kappa_x + c_{35}\,\gamma_z\kappa_y + c_{36}\,\gamma_z\kappa_z + c_{45}\,\kappa_x\kappa_y + c_{46}\,\kappa_x\kappa_z + c_{56}\,\kappa_y\kappa_z\right)\right] \end{aligned} \tag{C.4}$$

With the Green law, a fully-coupled constitutive law containing 21 constants c_{ij} $(i, j = 1, \ldots, 6)$, that, in the perspective of homogenization, must be properly identified to allow the equivalent beam model to best describe the macroscopic behavior of the building, is found. It reads as:

$$\begin{pmatrix} N \\ T_y \\ T_z \\ M_x \\ M_y \\ M_z \end{pmatrix} = \begin{pmatrix} c_{11} & c_{12} & c_{13} & c_{14} & c_{15} & c_{16} \\ & c_{22} & c_{23} & c_{24} & c_{25} & c_{26} \\ & & c_{33} & c_{34} & c_{35} & c_{36} \\ & & & c_{44} & c_{45} & c_{46} \\ & & & & c_{55} & c_{56} \\ \mathrm{SYM} & & & & & c_{66} \end{pmatrix} \begin{pmatrix} \varepsilon \\ \gamma_y \\ \gamma_z \\ \kappa_x \\ \kappa_y \\ \kappa_z \end{pmatrix} \tag{C.5}$$

in which

$$\mathbf{C} = \begin{pmatrix} c_{11} & c_{12} & c_{13} & c_{14} & c_{15} & c_{16} \\ & c_{22} & c_{23} & c_{24} & c_{25} & c_{26} \\ & & c_{33} & c_{34} & c_{35} & c_{36} \\ & & & c_{44} & c_{45} & c_{46} \\ & & & & c_{55} & c_{56} \\ \mathrm{SYM} & & & & & c_{66} \end{pmatrix} \tag{C.6}$$

is the constitutive matrix. By substituting the constitutive relations Eq. (C.5) and the strain-displacement laws Eq. (C.1), the equilibrium (Eq. (C.2)) the field equations can be recast in terms of the displacement. Assuming the structure is initially at rest, the resulting elasto-dynamic problem takes the form of a system of coupled partial differential equations, supplemented by geometric and mechanical boundary conditions at the beam ends. Introducing the displacement, the load and boundary load vectors $\mathbf{u} = (u, v, w, \theta_x, \theta_y, \theta_z)^T$, $\mathbf{p} = (p_x, p_y, p_z, c_x, c_y, c_z)^T$ and $\mathbf{P} = (P_x, P_y, P_z, C_x, C_y, C_z)^T$, the governing equations admit the following compact matrix form:

$$\begin{aligned} -\mathbf{M}\ddot{\mathbf{u}} + \mathbf{K}_2\mathbf{u}'' + \mathbf{K}_1\mathbf{u}' + \mathbf{K}_0\mathbf{u} + \mathbf{p} &= \mathbf{0}, \\ \mathbf{u}_A &= \mathbf{0}, \\ \mathbf{B}_1\mathbf{u}'_B + \mathbf{B}_0\mathbf{u}_B &= \mathbf{P}, \end{aligned} \tag{C.7}$$

where the mass matrix $\mathbf{M}$and the stiffness matrices $\mathbf{K}_i$ $(i = 0, 1, 2)$ are defined as

$$\mathbf{K}_2 \coloneqq \mathbf{C}, \qquad \mathbf{K}_1 \coloneqq \begin{pmatrix} 0 & 0 & 0 & 0 & c_{13} & -c_{12} \\ & 0 & 0 & 0 & c_{23} & -c_{22} \\ & & 0 & 0 & c_{33} & -c_{23} \\ & & & 0 & c_{34} & -c_{24} \\ & & & & 0 & -c_{25} - c_{36} \\ \text{SKW} & & & & & 0 \end{pmatrix},$$

$$\mathbf{K}_0 \coloneqq \begin{pmatrix} 0 & 0 & 0 & 0 & 0 & 0 \\ & 0 & 0 & 0 & 0 & 0 \\ & & 0 & 0 & 0 & 0 \\ & & & 0 & 0 & 0 \\ & & & & -c_{33} & c_{23} \\ \text{SYM} & & & & & -c_{22} \end{pmatrix}. \quad \mathbf{M} \coloneqq \begin{pmatrix} m & 0 & 0 & 0 & I_y & -I_z \\ & m & 0 & -I_y & 0 & 0 \\ & & m & I_z & 0 & 0 \\ & & & I_{xx} & 0 & 0 \\ & & & & I_{yy} & -I_{yz} \\ \text{SYM} & & & & & I_{zz} \end{pmatrix}, \tag{C.8}$$

while the boundary operators are:

$$\mathbf{B}_1 := \mathbf{K}_2, \quad \mathbf{B}_0 := \begin{pmatrix} 0 & 0 & 0 & 0 & c_{13} & -c_{12} \\ 0 & 0 & 0 & 0 & c_{23} & -c_{22} \\ 0 & 0 & 0 & 0 & c_{33} & -c_{23} \\ 0 & 0 & 0 & 0 & c_{34} & -c_{24} \\ 0 & 0 & 0 & 0 & c_{35} & -c_{25} \\ 0 & 0 & 0 & 0 & c_{36} & -c_{26} \end{pmatrix}. \tag{C.9}$$

C.2 Identification of the elastic and inertial constants

C.2.1 Elastic constants

The identification of the elastic constants of the equivalent model is performed with the mixed homogenization approach through an analytical identification procedure. The approach relies on the a priori definition of the target model and on the derivation of explicit micro-macro relationships obtained by enforcing the equality of the elastic energy stored by the cell of the fine model and that of the segment of the equivalent beam of the same length, when the two systems undergo the same displacements at the ends.

First of all, the analytical procedure for rigid floors (membrane and flexural stiffness) developed in [33] is here recalled for a regular spatial frame made of n_c columns of height $h_c := h$, and n_y-1 and n_z-1 beams of length h_b, both modeled as Timoshenko beams. The analysis is performed for a single elastic element (column) of length h, which represents a segment of the equivalent model. The element is clamped at ends F (foot) and H (head), and subjected to displacements and rotations applied at H:

$$u\left(h\right)=u_H,\quad v\left(h\right)=v_H,\quad w\left(h\right)=w_H,\quad \theta_x\left(h\right)=\theta_{Hx},\quad \theta_y\left(h\right)=\theta_{Hy},\quad \theta_z\left(h\right)=\theta_{Hz}. \tag{C.10}$$

The elastic energy of the $k-$th column element is expressed as:

$$\tilde{U}_k=\frac{1}{2}\int_0^h\left(EA_c\varepsilon^2+GA^*_{cy}\gamma_y^2+GA^*_{cz}\gamma_z^2+GJ_c\kappa_x^2+EI_{cy}\kappa_y^2+EI_{cz}\kappa_z^2\right)\mathrm{d}x \tag{C.11}$$

The following interpolation functions are adopted, which exactly satisfy the linear elastic problem

$$\begin{aligned}
u\left(x\right)&=\frac{u_H}{h}x,\\
v\left(x\right)&=\frac{1}{1+\mu_{cz}}\left[\left(-\frac{2x^3}{h^3}+\frac{3x^2}{h^2}+\frac{x}{h}\mu_{cz}\right)v_H+\frac{x}{2}\left(\frac{x}{h}-1\right)\left(2\frac{x}{h}+\mu_{cz}\right)\theta_{Hz}\right],\\
w\left(x\right)&=\frac{1}{1+\mu_{cy}}\left[\left(-\frac{2x^3}{h^3}+\frac{3x^2}{h^2}+\frac{x}{h}\mu_{cy}\right)w_H+\frac{x}{2}\left(1-\frac{x}{h}\right)\left(2\frac{x}{h}+\mu_{cy}\right)\theta_{Hy}\right],\\
\theta_x\left(x\right)&=\frac{\theta_{Hx}}{h}x,\\
\theta_y\left(x\right)&=\frac{1}{1+\mu_{cy}}\left[6\left(\frac{x}{h}-1\right)\frac{x}{h}\frac{w_H}{h}+\frac{x}{h}\left(3\frac{x}{h}-2+\mu_{cy}\right)\theta_{Hy}\right],\\
\theta_z\left(x\right)&=\frac{1}{1+\mu_{cz}}\left[6\left(-\frac{x}{h}+1\right)\frac{x}{h}\frac{v_H}{h}+\frac{x}{h}\left(3\frac{x}{h}-2+\mu_{cz}\right)\theta_{Hz}\right],
\end{aligned} \tag{C.12}$$

where $\mu_{c\nu} := 12EI_{c\nu}/GA^*_c h^2$ denotes the non-dimensional stiffness ratio. From Eq. (C.12), the scalar strain measures are derived through the relations Eq. (C.1) and, by substituting in Eq. (C.11), allows to rewrite the scalar energy of the $k-$th element as

$$\begin{aligned}
\tilde{U}_k=\frac{1}{2}\Bigg[&\frac{EA_c}{h}u_H^2+\frac{12EI_{cz}}{\left(1+\mu_{cz}\right)h^3}v_H^2+\frac{12EI_{cy}}{\left(1+\mu_{cy}\right)h^3}w_H^2+\frac{GJ_c}{h}\theta_{Hx}^2+\frac{4+\mu_{cy}}{1+\mu_{cy}}\frac{EI_{cy}}{h}\theta_{Hy}^2\\
&+\frac{4+\mu_{cz}}{1+\mu_{cz}}\frac{EI_z}{h}\theta_{Hz}^2-\frac{12EI_{cz}}{\left(1+\mu_{cz}\right)h^2}v_H\theta_{Hz}+\frac{12EI_{cy}}{\left(1+\mu_{cy}\right)h^2}w_H\theta_{Hy}\Bigg].
\end{aligned} \tag{C.13}$$

The analysis is then extended to the entire cell which, as previously discussed, consists of two adjacent floors, each endowed with half of the global stiffness, connected by n_c elements (columns) of length h. Accordingly, the elastic energy of the cell is obtained as the sum of the energies of the single elements (Eq. (C.13)), and the assembly procedure is carried out by applying the displacements u_G, v_G and w_G, together with the rotations

θ_x, θ_y and θ_z, at the reduction displacements' pole O (which in this case is chosen as the centroid G of the cross-section $\mathcal{D}_{i+1}$). Since the cross-section behaves as a rigid body, the rotation at the top end of the $k-$th column element, for $k = 1, \ldots, n_c$, coincides with the floor's rotation; moreover, under the assumption of linear kinematics, the displacements at the top of the $k-$th element, located at coordinates (y_k, z_k) are obtained through the rigid displacement formula.

$$u_k = u_G - \theta_z y_k + \theta_y z_k, \quad v_k = v_G - \theta_x z_k, \quad w_k = w_G + \theta_x y_k \tag{C.14}$$

The total elastic energy of the cell is therefore

$$\tilde{U} = \sum_{k=1}^{n_c} \tilde{U}_k \tag{C.15}$$

and the corresponding energy density is evaluated as $\tilde{\phi} := \tilde{U}/h$.

Finally, by expressing the end displacements in terms of the strain measures, the equivalence between the discrete and continuous energies is enforced, thereby enabling the homogenization procedure. To this end, the strain-displacement relationships (Eq. (C.1)) are integrated over the interval $(x_i,\ x_{i+1})$, assuming a suitable strain test field, which is here taken to be constant. This assumption is admissible only when the variables involved vary at a scale that is much larger than the cell height; accordingly, the validity of the equivalent model is limited to wavelengths much larger than the cell itself. Once rigid-body motions are removed, the end displacements read

$$\begin{aligned}
u\,(x_i) &= 0, \qquad & u\,(x_{i+1}) &= \varepsilon\, h, \\
v\,(x_i) &= 0, \qquad & v\,(x_{i+1}) &= \gamma_y\, h + \frac{1}{2}\kappa_z\, h^2, \\
w\,(x_i) &= 0, \qquad & w\,(x_{i+1}) &= \gamma_z\, h - \frac{1}{2}\kappa_y\, h^2, \\
\theta_x\,(x_i) &= 0, \qquad & \theta_x\,(x_{i+1}) &= \kappa_x\, h, \\
\theta_y\,(x_i) &= 0, \qquad & \theta_y\,(x_{i+1}) &= \kappa_y\, h, \\
\theta_z\,(x_i) &= 0, \qquad & \theta_z\,(x_{i+1}) &= \kappa_z\, h.
\end{aligned} \tag{C.16}$$

Substituting Eq. (C.16) into $\tilde{\phi}$, and imposing the equality $\phi = \tilde{\phi}\ \forall\,(\varepsilon, \gamma_y, \gamma_z, \kappa_x, \kappa_y, \kappa_z)$, where ϕ has already been defined in Eq. (C.4), the elastic constants $\mathbf{C} := (c_{ij})$ are found. Denoting by $E\,(x_E, y_E)$ and $S\,(x_S, y_S)$ the extensional and shear stiffness centroids, respectively, evaluated under the hypotheses of rigid cross-section, the constitutive law takes the form:

$$
\begin{aligned}
c_{11} &= \sum_{k=1}^{n_c} EA_k, & c_{15} &= c_{11} z_E, \\
c_{22} &= \sum_{k=1}^{n_c} \frac{12EI_{zk}}{(1+\mu_{zk})\,h^2}, & c_{16} &= -c_{11} y_E, \\
c_{33} &= \sum_{k=1}^{n_c} \frac{12EI_{yk}}{(1+\mu_{yk})\,h^2}, & c_{24} &= -c_{22} z_S, \\
c_{44} &= \sum_{k=1}^{n_c} GJ_k + n_y \frac{12EI_{zk}}{(1+\mu_{zk})\,h^2} \sum_{k=1}^{n_z} z_k^2 + n_z \frac{12EI_{yk}}{(1+\mu_{yk})\,h^2} \sum_{k=1}^{n_y} y_k^2, & c_{34} &= c_{33} y_S, \\
c_{55} &= \sum_{k=1}^{n_c} EI_{yk} + n_y EA_k \sum_{k=1}^{n_z} z_k^2, & c_{56} &= \sum_{k=1}^{n_c} EA_k y_k z_k, \\
c_{66} &= \sum_{k=1}^{n_c} EI_{zk} + n_z EA_k \sum_{k=1}^{n_y} y_k^2,
\end{aligned}
\tag{C.17}
$$

with

$$
\begin{aligned}
y_E &= \frac{\sum_{k=1}^{n_c} EA_k y_k}{\sum_{k=1}^{n_c} EA_k}, & z_E &= \frac{\sum_{k=1}^{n_c} EA_k z_k}{\sum_{k=1}^{n_c} EA_k}, \\
y_S &= \frac{\sum_{k=1}^{n_c} \frac{12EI_{yk}}{\left(1+\mu_{yk}\right)h^2} y_k}{\sum_{k=1}^{n_c} \frac{12EI_{yk}}{\left(1+\mu_{yk}\right)h^2}}, & z_S &= \frac{\sum_{k=1}^{n_c} \frac{12EI_{zk}}{(1+\mu_{zk})h^2} z_k}{\sum_{k=1}^{n_c} \frac{12EI_{zk}}{(1+\mu_{zk})h^2}},
\end{aligned}
\tag{C.18}
$$

where in both the Eqs. (C.17) and (C.18) the subscript $\xi = c$ is omitted, since, under the rigid-floor assumption, the only components contributing to the cell's elastic energy are the column elements.

In the present Appendix, however, the cross-section is free to undergo out of plane warping which, since the system under consideration is embedded in a 3D space, arises from shear and torsional deformation. It is chosen to account for the warping phenomenon in an approximate manner, namely with a corrective coefficient denoted as shear factor already introduced in [60]. This factor multiplies the stiffnesses obtained under the rigid-floor assumption and therefore reduces the macroscopic stiffness of the equivalent beam model. The shear factors, in the case where all beams exhibit the same cross-section and length, and all columns also share identical cross-sectional and geometric properties (even though the characteristics of the beams may differ from those of the columns), are expressed as

$$
\begin{aligned}
\chi_y &= \frac{\frac{n_y-1}{n_y}\eta_y \frac{h_c}{h_b}}{1+\frac{n_y-1}{n_y}\eta_y \frac{h_c}{h_b}} \quad \text{with } \eta_y = \frac{EI_{by}}{EI_{cz}} \frac{1+\alpha_{cz}}{1+\alpha_{by}}, \\
\chi_z &= \frac{\frac{n_z-1}{n_z}\eta_z \frac{h_c}{h_b}}{1+\frac{n_z-1}{n_z}\eta_z \frac{h_c}{h_b}} \quad \text{with } \eta_z = \frac{EI_{by}}{EI_{cy}} \frac{1+\alpha_{cy}}{1+\alpha_{by}}.
\end{aligned}
\tag{C.19}
$$

In a heuristic manner, the elastic constants affected by warping are thus evaluated as

$$\begin{aligned}
c_{22} &= \chi_y \sum_{k=1}^{n_c} \frac{12EI_{zk}}{(1+\mu_{zk})\,h^2}, \\
c_{33} &= \chi_z \sum_{k=1}^{n_c} \frac{12EI_{yk}}{(1+\mu_{yk})\,h^2}, \\
c_{44} &= \sum_{k=1}^{n_c} GJ_k + n_y\chi_y \frac{12EI_{zk}}{(1+\mu_{zk})\,h^2} \sum_{k=1}^{n_z} z_k^2 + n_z\chi_z \frac{12EI_{yk}}{(1+\mu_{yk})\,h^2} \sum_{k=1}^{n_y} y_k^2,
\end{aligned} \tag{C.20}$$

Simple analytical expressions for the shear factor, such as Eq. (C.19), can be derived only for simple case studies. When columns and beams with different cross-sections are introduced, or when geometric irregularities arise due to the lack of symmetry or to particular layouts, formulating a shear factor that remains both simple and accurate becomes significantly more demanding. Nevertheless, a weighted average of the stiffness contributions of beams and columns can be adopted to compute an equivalent (averaged) moment of inertia to adopt in Eq. (C.19).

Moreover, when the cross-section is no longer rigid and lacks symmetry axes, the expressions used to evaluate the extensional stiffness centroid E (Eq. (C.18)) remain valid, while those employed for determining the shear stiffness centroid S no longer hold. Indeed, the location of S depends on the distribution of the shear stresses τ, and thus on the geometrical and mechanical characteristics of the cross-section, including its in-plane and out-of-plane deformability. Consequently, Eq. (C.20) provides only an approximate means of evaluating the elastic constants when the cross-section is assumed to behave as rigid only within its own plane.

C.2.2 Inertial properties

As for the identification of the elastic constants, the inertial properties are determined by enforcing the energy equivalence between the kinetic energy of the cell (fine model) $\tilde{\mathcal{T}}$ and a beam segment (coarse model) $\mathcal{T}$ of equal length, h, subjected to a uniform velocity field. Unlike the identification of the elastic coefficients, the cell is made of a floor, half column below and half column above it. The masses are assumed to be lumped at the joints; accordingly, owing to the rigid displacement map given by Eq. (C.14), the kinetic energy is unaffected by any warping deformation of the floors. Neglecting rotational inertia with respect to the translational one, the kinetic energies read

$$\tilde{\mathcal{T}} = \frac{1}{2}\sum_{k=1}^{n_c} M_i \left(\dot{u}_k^2 + \dot{v}_k^2 + \dot{w}_k^2\right), \quad \mathcal{T} = \frac{h}{2}\left[m\left(\dot{u}^2 + \dot{v}^2 + \dot{w}^2\right) + I_x\dot{\theta}_x^2 + I_y\dot{\theta}_y^2 + I_z\dot{\theta}_z^2\right] \tag{C.21}$$

where M_i denote the lumped masses, and $\dot{u}_i$, $\dot{v}_i$, $\dot{w}_i$ are the correspondent translational velocities. By substituting the rigid displacement relations of Eq. (C.14) into Eq. (C.21) and enforcing the equivalence $\tilde{\mathcal{T}} = \mathcal{T}$, the following inertial properties of the equivalent beam model are obtained:

$$
\begin{aligned}
&m=\frac{1}{h}\sum_{k=1}^{n_c}M_k, \quad I_{xx}=\frac{1}{h}\sum_{k=1}^{n_c}M_k\left(y_k^2+z_k^2\right), \quad I_{yy}=\frac{1}{h}\sum_{k=1}^{n_c}M_k z_k^2, \quad I_{zz}=\frac{1}{h}\sum_{k=1}^{n_c}M_k y_k^2,\\
&I_y=\frac{1}{h}\sum_{k=1}^{n_c}M_k z_k, \quad I_z=\frac{1}{h}\sum_{k=1}^{n_c}M_k y_k, \quad I_{yz}=\frac{1}{h}\sum_{k=1}^{n_c}M_k y_k z_k.
\end{aligned}
\tag{C.22}
$$

C.3 Numerical results

Numerical analyses are performed on two spatial frame structures, taken as case studies, composed of $n_x = 20$ floors with height $h = 4$ m. The buildings are made of concrete with elastic modulus $E = 3\times10^7$kN/m^2, Poisson's coefficient $\nu = 0.2$ and mass density $\rho = 2500\,\mathrm{kg/m^3}$.

The first configuration, case study I, is characterized by double symmetry of the floor plan, equal spans, and uniform cross-sections for all beams. The columns also share the same cross-section, which differs from that of the beams but is identical among themselves. The second configuration, case study II, introduces a controlled degree of asymmetry: the floor plan is symmetric with respect to only one principal axis, the spans remain equal, and the beams retain the same cross-section, while the columns exhibit a distinct cross-section among themselves. These two configurations may be classified as a regular frame and a semi-regular frame (see Fig. C.2), respectively.

As for the static analysis, a horizontal point force $P_z = 50$ kN is applied at each floor, except for the top free end, where a reduced force $P_z = 25$ kN is considered (see Fig. C.2). Beams and columns are modeled as Timoshenko beams, whose cross-sections geometries are reported in Tab. C.1.

Case study	**Type**	**Cross-sections** [cm]	A $[\mathrm{m}^2]$	A^*_ν $[\mathrm{m}^2]$	I_y $[\mathrm{m}^4]$	I_z $[\mathrm{m}^4]$	J $[\mathrm{m}^4]$
I, II	beam	40×70	0.28	0.23	1.14×10^{-2}	3.73×10^{-3}	9.61×10^{-3}
I	column	60×60	0.36	0.30	1.08×10^{-2}	1.08×10^{-2}	1.83×10^{-2}
II	column	70×70	0.49	0.41	2×10^{-2}	2×10^{-2}	3.39×10^{-2}
		70×50	0.35	0.29	7.29×10^{-3}	1.43×10^{-2}	1.63×10^{-2}
		50×70	0.35	0.29	1.43×10^{-2}	7.29×10^{-3}	1.63×10^{-2}
		40×100	0.40	0.33	3.33×10^{-2}	5.33×10^{-3}	1.59×10^{-2}

Table C.1. Cross-sections properties for the case studies I, II.

To validate the homogenized beam model, an FE model is built up in which, to account for the in-plane membrane stiffness of each floor, although its contribution to the overall cross-section stiffness is marginal, a body constraint is introduced at every level, ensuring that all joints belonging to the same floor share identical translations in the $y-$ and $z-$ directions and identical rotation about the $x-$axis. Each structural element is modeled without meshing refinement in the static analysis, whereas in the dynamic analysis every member is discretized into twenty finite elements.

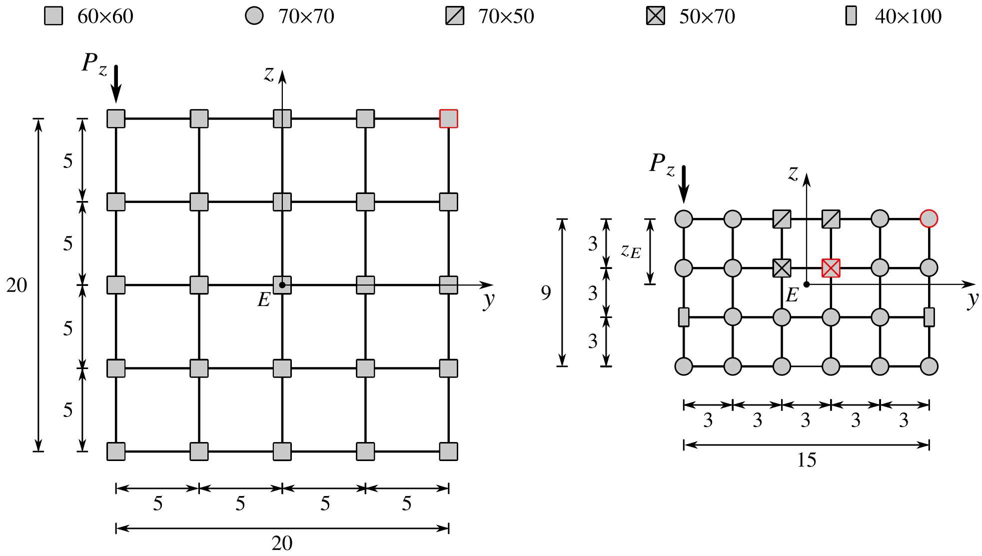

(a) (b)

Figure C.2. Case study: (a) I; (b) II.

Concerning the equivalent beam model, the centroid of the extensional stiffnesses, E (y_E, z_E), whose coordinates $(10, 10)$ and $(7.5, 4.63)$ for case studies I and II, respectively, is adopted as the reduction point O for computing the elastic properties. In Tab. C.2, all the nonzero elasto-geometric characteristics of the equivalent beam model are reported. The coarse model is loaded with distributed forces and moments, $p_z = -P_z/h$ and $c_x = (P_z/h)\, y_E$, respectively, and the column alignments selected for the comparison between the fine and coarse models are shown in red in Fig. C.2. The static solution of the equivalent beam model is obtained in closed form for both case studies. As for the dynamic eigenvalue problem, an exact solution is derived only for case study I, while in case study II the governing equations are too coupled to admit a closed form solution; therefore, the finite-difference method is employed.

The aim of the following analyses is to assess the capability of the analytically identified equivalent beam model to reproduce the static and dynamic responses of spatial frames. In the following figures, the displacement and abscissa unit is m, the dark gray continuous line describes the equivalent beam model's solution, the light gray dots represent the FE solution.

		Case study I	Case study II
c_{11}	[kN]	2.70×10^{8}	3.31×10^{8}
c_{22}	[kN]	2.32×10^{6}	3.50×10^{6}
c_{33}	[kN]	2.32×10^{6}	3.42×10^{6}
c_{44}	[kN$\times$m^2]	2.37×10^{8}	1.52×10^{8}
c_{55}	[kN$\times$m^2]	1.35×10^{10}	3.78×10^{9}
c_{66}	[kN$\times$m^2]	1.35×10^{10}	8.93×10^{9}
c_{24}	[kN$\times$m]	[$-$]	-6.35×10^{4}
χ_y	[$-$]	0.41	0.41
χ_z	[$-$]	0.41	0.36
m	[kg/m]	5.97×10^{4}	4.75×10^{4}
I_{xx}	[kg$\times$m]	5.64×10^{6}	1.71×10^{6}
I_{yy}	[kg$\times$m]	2.87×10^{6}	5.10×10^{5}
I_{zz}	[kg$\times$m]	2.76×10^{6}	1.20×10^{6}
I_y	[kg]	$-$	2.55×10^{3}

Table C.2. Elasto-geometric, mass coefficients and shear factors of the equivalent beam model of case study I (regular layout) and case study II (semi regular layout).

Statics

The analytical (exact) solution of the equivalent beam model is compared with numerical results obtained by FE models relevant to the macro beam model in terms of: (i) lateral displacement of the alignment of columns highlighted in red in Fig. C.2, namely $w\,(x) = w_O + \theta_x\, y_k$; (ii) torsional angle $\theta_x\,(x)$ of the cross-section; and (iii) vertical displacement of the floor at selected floors $x = \bar{x}$ and abscissa y_k, namely $u\,(\bar{x}, y_k, z) = u_O\,(\bar{x}) - \theta_z\,(\bar{x})\, y_k + \theta_y\,(\bar{x})\, z$.

In Fig. C.3a and Fig. C.4a results for case studies I and II in terms of lateral and torsional displacements, are reported.
As expected, for case study I (the regular layout) an excellent agreement is observed between the equivalent beam model and the FE model; in fact, the percentage error evaluated at $x = \ell$ is about 1.68% for $w\,(x)$ and 0.93% for $\theta_x\,(x)$. Instead, for case study II (the semi regular layout) the error starts to increase, about -20.30% and 13.94% for $w\,(x)$ and $\theta_x\,(x)$, respectively. These results clearly indicate that the coarse model does not adequately capture torsional effects; consequently, since the lateral displacements are evaluated using the rigid displacement formula (Eq. (C.14)), the error also affects $w\,(x)$. Furthermore, the farther the chosen column alignment lies from the reduction pole, the larger the resulting error. This occurs because, in the displacement's evaluation the torsional angle $\theta_x\,(x)$ multiplies the abscissa $y_k$of the considered column, thereby amplifying the torsional error already present. In fact, for column alignments located closer to E the percentage error decreases; for example at $(1.5, 1.63)$ it is -1.68%.
It becomes clear that the procedure used to identify the elastic constants through the shear-factor method is able to reproduce the global response of spatial frames with reasonable accuracy, but only when the structural layout is sufficiently regular. This limitation stems

not only from the inherently approximate nature of the method, but also from the lack of a rigorous definition of the shear factor when beams and columns are assigned different cross-sections. In fact, for the semi-regular frame studied in this Appendix, its value has been derived from a weighted average of the column's and beam's geometric properties, thereby further reducing the accuracy of the identification. Moreover, in case studies where the spatial frame does not exhibit double symmetry in plan, an additional problem arises: the stiffness centers E and S do not coincide and, as already mentioned, while the evaluation of E is straightforward, regardless of whether the cross-section is rigid (in plane and out of plane) or not, the evaluation of S is significantly more complex. Its analytical identification relies on overly strong approximations, ultimately leading to errors considerably larger than those obtained through numerical (and therefore exact) evaluation.

In Fig. C.3b and C.4b are also reported the comparisons in terms of out of plane displacements of the cross-sections at selected abscissas $\bar{x} = h, \ell/2, \ell$. In both the regular and semi-regular spatial frames, the equivalent beam model is able to provide the deformation of the cross-sections only on average. This is a limitation due to the decision to adopt a rigid cross-section model as the target one.

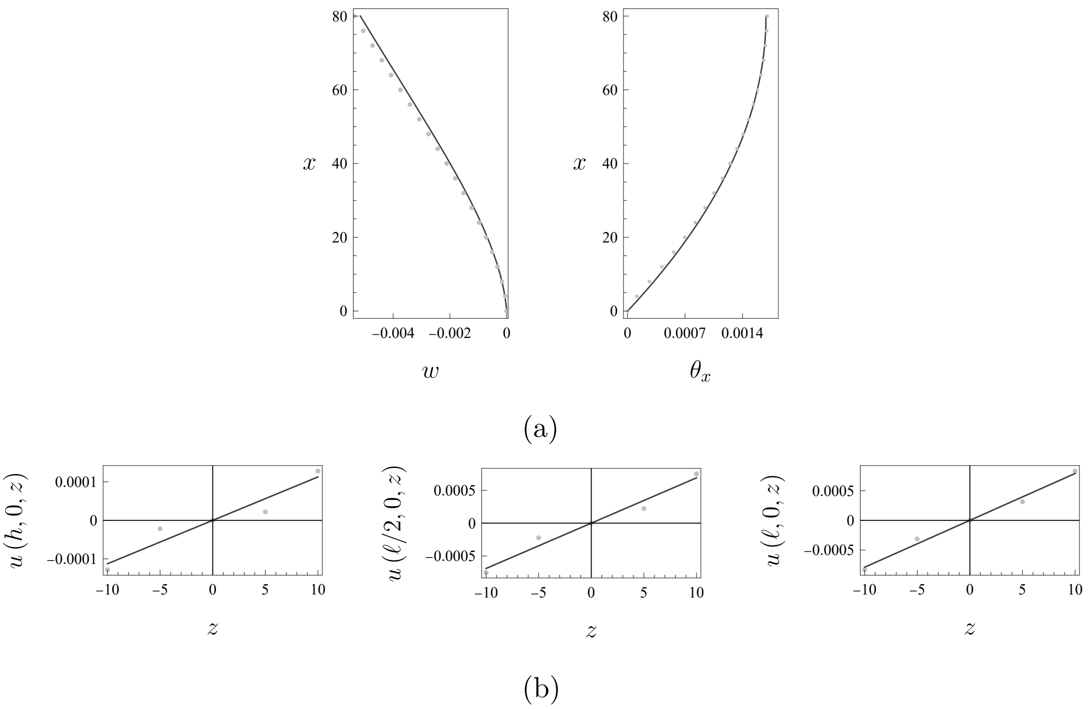

Figure C.3. Static response of the equivalent model vs. FE model for case study I: (a) lateral displacement in $(10, 10)$ and torsional displacement of the cross-section, (b) vertical displacements of the cross-section joints at $u\,(h, 0, z)$, $u\,(\ell/2, 0, z)$ and $u\,(\ell, 0, z)$, respectively. Light gray dots: discrete FE solution. Dark gray line: homogenized beam model.

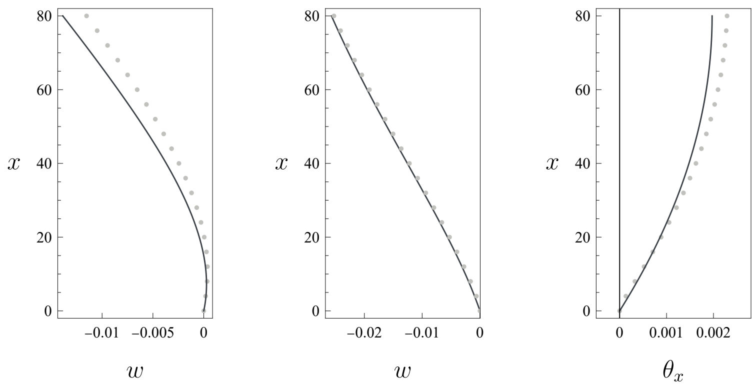

(a)

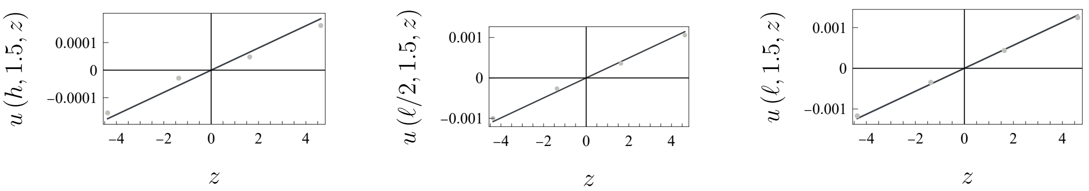

(b)

Figure C.4. Static response of the equivalent model vs. FE model for case study II: (a) lateral displacement in $(7.5, 4.63)$, $(1.5, 1.63)$ and torsional displacement of the cross-section, (b) vertical displacements of the cross-section joints at $u\,(h, 1.5, z)$, $u\,(\ell/2, 1.5, z)$ and $u\,(\ell, 1.5, z)$, respectively. Light gray dots: discrete FE solution. Dark gray line: homogenized beam model.

It is important to remark that the reference model adopted throughout this work is the Timoshenko beam model, that is, a one-dimensional continuum formulation based on the assumption of rigid cross-sections, both in and out of plane. In the FE model, the in plane stiffness is ensured by enforcing a body constraint, which effectively accounts, albeit in an approximate manner, for the presence of the floor, which is not explicitly modeled. Conversely, the out of plane stiffness, and consequently the cross-section's ability to undergo warping, is entirely governed by the stiffness of the beams at each cross-section. Therefore, an increase in the beam height results in a corresponding increase in the flexural stiffness of the cross-section and, for this reason, the case studies analyzed herein employ beams with relatively large cross-sections. This aspect can be demonstrated by studying the regular frame, case study I, for which it has been shown that the equivalent Timoshenko beam model accurately reproduces the system's response when beams with a 40×70 cross-section are used, with beams with a 30×40 cross-section (see Fig. C.5).

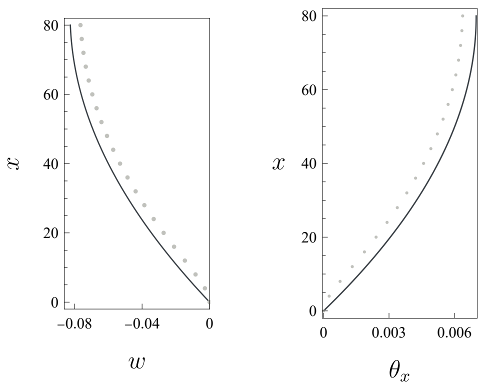

(a)

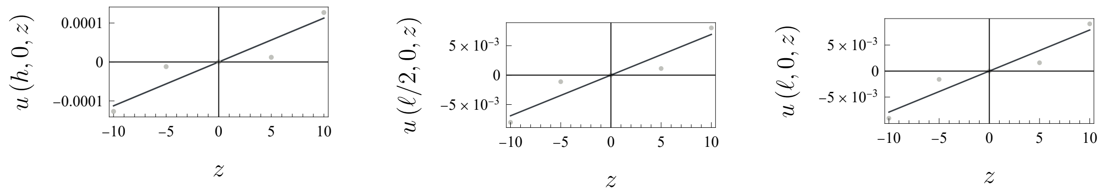

(b)

Figure C.5. Static response of the equivalent model vs. FE model for case study I with beams 30×40: (a) lateral displacement in $(10, 10)$ and torsional displacement of the cross-section, (b) vertical displacements of the cross-section joints at $u(h, 0, z)$, $u(\ell/2, 0, z)$ and $u(\ell, 0, z)$, respectively. Light gray dots: discrete FE solution. Dark gray line: homogenized beam model.

Free dynamics

The dynamic eigenvalue problem is formulated by imposing $\mathbf{p} = \mathbf{P} = \mathbf{0}$ and $\mathbf{u} = \hat{\mathbf{u}}(x)\, e^{\lambda t}$, where λ and $\hat{\mathbf{u}}(x)$ denote the eigenvalues and eigenvectors of the system, respectively, in Eqs. (C.7). This substitution transforms the governing equations into the following (spatial) boundary value problem.

$$\begin{aligned} \mathbf{K}_2\hat{\mathbf{u}}'' + \mathbf{K}_1\hat{\mathbf{u}}' + \mathbf{K}_0\hat{\mathbf{u}} - \lambda^2\mathbf{M}\hat{\mathbf{u}} &= \mathbf{0} \\ \hat{\mathbf{u}}_A &= \mathbf{0} \\ \mathbf{B}_1\hat{\mathbf{u}}'_B + \mathbf{B}_0\hat{\mathbf{u}}_B &= \mathbf{0} \end{aligned} \tag{C.23}$$

Owing to the conservative nature of the system, the resulting eigenvalues appear in purely imaginary, namely $\lambda_j = \pm i\omega_j$, with ω_j being the angular frequency of the $j-$th mode. In this scenario, when the equation of motion remains sufficiently uncoupled, the closed-form solution is theoretically attainable, although it still requires the numerical solution of the dispersion relation between the eigenvalue λ and the wave-number μ.

For the cases at hand, as already mentioned, an exact analytical solution is feasible only for case study I, whereas the solution of case study II is obtained with the finite difference method. This latter is addressed by transforming the differential problem Eq. (C.23) into an algebraic one. To this end, the equations of motion are discretized dividing the domain $[0, \ell]$ in L elements and $L+1$ nodes of coordinates $x_i = i\Delta$ $(i = 0, 1, \ldots, L)$, with $\Delta := \ell/L$. Given the boundary condition adopted for the dynamic analysis, a dummy node $L+1$, of coordinates $x_{L+1} = (L+1)\,\Delta$, is added. By using central finite differences, the derivatives era approximated as follows:

$$\hat{\mathbf{u}}_i = \hat{\mathbf{u}}\left(x_i\right), \quad \hat{\mathbf{u}}_i' = \frac{\hat{\mathbf{u}}_{i+1} - \hat{\mathbf{u}}_{i-1}}{2\Delta}, \quad \hat{\mathbf{u}}_i'' = \frac{\hat{\mathbf{u}}_{i+1} - 2\hat{\mathbf{u}}_i + \hat{\mathbf{u}}_{i-1}}{\Delta^2}. \tag{C.24}$$

Therefore, Eq. (C.23) in compact form reads as

$$\left(\mathbf{K} - \lambda^2 \mathbf{M}\right) \mathbf{u} = \mathbf{0} \tag{C.25}$$

where $\mathbf{K}$ and $\mathbf{M}$ are the (discrete) stiffness and mass matrices, having dimensions $6\,(L+2) \times 6\,(L+2)$, and $\mathbf{u} = \left(\hat{\mathbf{u}}_0, \ldots, \hat{\mathbf{u}}_L, \hat{\mathbf{u}}_{L+1}\right)^T$. Eq. (C.25) is solved by standard numerical algorithms.

The analytical solutions are compared up to the sixth mode with FE results for both case studies. The comparison between the frequencies is reported in Tab. C.3 where $\epsilon = 100\left(\omega_{EQ} - \omega_{FE}\right)/\omega_{EQ}$ is the percentage error. A very good correspondence is found between the two models for both case studies; in fact the greater difference is up to about 3% in case study I for the sixth mode. As for case study II, to obtain a percentage error lower than 1% on the first mode, the equivalent beam model was discretized using $L = 300$. Naturally, increasing L allows the finite-difference solution, being an approximate scheme, to progressively approach the exact one. Even though L is high for the semi-regular case, the number of degrees of freedom of the equivalent model remains significantly smaller than that of the FE model, and therefore the computational effort is considerably reduced.

Case study I is affected by purely flexural or torsional modes due to the bi-symmetric layout, while case study II is affected by extensional-flexural and flexural-torsional modes. In Fig. C.6 and C.7 are reported the modal shapes of the first six modes for both case studies and, as expected, the good accordance already observed from the frequencies' comparison, is confirmed.

Case study	**Mode**	**Type**	ω_{EQ} [rad]	ω_{FE} [rad]	ϵ [−]
I	1,2	1st Flexural (x, z)-plane, 1st Flexural (x, y)-plane	3.52	3.50	−0.61
	3	1st Torsional	4.03	4.14	−2.69
	4,5	2nd Flexural (x, z)-plane, 2nd Flexural (x, y)-plane	10.71	10.77	−0.60
	6	2nd Torsional	12.08	12.48	−3.34
II	1	1st Extensional - Flexural (x, z)-plane	3.59	3.56	1.00
	2	1st Extensional - Flexural (x, y)-plane	4.32	4.23	2.02
	3	1st Torsional	5.63	5.48	2.80
	4	2nd Extensional - Flexural (x, z)-plane	12.30	12.47	−1.36
	5	2nd Extensional - Flexural (x, y)-plane	13.57	13.56	0.06
	6	2nd Torsional	16.90	16.65	1.52

Table C.3. Angular frequencies of the first six modes for case studies I and II. ω_{EQ} and ω_{FE} refer to Equivalent beam Model and the FE Model, respectively.

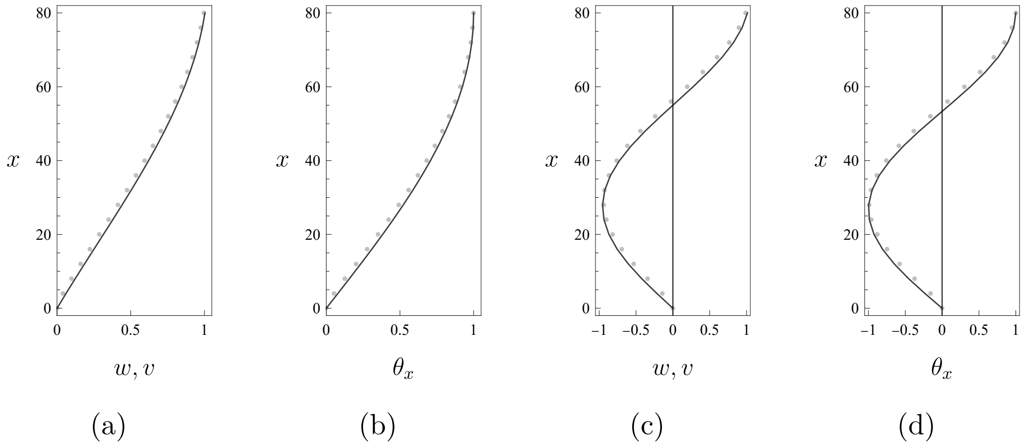

Figure C.6. Modal shapes of the equivalent model vs. discrete FE model for case study I: (a,b) first flexural and torsional mode; (c,d) second flexural and torsional mode, respectively. Light gray dots: discrete FE solution. Dark gray line: homogenized beam model.

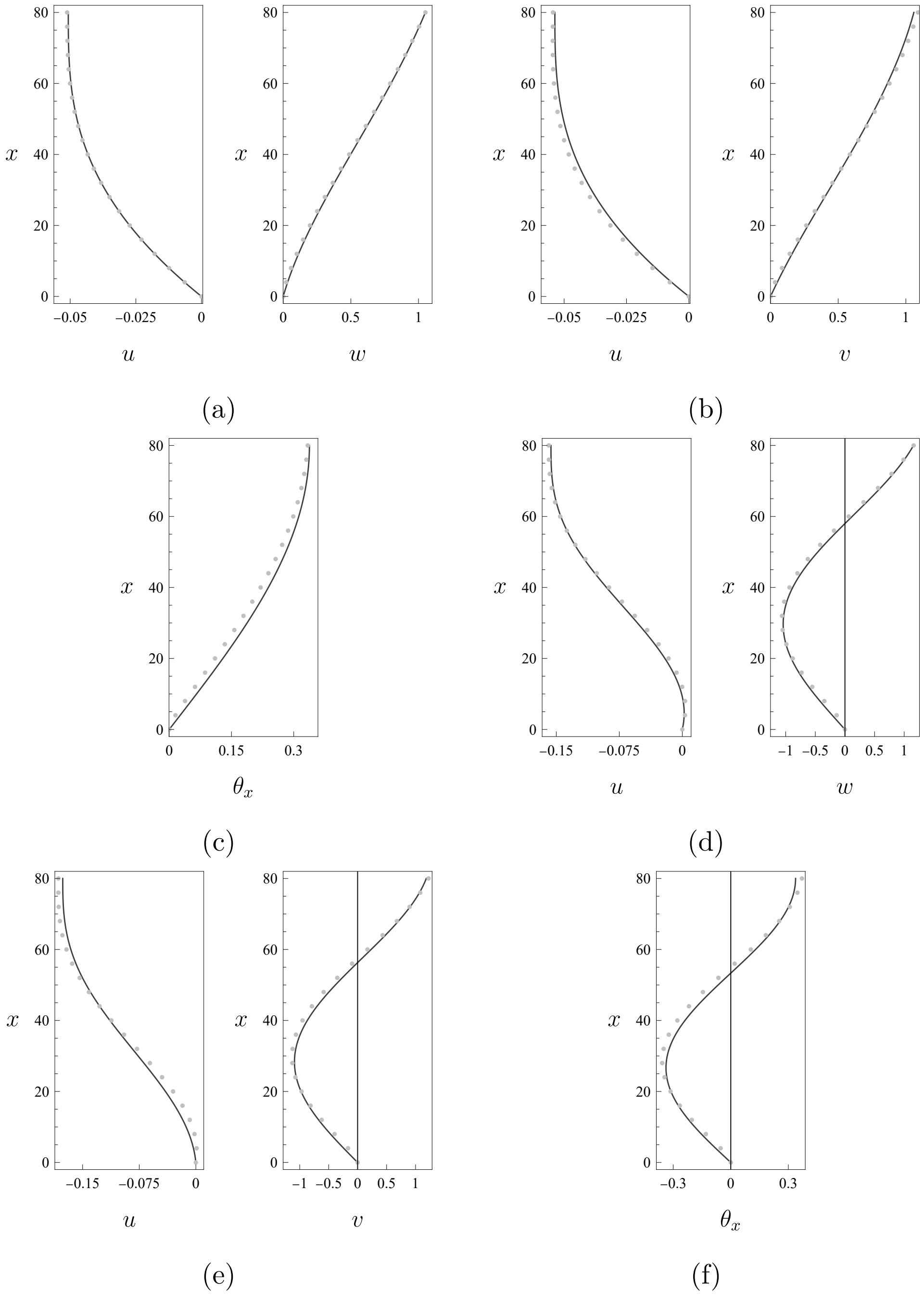

Figure C.7. Modal shapes of the equivalent model vs. discrete FE model for case study II: (a) first extensional-flexural (x, z)-plane; (b) first extensional-flexural (x, y)-plane; (c) first torsional; (d) second extensional-flexural (x, z)-plane; (e) second extensional-flexural (x, y)-plane; (f) second torsional. Light gray dots discrete FE solution. Dark gray line: homogenized beam model.

C.4 Conclusions

In this Appendix, an equivalent beam model was formulated in the framework to analyze the static and the dynamic of some spatial frames taken as case studies. The constitutive law was determined via the analytical mixed homogenization procedure and the warping of the cross-section, caused by shear and torsion, is approximately taken into account through a corrective factor ("shear" factor). The inertial properties are analytically identified under the hypothesis of lumped masses at joints. The limits of applicability of the Timoshenko beam model have been discussed by finite-element analyses. The following conclusions are drawn.

The results presented in this Appendix show that when the structural layout is sufficiently regular and the number of floors is large, the mixed homogenization approach, based on selecting a rigid cross-section beam as the target model and accounting for out-of-plane deformability through the introduction of a shear factor, can be a powerful tool for evaluating the global response of spatial frames characterized by rigid in plane but deformable out of plane cross-section.

For realistic case studies that do not necessarily fall into the category of very tall, highly regular buildings, like skyscrapers, the mixed homogenization technique remains a promising strategy for model reduction and for gaining insight into the global structural behavior. However, in such configurations, it is generally insufficient to rely on a rigid cross-section beam as the target model or to account for warping and out of plane deformability solely through a reduction of the shear stiffness via an empirical shear factor, as was done here for illustrative purposes.
In these more complex configurations, it is instead advisable to select, as equivalent continuum, a target model endowed with a richer kinematics, capable of explicitly describing out of plane warping and more general deformation patterns of the cross-section, such as a generalized beam model. Within this enhanced framework, the mixed homogenization approach could be systematically extended to derive effective elastic and inertial properties that more faithfully reflect the true 3D behavior of realistic spatial frames, beyond the limitations inherent to rigid-section formulations.

Bibliography

[1] A. Misra, N. Nejadsadeghi, M. De Angelo, and L. Placidi. Chiral metamaterial predicted by granular micromechanics: verified with 1d example synthesized using additive manufacturing. *Continuum Mechanics and Thermodynamics*, 32:1497–1513, 2020.

[2] M. De Angelo, L. Placidi, N. Nejadsadeghi, and A. Misra. Non-standard timoshenko beam model for chiral metamaterial: Identification of stiffness parameters. *Mechanics Research Communications*, 103:103462, 2020.

[3] N. Nejadsadeghi, F. Hild, and A. Misra. Parametric experimentation to evaluate chiral bars representative of granular motif. *International Journal of Mechanical Sciences*, 221:107184, 2022.

[4] N. Nejadsadeghi, M. De Angelo, A. Misra, and F. Hild. Multiscalar dic analyses of granular string under stretch reveal non-standard deformation mechanisms. *International Journal of Solids and Structures*, 239-240:111402, 2022.

[5] T. Maconachie, M. Leary, B. Lozanovski, X. Zhang, M. Qian, O. Faruque, and M. Brandt. Slm lattice structures: Properties, performance, applications and challenges. *Materials & Design*, 183:108137, 2019.

[6] A. Nazir, K. M. Abate, A. Kumar, and J. Jeng. A state-of-the-art review on types, design, optimization, and additive manufacturing of cellular structures. *The International Journal of Advanced Manufacturing Technology*, 104:3489–3510, 2019.

[7] F. dell'Isola, P. Seppecher, M. Spagnuolo, E. Barchiesi, F. Hild, T. Lekszycki, I. Giorgio, L. Placidi, U. Andreaus, M. Cuomo, et al. Advances in pantographic structures: design, manufacturing, models, experiments and image analyses. *Continuum Mechanics and Thermodynamics*, 31:1231–1282, 2019.

[8] F. dell'Isola, P. Seppecher, J. J. Alibert, et al. Pantographic metamaterials: an example of mathematically driven design and of its technological challenges. *Continuum Mechanics and Thermodynamics*, 31(4):851–884, 2019.

[9] A. Ciallella, I. Giorgio, E. Barchiesi, G. Alaimo, A. Cattenone, B. Smaniotto, A. Vintache, F. D'Annibale, F. dell'Isola, F. Hild, et al. A 3d pantographic metamaterial

behaving as a mechanical shield: experimental and numerical evidence. *Materials & Design*, page 112554, 2023.

[10] G. P Borikar, A. R. Patil, and S. B. Kolekar. Additively manufactured lattice structures and materials: Present progress and future scope. *International Journal of Precision Engineering and Manufacturing*, 24(11):2133–2180, 2023.

[11] E. Barchiesi, M. Spagnuolo, and L. Placidi. Mechanical metamaterials: a state of the art. *Mathematics and Mechanics of Solids*, 24(1):212–234, 2019.

[12] A. Casalotti, F. D'Annibale, and G. Rosi. Multi-scale design of an architected composite structure with optimized graded properties. *Composite Structures*, page 112608, 2020.

[13] A. Carcaterra, F. dell'Isola, R. Esposito, and M. Pulvirenti. Macroscopic description of microscopically strongly inhomogenous systems: A mathematical basis for the synthesis of higher gradients metamaterials. *Archive for Rational Mechanics and Analysis*, 218(3), 2015.

[14] E. Turco, E. Barchiesi, I. Giorgio, and F. dell'Isola. A lagrangian hencky-type nonlinear model suitable for metamaterials design of shearable and extensible slender deformable bodies alternative to timoshenko theory. *International Journal of Non-Linear Mechanics*, 123:103481, 2020.

[15] I. Giorgio, A. Misra, and L. Placidi. *Geometrically Nonlinear Cosserat Elasticity with Chiral Effects Based upon Granular Micromechanics*, pages 273–292. 02 2023.

[16] J. P. McInerney, O. Oudghiri-Idrissi, C. L. Willey, S. Tol, X. Mao, and A. Juhl. Topological polarization of kagome tubes and applications toward vibration isolation. *Phys. Rev. Appl.*, 24:044037, Oct 2025.

[17] L. D'Alessandro, R. Ardito, F. Braghin, and A. Corigliano. Low frequency 3d ultra-wide vibration attenuation via elastic metamaterial. *Scientific Reports*, 9, 05 2019.

[18] A. K. Noor. Continuum modeling for repetitive lattice structures. *Applied Mechanics Reviews*, 41(7):285–296, 1988.

[19] H. Tollenaere and D. Caillerie. Continuous modeling of lattice structures by homogenization. *Advances in Engineering Software*, 29(7):699 – 705, 1998.

[20] C. Chesnais, C. Boutin, and S. Hans. *Structural Dynamics and Generalized Continua*, pages 57–76. Springer Berlin Heidelberg, Berlin, Heidelberg, 2011.

[21] C. Pan, Y. Han, and J. Lu. Design and optimization of lattice structures: A review. *Applied Sciences*, 10(18):6374, 2020.

[22] J. Somnic and B. W. Jo. Status and challenges in homogenization methods for lattice materials. *Materials*, 15(2):605, 2022.

[23] M. J. Chajes, K. M. Romstad, and D. B. McCallen. Analysis of multiple-bay frames using continuum model. *Journal of Structural Engineering*, 119(2):522–546, 1993.

[24] K. A. Zalka. *Global structural analysis of buildings.* CRC Press, 2002.

[25] G. Potzta and L.P. Kollár. Analysis of building structures by replacement sandwich beams. *International Journal of Solids and Structures*, 40(3):535–553, 2003.

[26] C. Boutin and S. Hans. Homogenisation of periodic discrete medium: Application to dynamics of framed structures. *Computers and Geotechnics*, 30(4):303–320, 2003.

[27] S. Hans and C. Boutin. Dynamics of discrete framed structures: A unified homogenized description. *Journal of Mechanics of Materials and Structures*, 3(9):1709–1739, 2008.

[28] A. Luongo. Statics, dynamics, buckling and aeroelastic stability of planar cellular beams. In N. Challamel, J. Kaplunov, and I. Takewaki, editors, *Modern trends in structural and solid mechanics*, pages 143–165. ISTE-Wiley, 2021.

[29] S. Di Nino and A. Luongo. Nonlinear aeroelastic behavior of a base-isolated beam under steady wind flow. *International Journal of Non-Linear Mechanics*, 119:103340, 2020.

[30] F. D'Annibale, M. Ferretti, and A. Luongo. Shear-shear-torsional homogenous beam models for nonlinear periodic beam-like structures. *Engineering Structures*, 184:115–133, 2019.

[31] G. Piccardo, F. Tubino, and A. Luongo. A shear–shear torsional beam model for nonlinear aeroelastic analysis of tower buildings. *Zeitschrift für angewandte Mathematik und Physik*, 66(4):1895–1913, 2015.

[32] G. Piccardo, F. Tubino, and A. Luongo. Equivalent nonlinear beam model for the 3-d analysis of shear-type buildings: Application to aeroelastic instability. *International Journal of Non-Linear Mechanics*, 80:52–65, 2016.

[33] G. Piccardo, F. Tubino, and A. Luongo. Equivalent timoshenko linear beam model for the static and dynamic analysis of tower buildings. *Applied Mathematical Modelling*, 71:77–95, 2019.

[34] M. Ferretti. Flexural torsional buckling of uniformly compressed beam-like structures. *Continuum Mechanics and Thermodynamics*, 30(5):977–993, 2018.

[35] M. Ferretti, F. D'Annibale, and A. Luongo. Modeling beam-like planar structures by a one-dimensional continuum: an analytical-numerical method. *Journal of Applied and Computational Mechanics*, 7(Special Issue):1020–1033, 2021.

[36] M. Ferretti and F. D'Annibale. Buckling of planar micro-structured beams. *Applied Sciences*, 10(18):6506, 2020.

[37] F. D'Annibale, M. Ferretti, and A. Luongo. Static and dynamic responses of micro-structured beams. *Applied Sciences*, 10(19), 2020.

[38] C. T. Sun, B. J. Kim, and J. L. Bogdanoff. On the derivation of equivalent simple models for beam-and plate-like structures in dynamic analysis. In *Dynamics Specialists Conference*, page 624, 1981.

[39] T. Li and Y. Li. Prediction of the anisotropy of chiral mechanical metamaterials via micropolar modeling. *Journal of Applied Mechanics*, 89(10):101006, 2022.

[40] M. Askari, D. A. Hutchins, P. J. Thomas, L. Astolfi, R. L. Watson, M. Abdi, M. Ricci, S. Laureti, L. Nie, S. Freear, R. Wildman, C. Tuck, M. Clarke, E. Woods, and A. T. Clare. Additive manufacturing of metamaterials: A review. *Additive Manufacturing*, 36:101562, 2020.

[41] L. Mizzi, A. Simonetti, and A. Spaggiari. Mechanical properties and failure modes of additively-manufactured chiral metamaterials based on euclidean tessellations: an experimental and finite element study. *Rapid Prototyping Journal*, 30(11):59–71.

[42] N. Karathanasopoulos, F. Dos Reis, M. Diamantopoulou, and J.-F. Ganghoffer. Mechanics of beams made from chiral metamaterials: Tuning deflections through normal-shear strain couplings. *Materials & Design*, 189:108520, 2020.

[43] I. Giorgio, F. dell'Isola, and A. Misra. Chirality in 2d cosserat media related to stretch-micro-rotation coupling with links to granular micromechanics. *International Journal of Solids and Structures*, 202:28–38, 2020.

[44] M. Ji, Y. Cho, S.-J. Lee, and K. Park. Design and analysis of three-dimensional chiral metamaterials for enhanced torsional compliance. *Smart Materials and Structures*, 2024.

[45] T. Li and Y. Li. Mechanical behaviors of three-dimensional chiral mechanical metamaterials. *Composites Part B: Engineering*, 270:111141, 2024.

[46] G. Lin, J. Li, P. Chen, W. Sun, S. Chizhik, A. Makhaniok, G. Melnikova, and T. Kuznetsova. Buckling of lattice columns made from three-dimensional chiral mechanical metamaterials. *International Journal of Mechanical Sciences*, 194:106208, 03 2021.

[47] Healey TJ. Material symmetry and chirality in nonlinearly elastic rods. *Mathematics and Mechanics of Solids*, 7(4):405–420, 2002.

[48] C. R. Calladine and H. Drew. *Understanding DNA: the molecule and how it works.* Academic press, 1997.

[49] G. A. Costello. *Theory of wire rope.* Springer Science & Business Media, 1997.

[50] E. Barchiesi, F. dell'Isola, P. Seppecher, and E. Turco. A beam model for duoskelion structures derived by asymptotic homogenization and its application to axial loading problems. *European Journal of Mechanics - A/Solids*, 98:104848, 2023.

[51] E. Turco, E. Barchiesi, and F. dell'Isola. In-plane dynamic buckling of duoskelion beam-like structures: discrete modeling and numerical results. *Mathematics and Mechanics of Solids*, 27(7):1164–1184, 2022.

[52] R.. McAvoy and E. Barchiesi. Towards the galerkin approximation of tetraskelion metamaterials. *Continuum Mechanics and Thermodynamics*, 37(6), 2025.

[53] I. Giorgio, F. Hild, E. Gerami, F. dell'Isola, and A. Misra. Experimental verification of 2d cosserat chirality with stretch-micro-rotation coupling in orthotropic metamaterials with granular motif. *Mechanics Research Communications*, 126:104020, 2022.

[54] B. E. Abali and E. Barchiesi. Additive manufacturing introduced substructure and computational determination of metamaterials parameters by means of the asymptotic homogenization. *Continuum Mechanics and Thermodynamics*, 33, 07 2021.

[55] C. Pancella and F. D'Annibale. A timoshenko-like equivalent beam model for the static analysis of a chiral metamaterial. *Continuum Mechanics and Thermodynamics*, 37(4):59, July 2025.

[56] F. Trentadue, G. Caramia, D. De Tommasi, N. Marasciuolo, and G. Vitucci. Elastic stability of a lattice of cross-braced shear deformable beams. *European Journal of Mechanics - A/Solids*, 102:105118, 2023.

[57] N. Marasciuolo, D. De Tommasi, F. Trentadue, and G. Vitucci. Tailored multiscale instabilities in a grid metamaterial. *Extreme Mechanics Letters*, 75:102284, 2025.

[58] M. Ferretti, F. D'Annibale, and A. Luongo. Buckling of tower buildings on elastic foundation under compressive tip forces and self-weight. *Continuum Mechanics and Thermodynamics*, 35, 08 2020.

[59] A. Luongo and D. Zulli. Free and forced linear dynamics of a homogeneous model for beam-like structures. *Meccanica*, 55(4):907–925, 2020.

[60] A. Luongo, F. D'Annibale, and M. Ferretti. Shear and flexural factors for static analysis of homogenized beam models of planar frames. *Engineering Structures*, 228:111440, 2021.

[61] R. Schardt. *Verallgemeinerte Technische Biegetheorie*. Springer Berlin, Heidelberg, 1989.

[62] R. Schardt. Generalized beam theory—an adequate method for coupled stability problems. *Thin-Walled Structures*, 19(2):161–180, 1994.

[63] J.M. Davies, P. Leach, and D. Heinz. Second-order generalised beam theory. *Journal of Constructional Steel Research*, 31(2):221–241, 1994.

[64] J.M. Davies and P. Leach. First-order generalised beam theory. *Journal of Constructional Steel Research*, 31(2):187–220, 1994.

[65] N. Silvestre and D. Camotim. Second-order generalised beam theory for arbitrary orthotropic materials. *Thin-Walled Structures*, 40:791–820, 09 2002.

[66] N. Silvestre and D. Camotim. First-order generalised beam theory for arbitrary orthotropic materials. *Thin-Walled Structures*, 40(9):755–789, 2002.

[67] G. Ranzi and A. Luongo. A new approach for thin-walled member analysis in the framework of gbt. *Thin-Walled Structures*, 49(11):1404 – 1414, 2011.

[68] G. Piccardo, G. Ranzi, and A. Luongo. A complete dynamic approach to the generalized beam theory cross-section analysis including extension and shear modes. *Mathematics and Mechanics of Solids*, 19(8):900–924, 2014.

[69] G. Piccardo, G. Ranzi, and A. Luongo. A direct approach for the evaluation of the conventional modes within the gbt formulation. *Thin-Walled Structures*, 74:133–145, 2014.

[70] M. B. Rubin. *Cosserat theories : shells, rods, and points"*. Solid mechanics and its applications vol. 79. 2000.

[71] S. S. Antman and W. H. Warner. Dynamical theory of hyperelastic rods. *Archive for Rational Mechanics and Analysis*, 23(2):135–162, 1966.

[72] J. C. Simo. A finite strain beam formulation. the three-dimensional dynamic problem. part i. *Computer Methods in Applied Mechanics and Engineering*, 49(1):55–70, 1985.

[73] J.C. Simo and L. Vu-Quoc. On the dynamics in space of rods undergoing large motions — a geometrically exact approach. *Computer Methods in Applied Mechanics and Engineering*, 66(2):125–161, 1988.

[74] G. Ruta, M. Pignataro, and N. Rizzi. A direct one-dimensional beam model for the flexural-torsional buckling of thin-walled beams. *Journal of Mechanics of Materials and Structures - J MECH MATER STRUCT*, 1:1479–1496, 12 2006.

[75] M. Pignataro, N. Rizzi, G. Ruta, and V. Varano. The effects of warping constraints on the buckling of thin-walled structures. *Journal of Mechanics of Materials and Structures - J MECH MATER STRUCT*, 4:1711–1727, 02 2010.

[76] S. S. Antman. The theory of rods. In *Linear Theories of Elasticity and Thermoelasticity*, pages 641–703. Springer, 1973.

[77] S. S. Antman. *Nonlinear problems of elasticity*. Springer-Verlag, 2005.

[78] A. Luongo and D. Zulli. *Mathematical models of beams and cables.* John Wiley & Sons, 2013.

[79] I. Elishakoff. Who developed the so-called timoshenko beam theory? *Mathematics and Mechanics of Solids*, 25(1):97–116, 2020.

[80] A. Luongo and D. Zulli. A non-linear one-dimensional model of cross-deformable tubular beam. *International Journal of Non-Linear Mechanics*, 66:33–42, 2014. 4th Canadian Conference on Non-linear Solid Mechanics.

[81] M. Pignataro, N. Rizzi, and A. Luongo. *Bifurcation, Stability and Postcritical behaviour of elastic structures.* Elsevier Science Publisher, 1990.

[82] A. Luongo, M. Ferretti, and S Di Nino. *Stability and Bifurcation of Structures: Statical and Dynamical Systems.* 2023.

[83] A. Cazzani, F. Stochino, and E. Turco. On the whole spectrum of timoshenko beams. part i: a theoretical revisitation. *Zeitschrift für angewandte Mathematik und Physik*, 67(2):24, 2016.

[84] A. Cazzani, F. Stochino, and E. Turco. On the whole spectrum of timoshenko beams. part ii: further applications. *Zeitschrift für angewandte Mathematik und Physik*, 67(2):25, 2016.

[85] G. Capriz. A contribution to the theory of rods. *Riv. Mat. Univ. Parma*, 7(4):489–506, 1981.

[86] H. Altenbach, M. Bîrsan, and V. A. Eremeyev. Cosserat-type rods. In *Generalized Continua from the Theory to Engineering Applications*, pages 179–248. Springer, 2013.

[87] D. J. Steigmann and M. G. Faulkner. Variational theory for spatial rods. *Journal of Elasticity*, 33(1):1–26, 1993.

[88] I. Elishakoff. *Handbook on Timoshenko-Ehrenfest Beam and Uflyand-Mindlin Plate Theories.* World Scientific Publishing Company, 2016.

[89] H. Leclerc, J. Neggers, F. Mathieu, S. Roux, and F. Hild. Correli 3.0, 2015. *IDDN. FR*, 1(000).

[90] Hansen, P. C. *The L-Curve and its Use in the Numerical Treatment of Inverse Problems*, pages 119–142. WIT Press, 2001.